JWST : From a super-deblended infrared catalog to the study of high redshift dusty star-forming galaxies

Aurélien Le Bail

To cite this version:

Aurélien Le Bail. JWST : From a super-deblended infrared catalog to the study of high redshift dusty star-forming galaxies. Cosmology and Extra-Galactic Astrophysics [astro-ph.CO]. Université Paris-Saclay, 2023. English. NNT : 2023UPASP088 . tel-04278212

HAL Id: tel-04278212
https://theses.hal.science/tel-04278212v1

Submitted on 9 Nov 2023

JWST: From a super-deblended infrared catalog to the study of high redshift dusty star-forming galaxies

JWST : De l'élaboration d'un catalogue infrarouge à l'étude des galaxies poussiéreuses lointaines

Thèse de doctorat de l'université Paris-Saclay

École doctorale n°127, Astronomie et Astrophysique d'île-de-France (AAIF)
Spécialité de doctorat: Astronomie et Astrophysique
Graduate School : Physique. Référent : Faculté des sciences d'Orsay

Thèse préparée dans l'unité de recherche **Astrophysique, Instrumentation et Modélisation de Paris-Saclay** (Université Paris-Saclay, CNRS, CEA), sous la direction de **Emanuele DADDI**, Docteur en astrophysique

Thèse soutenue à Paris-Saclay, le 18 septembre 2023, par

Aurélien LE BAIL

Composition du jury

Membres du jury avec voix délibérative

Simona MEI Professeure, Astroparticule et Cosmologie (Université Paris Cité, CNRS/IN2P3, France)	Présidente
Johan FYNBO Professeur, The Cosmic Dawn Center (Institut Niels Bohr, Université de Copenhague, Danemark)	Rapporteur & Examinateur
Arjen VAN DER WEL Professeur, Sterrenkundig Observatorium (Université de Gand, Belgique)	Rapporteur & Examinateur
Laure CIESLA Docteure, Laboratoire d'Astrophysique de Marseille (Université Aix-Marseille, CNRS, France)	Examinatrice
Jérémy FENSCH Professeur associé, Centre de Recherche Astrophysique de Lyon (ENS Lyon, Université de Lyon, France)	Examinateur

THESE DE DOCTORAT

NNT : 2023UPASP088

université
PARIS-SACLAY

ÉCOLE DOCTORALE
Astronomie
et Astrophysique
d'Île-de-France (AAIF)

Titre: JWST: De l'élaboration d'un catalogue infrarouge à l'étude des galaxies poussiéreuses lointaines

Mots clés: Galaxie, Formation, Evolution, Bulbe, Formation d'etoiles

Résumé : Le jour de Noël 2021, le télescope spatial le plus puissant jamais construit par l'humanité a été envoyé dans l'espace. Ce télescope, le *James Webb*, avec son immense miroir et sa grande sensibilité dans l'infrarouge, promettait de révolutionner notre compréhension de l'Univers. Dans le cadre de la collaboration CEERS dirigée par S. Finkelstein, et afin d'être prêts dès la réception des premières images du télescope, j'ai construit un catalogue de sources brillantes dans l'infrarouge lointain ($24mu$m - 1.1mm). Pour ce faire, j'ai appliqué la méthode de pointe du "super-débruitage" développée par E. Daddi, D. Liu et S. Jin. Cette méthode repose sur une sélection active des sources à fitter basée sur des prédictions issues du fit de la distribution spectrale d'énergie (SED) de chaque galaxie. Ainsi, en mesurant des flux dans des images de plus en plus confuses, j'ai pu sélectionner les sources que je savais être les plus brillantes. Afin de mesurer les flux les plus réalistes possible, j'ai effectué des simulations de type Monte-Carlo pour corriger les biais de mesure et obtenir des incertitudes quasi-gaussiennes. Pour construire ce catalogue, j'ai exploité toutes les images prises par différents télescopes IR spatiaux et terrestres, à savoir *Spitzer*, *Herschel*, *JCMT*, *LMT* et le *VLA*, ce dernier permet une meilleure sélection des sources, en particulier à grand redshift. Sur la base de ce catalogue, qui est le catalogue infrarouge lointain le plus profond existant dans le champ EGS, j'ai sélectionné les sources les plus brillantes afin de les étudier à travers l'œil du *JWST*. J'ai étudié la morphologie et les propriétés physiques d'un échantillon de 22 galaxies poussiéreuses formant activement des étoiles (DSFG) sélectionnées dans l'IR au midi cosmique ($z \sim 2$), en utilisant les images de la caméra proche infrarouge du *JWST* obtenues dans le champ EGS pour CEERS. La résolution des images NIRCam m'a permis de résoudre spatialement ces galaxies jusqu'à 4.4μm et d'identifier leur bulbe/noyau même lorsqu'elles étaient très éteintes par la poussière. Sur la base d'images rouge-vert-bleues utilisant les filtres F115W, F200W et F444W, j'ai divisé chaque galaxie en plusieurs régions uniformément colorées, fitté leur SED respective et mesuré leur atténuations due à la poussière, leur masses stellaires, leur taux de formation d'étoiles et leur âges. Après avoir classé chaque région comme étant active ou passive, j'ai répartis les galaxies en trois classes, selon que la formation active d'étoiles était située dans le noyau, dans le disque ou dans les deux. Les principaux résultats sont les suivants : (i) ~ 70% de mes DSFGs ont un noyau actif compact fortement atténué par la poussière et qui peut contenir jusqu'à 80% de la formation d'étoiles de la galaxie mais seulement 20-30% de sa masse stellaire, et qui est toujours entouré d'un disque massif plus grand et moins atténué ; (ii) 64 % (27 %) des disques sont significativement (fortement) désaxés, probablement en raison d'une accrétion asymétrique de gaz froid, de fusions majeures et/ou d'instabilités à grande échelle ; (iii) 23 % des galaxies ont un coeur actif au sein d'un disque éteint, elles subissent une extinction de l'extérieur vers l'intérieur, souvent facilitée par leur forte asymétrie qui induit des instabilités à petite et à grande échelle ; (iv) certaines galaxies abritent des disques très hétérogènes en termes de couleurs RVB : ces disparités sont le résultat d'une atténuation in-homogène de la poussière ; et (v) j'ai trouvé des preuves surprenantes de l'existence de sous-structures en forme d'amas globulaire dans des régions éteintes. Le travail réalisé dans le cadre de cette thèse démontre l'incroyable puissance du *JWST* ainsi que son impact, puisqu'il permet pour la première fois de sonder les galaxies lointaines dans l'infrarouge et de les résoudre spatialement, permettant ainsi de révéler la complexité de leur formation et de leur évolution.

universite
PARIS-SACLAY

ÉCOLE DOCTORALE
Astronomie
et Astrophysique
d'Île-de-France (AAIF)

Title: JWST: From a super-deblended infrared catalog to the study of high redshift dusty star-forming galaxies

Keywords: Galaxy, Formation, Evolution, Bulges, Star-Formation

Abstract: On Christmas Day 2021, the most powerful space telescope ever built by mankind was sent into space. This telescope, the *James Webb*, with its huge mirror and high sensitivity in the infrared promised to revolutionize our understanding of the distant Universe. Within the framework of the CEERS collaboration led by S. Finkelstein, and in order to be fully prepared for the reception of the first images of the telescope, I built a catalog of bright sources in the far infrared (24μm - 1.1mm). To achieve this, I applied the state-of-the-art "super-deblending" method developed by E. Daddi, D. Liu and S. Jin. This method relies on an active selection of priors to fit based on predictions from spectral energy distribution (SED) fitting of each galaxy. Thus, by measuring fluxes in more and more confused images, I was able to select only the sources that I knew would be the brightest. In order to measure the most realistic fluxes, I performed Monte-Carlo simulations to correct the measurement bias and obtain Gaussian uncertainties. To build this catalog, I exploited all the images taken by different space-based and ground-based IR telescopes, namely *Spitzer*, *Herschel*, *JCMT*, *LMT* and the *VLA* for the radio allowing a better selection of priors, especially at high redshift. Based on this catalog, which is the deepest existing far-infrared catalog in the EGS field (which is the field of interest in this manuscript), I selected the brightest sources around cosmic noon ($1.5 < z < 3$) in order to study them through the eye of the *James Webb Space Telescope*. I investigated the morphology and physical properties of a sample of 22 IR-selected dusty star-forming galaxies (DSFGs) at Cosmic Noon ($z \sim 2$), using *JWST* Near Infra-Red Camera images obtained in the EGS field for the CEERS survey. The exceptional resolution of the NIRCam images allowed me to spatially resolve these galaxies up to 4.4μm and identify their bulge/core even when very extinguished by dust. Based on red-green-blue images using the F115W, F200W and F444W filters, I divided each galaxy in several uniformly colored regions, fitted their respective SED and measured dust attenuations, stellar masses, star formation rates and ages. After classifying each region as star-forming or quiescent, I assigned galaxies to three classes, depending on whether active star-formation was located in the core, in the disk or in both. The main results are: (i) ~ 70% of my DSFGs have a compact highly dust attenuated star-forming core that can contain up to 80% of the star-formation of the galaxy but only 20-30% of its stellar mass, and is always surrounded by a larger, less attenuated massive disk (no blue nuggets); (ii) 64% (27%) of disks are significantly (strongly) lopsided, likely due to asymmetric cold gas accretion, major mergers and/or large scale instabilities; (iii) 23% of galaxies have a star-forming core embedded in a quiescent disk, they are undergoing outside-in quenching, often facilitated by their strong lopsidedness inducing small and large scale instabilities; (iv) some galaxies host highly heterogeneous disks in terms of RGB colors: these are driven by in-homogeneous dust attenuation; and (v) I found surprising evidence for clump-like substructures being quiescent and/or residing in quiescent regions. The work carried out as part of this thesis demonstrates the incredible power of the *JWST* and its impact, as it enables for the first time to probe distant galaxies in the infrared and resolve them spatially, revealing the complexity of their formation and evolution.

école normale supérieure paris—saclay

université PARIS-SACLAY

Financement: Cette thèse est financée par un contrat doctoral spécifique pour normalien (CDSN). Les CDSN sont attribués par le ministère de l'éducation nationale, de l'enseignement supérieur et de la recherche aux écoles normales supérieures afin d'inciter leurs élèves à effectuer une thèse de doctorat. Les sujets de recherche associés à ces contrats ont vocation à concerner toutes les disciplines enseignées au sein de l'École et, au sein de celles-ci, toutes les thématiques. Les projets de recherche interdisciplinaires ou les thématiques pionnières sont également concernées. Les doctorants bénéficiant d'un CDSN ont vocation à être affectés aux meilleurs laboratoires de recherche français et sur l'ensemble du territoire. L'ENS transfert par convention le financement de chaque contrat à l'établissement de destination du futur normalien doctorant, ici l'université Paris-Saclay.

Laboratoire d'acceuil: Cette thèse a été effectuée au sein du Laboratoire de Cosmologie et d'Évolution des Galaxies (LCEG). Ce laboratoire est une des composantes du département d'Astrophysique (DAp) de l'Institut de Recherche sur les lois Fondamentales de l'Univers (IRFU) au sein de la Direction de la Recherche Fondamentale (DRF) du Commissariat à l'énergie atomique et aux énergies alternatives (CEA). Le DAp est membre de l'unité mixte de recherche Astrophysique, Instrumentation et Modélisation.

cea irfu

Remerciements/Acknowledgments:

Like all scientific projects, this thesis is the result of teamwork. I had the chance to be surrounded by wonderful people who taught me many things.

First, I want to acknowledge the CEERS collaboration and especially Steve Finkelstein from UT Austin and Mark Dickinson from NoirLab who allowed me to join them on day one of my thesis. They allowed me to be among the first people on Earth to get access to the amazing images of the *James Webb Space Telescope*.

Then, I want to acknowledge all the wonderful astronomers from the LCEG group at CEA that welcomed me and were my first contact with the scientific world, they immediately made me feel like one of their own. Thank you to Boris Kalita, Mengyuan Xiao, Chiara D'Eugenio, Carlos Gomez-Guijarro and to Frederic Bournaud, the head of the group. A special thank you to Shuowen Liu, who had left CEA by the time I arrived but still taught me everything I know on superdeblending, this work could not have been carried out without his precious help.

I also want to acknowledge my colleagues that arrived at the same time or later than me, they were always supportive and I learnt many things on their side. Thank you to Benjamin Magnelli, Lucas Leroy, Shiying Lu, Sicen Guo, Maxime Tarrasse, Yipeng Liu. A special thank you to Rose Coogan who taught me a lot and shared with me her adventure as an ESA astronaut candidate, I can't wait to see the movie "Becoming an astronaut".

I thank all the colleagues and friends from other groups with whom I had the chance to chat, have lunch with and have fun. You all made my stay at CEA memorable.

A very special thank you to Emanuele Daddi and David Elbaz who accepted me for the position and gave me a chance to prove myself. I thank them for all their support and wisdom, they taught me how to be a scientist and how to be a good astronomer. I could not have wanted better mentors. I am very grateful to Emanuele for always having my back and being here for me, especially when he went through a deeply painful event in his personal life.

Thank you to Vianney Lebouteiller and Marc Sauvage who were on my thesis committee and always made sure that everything was going smoothly and more or less according to plan. Their external view on the projects were always appreciated.

I want to thank CEA as an entity for letting me work and learn in very good conditions and allowing me to travel and meet colleagues from all around the world in conferences and giving me a chance to share my science at the same time.

Je tiens à remercier mes frères et soeurs Sophie, Maxime, Camille et Amandine qui m'ont toujours soutenu dans mes projets. Je remercie aussi mes parents Claude et Marie-Christine qui ont tout fais pour que les conditions de ma réussite à l'école soient réunies, n'hésitant pas à faire des sacrifices si nécessaire, de la primaire jusqu'au doctorat. Tous cela n'aurait pas été possible sans leur soutiens inconditionnel et leur volonté de me voir me dépasser.

Lastly, I want to thank a wonderful man who I met in Texas during my stay in Austin for the CEERS collaboration meeting. I want to thank him, because even if I met him toward the very end of my thesis, his support when I was writing this manuscript helped me in so many ways. Thank you Bacilio, for helping me become the Doctor I am now, and for letting me discover what falling in love means.

Contents

1 - INTRODUCTION

1.1 . A BRIEF OVERVIEW

For a very long time, we thought that our Universe wasn't larger than the Milky Way, our galaxy. The first hint that the universe was larger than the most distant stars one can see with the naked eye on a clear night came with the invention of the first telescopes. They allowed astronomers to observe strange fuzzy objects that were then called nebulae. The first nebulae were observed by C. Huygens in the mid-17^{th} century. Already in 1750 and 1755, T. Wright and I. Kant respectively explained that these objects could be at much larger distance than the stars and that the Milky Way could actually be one of these objects among many others. There fuzziness would then be explained by the great distance separating them from the observer. Many of these nebulae were catalogued by Messier in 1771 followed by the Herschel family. The debate about the nature of these nebulae would not be settled until 1925 when Edwin Hubble identified Cepheids in some of the nebulae and deduced that they were extremely distant objects. Hence, nebulae and spiral nebulae became galaxies and spiral galaxies. A few years later was established the so called Hubble-Lemaître law which states that galaxies systematically move away from us and that the farther they are, the higher the velocity. This law is the experimental proof that the universe is expanding. The fact that the universe is expanding would then lead G. Lemaître to deduce that the universe must have been more compact in the past, leading him to propose the hypothesis of the primeval atom in 1931. We know this hypothesis today has the Big Bang theory.

At the beginning of galaxy observations, as astronomers rapidly observed that there was a large diversity of galaxies, they decided to classify them based on their morphology. Some galaxies have clear spiral arms and/or bars, others are much more elliptical and some presenting exotic features are classified as irregular. The main issue with this kind of classification is that the morphology of the galaxy depends on its orientation relative to the line of sight, but also on the wavelength we are looking at. This is why galaxies were then classified depending on an intrinsic parameter which is their capacity at forming stars. While elliptical galaxies are mostly passive or quiescent, meaning populated by old stars, most of the others are active or star-forming, meaning that they produce new stars.

To study the formation and evolution of galaxies, it is necessary to have a broader cosmological framework. This framework relies on the observation of the expansion of the universe and of the cosmic microwave background (CMB) in 1965 by A. Penzias and R. Wilson. The CMB is considered as the afterglow of the Big Bang; just as the Yucatán crater is a signature of an asteroid hitting the Earth a long time ago, the CMB implies the Big Bang. Based on this two observations, astronomers have developed a model called standard cosmology. This model relies on the Big Bang theory and the so-called ΛCDM cosmological framework. In this scenario, the Universe is homogeneous and isotropic on large scales and is made of ordinary (baryonic) matter, neutrinos, photons and cold dark matter (CDM). CDM is a mysterious component representing 84% of the matter in the Universe, it interacts only through the gravitational force. Moreover, to explain today's acceleration of the expansion of the Universe, astrophysicists had to add another mysterious element, the dark energy. Dark energy is assumed to be a constant form of energy density indicated by Λ, its nature remains unknown to this day. Globally, the dark matter represents $\sim 70\%$ of the matter-energy budget of the Universe, the CDM $\sim 25\%$ and the ordinary matter, meaning all the stars, planets, black holes, the gas, the dust, everything we see, only represents $\sim 5\%$ of the Universe matter-energy budget.

There are two main approaches to the study of the formation and evolution of galaxies. The first approach is through simulations based on the standard cosmology and the laws of physics. There are two kinds of simulations, the hydrodynamical simulations which follow with high consistency the evolution of gas, stars and dust in the galaxies. It is very time consuming, hence not adapted for large scale simulations. The other kind of simulations are semi-analytic simulations which are based on a set of hypothesis tuned to reproduce the galaxies observed in the nearby Universe. These simulations are less computationally expensive, hence practical for large scale simulations. The two methods are complementary.

The other approach to study galaxy evolution is simply direct observation of galaxies. Here again there are two types of observations; the archaeological approach consist in observing local galaxies and consider them as fossils and astronomers try to reconstruct their history. The other approach is the look-back approach. This approach uses the fact that the light travels at a finite speed, the light from an extremely distant galaxy takes millions of years to reach us. Hence, if astronomers are able to collect this light, they will observe such a galaxy as it was millions of years ago. This approach implies to observe large sample of galaxies and extract their properties based on statistics, and strongly relies on the assumption that the Universe is homogeneous, hence the properties of galaxies are assumed to not depend on their position on the sky but only on their cosmological distance which is a tracer of the cosmic time at which astronomers are observing them. To measure the cosmological distance of an object, i.e. to measure for how long the light has been travelling since it was emitted, astronomers use the fact that the Universe is expanding: as the light travels the wavelength broadens. The ΛCDM model gives a direct link between the change in wavelength, called the redshift (indicated by the letter z) and defined as: $\lambda_{obs} = (1 + z) \times \lambda_{rest}$ with λ_{obs} the observed wavelength and λ_{rest} the rest-frame (i.e. emitted) wavelength and the cosmic time of emission from the observed object. Hence, by analysing the light from an object, especially recognizable spectral lines, astronomers can precisely measure the distance of an object and the cosmic time at which it is located. This approach also justifies the constant need to build more sensitive telescopes able to reach deeper and deeper into space. This is the approach I chose for my study.

The main object of this study is the evolution of star forming galaxies, I describe in the next section the general properties of such galaxies.

1.2 . WHAT IS A STAR FORMING GALAXY ?

Most of star-forming galaxies (SFG) have a spiral morphology, some of them can have a central bulge, and/or a bar. Some galaxies have a more complex morphology. Figure 1.1 shows a sample of SFG with various morphologies. Typically, SFG in the local Universe have a half-light radius of $3 - 4$kpc, it can be as low as 1kpc for dwarf galaxies and up to ~ 10kpc. More massive galaxies tend to be wider than less massive galaxies (Cebrián & Trujillo 2014).

From theory and simulations, astronomers have access to models of the emission of galaxies. By comparing these models with the observations, they can retrieve physical properties of galaxies. The luminosity of a galaxy through the electromagnetic spectrum is called the spectral energy distribution (SED). Figure 1.2 shows the typical SED of a star-forming galaxy, it is the sum of three main components:

1. *Radiation from stars.* Mostly black-body emission from stars (in blue in the Figure). The shape is mostly affected by the ages (young stars emit in the UV while older stars emit in the near-IR), by the metal abundances (introducing absorption or emission lines) and by dust extinction (hatched region in the Figure illustrates the effect of dust).

2. *Radiation from interstellar gas.* Gas radiation can originate from several processes depending on its temperature, density and ionisation. It is mostly responsible for the strong emission lines observed in SFG. Gas emissions are shown in green in the Figure.

3. *Radiation from dust grains.* Dust emission originates from three processes, polycyclic aromatic hydrocarbons (PAHs) emit in the mid-IR ($3-13\mu$m), small dust grains (size $\sim 0.01\mu$m) absorb the UV light from young stars and emit grey body radiation in the mid-IR. Bigger dust grains (up to 0.25μm), in equilibrium with stellar radiation field emit in the far-IR. Dust emission appears in red in Figure 1.2.

As illustrated by the SED, a normal SFG is composed of three main compo-

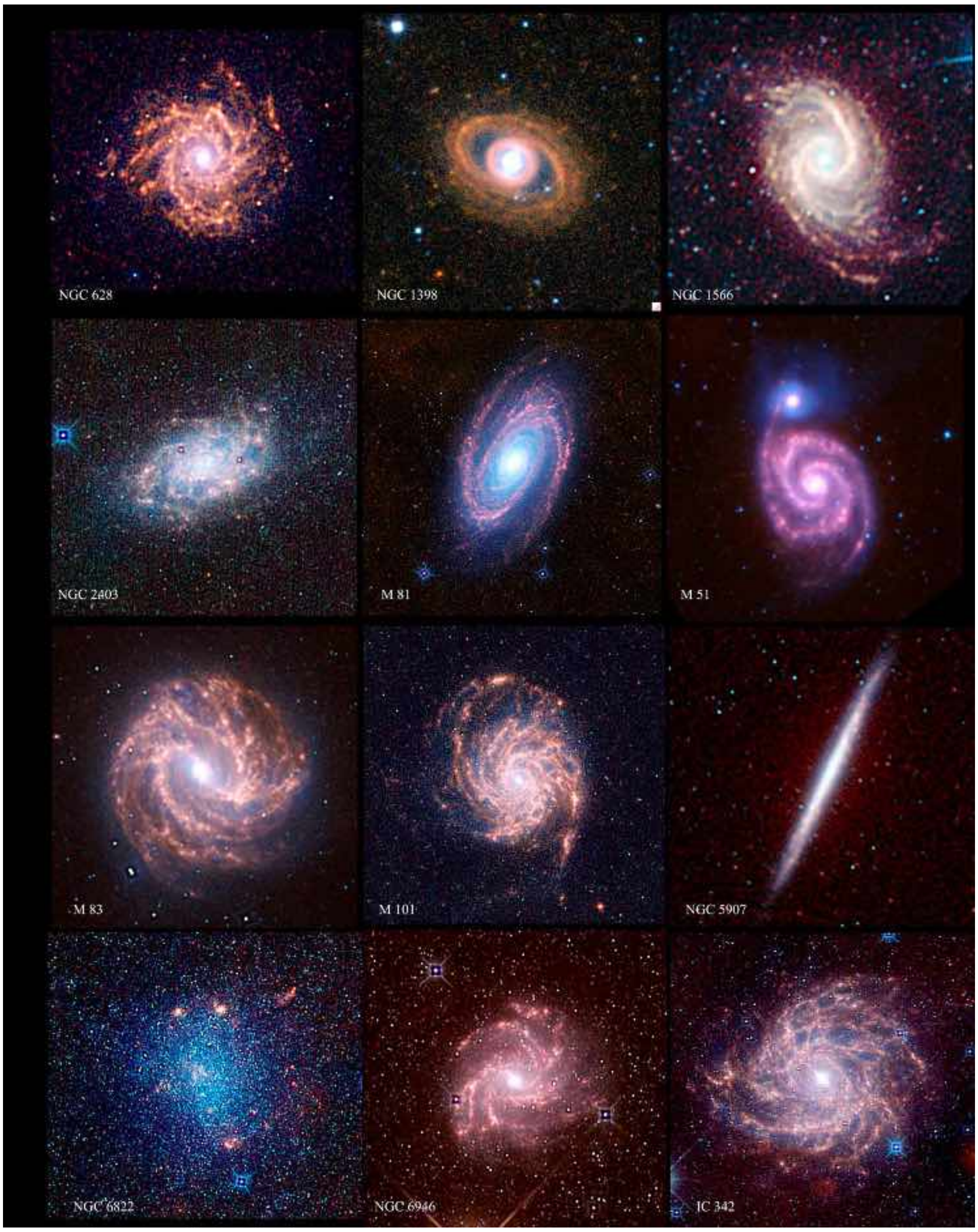

Figure 1.1: Cutouts of star-forming galaxies observed in the near-IR with the WISE space telescope presenting various morphologies (Jarrett et al. 2013).

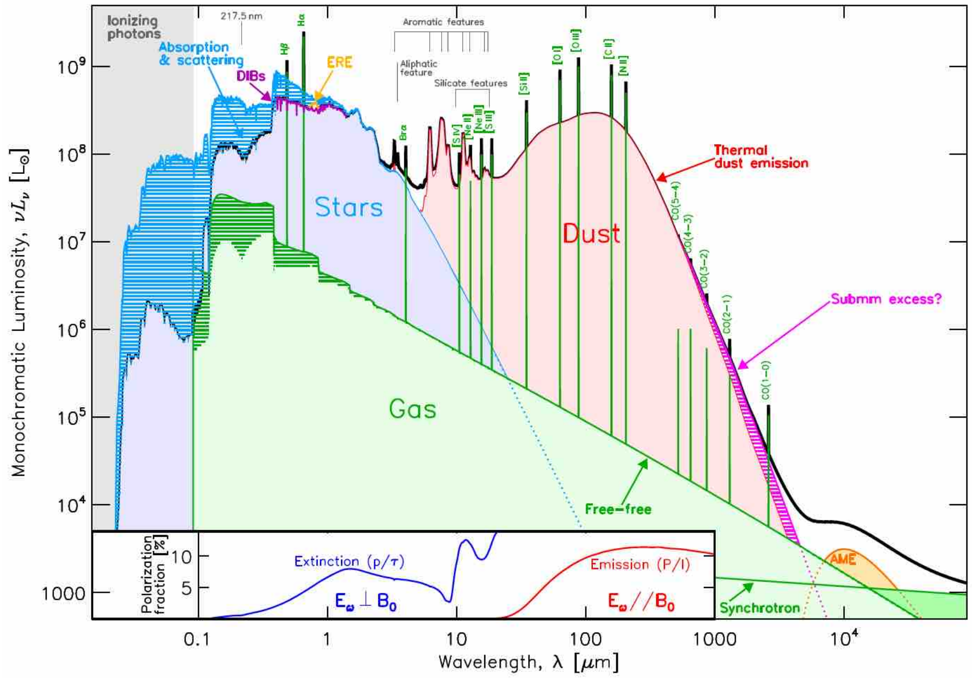

Figure 1.2: Spectral energy distribution (SED) of a typical star-forming galaxy. The blue hatched area shows the power absorbed by dust. This Figure was taken from Galliano et al. 2018.

nents: stars, interstellar gas and dust. Some galaxies host a central supermassive black hole surrounded by an accretion disk with strong radiation called an active galactic nucleus (AGN):

STARS The distribution of stars in a typical SFG can be divided in two components: a disk and a bulge. In both components, the surface brightness (or flux) follows a Sérsic profile:

$$I_\lambda(R) = I_{\lambda,e} \times exp\left\{-b(n) \times \left[\left(\frac{R}{R_e}\right)^{1/n} - 1\right]\right\}, \tag{1.1}$$

where R is the radius, $I_{\lambda,e}$ is the surface brightness at the wavelength λ and the effective radius R_e, n is the Sérsic index, $b(n) = 2n - 1/3 + 4/(405n)$. Usually most of the star-formation occurs in the disk (mainly in the spiral arms) that is populated by both very young stars and older stars and has a typical Sérsic index of 1. The disk is rotating, its rotation velocity ranges from a few tens to a few hundreds of kilometers per second. The disk rotation is coherent, hence the velocity dispersion inside the disk is smaller than the rotation velocity, usually by a factor of ~ 10 for large spiral galaxies. In that case, the disk is thin, if the factor is smaller and closer to 1, the disk can be thicker. At the center of the SFGs, there usually is a spheroidal component called stellar bulge, with a higher Sérsic index. We observe two kinds of bulges, the classical bulges ($2 < n \lesssim 4$) dominated by random motion of stars and high central surface brightness and the pseudobulges ($n \lesssim 2$) that are rotating bulges, less concentrated and more actively star-forming. The difference of Sérsic index makes it necessary to make a bulge-disk decomposition when fitting the surface brightness profile of a SFG by using a two component function. Sometimes, large scale instabilities in the disk lead to the formation of a bar mostly populated by old stars, hence more visible in the near-IR, 60% of local SFGs have a bar (galaxy M83, first column third row in Figure 1.1 has a bar). A fundamental property of SFGs is their capacity of forming new stars. This is probed by the star formation rate (SFR) defined as the stellar mass (usually given in terms of solar masses) produced each year by the galaxy and the star formation history (SFH) which describes the evolution of the SFR with time.

INTERSTELLAR GAS The interstellar medium (ISM) of SFGs is filled with gas in different forms. The neutral atomic gas, mostly composed of hydrogen (noted H I) and detected through the hydrogen emission line at 21cm. The neutral gas interacts via collision, affecting the velocity of particles, hence their temperature. Neutral gas is the most abundant component of the ISM, and the H I distribution can be up to two times larger than the optical size of the stellar distribution. There also is photoionised gas, which is neutral gas that has been ionised by close young massive O and B stars emitting UV photons. These regions are usually called H II regions and are responsible for the Balmer and Lyman series recombination lines in the spectrum. Hα emission can be used to trace spiral arms or gas outflows. The photoionised gas is mostly concentrated in the inner star-forming regions and is often used as a SFR estimator. It is also responsible for the emission of the radio continuum of SFGs via the process of bremsstrahlung. Some gas is ionised by collision if the velocity is high enough, this happens when a shock wave travels through the ISM. Finally, there is the molecular gas, sitting usually in big clouds made of H$_2$ molecules at low temperatures (~ 10K). Most of the stars in SFGs are formed in these clouds. The high density of the clouds allow to easily block the UV light from young stars, protecting the molecular gas. As H$_2$ is nearly undetectable because of its symmetry and the absence of emission lines, molecular clouds are usually detected using carbon monoxide (CO) which has emission lines, hence is much easier to detect. CO detections can be used to measure the mass of the molecular gas. The presence of gas in the galaxy is closely related to star-formation, to measure the time a galaxy can continue forming stars at the current rate given the present gas supply, we define the depletion time $t_{depl} \equiv \frac{M_{gas}}{SFR}$. The SFR surface density is directly linked to the gas density via the Schmidt-Kennicut law:

$$\Sigma_{SFR} = B \times \left(\frac{\Sigma_{gas}}{1 M_{\odot} pc^{-2}}\right)^{\alpha} M_{\odot} yr^{-1} kpc^{-2}, \tag{1.2}$$

where Σ_{gas} is the total gas surface density corrected for the helium fraction, $B \approx 1 \times 10^{-4}$ and $\alpha \approx 1.4$.

INTERSTELLAR DUST Dust represent about 1% of the total ISM mass. However, it has an impact on the SED in a very large range of wavelength as it absorbs the UV and optical light and re-emit it in the IR. We define the dust extinction at a specific wavelength as:

$$A_{\lambda} \equiv -2.5 \times log\left(\frac{F_{\lambda}}{F_{\lambda,0}}\right) \simeq 1.086 \times \tau_{\lambda}, \tag{1.3}$$

where F_{λ} and $F_{\lambda,0}$ are the measured and intrinsic fluxes of the source respectively, and τ_{λ} is the optical depth due to dust extinction assuming an exponential decrease of the flux ($F_{\lambda} = F_{\lambda,0} \times exp(-\tau_{\lambda})$). $A(\lambda)$ is called the extinction curve, it is specific to each galaxy, but generally is close to $A_{\lambda} \propto \lambda^{-1}$. This means that the bluer wavelength are much more attenuated than redder wavelength. This is why astronomers usually refers to the dust extinction effect as reddening of the SED. For a complete overview of the dust effect in the UV and optical, see Draine (2003).

AGN A great number of the SFGs have activities at their core incompatible with normal stellar activity. These SFGs are said to host an active galactic nucleus (AGN). The most accepted picture is that the AGN energy is powered by accretion onto a supermassive black hole (SMBH) at the center of the galaxy. The accreted matter forms an accretion disk around the SMBH. AGN are known to be extremely luminous, obscure in the UV and optical but bright in IR, X-ray, gamma-ray and radio. AGN broaden emission lines and emit relativistic plasma jets with a velocity close to the speed of light. Figure 1.3 summarizes this model. Several kinds of AGN exist depending mainly on the light of sight: the quasars (or quasi stellar objects, QSOs) are the brightest type of AGN, they are very compact, some are radio-loud, the radio emission originates from synchrotron emission. The Seyfert galaxies are like QSOs but with a disk and less luminous. The radio galaxies are similar to QSOs but have a larger host galaxy that can be studied. Finally, the blazars which are AGNs with the jets close to the line of sight making these galaxies fluxes highly variable, they also are very bright in the X-ray. Usually Type 1 AGN are AGN with broad emission lines, when they are not visible, we have Type 2 AGN. According to theory, the broad lines come from the central region of the AGN, called broad line region while the narrow lines originates from the dusty torus, called narrow line region (see Figure 1.3). It is important to assess the presence of an AGN in a galaxy as it emits in the IR, just like the dust re-emitting the stellar light, hence, ignoring the presence of an AGN could lead to overestimate the dust luminosity and SFR of the galaxy. For more details on AGN, see Padovani et al. (2017).

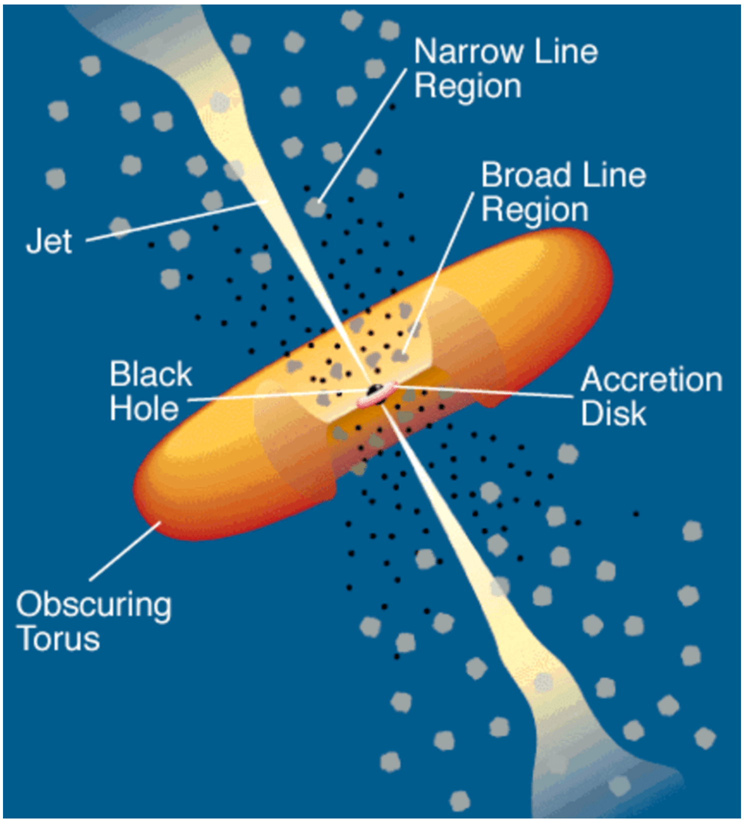

Figure 1.3: A picture of the most accepted active galactic nuclei model. Credit: C.M. Urry & P. Padovani.

All the SFGs are very different, they come with different morphologies, SFR, stellar masses. However, astronomers have been able to find some scaling relations, there is some consistency in the way stars are formed. Here I will only present three of these scaling relations:

MASS-METALLICITY RELATION Observations showed that the more massive galaxies also had higher metallicity. The metallicity of a galaxy can be expressed as the stellar metallicity Z or as the gas abundances (in unit of $12 + log(O/H)$) tracing the metallicity of the ISM. Both definition are not independent. I show in Figure 1.4 the mass metallicity relation using both indicators, this is taken from Ma et al. (2016). The relation is linear in log space up to $M_* \sim 10^{10} M_\odot$ and flattens at higher masses. In the linear part, the mass-metallicity relation is:

$$log\Big(\frac{Z}{Z_\odot}\Big) = F + \eta \times log\Big(\frac{M_*}{10^{10} M_\odot}\Big), \tag{1.4}$$

where $\eta \approx 0.35$ and $F \approx -0.1$.

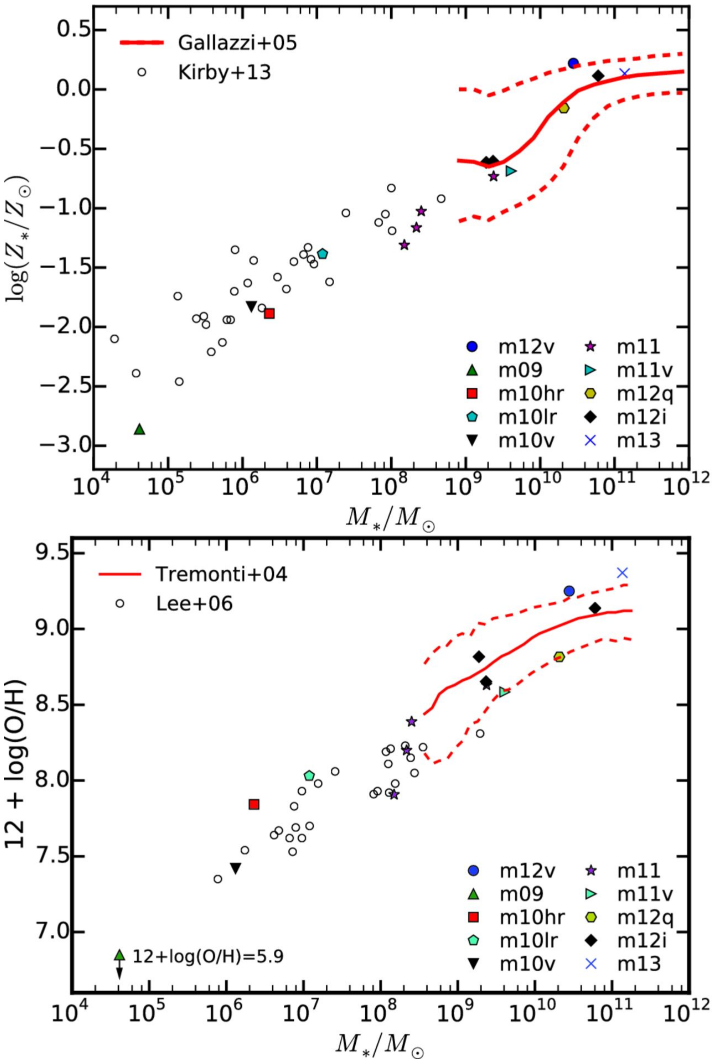

Figure 1.4: Upper panel: Stellar mass–stellar metallicity relation at $z = 0$. The red solid and dashed curves are the median and 1σ dispersion of the SDSS mass-metallicity in the local Universe. Lower panel: Stellar mass–gas-phase oxygen abundance relation at $z = 0$. The red solid and dashed curves represent the median and 2σ dispersion of the SDSS mass-metallicity relation at $z \sim 0.1$. Both plots are from Ma et al. (2016).

STAR FORMATION MAIN SEQUENCE Observations showed that the stellar mass of SFGs correlates with their SFR. There has been many attempt to make an accurate model of the star-formation main sequence. For my thesis, I decided to use the main sequence from Schreiber et al. (2015):

$$log(SFR_{MS}[M_{\odot}yr^{-1}]) = m - m_0 + a_0 r - a_1[max(0, m - m_1 - a_2 r)]^2, \quad (1.5)$$

where $r \equiv log(1+z)$, $m \equiv log(M_*/10^9 M_{\odot})$, $m_0 = 0.5 \pm 0.07$, $a_0 = 1.5 \pm 0.15$, $a_1 = 0.3 \pm 0.08$, $m_1 = 0.36 \pm 0.3$ and $a_2 = 2.5 \pm 0.6$. The main sequence is illustrated in Figure 1.5 for different redshift range. The total scatter of the main sequence is about 0.6dex (Rodighiero et al. 2011). The galaxies that are passive or quiescent don't form stars, they fall below this main sequence. A way to study the evolution of the main sequence with redshift is to calculate the specific star-formation rate (sSFR) defined as $sSFR = \frac{SFR}{M_*}$.

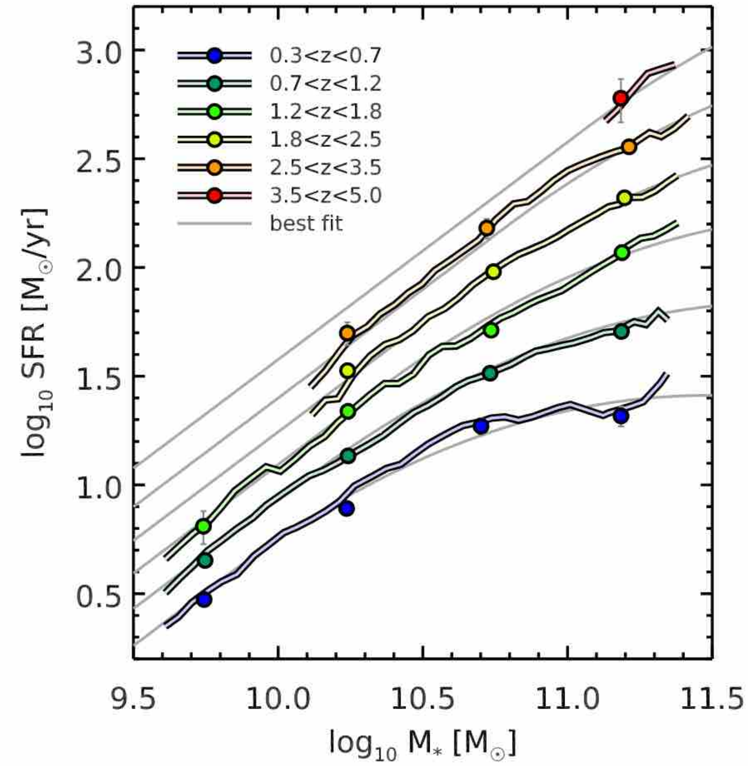

Figure 1.5: Evolution of the average SFR of SFGs with mass and redshift. The results from stacking are shown as colored filled circles, the colors corresponding to the different redshifts as indicated in the legend. In the background, the light gray curves are the best-fit relation for the main sequence. This plot is from Schreiber et al. (2015).

MASS-SIZE RELATION The galaxies follow a correlation between their stellar mass and optical size. The scatter is narrow and was fitted by Schreiber et al. (2015):

$$R_e = A \times \left(\frac{M_*}{5 \times 10^{10} M_\odot} \right)^{\alpha} [kpc], \tag{1.6}$$

where A and α depend on the redshift (see Table 1 of Schreiber et al. (2015)).

Most of the SFGs follow these scaling relation. However, a small number are outliers. Most of the time the outliers are also irregular galaxies, meaning that they do not necessarily have a bulge and a disk. Most of the time, starbursts are the results of a major merger that completely disrupt the galaxies involved. They are SFGs with a much higher SFR than expected for their stellar mass. These galaxies are called starburst galaxies. Usually the excess of star-formation is concentrated in the core of the galaxy and last less than 100Myr. The intense burst of star formation causes important dust thermal emission making starburst bright in the IR. Starbursts can then be selected via their IR luminosity (L_{IR}), if $log(L_{IR}/L_\odot) > 11$, they are called luminous IR galaxies, if $log(L_{IR}/L_\odot) > 12$ they become ultra-luminous IR galaxies. One of the most important thing when fitting the SED of an IR galaxy is to be sure to decipher the luminosity from a potential starburst from the luminosity coming from a potential AGN. Multi-wavelength data is then crucial to discriminate AGN from starburst.

Now that we have a good idea of what is a SFG, I decided to make a recap of what is the current knowledge on the formation and evolution mechanisms of SFGs.

1.3 . GALAXY FORMATION

Before diving into the theories of galaxy formation and evolution, it is important to have an idea of the different physical processes at play in SFGs. This is what I do in the first section.

1.3.1 . MAIN INGREDIENTS

The main driver of the formation and evolution of galaxies is the gas. To efficiently form stars, the gas needs to be cold. Gases can heat and cool by different mechanisms.

One way the gas can cool is through emission, if the gas is optically thin, the emitted photons will escape and the gas will loose energy. Two different processes are responsible depending on the temperature. For gases at temperature higher than 10^4K, the hydrogen gas is ionised and the radiative cooling mechanisms are Bremsstrahlung, recombination, radiative de-excitation and collisional ionisation or excitation. To simplify, we usually consider a collisional ionisation equilibrium. For gases at lower temperature, the hydrogen is neutral, making the radiative cooling inefficient as there are no free electrons. For the neutral gas to cool below 10^4K requires metals or molecules which can radiate at these temperatures.

The gas can be heated via absorption of radiation, the process is called photoheating. It happens in presence of an ultraviolet background radiation field which is mainly produced by massive stars and AGN. The gas is heated through collisions with ionised free electrons.

The gas can also be heated or cooled via Compton scattering, this happens when the gas is in a radiation field. Depending on the energy difference between the photons ($h\nu$) of the field and the electrons in the gas ($k_B T$). In one case, the photons will transfer their energy to the gas, it's Compton heating, it mostly occurs near AGN in X-ray or gamma-ray radiation fields. In the other case, the photons will absorb the energy of the electrons, it's Compton cooling (or inverse Compton scattering). It happens mostly when hot gas interacts with the CMB at low redshift.

In the case of gas accretion in a dark matter halo, there are two main possibilities, the infalling gas can be shock heated and is hot when reaching the center of the halo, it's the hot mode accretion. It is also possible that the gas is efficiently cooled and is still cold when reaching the center of the halo, triggering star formation, it's the cold mode accretion. There is a critical halo mass above which the cold mode is no longer possible. This means that there is a maximum mass above which it is impossible to form more stars. Above this limit, the gas is shock heated and galaxies cannot form new stars unless they are at a sufficiently high redshift, then accretion through cold gas streams should be possible. This is a result of simulations, the critical halo mass is $\approx 5 - 7 \times 10^{11} M_{\odot}$. Figure 1.6 summarize the different accretion scenarios (Dekel & Birnboim (2006)).

Another key ingredient is star formation, the transformation of gas into stars. This requires a very cold gas (T $\lesssim 30$K) at high densities. Such low temperature is achievable in metal or molecules rich gas. When the density is high enough, there is a gravitational collapse. A star is born. I will not detail here the complex chemistry of star formation as it is not the object of the thesis. Star formation consumes the available gas from the ISM, but when old stars die and explode, they return part of the gas, enriched with heavier metals to the ISM allowing new generations of stars to be formed.

Star formation mainly occurs in giant molecular clouds (GMCs). These clouds are local overdensities compared to the ISM and are formed by gravitational instabilities in the disk of SFGs, also called Toomre instabilities (Toomre 1964). The Toomre criterion Q compares the kinetic energy linked to the velocity dispersion inside the disk to the gravitational potential of the gas. If

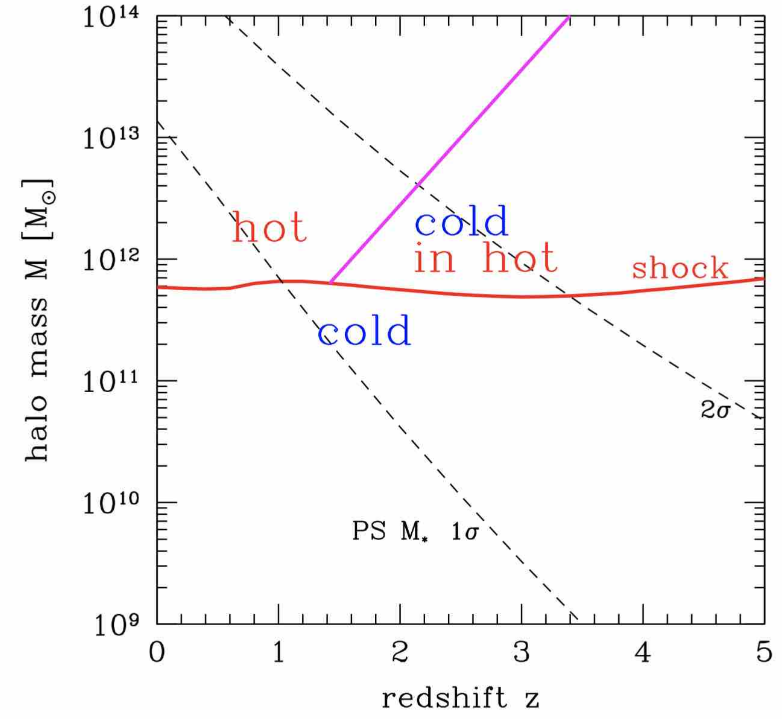

Figure 1.6: Cold streams and shock-heated medium as a function of halo mass and redshift. The nearly horizontal curve is the typical threshold mass for a stable shock in the spherical infall below which the flows are predominantly cold and above which a shock-heated medium is present. The inclined solid curve is the upper limit for cold streams; this upper limit is valid at redshifts higher than $z_{crit} \sim 1-2$. The hot medium in $M > M_{shock}$ haloes at $z > z_{crit}$ hosts cold streams which allow disc growth and star formation, while haloes of a similar mass at $z < z_{crit}$ are all hot, shutting off gas supply and star formation. This plot is from Dekel & Birnboim (2006).

the kinetic energy is dominant, the clouds cannot form or are immediately destroyed by the velocity dispersion inside the disk. However, if the velocity dispersion is too low to counteract the gravitational potential, then the disk will fragment into GMCs, triggering star formation. Spiral arms can also favor the formation of GMCs as they rotate at a constant velocity usually slower than the gas, producing shocks and compression when the gas hits the spiral arm.

Another key ingredient in galaxy evolution is feedback processes. There are mainly two different feedbacks: the stellar or supernova feedback and the AGN feedback. The main stellar feedback is the shock happening when an old star explodes into a supernova. The shockwave, or supernova remnant is slowed down by the surrounding ISM that accumulates in its shell. However, most of the energy from the supernova is not transmitted to the ISM trough kinematics but through emission in the X-ray, UV/optical as it cools down but also in the radio. O and B stars lose there outer layer of mass due to strong stellar winds eventually forming a bubble that will transfer kinetic energy to the ISM. Most of O and B star are in cluster, this can lead to a superbubble that is first driven by the winds and then by the supernova of the stars in the cluster exploding one after another (for more details see Dyson & Williams (1997)). Some winds can also be driven by momemtum, the gas would acquire the momentum through radiation pressure from massive stars onto dust grains (Murray et al. 2005). These feedback processes are negative feedback as they tend to suppress star-formation, however, by inducing compression of gas, stellar feedback can also be positive, meaning enhancing star formation.

AGN feedback can take several forms. In the quasar mode feedback, the AGN is extremely luminous, the radiative feedback is dominant, ionising the ISM and heating it. It also create AGN-driven winds leading to gas outflows. These are negative feedback as they suppress the star formation. There is also the radio mode feedbacks that are jets and radio lobes produced by the central SMBH. These mechanical feedbacks can be responsible for halting the cooling of the core of a galaxy.

Finally, one of the most important processes of galaxy evolution is mergers. Galaxies do not evolve isolated, they merge with one another. A merger does not necessarily happen between two galaxies, multiple merging is possible. When the galaxies are gas-rich, it's called a wet merger, if the merging galaxies are gas-poor, it's a dry merger, the energy won't be dissipated. The merging of galaxies is mostly collisionless due to the low density. Only the gas which is dissipative can be compressed during the merging triggering enhanced star-formation. The resulting galaxy is virialized via collisionless relaxation. Merging galaxies can also induce dynamical friction that will heat the gas and suppress star formation. If two galaxies are close enough but not merging, a tidal force might be at play leading to so-called tidal tails made from material stripped from one of the galaxies. If both galaxies have gas, then there also is ram-pressure stripping depriving the galaxies of their gas

Now that we have all the ingredients, let's try to understand how SFGs are formed and what possible processes can cause them to quench.

1.3.2 . THEORY OF GALAXY FORMATION

Galaxies are way too complex objects to be understood only using theory and calculation. The only way to try and understand the formation of such complex objects is through numerical simulations.

The origin of galaxies is found in the collapse of matter overdensities in the early Universe. These overdensities are mostly made of dark matter, but also contain a fraction of primordial gas. As the dark matter halos grows hierarchically, meaning that small halos merge to form bigger halos, the gas starts to turn into stars, leading to the galaxies we know today. The fact that every galaxy is singular, has its own morphology and properties can let us believe that the formation of galaxies is somewhat chaotic. However, the existence of the tight scaling relations demonstrates that there must be some dominant physical mechanisms driving the formation of galaxies.

Let's first focus on the formation of the disk of SFGs. The disks are rationally supported. The baryonic matter making the disk gets its angular momentum from the rotating dark matter halo. The dark matter halo get its own angular momentum via interactions with the tidal field of the surrounding density distribution. The intensity of the angular momentum will set the size of the disk. At the end, the disk will have the same specific angular momentum as the dark matter halo. This implies that the stars in the disks are formed from gas that acquired its angular momentum from tidal torques and conserved it during the formation of the disk.

Several theories exists to explain the exponential profile of the surface brightness of disks. One of them is hydrodynamical, the presence of shear viscosity could lead to an exponential profile. An other states that disks are not intrinsically exponential, they become it via the formation of spiral arms invoking radial stellar migration. However astrophysicists still ignore what mechanisms drives the formation of these spiral arms despite numerous simulations.

In most disks, the vertical distribution of stars needs to be modeled by a double exponential linked to a thick and a thin disk. Observations shows that the stars in the thick disk are older than those in the thin disk. There are two possible scenarios to explain this, either the first stars formed at a more perturbed epoch, higher velocity dispersion leading to thicker disk. The perturbations could originate from mergers, accretion, denser environment at earlier epochs. Or the first stars formed in a thin disk that got thicker later because of an increase of vertical velocity dispersion.

In most galaxies at $z < 1$, we observe a bar. The bar is thought to form via a large scale, or global gravitational instability. A lot of simulations have been carried out, the main findings are that the bar is easy to form especially when the disk is thin and has low gas fraction, but seems to appear in all cases, sometimes with a delay in the least favorable cases. The bar rotates as a rigid object, but could be destroyed by an instability leading to the formation of a pseudobulge, by a major merger or other processes. The stars inside the bar are not fixed, they can travel through the bar either parallel or perpendicular to the long axis. Bars facilitate the transportation of matter to the center of the galaxy by creating strong gas inflows.

1.3.3 . QUENCHING OF STAR FORMATION

All galaxies are not SFGs, some are passive galaxies, they are populated by old stars and don't form any new stars. This galaxies usually have an elliptical morphology, the star-forming disk is gone in favor of a large massive bulge.

One of the most important questions in the study of the evolution of galaxies is what event could be so dramatic as to completely stop the star-formation of a galaxy and virtually kill it ?

Today we have five main hypothesis on the quenching mechanisms:

MASS QUENCHING As the galaxy evolves, it gets more and more massive. At some point, the galaxy mass will reach the mass limit authorized by the dark mater halo and the accretion of cold gas will be prevented (see Figure 1.6). This will lead to a mass quenching.

ENVIRONMENTAL QUENCHING Sometime in a dense environment, the central massive galaxy can induce quenching of star formation in a satellite galaxy. It can happen via tidal forces or ram pressure stripping, that will remove the cold gas from the satellite galaxies. It can remove all the ISM cold gas leading to a rapid quenching or only remove the outer gas leading to a much slower quenching also called starvation.

NEGATIVE FEEDBACK This can happen because of negative feedback from supernova and AGN which can heat and/or push the gas away triggering an inside-out quenching.This scenario can be favored after a major merger and/or a starburst episode. It won't necessarily quench the galaxy forever, rejuvenation events are possible if there is new inflows of cold gas.

PREVENTING THE COOLING OF GAS Even if a galaxy reaches the mass limit preventing cold gas accretion, the hot gas inside the galaxy can undergo radiative cooling and keep the star formation going. We have never observed star formation in a cooling region of a massive galaxy. This means that there must be some source of heating preventing the cooling. The best candidates for heating the gas are stellar and AGN feedbacks.

INSIDE-OUT QUENCHING Observations suggest that the central part of SFGs at $z \sim 2$ can experience a process leading to a rapid consumption of its gas reservoir, resulting in the formation of a bulge. Then, the quenching propagates toward the outer part of the galaxy that is still star-forming through cold gas accretion. Mass or environmental quenching will then induce the complete quiescence of the galaxy.

At the end of this section, we have a broad understanding of what are SFGs, how they were formed and what is the current knowledge on their evolution and possible death via several quenching mechanisms. In the next section we will see how to do practically to observe and study SFGs.

1.4 . OBSERVING GALAXIES

1.4.1 . MAIN OBSERVABLES

In this section we review the main physical properties one can probe by observing distant galaxies

REDSHIFT There are two main possibilities to measure the redshift of a galaxy. If we have access to a spectrum, we can measure the redshift based on the observed wavelength of a specific emission line. This method is the most accurate, it's the spectroscopic redshift. If we do not have access to a spectrum, we can measure a photometric redshift. It relies on the photometry, a measure of the flux of the source in several bands, then by fitting the SED with several templates, we can estimate the redshift of the galaxy. Usually the photometric redshift has large uncertainties and comes with a probability density function allowing to estimate these uncertainties.

STAR FORMATION RATE The SFR is estimated based on the SED, several indicators exist to measure it. The SFR is usually defined as $SFR = C \times L_{indicator}$ where C is a conversion factor and $L_{indicator}$ the luminosity in the corresponding band. One of these indicator is Hα which traces the H II regions which exist only if O and B stars are present. Since these stars have a very short lifetime ($\lesssim 30$Myrs), it's a good tracer of recent star-formation. Another indicator is the UV continuum luminosity which originates mostly from young stars. However the UV continuum is strongly affected by dust extinction. That is why we usually also use the infrared luminosity as an indicator of the star-formation undergoing in dusty regions. The total SFR will then be defined as $SFR_{tot} = SFR_{UV} + SFR_{IR}$. The radio emission is correlated to IR luminosity and hence can also be used as an indicator, the radio is not affected by dust. Finally, X-ray being linked to massive stars and supernova could also be used as an indicator.

STELLAR MASS The measure of the stellar mass is based on the assumption made on the stellar population when fitting the SED.

INTERSTELLAR GAS The properties of the gas are derived from spectroscopic observations. Metallicity can be estimated by measuring flux ratios. Some properties of the galaxy can be constrained based on diagnostic diagrams.

INTERSTELLAR DUST The dust emission in the FIR can be used to measure its temperature, its mass as well as obtain constraints on the size of the grains. Spectroscopic observations allow to have information on the chemical composition of the dust. By assuming a dust-to-gas ratio, we can use the dust mass as a probe of gas mass. The dust extinction can be estimated by two methods, the first method is based on the measurement of the flux ratio of recombination lines, the second one is based on the measure of the spectrum slope in the UV. Both of these methods require a lot of assumption, hence there usually is non negligible uncertainties on the estimation of the dust attenuation. The measurement of the dust extinction is necessary as it allows to lift some degeneracy with old stars emission and high metallicity.

MORPHOLOGY AND STRUCTURE When looking at distant galaxies, the primary limitation is the diffraction limit linked to the fact that the galaxies we observe are small on the sky ($\sim 1"$) and the telescopes mirror are finite. The finite size of the mirror determines the spatial resolution we will be able to reach as it is linked to the point spread function (PSF). The first step to reach better spatial resolution was to move into outer space to avoid the atmosphere perturbations. From there the only way to improve is to get bigger mirrors to reduce the PSF full width half maximum. When we succeed to spatially resolve galaxies, we can extract useful information from the images like the morphology (spiral arms, bars, bulges..), we can count the clumps, measure the asymmetry or the compactness of the galaxy (Conselice 2003).

This list is non exhaustive, there are many more properties that we could probe, however, for this manuscript, it is not necessary to present them all.

1.4.2 . OBSERVING DISTANT GALAXIES

Observing distant galaxies rapidly becomes a challenge as they are very faint. It is nearly impossible to observe them from the ground because of the airglow producing a high sky background.

Several surveys have been conducted to observe large parts of the sky with long exposure time with several telescopes with the hope to observe distant galaxies. However, when looking at the distant galaxies, the surveys are strongly biased as we only detect the most luminous galaxies (Malmquist bias), as we look at a small portion of the sky, we could be looking at an underdense or over-dense region compared to the rest (cosmic variance bias). An other possible bias is statistical, linked to the fact that if we have a very low number of faint sources, it can introduce a bias when estimating the error bars on statistically derived properties (Eddington bias).

Despite these biases, some efficient selection methods have been developed at different wavelength to construct sample of high redshift galaxies:

SELECTION IN THE OPTICAL At $z > 1$, the observed optical light corresponds to the rest-frame UV light meaning that here, we will select young SFGs with low dust attenuation. The selection method consists in using the Lyman-break. Indeed, the UV continuum is brutally stopped below Lyα ($\lambda_{rest} < 1216$Å). As the spectrum is redshifted, it becomes easy to have a redshift selection as the highest redshift sources will be invisible at shorter wavelength and become bright when we probe over Lyα. The selection is illustrated in Figure 1.7 (Finkelstein et al. 2015). These galaxies are known as Lyman break galaxies (LBGs), they are SFGs with low attenuation, as expected from the selection. They have quite high sSFRs ($\sim 1-6 \times 10^9 yr^{-1}$), have rotating disks fragmented in clumps, signature of minor mergers and instabilities.

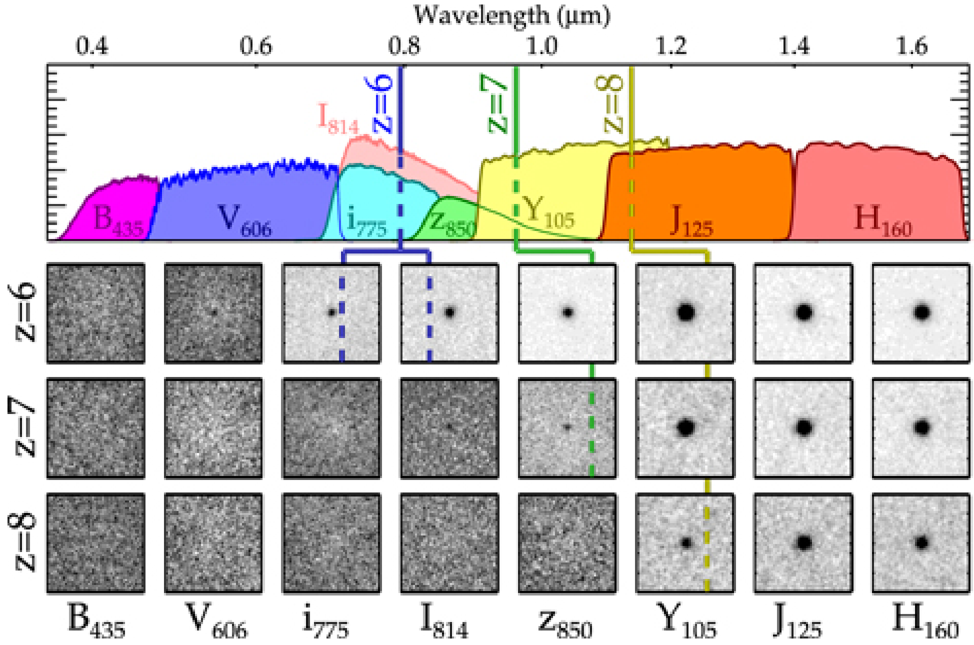

Figure 1.7: Upper panel: filter transmission curves for the filter set used in to observe the galaxies. The vertical lines denote the relative position of the Lyα break (rest 1216Å) in a given filter for galaxies at the center of the three redshift bins. Lower panel: negative image stacks of galaxies in the three redshift bins. This plot is from Finkelstein et al. (2015).

SELECTION IN THE NEAR-IR Selecting SFGs in the near-IR is better than in the optical since we are less affected by dust extinction, which allows to select dusty galaxies. The near-IR is a good tracer of the stellar mass as it correlates with the integrated light of evolved stars and not UV radiations emitted by short-lived stars. To select only SFGs, we use a color-color diagram comparing the $B - z$ and $z - K$ observed colors where the plane can be divided between SFGs and quiescent galaxies (see Figure 1.8, Daddi et al. 2004). The near-IR selected galaxies are not all star-forming, some of them are quiescent even at $z \sim 1-2$. The SFGs

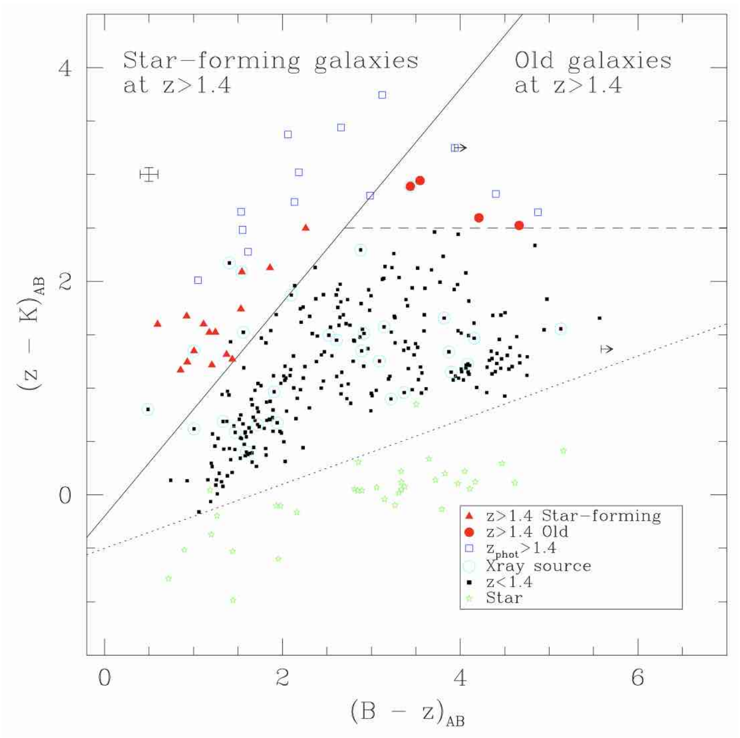

Figure 1.8: Two color $(z - K)$ vs $(B - z)$ diagram. Galaxies at high redshifts are highlighted: solid triangles represent galaxies at $z > 1.4$ with features typical of young star forming systems; solid circles are for $z > 1.4$ galaxies with old stellar populations; empty squares are objects with no measured spectroscopic redshift and $z_{phot} > 1.4$. Sources detected in the X-ray are circled. Stars show spectroscopically identified galactic objects. The diagonal solid line defines the region $BzK \equiv (z - K) - (B - z) \gtrsim -0.2$ that is efficient to isolate $z > 1.4$ star forming galaxies. The horizontal dashed line further defines the region $z - K > 2.5$ that contains old galaxies at $z > 1.4$. The error bar located in the top-left part of the diagram shows the median error in the $(z - K)$ and $(B - z)$ colors of objects at $z > 1.4$. The dotted diagonal defines the region occupied by stars. This plot is from Daddi et al. (2004).

are more star-forming and more massive and dustier than the optically selected galaxies. In the IR a central bulge-like component appears. The quiescent galaxies at high redshift are spheroids with a Sérsic index $n > 2$. There are similar to local quiescent galaxies except a few sample that have a disk and are rotating. Star-forming and quiescent galaxies have different colors mostly because of the difference of stellar population. The bimodality observed in the BzK diagram persist up to $z \sim 2$

SELECTION IN THE IR-MM Dusty star forming galaxies emit in the far-IR and sub-mm, by selecting them in the mm, we directly select the most massive and dusty galaxies. The galaxies at higher redshift are brighter in the sub-mm than low redshift galaxies due to the broad peak of dust emission. The selected galaxies are sub-millimeter galaxies (SMGs). SMGs are extremely luminous object with a SFR that can go up to $SFR_{IR} > 1000 M_{\odot} yr^{-1}$. Less luminous galaxies tend to have warmer dust. Most of them are starbursts triggered by major merger, they have a disturbed morphology.

SELECTION IN THE RADIO The radio allows to select high-redshift AGN that are radio-loud but invisible in the optical/NIR because of the orientation. This selection allows to study and select QSOs.

SELECTION IN THE X-RAYS These surveys are efficient to select high redshift AGN.

Based on all these surveys at different wavelengths, astrophysicists have been able to compare high redshift galaxies to local galaxies, and put empirical constraints on galaxy evolution.

1.4.3 . OBSERVATION OF GALAXY EVOLUTION

Many properties evolve with redshift, I decided to present here the most relevant with my work:

GALAXY MORPHOLOGIES AND SIZES Until a year ago, the only telescope having the necessary spatial resolution to investigate the morphologies of galaxies in the UV/optical was the *HST*. But for a year now we have the *JWST* that completely outdated *HST* in terms of morphology. Kartaltepe et al. (2023) studied the morphologies of galaxies with *JWST*, their main conclusions are that galaxies with a disk make up a large fraction of their sample at all redshifts, from ~ 60% at $z = 3 - 4$ to $\sim 30\%$ at $z > 6$. While the fraction of irregular galaxies stays constant around $\sim 45\%$. Most of the galaxies that *HST* didn't resolve or classified as irregular where actually disk affected by dust extinction making it hardly visible with *HST*. They confirm that the Sérsic index is not enough to classify a galaxy as disk-dominated or spheroid-dominated. However, smaller galaxies tend to be rounder. A surprise is the observation of a lot of compact galaxies that were not predicted by the simulations. What this study demonstrates is that the Hubble Sequence was already in place at $z > 3$.

GALAXY MERGERS Observations shows that mergers were more frequent in the past. This evolution is consistent with the idea that the structures grow hierarchically.

THE STAR FORMATION RATE The SFR is estimated from the luminosity function. Observations show that at higher redshifts, the galaxies are much more IR-luminous (See Figure 1.9, Gruppioni et al. 2013), meaning that in the past, galaxies had greater SFR.

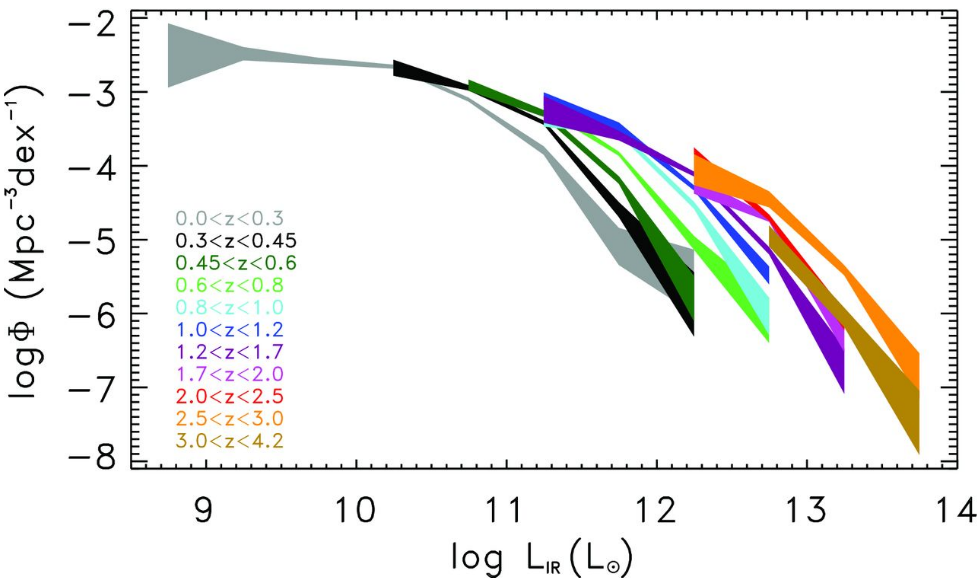

Figure 1.9: The evolution of the IR luminosity function of SFGs as derived by the *Herschel* surveys. This plot is from Gruppioni et al. (2013).

STAR FORMATION RATE DENSITY The star formation rate density (SFRD) is defined as the SFR per unit of comoving volume. The SFRD increases exponentially between $z \sim 10$ and $z \sim 2$. The SFRD reaches a peak at $z \sim 2$ and then decreases exponentially until today. As of today we do not have a clear explanation as to why the SFRD as been decreasing these last 10 billion years. The epoch at $z \sim 2$ is defined as 'Cosmic Noon' as it was the moment in the history of the Universe when the most stars were forming. This mysterious epoch is subject to a lot of investigations, my work being one of them. Figure 1.10 shows the evolution of the SFRD with redshift (for more info see Madau & Dickinson (2014)). When we only have an estimate of the SFR from the UV, it has to be corrected to take into account the SFR_{IR}.

STAR FORMATION MAIN SEQUENCE The Main Sequence observed in the local universe seem to hold even at high redshift. The slope of the Main Sequence remains constant but, as the galaxies SFR is higher in the past, the normalisation increases with redshift. The fact that across cosmic time the Main Sequence evolves smoothly is a sign that there is a dominant process of star formation: accretion via streams of cold gas. However, it has been proven that galaxies in the Main Sequence do not necessarily evolve quietly (see Chapter 5.1).

SPECIFIC STAR FORMATION RATE The sSFR increases rapidly with redshift. Galaxies in the past were much more efficient at forming stars than today. This is consistent with the idea that the most massive galaxies

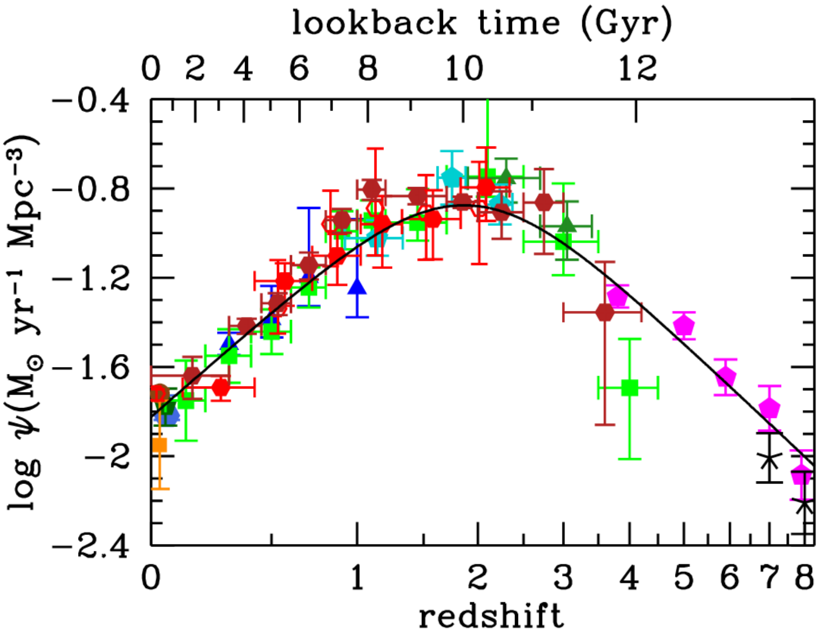

Figure 1.10: The history of cosmic star formation from far-UV+IR rest-frame measurements. The data points with symbols are given in Table 1 of Madau & Dickinson (2014). This plot is from Madau & Dickinson (2014).

formed earlier and faster than less massive galaxies.

This concludes the brief overview of SFGs and their formation and evolution. I will now focus more on my work.

1.5 . THESIS MOTIVATIONS

1.5.1 . THE JAMES WEBB SPACE TELESCOPE

The *James Webb Space Telescope* (*JWST*) is a brand new near-IR space telescope. Its main scientific goals are searching for the first galaxies that formed in the early universe, studying galaxies at different redshifts to probe the evolution of galaxies, observing the life cycle of stars, from the first stellar nurseries to the formation of planetary systems and measuring physical and chemical properties of planetary systems, including our own solar system, and investigating the potential for life on planets that orbit other stars.

The telescope was launch on Christmas Day 2021, and delivered its first images in July 2022, just a year ago. I was lucky enough to be among the firsts to play with these incredible images.

For this thesis, I used only the Near-IR camera NIRCam. NIRCam can probe from 0.5μm to 6μm and offers an unmatched spatial resolution with PSF FWHM ranging from $0.040''$ to $0.145''$ for the F115W and F444W filters respectively. In Figure 1.11, I show a comparison between the NIRCam view of a field and the same field viewed with the *Spitzer* telescope at the same wavelength. The improvement is impressive, NIRCam will resolve all the blending problems we had with IRAC. It also is much more sensitive, a tremendous amount of faint galaxies previously invisible with IRAC are popping up.

When in comes to SFGs, NIRCam will be able to probe the near-IR, and be able to observe all the dusty SFGs at least up to $z \sim 3$, and probe the central bulge-like component that was observed for these galaxies. We will also be able to resolve SMGs and study these galaxies completely, their dusty central component and their unobscured larger disk if they have one.

1.5.2 . OPEN QUESTIONS

The main objective of this thesis is to better understand the evolution of massive SFGs at Cosmic Noon. To do so I will select them in the far-IR and study them with NIRCam. With this thesis I want to shed some light on open questions.

First, for the first time we will have access to resolved images of DSFGs at $z \sim 2$, that will allow to probe their morphology. Are there disks already at Cosmic Noon ? Are we witnessing mergers, interactions ? What processes are responsible for their starbursting nature ? Do they look like what we expect from theory and simulation ?

Second, we know that around $z \sim 2$, something happened causing the SFRD to decrease exponentially, by looking at these SFGs, I hope to be able to find some clue on what could cause the general quenching of galaxies in the last 10 billion years

Third, due to their high density of dust, these galaxies are nearly invisible with *HST* which probe the optical. The dust column density makes these galaxies mysterious, the *JWST* should be able to reveal them to us.

Finally, thanks to ALMA, we have some high resolution images of SMGs, these galaxies appear compact in the mm, but are they also compact in the near-IR ? Are they main sequence galaxies or starburst ? Are they compact or just the obscured part of a larger system ?

The *JWST* is opening a new era, in just a year it changed the way we look at galaxy formation and evolution and will probably continue to do so. If I had the incredible opportunity to work with these images, it's because I am member of an international collaboration that I present briefly in the next section.

1.5.3 . CEERS COLLABORATION

The Cosmic Evolution Early Release Science (CEERS) survey is an international collaboration lead by Steve Finkelstein (P.I.), Mark Dickinson and Casey Papovitch of about ~ 100 scientist all over the globe. As an early science

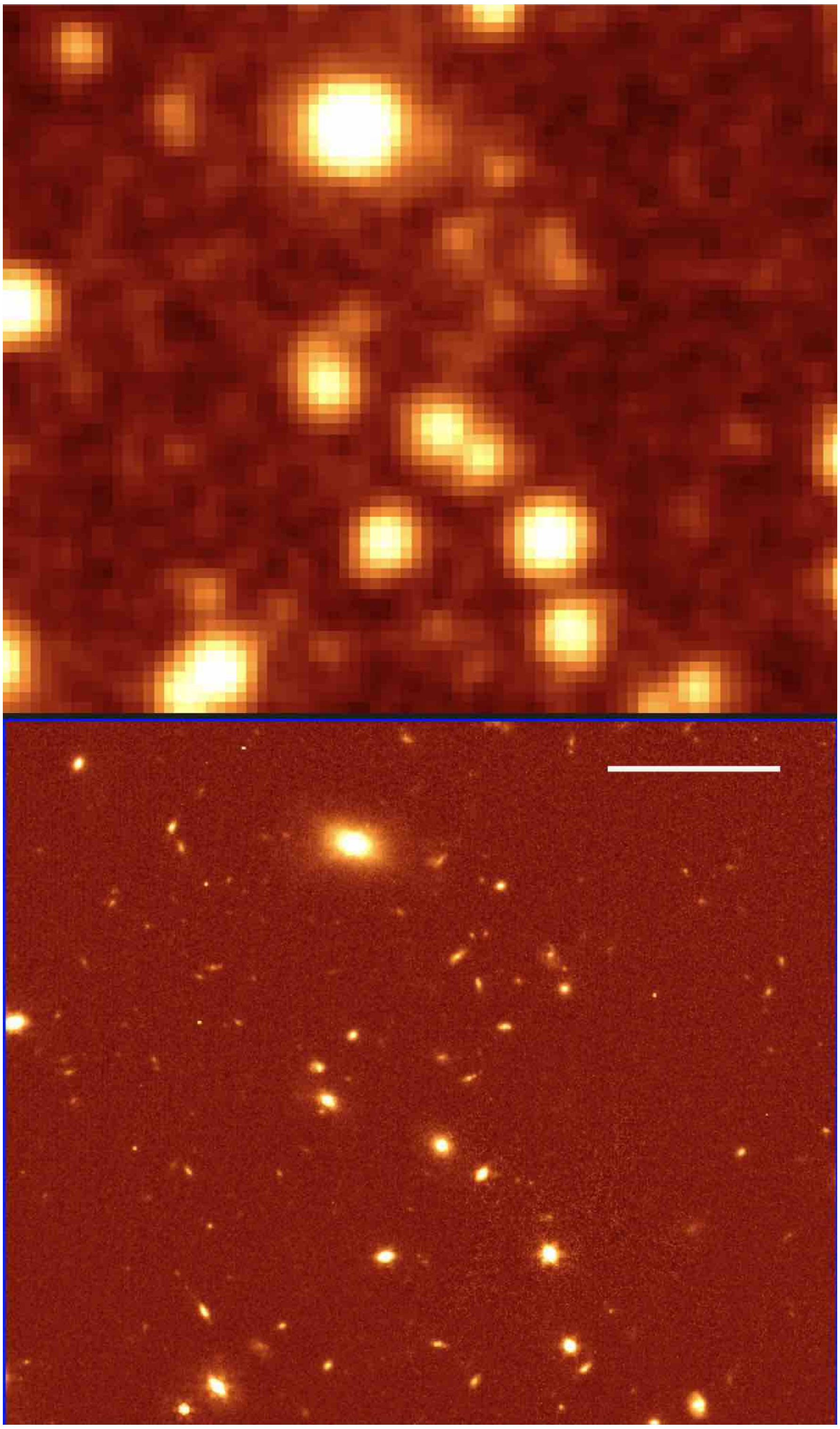

Figure 1.11: Upper panel: *Spitzer*/IRAC cutout of a portion of the EGS field observed with the Channel 4. Lower panel: Same field observed with *JWST*/NIRCam F444W filter, the white segment is 10arcsec long.

project (ERS), CEERS was assured to get telescope time in the first year of operation. Luckily, the EGS field that we observe was visible exactly when the telescope started its science observations, making of CEERS one of the very first observations.

One of the main goals of CEERS was, as an ERS, to demonstrate, test, and validate efficient extra-galactic surveys with coordinated, overlapping parallel observations with the *JWST* instrument suite.

CEERS will also address key *JWST* science goals, including constraining the abundance and physical nature of galaxies at $z \sim 9 - 13$; constraining the physical conditions of star-formation and black hole growth via line diagnostics of galaxies at $z > 3$; quantifying the first bulge and disk structures at $z > 3$; and characterizing galaxy mid-IR emission to study dust-obscured star-formation and supermassive black hole growth at $z \sim 1 - 3$.

As a new member I was happy to learn to collaborate within such a important collaboration.

2 - LAYING THE FOUNDATIONS OF THE SUPER-DEBLENDED CATALOG

In this first chapter, I will explain and recall why it is necessary to look at galaxies in the far-IR and why we need to use this specific “super-deblending" technique in this part of the sky. I will continue with how I gathered data and prepared a complete list of potentially far-IR bright galaxies.

2.1 . WHY BUILDING A FAR INFRARED CATALOG ?

When looking at galaxies in the UV/optical part of the spectrum, we observe the light from young stars and use that information to estimate the star formation rate of the galaxies. However, the most star-forming regions of galaxies are known to be dusty, i.e. a great number of young stars are hidden behind a curtain of dust, making them invisible in the UV/optical. As the dust absorbs most of the UV and optical light, it gets warmer and emits light in the IR. This effect is illustrated in Figure 2.1 where the dust absorption is showed in the blue hatched area (Figure taken from Galliano et al. 2018). Hence, the FIR emission is a good tracer of the young stellar population and SFR. The efficiency of the FIR luminosity to trace SFR depends on the contribution of young stars to the heating of the dust, and on the optical depth of the dust in the star-forming regions. The simplest model is assuming that emission from young stars dominate in the UV–optical, and that the dust opacity is high everywhere. In that case the FIR luminosity measures the total luminosity of the starburst and is the ultimate SFR tracer, providing what is essentially a calorimetric measure of the SFR. Such conditions exist in the starbursting cores that power many IR-luminous galaxies. Hence, by tracing the light emitted in the FIR, we are able to detect the dusty star-forming regions and measure their star-formation rate with a much better accuracy than what we would measure by only probing UV-optical light (Draine & Li (2007); Aretxaga et al. (2011); Magdis et al. (2012); Karim et al. (2013); Ciesla et al. (2014); Tan et al. (2014); Aravena et al. (2016); Oteo et al. (2016); Cowie et al. (2017); Dunlop et al. (2017); Elbaz et al. (2018); Puglisi et al. (2017)). However, old stars and Active Galactic Nuclei (AGN) can also participate to the FIR emission making the connection between FIR luminosity and SFR less straight forward. That is why it is necessary to have information on the full spectrum, as young stellar population should still be visible in the UV-optical if the region is not too dusty and the AGN can result in strong radio and/or X-ray emissions, to have the best estimates of SFR.

In this work, I chose the Extended Groth Strip (EGS). This field has been the

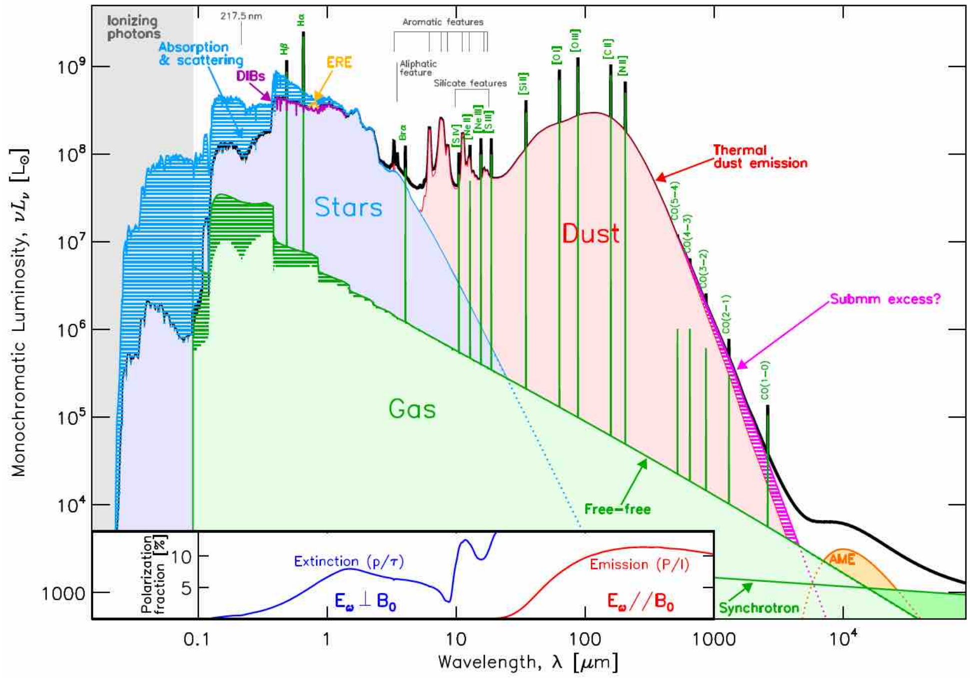

Figure 2.1: Spectral energy distribution (SED) of a typical late-type galaxy. The blue hatched area shows the power absorbed by dust. This Figure was taken from Galliano et al. 2018.

site of several surveys from the X-ray to the radio, notably the All-wavelength Extended Groth Strip International Survey (AEGIS; Davis et al. 2007) and the Cosmic Assembly Near-infrared Deep Extra-galactic Legacy Survey (CANDELS; Grogin et al. 2011; Koekemoer et al. 2011). It as also been observed with the *Herschel Space Observatory* (hereafter *Herschel*; Pilbratt et al. 2010) and other ground-based (sub-)millimeter telescopes like JCMT 15m and the ASTE 10m telescopes. More importantly, the EGS field has been observed by the *James Webb Space Telescope* (JWST) for the Cosmic Evolution Early Realease Science (CEERS[1], PI: Steve Finkelstein) collaboration.

Unfortunately, the FIR and (sub-)millimeter have a very large point spread function (PSF), introducing colossal blending. Each galaxy emitting in the FIR appears as a large blob in the image. This is an issue as it leads to a high uncertainty on the galaxy at the origin of the FIR emission, most of the time we can find 10 to 30 galaxies resolved with *HST* or *JWST* inside such FIR blobs. Moreover, if more than one galaxy among these 10 to 30 emit in the FIR, they will be completely blended, making it nearly impossible to re-distribute the FIR flux among them. The confusion makes the photometric measurements for individual galaxies hardly possible. We show in Figure 2.2 a comparison of the same field of view observed both with *JWST* in the near-IR and *Herschel* in

---

[1] https://ceers.github.io/

the FIR where one can clearly see the difficulties we face when dealing with FIR images.

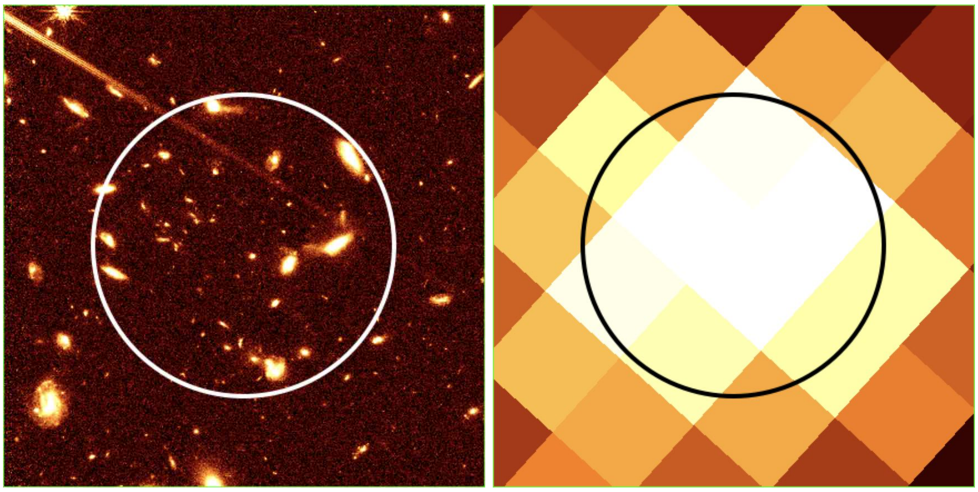

Figure 2.2: Left panel: *JWST*/NIRcam cutout of a $40'' \times 40''$ field of view at 200μm, the white circle is the FIR PSF size. Right panel: same field of view observed by *Herschel*/SPIRE at 350μm, the black circle is the 350μm PSF (FWHM = 25.15"). The blending problem appears clearly.

As a consequence, the constraints on the SED in the FIR are light due to high uncertainties on FIR fluxes, making the SFR estimations complicated. To tackle this problem, the widely used technique is to use priors from high resolution UV-optical bands to fit lower resolution images. The idea is to reverse the process, instead of blindly looking for bright FIR emission, one uses all the information in hand from high-resolution imaging in shorter wavelength and try to have a guess on which galaxies have a higher probability to be FIR bright and then PSF-fitting the FIR image at the position of these expected FIR-bright galaxies. Using this method, one can hope to reduce the blending from 10 to 30 to 2 to 5. The main issue being how to objectively choose the priors to fit. Indeed, some bright galaxies in the UV-optical bands will be faint in the FIR while faint UV-optical galaxies can be FIR bright.

In an attempt to go further and have a more efficient way to deblend highly-confused images, Liu et al. (2018) (hereafter L18) developed an innovating method called "super-deblending" to obtain prior-fitting multi-band photometry for FIR/(sub-)millimeter data sets in the GOODS-North field. Jin et al. (2018) (hereafter J18) used the same "super-deblending" approach but adapted it for the $2deg^2$ wide COSMOS field where the MIPS 24μm, radio and PACS data are shallower. The main idea behind the "super-deblending" was to not fit all the FIR bands independently but to use the information they learnt at each band to help deblend the next one. This technique relies on flux predictions: by fitting the SED of each prior between each IR band, they were able to predict which prior should be FIR bright in the next band and which shouldn't. Based on this, they built adapted prior catalogs for each band but also removed from the image the flux from faint sources that were not fitted so that they didn't bias the measurements of neighbouring brighter sources. By moving from high-resolution images to lower and lower resolution images, they were able to shrink the catalog of prior positions in a consistent and effective way. Finally, they also used extensive Monte-Carlo simulations to measure quasi-Gaussian uncertainties and correct both fluxes and uncertainties to take into account biases linked to the residual fluxes, the local noise variations or the crowding. This method produced the deepest FIR catalog in these two fields. This is the reason why, despite already existing individual FIR catalogs, I decided to apply this technique in the EGS.

2.2 . HOW TO BUILD THE CATALOG

As aforementioned, a critical step in the deblending is the selection of priors to fit. We have to deal with a dilemma: (1) the necessity to be as complete as possible as ignoring potentially FIR-bright sources could result in a bias when measuring fluxes of nearby sources; (2) the necessity to have reliable flux extraction, which require to have a low density of priors, ideally close to 1 source per beam.

The “super-deblending" technique has been developed precisely to tackle this dilemma. The first step is to build a prior catalog of all the potentially bright FIR sources that will be the starting point of the catalog for each band. To this aim, I used an existing complete catalog in the UV/optical (Stefanon et al. 2017) combined with the most recent *JWST*/NIRCam data from CEERS as prior to measure fluxes in deep *Spitzer*/MIPS $24\mu m$ and radio images. I explain in detail in Section 2.3 how I buildmy prior catalog based on these measurements.

Once I had a prior catalog of FIR bright source candidates, I applied the “super-deblending" technique which is a multi step technique meant to optimize the pool of priors fitted at each band. The aim is to reach a balance between the number of priors fitted, the quality of the fit, and the achievable deblending given the PSF size. I started with the most resolved image (*Herschel*/PACS $100\mu m$ with a 7.2" PSF FWHM) and fitted band after band toward more confused images (until *Herschel*/SPIRE $500\mu m$ with a 36.3" PSF FWHM).

The key step of the technique is to run SED fitting with the available photometry for each prior at each step in wavelength, and actively exclude excessively faint priors from the fitting and have their flux removed from the original images. In this way, the remaining priors can be fitted with less crowding ($\lesssim 1$ prior per beam), and the emission of fainter sources can also be better constrained. Also, as an indispensable feature of this technique, Monte Carlo simulations are used to precisely correct flux biases of various kinds and obtain calibrated and quasi-Gaussian flux uncertainties for the photometry in all bands. Furthermore, sources extracted in the residual images are also included in the prior list and fitted, further improving the completeness of the prior sample. Figure 2.3 summarizes the “super-deblending" technique, this flow chart was taken from L18 who first developed this method.

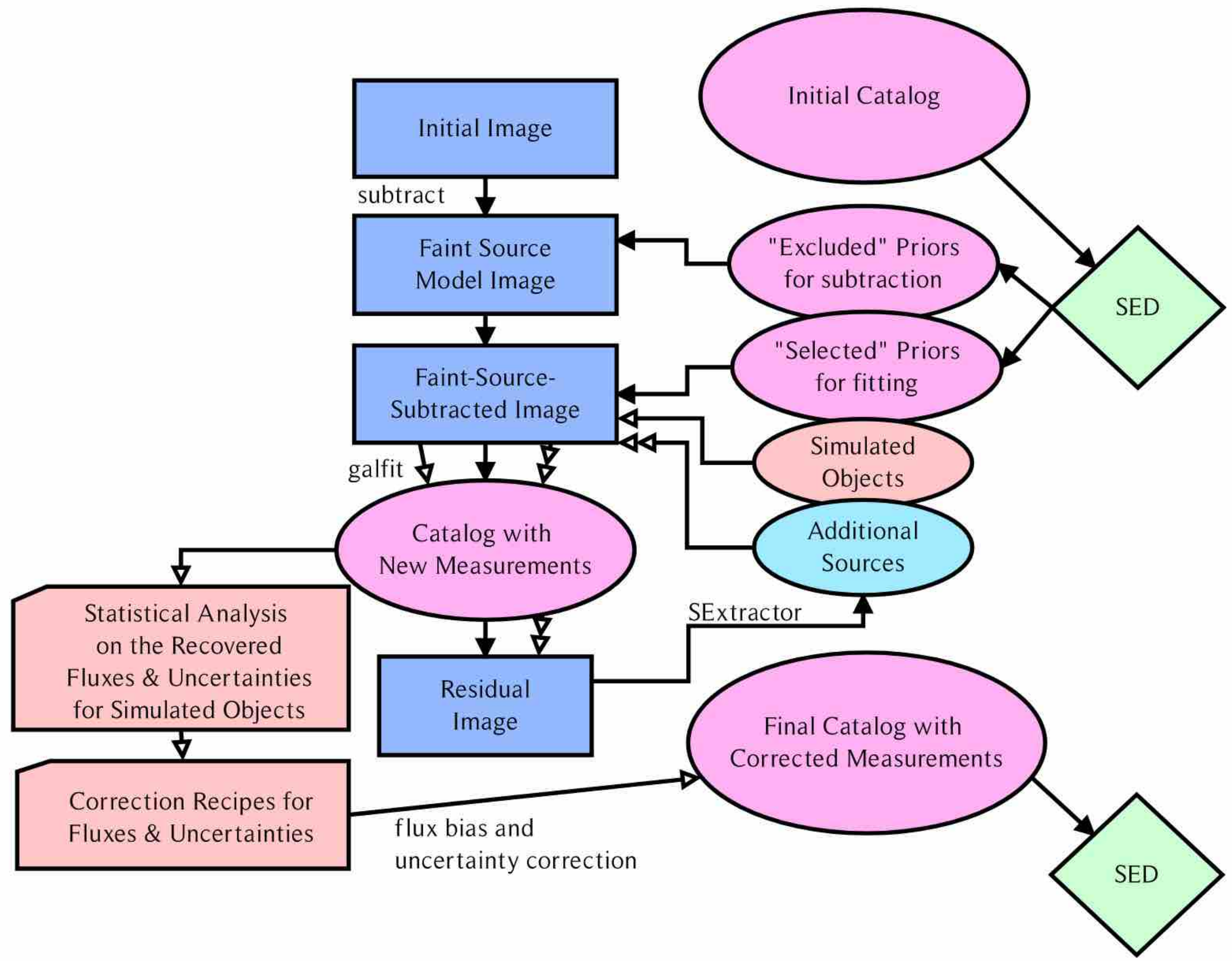

Figure 2.3: Flow chart of the super-deblending technique. Taken from Liu et al. 2018.

I emphasize that the "super-deblended" photometry technique was described in full in L18. I refer readers interested in the details of the method to that crucial reference if required for a better understanding of the technical parts, here I limit the detailed description only to specific variations with respect to L18; J18.

As mentioned in the previous section, the EGS field has been observed by a large number of facilities. The measurements used to makemy catalog were realized on imaging data sets from disparate surveys. MIPS $24\mu m$ data is from the second public data release of The Far-Infrared Deep Extragalactic Legacy Survey (FIDEL), a *Spitzer* Space Telescope Legacy Science program (Dickinson 2007). I used *Herschel*/PACS 100 and $160\mu m$ from the public data release of the PACS Evolutionary Probe PEP (Lutz et al. 2011). The SPIRE 250, 350 and $500\mu m$ are nested maps from the *Herschel* Multi-tiered Extra-galactic Survey (HerMES, Oliver et al. 2012). I used the SCUBA2 $850\mu m$ map from the S2CLS program (Geach et al. 2017) and the SCUBA2 450 and $850\mu m$ matched-filtered deeper maps from Zavala et al. (2017). The AzTEC 1.1mm matched-filtered image is from Aretxaga (2015). I used the radio VLA 1.4GHz imaging from Ivison et al. (2007) and the 3GHz imaging from a new VLA observation for the CEERS collaboration. These new VLA observation were taken primarily to aid this effort (PI: M. Dickinson, see Section 2.3.1 for more details). As some images did not cover the whole area of the prior catalog, in Figure 2.4, I show the coverage of the different images I extracted fluxes from. In the first "super-deblended" catalog produced by Liu et al. (2018) in the the GOODS-North field, they had much deeper FIR images. However, Jin et al. (2018) showed with their own version of the catalog in the COSMOS field that it could be adapted for shallower images. As I had, in the EGS field, comparable FIR depth as in the COSMOS field, I was confident that this technique was suited for my case. However, I made some adjustment to adapt it to the EGS field and improved it.

In the following Section, I detail how I built the prior catalog (Section 2.3).

2.3 . PREPARING THE BASIS OF THE CATALOG

Usually, for *Herschel* deblending works (Lee et al. 2013, Hurley et al. 2017), priors are blind-extracted detections from the less confused $24\mu m$ and/or radio bands because of their known correlation to the IR luminosity (Yun et al. 2001, Dale & Helou 2002, Delhaize et al. 2017). An efficient way to include fainter detections while reducing spurious ones is to use the prior-extraction method, where one fits the PSF at the position of known sources.

In the "Super-deblended" GOODS-N and COSMOS catalog, L18 and J18 selected *Spitzer* IRAC and K$_s$ sources as priors for the $24\mu m$ and radio images. In the EGS field, I have a highly complete UV/optical catalog, published by Stefanon et al. (2017) listing 41457 objects along with their photometry from UV

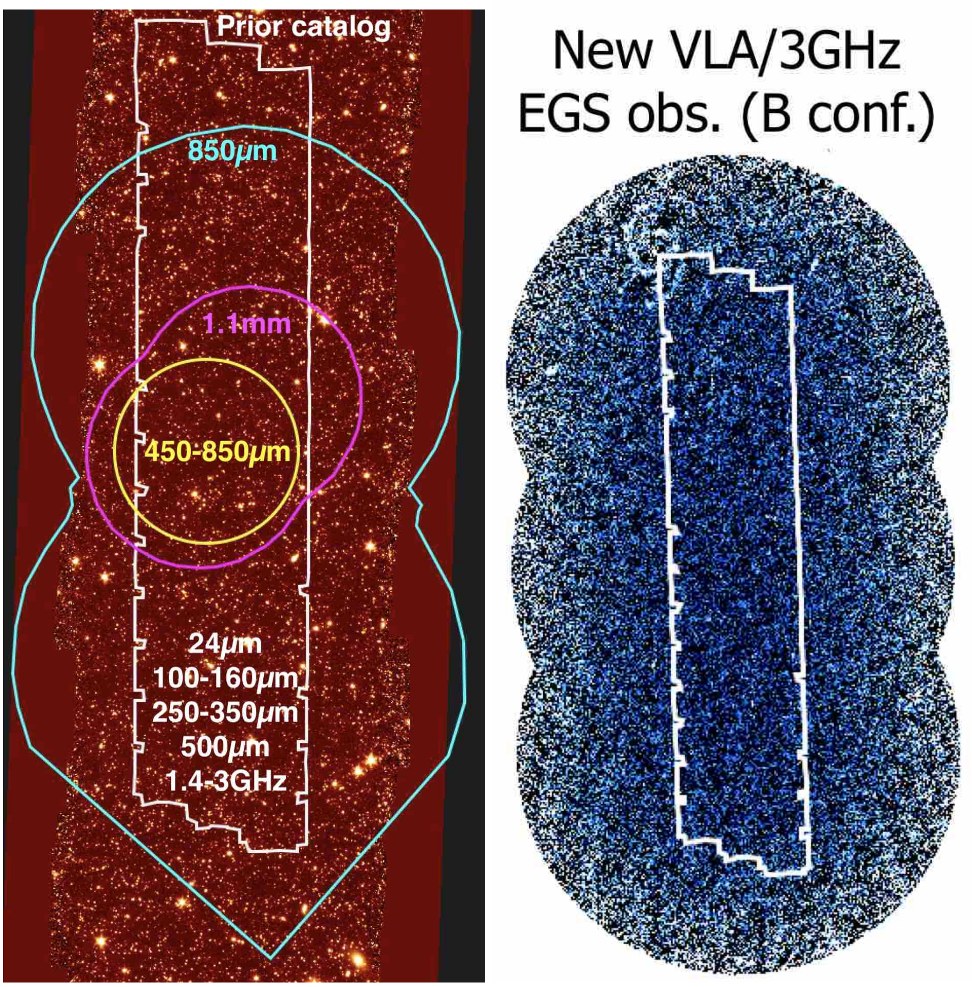

Figure 2.4: Left panel: Coverage of the super-deblended catalog: In white, the coverage of the prior catalog (based on *HST* observations). In cyan, the $850\mu m$ map coverage from the S2CLS program. In magenta, the SCUBA2 $450\mu m$ and $850\mu m$ maps coverage from Zavala et al. (2017). In yellow, the AzTEC 1.1mm image coverage from Aretxaga (2015). The MIPS, PACS, SPIRE and radio maps cover the full prior field. The background image is IRAC CH2, the catalog coverage is $\approx 8" \times 33"$. Right panel: Radio science image at 3GHz in the VLA/B-configuration covering the EGS field observed primarily to improve the super-deblending of the EGS field, the white contours delimits the “super-deblended" catalog coverage.

to IRAC channels, their photometric redshifts and their stellar mass. To get accurate redshift estimates, I used the more recent redshift compilation produced by Kodra et al. (2022), which includes photometric redshifts based on CANDELS (Grogin et al. 2011; Koekemoer et al. 2011) as well as grism-based redshifts from 3D-HST (Momcheva et al. 2016) and spectroscopic redshifts from the MOSDEF survey (Kriek et al. 2015). I have 2540 spectroscopic redshifts, 539 solid grism-based redshifts and 38378 photometric redshifts. This is important as the redshift plays an important role in the design of the prior catalog.

The use of the radio data is necessary, as I show in Figure 2.5 where I compare the expected flux density at 24μm and 3GHz for different redshift for the faintest 350μm detectable source in EGS. A source with the faintest 350μm detectable flux density would be expected to be bright enough at 24μm to be detected up to redshift ~ 4. Above this redshift, the 24μm flux would be too faint. This means that if I only based my prior selection on 24μm fluxes, this source would not have been selected, leading to a selection bias. To ensure that I did not miss any high redshift FIR sources, I looked at the radio continuum emission. The figure shows that whatever the redshift, if a source is detectable at 350μm, it should be bright enough in the radio to be detected at 3GHz. The radio image is then necessary to ensure the completeness of my catalog toward high redshift.

I also received the *JWST*/NIRCam data from the CEERS collaboration and decided to exploit them to improve the prior selection, indeed NIRCam is sensible to wavelength similar to *HST*/WFC3 and the first two channels of *Spitzer*/IRAC, but with a greater sensibility and better spatial resolution, allowing to detect deeply attenuated sources or high-redshift sources. As a member of the CEERS collaboration, I have access to a NIRCam photometric catalog produced by the collaboration (Finkelstein et al. in preparation). From this catalog I decided to use two pieces of information, the first one being the redshifts. I matched the Kodra et al. (2022) redshift catalog with the NIRCam catalog. For all the sources that had a redshift from Kodra et al. (2022) below 3, I kept it, as the UV and near-IR from *HST* are good enough to measure a reliable photometric redshift. When $z_{kodra+22} > 3$, I looked at the NIRCam counterpart, if the NIRCam redshift was better constrained (lower $\frac{dz}{1+z}$) and consistently above 3 ($z + dz > 3$), then I adopted the NIRCam photometric redshift along with the stellar mass estimated from SED fitting using the EASY (Brammer et al. 2008) and FAST (Kriek et al. 2018) softwares (Barro et al. in preparation). This led me to update the photometric redshift of 843 priors (2% of the full catalog).

The other piece of information I used was the better completeness of the NIRCam catalog compared to the Stefanon et al. (2017) catalog. I decided to add some new priors from the NIRCam catalog. To be added, a NIRCam source had to respect the following criteria:

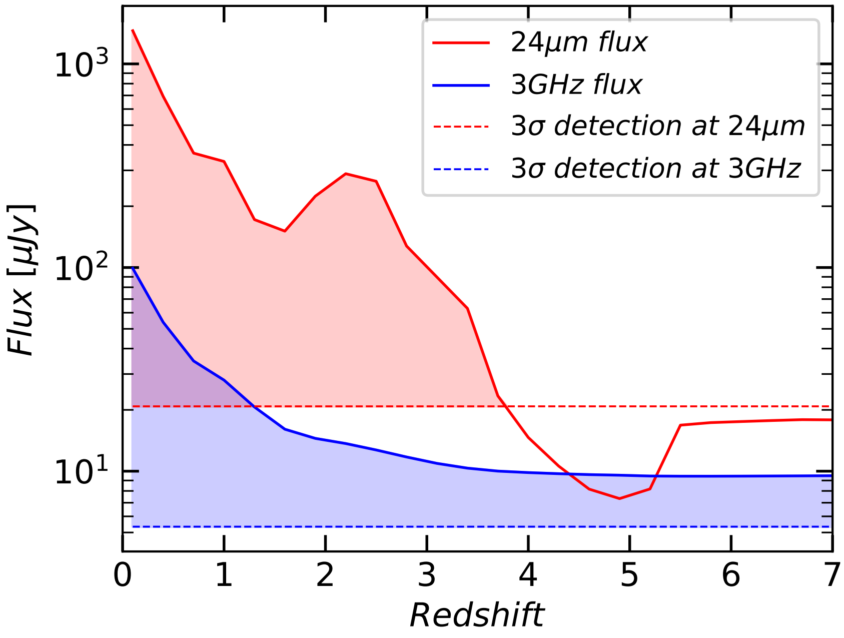

Figure 2.5: Flux density expected at $24\mu m$ (red) and 3GHz (blue) in the EGS field as a function of redshift for the faintest detectable source at 350μm. Red and blue horizontal lines show the 3σ detection limits at 24μm and 3GHz respectively. The SED template adopted is a Main Sequence template from Magdis et al. (2012) with redshift evolving q_{IR} (Magnelli et al. 2015) normalized to a 3σ detection at SPIRE 350μm ($S_{350\mu m} = 12mJy$).

- no counterpart in the Stefanon et al. (2017) catalog in a 1" radius
- a redshift lower than 8 and $\frac{dz}{1+z} < 0.09$
- at least a 2σ detection in the F356W and F444W filters, corresponding to the IRAC channel 1 and 2
- and $log(M_*) > 1.8 \times log(1 + 4 \times (z - dz)) + 8$, see Section 2.3.5 for more details on this threshold.

I decided to apply strong criteria to be conservative and make sure that I did not add spurious detections. Following this selection, I add 127 new priors (+0.3%) to the Stefanon et al. (2017) catalog.

I applied the prior-extraction method in the VLA $3GHz$ (Section 2.3.1), VLA $1.4GHz$ (Section 2.3.3) and MIPS $24\mu m$ (Section 2.3.4) images using my complete catalog of 41584 sources as prior.

2.3.1 . VLA 3GHz PHOTOMETRY

The correlation between radio and FIR emissions (Yun et al. 2001) makes the radio continuum emission an important tracer since high-redshift star-forming galaxies are expected to be bright in the radio while falling under the detection limit at $24\mu m$ (Jin et al. 2018; Magnelli et al. 2015; Delhaize et al. 2017, Figure 2.5). Radio emission is a tracer of star-formation at high redshift but can also be used to assess the presence of a so called radio loud AGN if we observe a radio excess compared to the expected continuum emissions.

The CEERS collaboration obtained two observations of the EGS field using the A and B configurations of VLA at 3GHz (Proposal IDs: VLA/21B-292 and VLA/22A-400, PI: M. Dickinson). These observations constitute the first deep radio mapping of the EGS field, and thus, are crucial to ensure the completeness ofmy catalog toward high-redshift. The data reduction was done through the default pipeline.

I had access to two images, with the A configuration image, I had a PSF FWHM of 0.7" and a 3σ detection threshold of 4μJy. With the B configuration image, I had a PSF FWHM of 2.3" and a 3σ detection threshold of 6μJy. The PSF of the A configuration allowed to resolve the most extended sources. This could become a problem as in my approach I considered all the sources as point-like. Extracting radio fluxes only from the A configuration would then be biased by a flux loss due to the spatial extension of the sources. The PSF of the B configuration being larger, it ensured that I didn't loose flux. However, it was shallower than the A configuration. For these reasons, I decided to fit both images. The PSFs being small, the prior density was low ($0.03 - \text{to} - 0.34$ sources/beam for A and B array respectively). Thus no blending problem for this band.

Both images were fitted using *Galfit* (Peng et al. 2002, 2010) and a 2D-Gaussian for PSF fitting. *Galfit* was not built to fit thousands of sources at the same time, so I divided the image in sub-images so that each sub-image had a size $\sim 10\times$ larger than the PSF FWHM. This allowed to have a reasonable number of prior in each box. To avoid any bias, the priors present in a buffer around the box were also taken into account. All the boxes are fitted together in parallel, this procedure allowed to save computational time. At the end, all the boxes were put back together to form the final output image for both the model and residuals. This technique was applied for all the images I fitted. This method has been developed and tested by Liu et al. (2018).

After fitting the 41584 prior positions, I obtained 1173 3σ detections in the A configuration and 1087 3σ detections in the B configuration. The fit was performed in two runs, the second run was used to improve the flux extraction of bright sources by allowing their position to vary up to 1 pixel. I used the Source Extractor (*SExtractor*) software (Bertin & Arnouts 1996) to extract any remaining sources from the residual. Each residual was visually checked to ensure that it was not a jet. I added 6 radio sources, detected in both configuration. The fluxes and uncertainties bias were carefully calibrated using extensive Monte-Carlo simulations. The simulations were also used to quantify the uncertainties and make them quasi-Gaussian, see Section 2.3.2 for more details.

To produce the final 3GHz radio catalog, I merged the results of both configuration. For all the priors with a 3σ detection in the B configuration (with the large PSF) I used the B flux as the real flux. For the remaining sources, I used a weighted average of the A and B extracted fluxes. After this procedure, I had 1722 3σ detections at 3GHz and a 1σ detection limit of 1.78μJy and a prior catalog of 41590 positions.

My catalog was compared with a blind-extraction catalog using PyBDSF (private communication). I show the comparison in Figure 2.6, the fluxes are consistent within error bars, the flux difference stays below 10%. One can see on the right panel that my method allows to have much better constrained fluxes than with a simple blind extraction method. I reached a 3σ detection level of 5.34μJy and only 8.43μJy with the PyBDSF blind extraction. The double distributions of uncertainties illustrate the method I chose to merge the A and B configuration measurements. I emphasize that the fact that I carefully calibrated the uncertainties using simulations let me believe that I do not underestimate them.

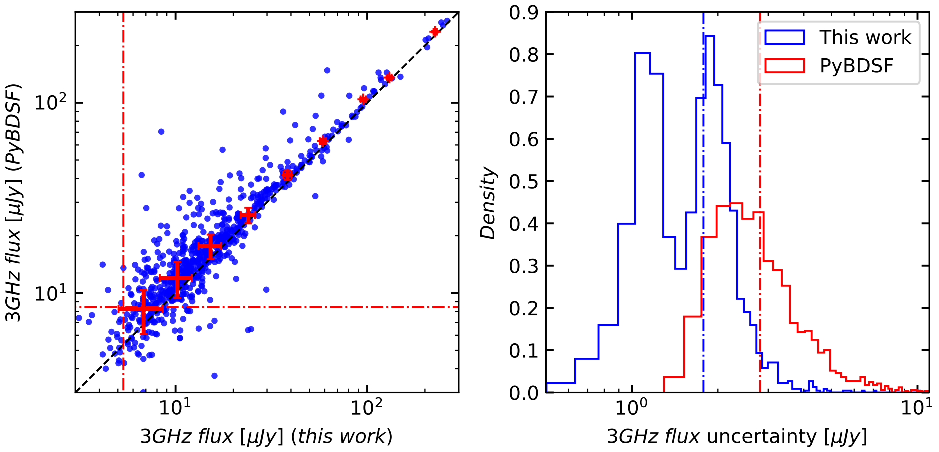

Figure 2.6: Comparison ofmy radio flux extraction using PSF-matching with a blind extraction using PyBDSF. Left panel: comparison of the fluxes at 3GHz, the red markers are median in bins with the median error in the bin and the black dotted line is the 1:1 correlation. The red lines are the 3σ detection limits. Right panel: comparison of the uncertainties on 3σ detections, the dotted lines are the median uncertainties ($1.78\mu Jy$ for this work and $2.81\mu Jy$ for the PyBDSF blind-extraction).

2.3.2 . MONTE CARLO SIMULATIONS

In this Section I describe the Monte-Carlo simulations I performed to estimate the flux biases and obtain quasi-Gaussian uncertainties for all the images I fitted. These simulations were also used to estimate the correct level of background for each image, except for the radio images because they are obtained via interferometry. I take the band PACS/100μm as an example here as it is in the far-IR images that the measurement biases are the strongest.

The Monte Carlo simulations for the super-deblended catalog have been developed and tested by Liu et al. (2018) and updated by Jin et al. (2018). I refer to those papers for a detailed presentation of the simulations. Here I am summarizing the method.

I identified three main parameters that could bias the flux measurements: the local noise, the local residuals and what I define as the crowdedness, in other words, the number of sources inside the beam. The crowdedness is defined as :

$$crowd_i = \sum_{j=1}^{N} e^{(}-d_{j,i}^2/d_{PSF}^2), \tag{2.1}$$

where $d_{j,i}$ is the angular distance from source j to current source i and d_{PSF} is the FWHM of the PSF, they both are in arcseconds.

The simulations were performed by adding on top of the original image mock sources. I chose the position randomly and the flux was randomly chosen between 3σ and 20σ. There were produced using the PSF with *galfit*. After fitting the image with the mock source, I compared the flux and error returned by *galfit* and the input flux value. This procedure was repeated 5000 times. I stress that for a mock source to be taken into account for the corrections, the simulated source had to be at a distance greater than 0.7" from any prior. This 0.7" was chosen because the minimal distance between two priors of my catalog is greater than 0.7" for 98.5% of priors, meaning that simulating two sources closer than this would have been unrealistic. The median minimal distance between 2 priors in my catalog is 2.1". This additional constraint avoided the creation of artificially over-blended regions that would have increased the uncertainties. I point out that this last criterion was new compared to L18; J18.

To correct the flux biases, I divided the mock sources into several bins on the three parameters and for each bin, the median value of $(S_{in} - S_{out})$ gave us the bias in each bin, the medians were fitted with a degree 2 polynomial. I started by estimating the flux bias due to the local noise estimated by *galfit* and corrected the fluxes accordingly by adding the corresponding bias estimated with the polynomial fit. The median of $(S_{in} - S_{out})$ was corrected to zero by adding a normalization bias if needed. The same method was repeated for the two other parameters, I estimated the flux bias due to the residual flux and corrected the fluxes accordingly. Finally, I corrected flux bias linked to the crowdedness. Both the local noise and the residuals were normalized by the RMS noise taken from the noise map, it allowed to take into account the fact that the depth of the image is not necessarily flat. Figure 2.7 illustrates the three steps for PACS/$100\mu m$.

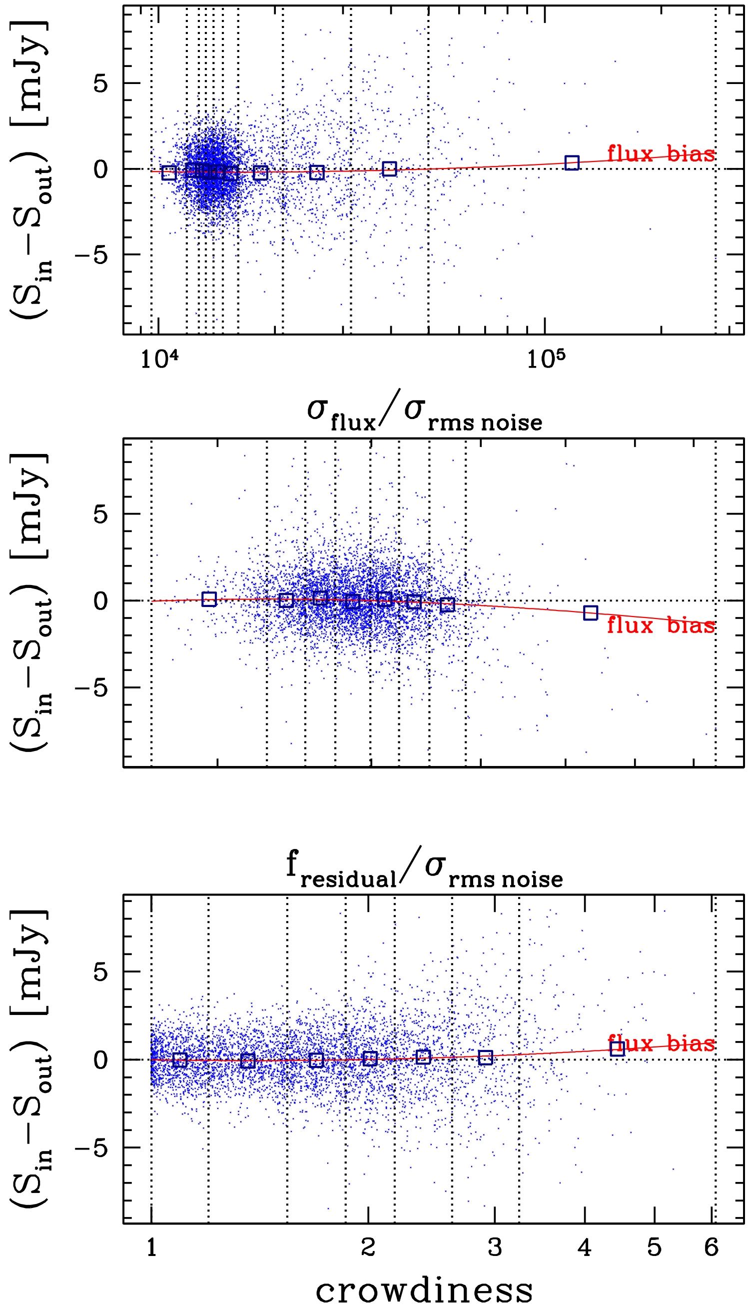

Figure 2.7: Flux bias estimation in PACS/100μm simulations. I first estimate the bias due to the *galfit* errors in the upper panel, then to the residuals in the middle panel and lastly to the local crowdedness in the lower panel.

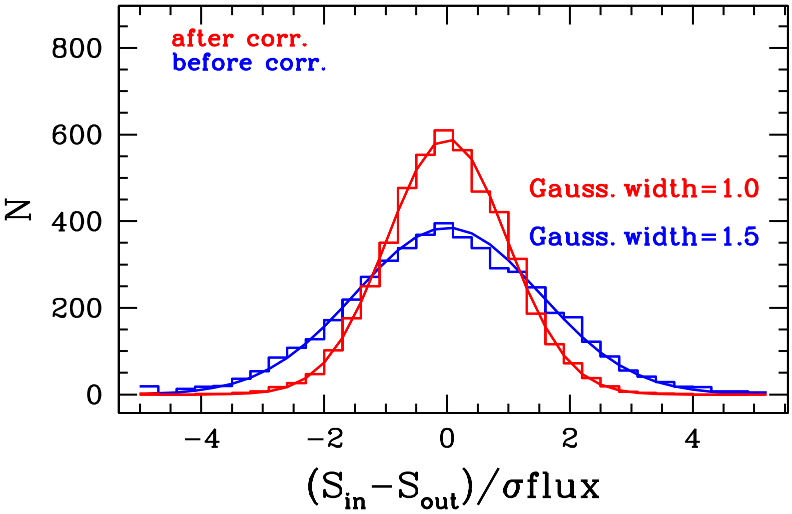

Figure 2.8: Errors bias corrections in PACS/$100\mu m$ simulations. The original distribution is shown in blue and the corrected one in red. We go from a quasi-Gaussian with a standard deviation of 1.5, signature of under-estimated errors, to 1 after correction, signature of well-calibrated errors.

To make the errors quasi-Gaussian, I used a similar approach. I used the same bins based on the three parameters and estimated the difference between the *galfit* errors and the actual errors given by the RMS of $(S_{in} - S_{out})$. Practically, I calculated the RMS of $(S_{in} - S_{out})$ in each bin and I fitted a degree 2 polynomial to the RMS/σ_{galfit} and corrected the errors accordingly by multiplying them by the factor given by the polynomial. The RMS of $(S_{in} - S_{out})/\sigma_{flux}$ is corrected to one by multiplying by a normalization factor if needed. Having a Gaussian distribution with a RMS of 1 ensured us that I did not either overestimate or underestimate the errors. The same method was repeated for the two other parameters, I estimated the errors bias due to the residual flux and corrected the errors accordingly. Finally, I corrected error bias linked to the crowdedness. Just like for the flux, both the local noise and the residuals were normalized by the RMS noise taken from the noise map. Figure 2.8 illustrates the evolution of the distribution of $(S_{in} - S_{out})/df$ before and after the correction of the errors. The original distribution (in blue) had a width greater than 1, this typically means that the *galfit* errors were generally underestimated. On the contrary, the corrected distribution (in red) had a width of 1, the uncertainties were well calibrated.

These simulations allowed us to calculate the fluxes biases and correction factor I needed to apply the the errors for all the flux and errors I extracted from the original images, depending on the three aforementioned parameters.

2.3.3 . VLA 1.4GHZ PHOTOMETRY

Before the VLA 3GHz observations of the EGS, the only other radio coverage of that field was at 20cm (1.4GHz) using also VLA (Ivison et al. 2007). This observations was shallower, with a 3σ detection level of $40\mu Jy$ and had a larger PSF FWHM of 4.1" compared to the 3GHz imaging. I decided to still fit this image as detections or upper limits could confirm a detection, or a radio excess, thus the presence of a radio loud AGN.

I built a gaussian circular PSF with FWHM of 4.1". I extracted the flux at the positions of my 41590 priors. I had a density of ~ 1 source per beam, so I was able to extract fluxes for all sources without huge blending problems. I fitted the image using *galfit*. Just like for 3GHz I ran a second pass to allow bright sources (at least 10σ) to vary position up to a pixel. I also used *SExtractor* to extract any remaining sources from the residual map, I didn't find any. I got 213 3σ sources with a median flux uncertainty $\sigma = 13.5\mu$Jy. The fluxes bias and uncertainties were corrected using extensive Monte-Carlo simulations (see Section 2.3.2 for more details).

In Figure 2.9 I compare my results to Ivison et al. (2007). They searched Signal/Noise images using the SAD detection algorithm (Biggs & Ivison 2006) and their catalog only contains 3σ sources. My measurements are consistent within errors, the difference is below 5% at all flux. On the right panel I show that my extraction method allowed us to better constrain the measured fluxes.

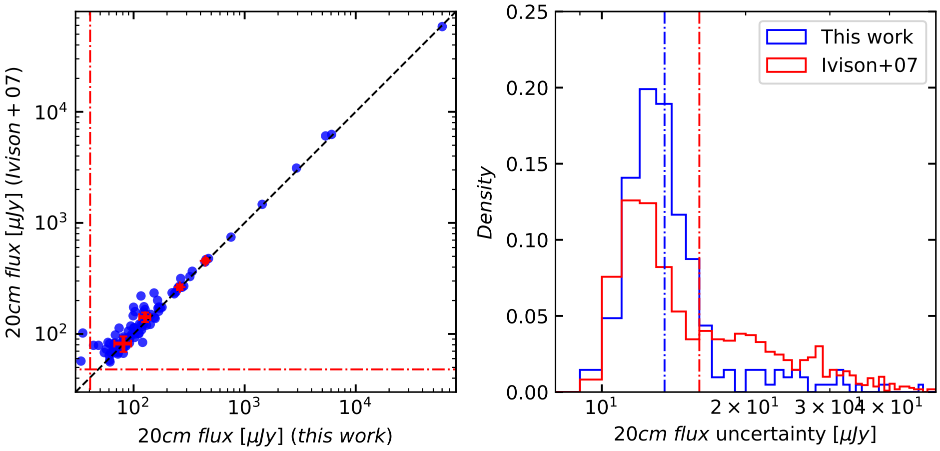

Figure 2.9: My 20cm photometry vs. measurements in Ivison et al. (2007). Left panel: 20cm fluxes comparison, red dotted lines are the 3σ detection limits, the black dotted line is the 1:1 correlation and the red markers are median in bins with the median error in the bin. Right panel: Comparison of the uncertainties on 3σ sources, vertical dotted lines are the median uncertainties ($13.5\mu Jy$ for this work and $16\mu Jy$ for Ivison et al. (2007)).

2.3.4 . MIPS 24μm PHOTOMETRY

The last photometric data needed to make my prior catalog was the *Spitzer*/MIPS $24\mu m$. The fitting was performed on an image from the second public data release of The FIDEL Survey, a *Spitzer* Space Telescope Legacy Science program (Dickinson 2007) with a 3σ detection threshold of $21\mu Jy$. I used a PSF made with *StarFinder* (Diolaiti et al. 2000), manually selecting isolated, bright objects. The PSF has a 5.7" FWHM.

The density of prior was ~ 2 source per beam. To have the most reliable flux extraction, I need to stay around 1 source per beam. The way I chose to tackle this problem was to make a two run procedure. I emphasize that this was not an issue for Liu et al. (2018) or Jin et al. (2018) as they add a less dense prior catalog. I first fitted the complete catalog using *galfit*, this allowed us to have upper limits on the faintest galaxies. These were useful as I showed in Figure 2.5 that some radio detected galaxies could be faint at $24\mu m$, having upper limits on these galaxies helped constrain the SED. Like the radio map, the image was fitted by dividing it into smaller boxes that contained only a handful of priors, to prevent any bias, the priors that are in a buffer around the box are also taken into account. After this first run, I had 2418 3σ detections with the median uncertainty being $9.2\mu Jy$. Just as for the radio, the fitting procedure was the same as in L18; J18: I used the first-pass results to get flux estimations and with the second-pass I allowed the position of the brightest objects (at least 10σ) to vary up to 1 pixel (1.2"). This two pass method lead to a cleaner residual map, hence improving the flux measurements of bright sources. The flux biases and uncertainties were corrected based on extensive Monte-Carlo simulations (see Section 2.3.2 for more details).

The most reliable fluxes are extracted at low density (around ~ 1 source per beam). This is why I decided to make a second run with less prior positions. I used a mass and redshift dependent cut to reduce the pool of priors. The threshold was following the same empirical trend from J18 : $log(M_*) > 1.8 \times log(1 + 4 \times z) + a$, with a being the offset allowing to choose the number of priors I wanted to keep in the pool : $a = 7.12$ to have $\langle\rho_{beam}\rangle = 1$. This priors selection was relevant because of the well known correlation between FIR luminosity and stellar masses in star-forming galaxies, also known as the Main-Sequence (Daddi et al. 2007; Elbaz et al. 2007; Noeske et al. 2007; Pannella et al. 2009; Karim et al. 2011; Rodighiero et al. 2011; Schreiber et al. 2015). I also decided to keep the 3σ detections from the first run that fell under the threshold. The selection of priors to keep for the second run is illustrated in Figure 2.10.

The second run was performed in the same way as the first one, but extracting fluxes in 19964 positions instead of 41590. At the end of the procedure, I had 2782 3σ detections with a median uncertainty of 6.94μJy. Just like for the radio, I ran *SExtractor* on the residuals to extract any additional sources. I found 5 of them. After re-fitting the image with the 5 additional

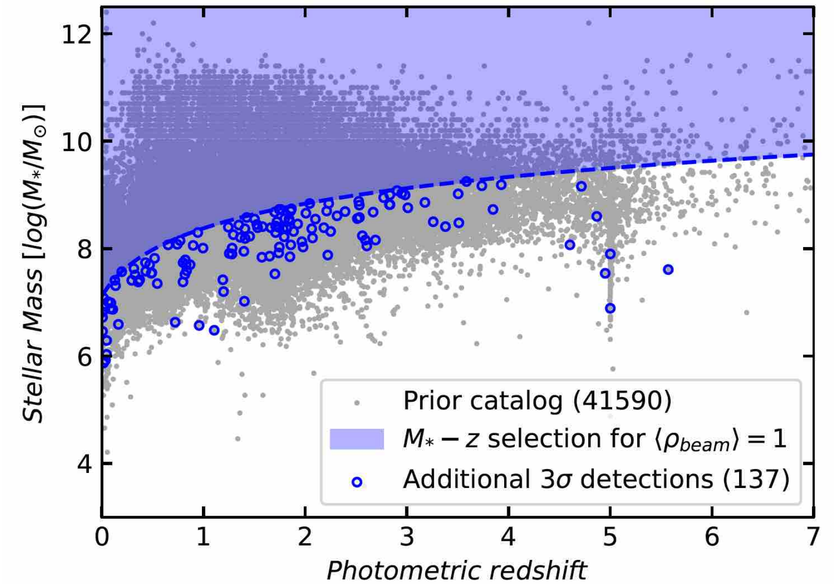

Figure 2.10: Selection of priors for the $24\mu m$ PSF-fitting photometry for $\langle\rho_{beam}\rangle = 1$ using a $M_* - z$ dependant threshold (blue dashed line). Blue circle markers are 3σ sources from the first run kept in the second run despite being below the threshold.

prior positions, I had 2773 3σ detections. The change in the number of detected sources was mostly driven by spurious detections.

A major difference with the radio is that the $24\mu m$ was not obtained via interferometry. This means that the background emissions could lead to a bias when extracting the fluxes. To tackle this problem, that was not raised in the previous super-deblended catalogs, I chose to explore the impact of the uniform background level required as an input parameter for *galfit* when PSF-fitting the image. Usually, the background is measured in the image, and then used as *galfit* input. Here, I decided to check if the quality of the fit was affected by the level of background. To do so, I ran Monte-Carlo simulations as described in Section 2.3.2. After each simulation, I got calibrated quasi-Gaussian uncertainties on the measured fluxes of the simulated sources. I ran several simulations, the only difference being the background level. I observed that changing the background level could change the median uncertainty by up to $\sim 15\%$. Hence, for all the images I fitted, I decided to systematically check which level of background allowed the lowest uncertainties. The risk here would have been that the level of background was not the 'real' background anymore, introducing a bias in the flux measurement. However, the Monte-Carlo simulations were also used to correct for such flux bias (see Section 2.3.2). The starting point to choose the background was the background measured in the image, and I explored around it keeping an eye on the bias I introduced as to achieve a balance between getting smaller error bars and introducing flux bias as illustrated in Figure 2.11.

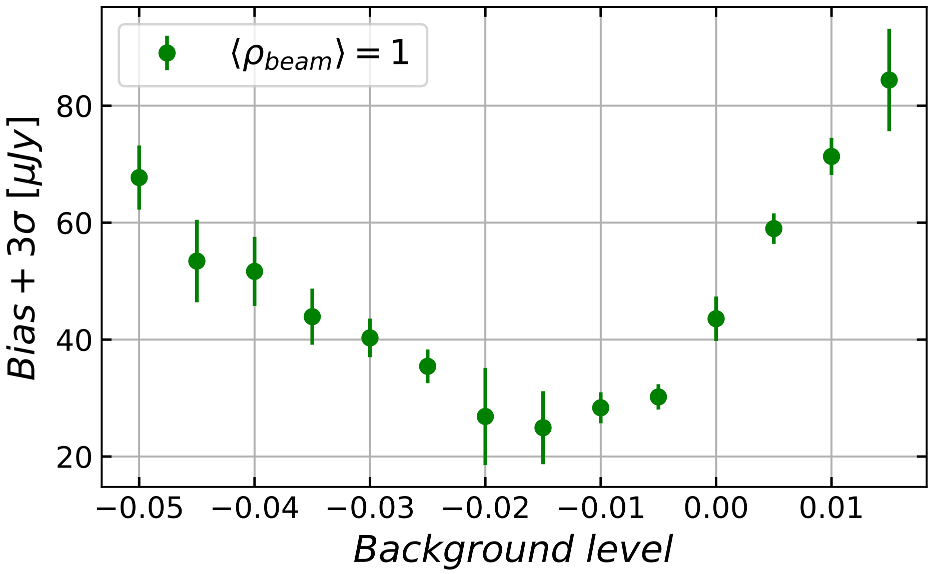

Figure 2.11: Effect of the background on the goodness of the fit for the MIPS/24μm image at 1 source per beam. Via Monte-Carlo simulations, I estimate the median uncertainty σ and the flux bias for several background level. This study allows us to chose the background level leading to the best performances. Each point is a different simulation, the error-bars were obtained by re-running the same simulation several time and measuring the standard deviation of the estimated bias and σ.

In Figure 2.12 I compare my $24\mu m$ photometry to the publicly available catalog from Magnelli et al. (2009). It is a catalog from the same image using IDL-based SVD+DAOPHOT type routine based on IRAC prior positions[2]. The two catalogs are consistent up to $\sim 100\mu Jy$. For fluxes higher than $100\mu Jy$, Magnelli et al. (2009) fluxes are on average 15% brighter than mine. This can be explained by the fact that my prior catalog is 3 times denser than theirs, thus they are sensible to blending, they did not take into account the fact that the light from bright sources could have several contributor. There is also the fact that I did not use the exact same PSF, and there could be a background effect. On the left panel of Figure 2.12, I compare the uncertainties of 3σ detected sources, our results are compatible, Magnelli et al. (2009) find a median error smaller than mine (5.24μJy vs 6.94μJy). I recall that Magnelli et al. (2009) doesn't take blending into account when estimating his uncertainties, which can be an important source of error, the PSF FWHM being 5.7".

2.3.5 . PRIOR SELECTION

---

[2] For more information on the catalog please contact B. Magnelli: benjamin.magnelli@cea.fr

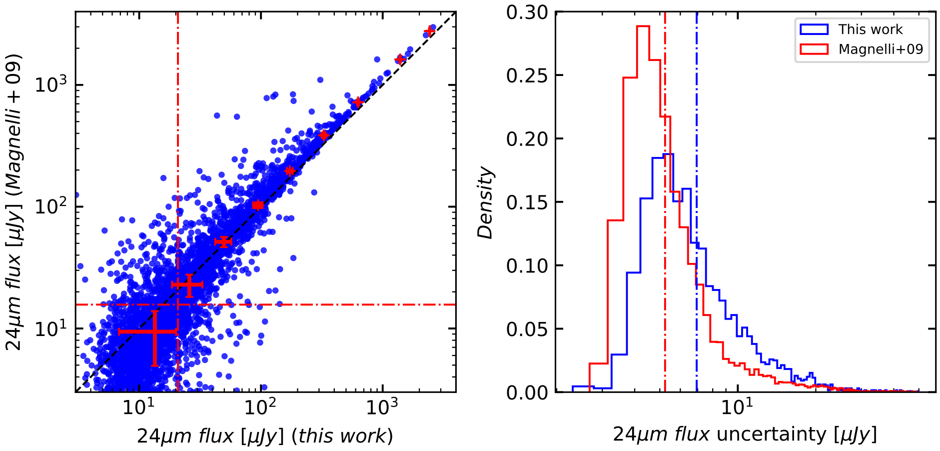

Figure 2.12: My $24\mu m$ photometry vs. measurements in Magnelli et al. (2009). Left panel: $24\mu m$ fluxes comparison, red dotted lines are the 3σ detection limits, the black dotted line is the 1:1 correlation and the red markers are median in bins with the median error in the bin. Right panel: Comparison of the uncertainties on 3σ sources, horizontal dotted lines are the median uncertainties ($6.94\mu Jy$ for this work and $5.24\mu Jy$ for Magnelli et al. (2009)).

I obtained 3339 sources with S/N > 3 24μm and/or radio flux based on the 41595 prior positions. As I went toward larger wavelength, the beam size got larger. If I had used the full catalog, the source density would have reached $20 - 85$ sources per beam for the SPIRE bands. The density would then be far too important to make any consistent flux extraction. I needed to reduce the pool of prior.

As the depth of the images I were using were comparable to the ones used in the COSMOS field, I decided to adopt the same selection process as described in Jin et al. (2018). The selection was based on the existing relation between star-formation, hence FIR luminosity for dusty galaxies, and the stellar mass, known as the Main Sequence (Daddi et al. 2007; Elbaz et al. 2007; Noeske et al. 2007; Pannella et al. 2009; Karim et al. 2011; Rodighiero et al. 2011; Schreiber et al. 2015). I decided to add to the 3339 MIPS and radio sources all the priors with a M_* and z such as $log(M_*) > 1.8 \times log(1 + 4 \times z) + 8$. In total, I had 7032 sources in my prior catalog for the FIR fitting. I show in Figure 2.13 the M_* vs z distribution of the MIPS/radio sources in blue, and the threshold I used to select the 3693 additional mass-selected priors.

The remaining 34563 sources were considered too faint to participate in the flux of the FIR images. They constitute the background, that was carefully estimated using extensive Monte-Carlo simulations. In the following, I call the prior catalog the catalog of 7032 $24\mu m$+radio+mass-selected sources.

At the end of this chapter, we have a clear idea of why it is necessary to build the most possibly accurate far-IR catalog. I now have a robust catalog

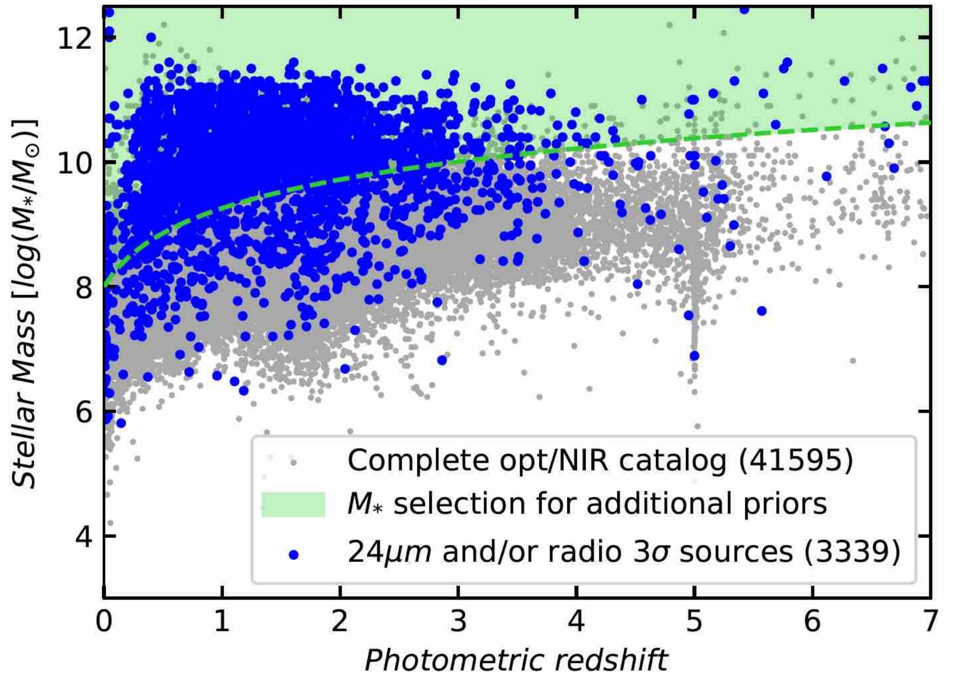

Figure 2.13: Selection of the priors for the FIR/sub-mm deblending. The blue dots are the $24\mu m$ and/or radio 3σ detections, the green dotted line is the threshold for the mass-selected ($log(M_*) = 1.8 \times log(1+4 \times z)+8$) additional priors. The grey dots are the sources from the full opt/NIR catalog.

of prior sources that have a high probability of being FIR bright, or at least having non-negligible FIR emission. In the next chapter, based on this catalog, I apply the next step of super-deblending technique: extracting FIR fluxes for each prior.

3 - BUILDING THE SUPER-DEBLENDED CATALOG

In this chapter, I detail the bulk of the making of the “super-deblended" catalog step by step, highlighting the my contributions to adapt and improve the method.

I had 9 images to fit, the order of fitting was chosen based on the beam size as it was easier to extract fluxes on images with a smaller beam thus more resolved. In Table 3.1 I show the list of images with their corresponding beam size and pixel scale as well as their coverage of the prior catalog. Based on this Table, the order of fitting was chosen to be: PACS/100, PACS/160, AzTEC/1.1, SCUBA2/850 (both images), SCUBA2/450, SPIRE/250, SPIRE/350 and I finished with the most confused image SPIRE/500. The detailed information about the origin of these images is mentioned in Section 2.2.

Table 3.1: Images used during the super-deblending procedure.

Band	Instrument	Beam size§ (arcsec)	Pixel size (arcsec)	Area‡ (arcmin^2)
$100\mu m$	*Herschel*/PACS	7.2	1.2	200.5 (100%)
$160\mu m$	*Herschel*/PACS	12	2.4	200.5 (100%)
$250\mu m$	*Herschel*/SPIRE	18.15	6.0	200.5 (100%)
$350\mu m$	*Herschel*/SPIRE	25.15	8.33	200.5 (100%)
$450\mu m$	JCMT/SCUBA2	11.4	2.0	66.0 (32.9%)
$500\mu m$	*Herschel*/SPIRE	36.3	12.0	200.5 (100%)
$850\mu m^{*}$	JCMT/SCUBA2	11.0	2.0	177.4 (88.5%)
$850\mu m^{\dagger}$	JCMT/SCUBA2	14.5	2.0	66.0 (32.9%)
$1.1\ mm$	LMT/AzTEC	8.0	1.0	38.9 (19.4%)

Notes.
§ Full width half maximum of the beam.
‡ In parenthesis is the fraction of the prior catalog covered by each image (see Figure 2.4).
* Image from Geach et al. (2017).
† Image from Zavala et al. (2017), deeper than Geach et al. (2017).

The density of priors is computed by

$$\langle \rho_{beam} \rangle \equiv \frac{N_{prior}}{A_{EGS}} \times \frac{\pi}{ln2} \times \theta^2_{beam}, \tag{3.1}$$

where N_{prior} is the number of priors, A_{EGS} is the area of the catalog (200.5 arcmin^2) and θ_{beam} is the beam size (FWHM) in arcmin. Our prior catalog of 7032 sources had a density of ~ 0.6 sources per beam at 100μm, this density was ideal to extract fluxes as it was below 1 source per beam.

3.1 . 100μm PHOTOMETRY

To extract fluxes from the PACS/$100\mu m$ image, I used the same method as for the MIPS/$24\mu m$. For the FIR images, I divided the images in boxes so that they were 2 to 5 $\times$ larger than the PSF FWHM, this was necessary because of the low resolution and blending. Starting here, the buffer becomes extremely important as a sources just outside the be could largely spreading in the box due to the large PSF. This has been tested via extensive simulations and was proven to be the optimal method to achieve the best photometric measurements (Liu et al. 2018). I extracted fluxes for all the 7032 priors. I made extensive Monte-Carlo simulations to measure the background level and fitted the image using *Galfit*.

Just as for $24\mu m$, I used a two-run procedure, the second run was used to let the brightest sources ($> 10\sigma$) vary their position up to 1 pixel (1.2"). After these two runs, I had 294 detections.

I used *SExtractor* to extract any additional sources from the residual that was not in my prior catalog. To be conservative and not risk to add spurious detections, I added only the sources with a 3σ peak estimated by *Sextractor*. I found 29 additional sources, 23 of them were actually in the Stefanon et al. (2017) catalog but were not selected when building the prior catalog, they were not detected at 24μm or in the radio and were below the mass limit (see Section 2.3.5. I added them to the priors list. The 6 other extracted sources were also added to the catalog.

After adding these sources, I needed to re-run the fitting as the presence of these priors could affect the flux extraction of the nearby sources. I show in Figure 3.1 the original image in the upper panel, the *galfit* model in the middle and the residuals in the lower panel, the residuals are clean, there is no sources left. After the second run, I had 305 detections and an updated prior catalog of 7061 priors.

However, *Galfit* is known for not necessarily reflecting real errors (Peng et al. 2002). To have a reliable estimation of the errors and correct possible flux biases, I decided to run Monte-Carlo simulations.

3.2 . 100μm SOURCE CATALOG

Once the simulations had been performed, I applied the correction to the fluxes and errors from *galfit*. Each prior had a different correction that depended on the three parameters: the *galfit* uncertainty, the local residual flux and the crowdedness. I precise that due to the high-pass-filtering processing, I had to scale up the fluxes by a factor of $\frac{1}{0.88}$ for $100\mu m$ fluxes and $\frac{1}{0.89}$ for $160\mu m$ fluxes (using data from the public data release of the PACS Evolutionary Probe PEP (Lutz et al. 2011)). After correcting the flux and errors, I obtained

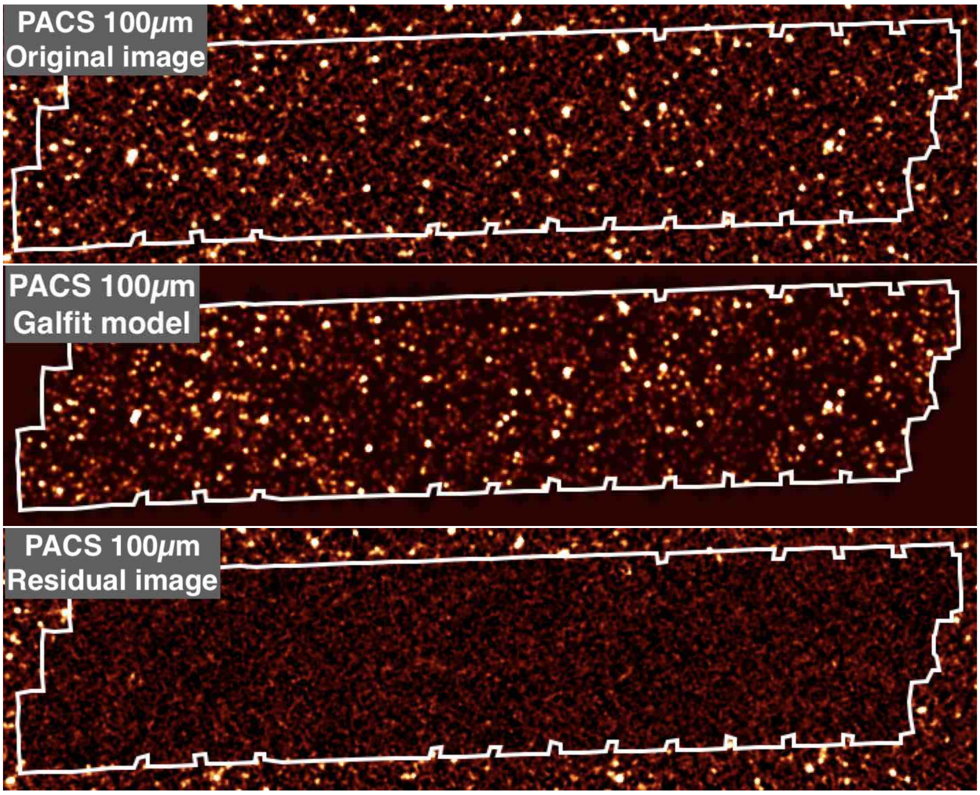

Figure 3.1: Fitting of the PACS/100μm image. Upper panel: Original image. Middle panel: model from PSF-fitting using *galfit*. Lower panel: residual map after subtraction of the model from the real image. The white contour delimits the perimeter of the prior catalog I used.

for PACS/$100\mu m$ a total of 305 3σ sources with median uncertainty of $1.29 mJy$. The detection rate was $\sim 4-5\%$, this was similar to the detection rate of Jin et al. (2018) at $100\mu m$ with a similar depth.

3.3 . COMPARISON TO LITERATURE

Now that I had a robust 100μm catalog, I needed to asses its quality. To do so, I compared my catalog with a publicly available catalog from *PACS Evolutionary Probe* (PEP, Lutz et al. 2011). The PEP catalog is a blind catalog, they did not use any prior. I matched my catalog with theirs, using a 2" constraints. I show in Figure 3.2 the comparison. The fluxes are consistent, the flux difference was on average less than 5%. My uncertainties were also similar to PEP, demonstrating that they were well calibrated. The fact that the median of my uncertainties was $\sim 6\%$ larger can be explained by the fact that Lutz et al. (2011) did not take into account the blending. The blending also explains the orange markers in the left panel of Figure 3.2 that are above the 3σ detec-

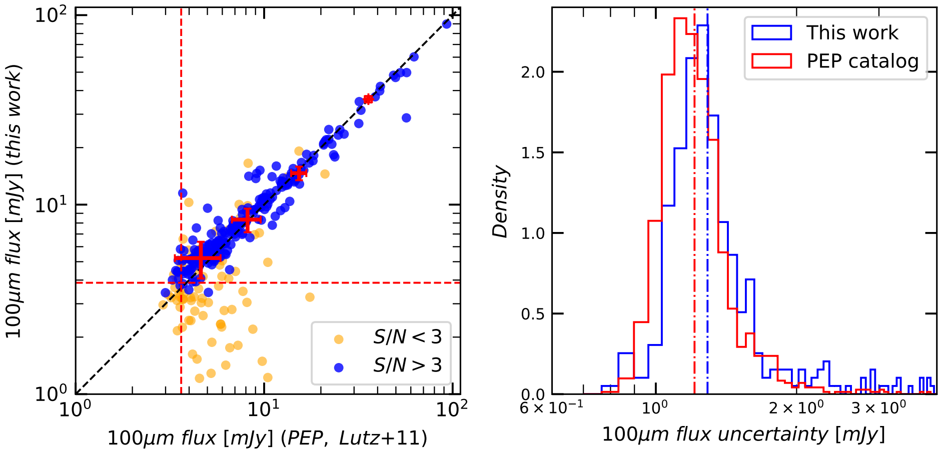

Figure 3.2: My $100\mu m$ photometry vs. measurements in Lutz et al. (2011). Left panel: $100\mu m$ fluxes comparison, blue markers are sources with $S/N > 3$ in both catalogs, orange markers are sources with $S/N < 3$ in at least one catalog, red dotted lines are the 3σ detection limits, the black dotted line is the 1:1 correlation and the red markers are median in bins with the median error in the bin. Right panel: Comparison of the uncertainties on 3σ sources, vertical dotted lines are the median uncertainties ($1.29\mu Jy$ for this work and $1.21\mu Jy$ for Lutz et al. (2011)).

tion limit of the PEP catalog (red vertical dotted line) but not detected in my catalog.

With the additional priors from the residual map, my updated prior catalog had 7061 positions. For the $160\mu m$ image, I then had a density of 1.6 sources per beam. The density was too high and needed to be reduced to perform efficient flux extraction. To select which priors to keep and which one to discard, I did not use the same method I used for $24\mu m$ (see Section 2.3.4). The super-deblending method consisted here in using all the available information I had on the priors to be sure to keep only the ones where I could be certain that there was a non-negligible emission at $160\mu m$. I describe how to achieve this in the following Sections.

3.4 . SED FITTING

From the prior catalog based on Stefanon et al. (2017), I had K_S and IRAC measurement for all the priors. For the priors I decided to add based on NIRCam, I used NIRCam/F356W and NIRCam/F444W as proxy for IRAC channels 1 and 2. Based on these photometric data and the fluxes I extracted in the radio and at $24\mu m$ and $100\mu m$, I could fit the SED of each prior. By fitting the SED, I could predict the flux that I expected for each prior in the 160μm PACS band.

I used the SED fitting recipes and parameters from Liu et al. (2018) and Jin et al. (2018). The SED fitting procedure was based on four components:

- (1) a stellar component (Bruzual & Charlot 2003) with a Small Magellanic Cloud attenuation law;
- (2) a mid-infrared active galactic nuclei (AGN) torus component (Mullaney et al. 2011);
- (3) dust continuum emission from the Magdis et al. (2012) library with the more updated $L_{IR}/M_{dust} - redshift$ evolution taken from Béthermin et al. (2015);
- (4) a power-law radio continuum with an evolving $q_{IR} = 2.35 \times (1 + z)^{-0.12} + log(1.91)$ (Magnelli et al. 2015; Delhaize et al. 2017).

For sources with a spectroscopic redshift, the fitting was performed at fixed redshift. When I only had a photometric redshift, I allowed redshift variations within $\pm 10\% \times (1 + z_{phot})$.

In addition to these four components, the SED fitting was adapted to each priors based on three parameters, that were estimated after a first run of the procedure:

- At the end of the SED fitting procedure, I could estimate the SFR_{IR} for each prior from their integrated L_{IR}, assuming $SFR_{IR} = L_{IR}/(1 \times 10^{10} L_{\odot}) M_{\odot} yr^{-1}$ (Daddi et al. 2010). I also had the stellar mass of each galaxy from Stefanon et al. (2017). I could then classify each prior as Main Sequence or starburst by measuring the distance to the Main Sequence from Sargent et al. (2014) at the fitted redshift. Sources were considered to be pure starbursts if $log(SFR/SFR_{MS}) > 0.6$ dex and $SFR/\sigma_{SFR} > 3$ and to be pure Main Sequence if $log(SFR/SFR_{MS}) < 0.4$ dex and $SFR/\sigma_{SFR} > 3$. In the second run of the SED fitting, I fitted them with the appropriate templates. When a clear classification couldn't be obtained, they were fitted with all templates. At this stage, I obtained 365 pure starburst ($\sim 5\%$) and 1182 pure Main Sequence ($\sim 17\%$).
- As I did not want the dust fitting to be biased by the presence of an AGN, if the observed radio fluxes were $2\times$ higher than the prediction from the FIR–radio correlation with a $> 3\sigma$ significance, I did not include the radio photometry in the fit. These sources were classified as radio-loud AGNs, at this stage I identified 138 of them ($\sim 2\%$).
- Finally, I knew that the presence of PAHs features at $24\mu m$ and the scatter of the FIR-radio correlation could bias the FIR fitting. This was why I decided, for sources with a combined $S/N \geq 5$ over the $100\mu m - 1.1mm$

range, to not fit the 24μm and radio photometry. At this stage, I had 103 such cases ($\sim 1.5\%$).

After the second run using the proper templates and fluxes based on the aforementioned parameters, I extracted fluxes predictions for each priors with an associated uncertainty allowing to evaluate the quality of the prediction. In the next Section, I explain what criteria I use to select the priors to fit at $160\mu m$.

3.5 . SELECTING PRIORS FOR 160μm

I now had for all 7061 priors a prediction of their flux at $160\mu m$. I wanted to keep as priors the priors with the brightest predicted flux. To choose where to put the threshold, I had to achieve a balance between two criteria. I wanted to be as complete as possible, in that case the selection limit had to be 1σ, the detection limit of the image. But, as already mentioned, to extract fluxes accurately, I must keep a density of priors below 1 source per beam. The threshold was selected as to respect both of these criteria. To be conservative, the threshold was not applied on the predicted fluxes, but on $F_{SED} + 2 \times \sigma_{SED}$. In Figure 3.3, I show the evolution of the density of priors in the PACS/160μm image with the selection threshold. Choosing a threshold so that the density is close to 1 source per beam would lead to have priors with a predicted flux below the detection limit. Thus I decided to choose a higher threshold, corresponding to the detection limit at $160\mu m$ ($\sigma_{160} = 2.77$mJy).

I only kept the priors with a predicted flux such that $F_{SED} + 2 \times \sigma_{SED} > 3mJy$. Thus, the prior catalog was reduced from 7061 to 2769 for the PACS/$160\mu m$ band reducing the prior density from 1.57 to 0.61 sources per beam.

The result of this selection was that I was going to ignore the presence of a lot of low luminosity sources that could perturb the measurement of the bright sources. The faintest ones will be taken into account by using extensive simulations to measure the background and estimates the flux biases as I did for 100μm. However, some rejected priors had a non negligible flux and couldn't be ignored. To ensure that this weak sources did not bias the measurement at $160\mu m$, I decided to use the predicted flux to remove them from the original PACS/$160mum$ image using a PSF convolution and *galfit*. To be conservative, I only removed priors from the map if $F_{SED} > 2 \times \sigma_{SED}$, following this criteria, I removed 1963 weak sources from the image. In Figure 3.4, I show the original image on the upper panel, the model of the weak sources in the middle panel and the weak sources subtracted image on the lower panel, that was used to extract $160\mu m$ fluxes. The subtracted flux represent nearly 30% of the total flux in the area delimited by the white contour.

Now that I had the image and the list of priors to fit, I re-did everything I did for PACS/$100\mu m$ for this band. In the next section, I summarize all the fol-

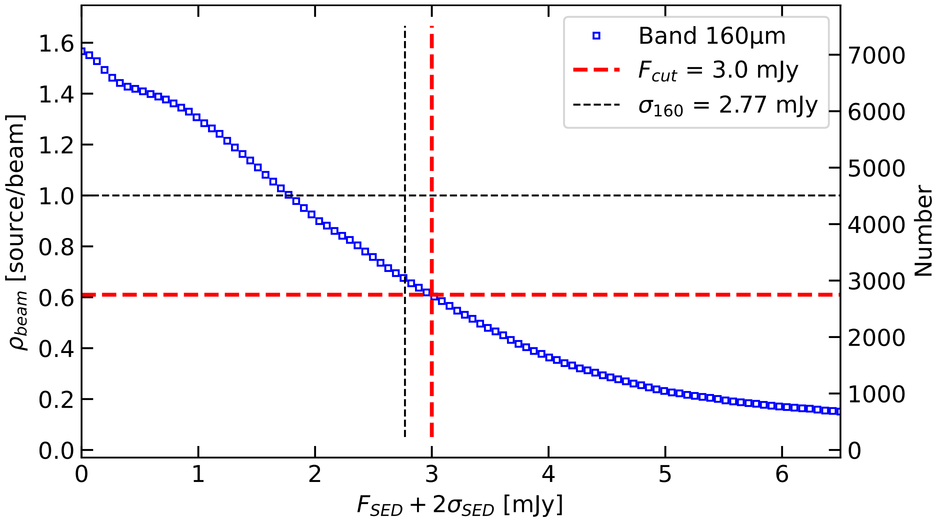

Figure 3.3: Density of priors at $160\mu m$ vs. selection threshold on predicted fluxes. On the right side of the panel, I show the total number of priors corresponding to each density. The fluxes are predicted using SED fitting based on available photometry. To be conservative, I apply the threshold on $F_{SED}+2\times\sigma_{SED}$. The red dotted lines show the two criteria to respect when selecting priors: Having a density below 1 source per beam (horizontal line) and selecting only bright sources (vertical line). The orange dotted line is the chosen threshold ($F_{cut} = 3.0mJy$).

lowing steps of the super-deblending, I only detail the parts that are different from the procedure I used for the PACS/$100mum$ band.

3.6 . THE SUPER-DEBLENDING CYCLE

In this Section, I summarize the remaining steps of the super-deblending technique. As they were very similar to what is described in the previous Sections, I do not give many details. I summarize the results in Table 4.1.

EXTRACTING PACS/$160\mu m$ FLUXES Based on the image I produced after removing the weak sources (see previous Section), I fitted the image using the same method as described in Section 3.1. I also performed extensive Monte-Carlo simulations as described in Section 2.3.2. From the residual images, he added 9 sources to the list of priors. At the end of the procedure, I had 217 3σ detections at 160μm with a median uncertainty of 2.77mJy.

COMPARING $160\mu m$ FLUXES TO SED PREDICTIONS The “super-deblending" technique relies on fitting the SED of a source using known fluxes to predict the flux in a new band. It was then important to verify that the prediction I made were meaningful, that is to say, the actual measured

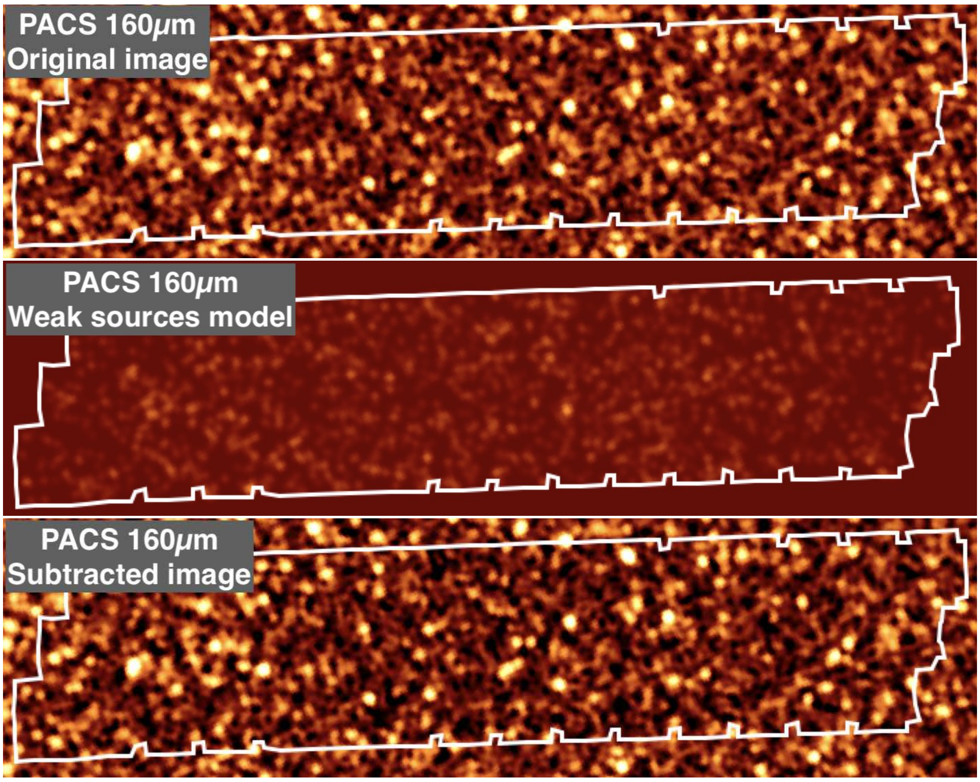

Figure 3.4: Removing weak sources from the PACS/$160\mu m$ image. Upper panel: Original image. Middle panel: model of weak sources from PSF-convolution using *galfit*. Lower panel: Resulting image from the subtraction of the faint sources that will be used for flux extraction. The white contour delimits the perimeter of the prior catalog I used. The colorbar is the same for all panel.

flux should not be far from the predicted value. That is why, at each band, after measuring the fluxes and correcting them for bias, I compared them to the SED predictions. I compared the measured fluxes at 160μm with the predicted fluxes in Figure 3.5. Globally, the measured fluxes were consistent with the SED predictions with a median $\chi^2 \sim 0.3$. When looking into more details, I also had a relatively good agreement between the fluxes of the 3σ detected sources that were also predicted bright (bright meaning a predicted flux greater than the 3σ detection limit: 8.31mJy, median $\chi^2 \sim 1.3$, in red in Figure 3.5). I also noted the presence of two outlier populations showed in green and blue in the Figure 3.5. The green markers are sources predicted bright but not detected leading to a positive difference in the right panel, either because of higher local noise, or possibly deboosted by the subtraction of faint sources. The blue markers are detected sources that were predicted fainter than the 3σ detection limit leading to a negative difference in the right panel, either because of lower local noise, isolated sources, or possible spurious detection. Globally, I had $\sim 5.5\%$ of priors for which $\chi^2 > 4$ meaning that the SED failed to predict the correct flux. The failed cases split nearly equally between predicted too faint or too bright. This justified the need to select the threshold on $F_{pred} + 2 \times \sigma_{pred}$ to ensure that I did not miss underestimated sources. The fact that the distributions in the right panel of Figure 3.5 are quite large is not surprising at this stage as the predictions were made based on a few measurements and depended a lot on the assumptions. However the fact that globally I had $\sim 94.5\%$ success rate on predicting the 160μm fluxes demonstrated the efficiency of the procedure.

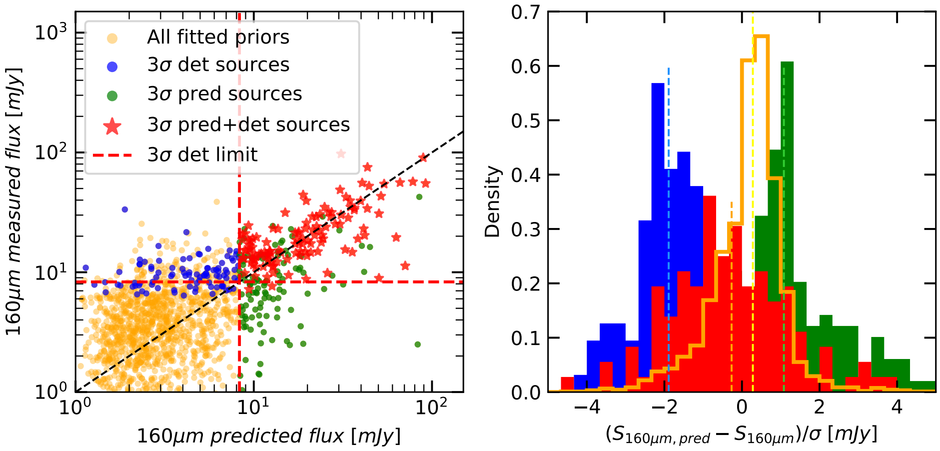

Figure 3.5: Comparison between measured fluxes and fluxes predicted by the SED fitting and used for the selection of priors to fit. Left panel: Flux comparison, the red dashed lines are the 3σ detection limits (8.31mJy), the orange, green, blue and red markers are fitted priors that were predicted fainter than 8.31mJy and not detected, predicted brighter than 8.31mJy but not detected, predicted fainter than 8.31mJy but detected and predicted brighter than 8.31mJy and detected respectively. Right panel: histogram of the difference normalized by the noise combining the error on the flux mesurements and on the SED prediction ($\sigma = \sqrt{\sigma_{meas}^2 + \sigma_{pred}^2}$), the color-code is the same as for the left panel, the orange unfilled histogram encompasses all the priors (green, blue and red markers included), lighter dashed lines are corresponding medians.

COMPARING $160\mu m$ FLUXES TO LITERATURE Just like for $100\mu m$, to assess further the quality of or flux extraction, I compared it to the literature (PEP, Lutz et al. 2011). I matched my catalog with the PEP catalog, using a 2" constrain. The fluxes were consistent, the flux difference was on average less than 8% and I had consistent uncertainties. Just like for $100\mu m$, the median of my uncertainties was slightly larger ($\sim 7\%$) probably because I took the blending noise into account.

PREDICTING $1.1mm$ FLUXES Based on the results of both PACS bands, I ran the SED fitting following the procedure described in Section 3.4. The next band was AzTEC/1.1mm. After the SED fitting procedure, I chose a threshold 0.6mJy driven by the depth of the map. It lead to a density of 0.1 source per beam and 1130 priors to fit. I subtracted 2269 weak sources from the image.

EXTRACTING AzTEC/$1.1mm$ FLUXES Using the same methods I extracted fluxes from the weak-sources subtracted AzTEC/1.1mm image. However, due to the fact that the noise was not flat for this image and that I only had a filtered image, I did not fit the science image but the signal-to-noise ratio image. This is also a novelty of my version of the super-deblended catalog as all the previous version did not meet this issue, or delt with it in a different way. This allowed to get better results with *galfit* and to easily calibrate the uncertainties. After running *SExtractor*, I added 24 sources to the list of priors. I obtained 32 3σ detections at 1.1mm with a median uncertainty of 0.54mJy. The number of detections can seem small, but I recall that the AzTEC map only covers a small part of the EGS field (see Figure 2.4 and Table 3.1). I did not compare my fluxes extracted from this map to the literature as it hasn't been done before.

PREDICTING $850\mu m$ FLUXES I ran the SED fitting on the updated catalog of 7094 priors. For the SCUBA2/$850\mu m$ band, I had two distinct images, one that covered most of the EGS field from Geach et al. (2017) but that was relatively shallow and a smaller one, but $3\times$ deeper from Zavala et al. (2017) (see Figure 2.4 and Table 3.1). Based on the predictions, I chose a threshold for each map: 0.4mJy for the Zavala et al. (2017) image corresponding to a density of priors of 0.8 sources per beam and 1.0mJy for the Geach et al. (2017) map corresponding to 0.3 sources per beam.

EXTRACTING SCUBA2/850μm FLUXES For the Zavala et al. (2017) map, I selected 2107 priors to fit and subtracted 5001 weak sources. After fitting with *galfit*, correcting the biases with extensive Monte-Carlo simulations and extracting additional sources from the residual image, I obtained 126 3σ detections with a median uncertainty of 0.33mJy. I added 13 priors from the Zavala et al. (2017). I ran the same analysis for the Geach et al. (2017) image, I selected 1251 priors and subtracted 5871 weak priors. After fitting, running simulations and extracting additional sources, I obtained 53 3σ detections with a median uncertainty of 1.04mJy. I added 15 sources from the Geach et al. (2017) image. For the same reason as for the AzTEC/1.1mm image, I fitted the SNR images at $850\mu m$ instead of the science image.

COMPARING 850μm FLUXES TO LITERATURE I compared the fluxes I measured in the Zavala et al. (2017) image with the blind catalog they produced. My fluxes were consistent within the error bars, the difference was less that 1σ for all fluxes, however, my fluxes tended to be $10-20\%$ brighter. This could be a sign that the Zavala et al. (2017) fluxes were too de-boosted since I am confident that my fluxes were well calibrated based on extensive simulations. My method makes sure that I measure the fluxes of individual sources. I had consistent uncertainties, I achieved a median uncertainty 15% smaller than Zavala et al. (2017) ($\sigma = 0.33$mJy vs 0.39mJy). Similarly I compared the fluxes of the larger but shallower image to the blind one extracted by Geach et al. (2017). My fluxes were consistent with a difference below 8% at all fluxes. My uncertainties were also consistent even if with My method, I was able to reach a median uncertainty 13% smaller (1.04mJy for my work vs 1.19mJy for Geach et al. (2017)).

COMBINING THE 850μm CATALOGS Before going to the next step, I needed to combine the two 850μm catalogs I built based on the two images I had. For each prior, if they were in only one of the catalog, I used the only flux I had, if they were in both catalog, then I combined them:

$$F_{850} = \frac{F_Z \times (1/\sigma_Z)^2 + F_G \times (1/\sigma_G)^2}{(1/\sigma_Z)^2 + (1/\sigma_G)^2} \tag{3.2}$$

$$\sigma_{850} = \frac{1}{\sqrt{(1/\sigma_Z)^2 + (1/\sigma_G)^2}} \tag{3.3}$$

with F_Z and σ_Z (respectively F_G and σ_G) being the flux and error and measured in the Zavala et al. (2017) map (resp. Geach et al. (2017)). After this procedure, my final SCUBA2/850μm catalog contained 172 3σ detections with a median uncertainty of 0.38mJy.

PREDICTING 450μm FLUXES Based on the 850μm and all the previous photometry, I ran a new SED fitting for the updated catalog of 7122 priors to predict the fluxes at 450μm. I chose a threshold at 2.05mJy, corresponding to ~ 0.7 sources per beam. I had 1598 weak sources to remove from the image and 2899 to fit.

EXTRACTING SCUBA2/$450\mu m$ FLUXES Just as for the 850μm images, I fitted the SNR image rather than the science image. After fitting with *galfit*, running the extensive Monte-Carlo simulations and extracting additional sources in the residuals, I obtained 99 3σ detections with a median uncertainty of 1.62mJy. I added 14 sources from the residuals to the catalog.

COMPARING 450μm FLUXES TO LITERATURE I compared my measurements with Zavala et al. (2017). The result of the comparison was similar to the comparison for the 850μm fluxes. My fluxes were consistent within error-bars, with a difference between $4-20\%$, but always less than 1σ. My fluxes also tended to be brighter. This confirmed what I had observed at 850μm, while I was in agreement with Geach et al. (2017) de-boosted flux, I had brighter fluxes than Zavala et al. (2017). I also achieved to go deeper, with a median uncertainty 30% smaller (1.62mJy vs 2.30mJy). This demonstrates the power of the super-deblending technique to select the correct priors to fit and the efficiency of my Monte-Carlo simulations to calibrate the errors.

PREDICTING 250μm FLUXES Based on the available fluxes, I re-ran the SEDs and predicted the fluxes at 250μm. The three remaining SPIRE bands were the most confused ones. The limiting factor when choosing the threshold to select which prior to fit was not the detection limit but the prior density. For SPIRE/250μm, the threshold was 4.7mJy, corresponding to a density of 1 source per beam. I had 2065 priors to fit and 2364 weak sources to remove from the map.

EXTRACTING SPIRE/250μm FLUXES The noise was relatively flat in the SPIRE images, so I directly fitted the science image. However, due to the large beam, I made only 1 run. I did not allow the bright sources to vary, the confusion was too important for it to have any effect. After running the Monte-Carlo simulations and extracting additional priors, I obtained 441 3σ detections with a median uncertainties of 2.13mJy. I added 6 sources to the list of priors, the prior catalog had then 7142 positions.

COMPARING 250μm FLUXES TO LITERATURE I compared my measurements with the publicly available catalog from Shirley et al. (2021). They measured the fluxes using XID^{+} based on prior selected using IRAC and MIPS/$24\mu m$ photometry. They did not have any 3σ detections, hence I compared my detected fluxes with $F_{Shirley}+\sigma_{Shirley}$ if $F_{Shirley}/\sigma_{Shirley} > 1.5$. I found that I had consistent fluxes within errors. My fluxes are $6-20\%$ fainter than the Shirley et al. (2021) upper limits. I compared the error bar for 1.5σ sources, I was able to have better constraints with a median uncertainty 33% smaller (2.38mJy vs 3.56mJy). I also compared the extracted flux with the prediction from the SED, they were consistent with a mean difference $\sim 0.3\sigma$, confirming my results.

PREDICTING 350μm FLUXES I ran the SED fitting for the 7142 priors. Here again, the limitation came from the large beam. I chose a threshold of 8.7mJy corresponding to 1 source per beam for SPIRE/$350\mu m$. I then had 1153 priors to fit and 2767 weak-sources to remove from the original image.

EXTRACTING SPIRE/$350\mu m$ FLUXES I proceeded exactly like for $250\mu m$. After a single *galfit* run on the weak-sources subtracted science image, the Monte-Carlo simulations and the extraction of additional priors using *SExtractor*, I had 159 detections with a median uncertainty of 3.95mJy. For this map, I had no additional priors to add to the catalog as none of the *SExtractor* sources were detected.

COMPARING $350\mu m$ FLUXES TO LITERATURE Like $250\mu m$, I compared to the Shirley et al. (2021) XID^+ fluxes. I adopted the same method and compared my 3σ detections with Shirley et al. (2021) upper limits for 1.5σ sources. My fluxes were consistent with the upper limit with a less than 10% difference at all fluxes on average. I also compared the 1.5σ error bars of the two catalogs. They were mainly consistent, my median uncertainty was 20% higher (4.51mJy vs 3.76mJy). I knew that my error-bars had been carefully calibrated with extensive simulations. Shirley et al. (2021) probably underestimated the errors due to the blending of faint sources. I also compared the extracted flux with the prediction from the SED, they were consistent with a mean difference $\sim 0.8\sigma$, confirming my results.

PREDICTING 500μm FLUXES Using all the photometry I extracted, I ran the SED fitting to predict the fluxes in the last band: SPIRE/$500\mu m$. Once again, I was limited by the large PSF. I chose a threshold of 6.4mJy corresponding to a density of 1 source per beam. I then had 542 sources to fit and 2938 weak-sources to remove from the image.

EXTRACTING SPIRE/500μm FLUXES Just like for the 2 other SPIRE bands, I ran *galfit* only once, without allowing a position variation for bright sources because of the large beam. I ran extensive Monte-Carlo simulations and ran *SExtractor*. I found no sources to add in the residuals. After the flux extraction, I had 48 3σ detections with a median uncertainty of 5.65mJy.

COMPARING $500\mu m$ FLUXES TO LITERATURE Like the other SPIRE bands, I compared to the Shirley et al. (2021) XID^+ fluxes. I adopted the same method and compared my 3σ detections with Shirley et al. (2021) upper limits for 1.5σ sources. My fluxes were consistent with the upper limit with a less than 15% difference at all fluxes on average. I also compared the 1.5σ error bars of the two catalogs. My uncertainties are higher, with my median uncertainty being 77% higher (6.54mJy vs 3.70mJy). I knew that my error-bars had been carefully calibrated with extensive simulations. Shirley et al. (2021) probably underestimated the errors due to the blending of faint sources. I also compared the extracted flux with the prediction from the SED, the measured fluxes were consistent with a mean difference $\sim 0.8\sigma$, confirming my results.

The “super-deblended" catalog is now finished. However, I still need to measure its performances to make sure that the catalog can be use do derive properties of galaxies or of the Universe at different epochs. This is the object of the next chapter.

4 - RESULTS AND ACHIEVEMENTS OF THE SUPER-DEBLENDED CATALOG

In this chapter, I explain how I evaluated the performances of my “super-deblended" catalog, and what impact it already had on within the scientific community.

The “super-deblended" catalog contains photometry from *Spitzer*, VLA, *Herschel*, SCUBA2 and AzTEC for up to 7142 prior galaxies in the EGS field. Table 4.1 gives a summary of the relevant photometric information in each band. For the labels, I decided to keep the CANDELS IDs when possible, ID 1 to 41457 are the sources from the Stefanon et al. (2017) catalog. The sources added based on NIRCam imaging have ID 50000 to 50126. For the sources added from the residual images using *SExtractor*, ID 50127 to 50132 are from the $3GHz$ image, ID 50133 to 50137 are from the 24μm map, ID 50138 to 50143 are from the PACS/100μm image, ID 50144 to 50152 are from the PACS/160μm map, ID 50153 to 50176 are from the 1.1mm image, the ID 50177 to 50189 are from the SCUBA2/850μm image from Zavala et al. (2017), the ID 50190 to 50204 are from the SCUBA2/850μm image from Geach et al. (2017), the ID 50205 to 50218 are from the SCUBA2/450μm and the ID 50219 to 50224 are from the SPIRE/250μm image.

4.1 . AN ILLUSTRATED EXAMPLE

I show in Figures 4.1, 4.2 and 4.3 an example of deblending around the prior ID12502. The first figure shows cutouts around the source in near-IR bands, 24μm and radio. One can see that some sources clearly identifiable in the HST and/or IRAC images were not selected as prior for the super-deblending (not circled in dashed white), this means that these sources were not detected at 24μm or in the radio and had a stellar mass below the limit defined in Section 2.3.5. I also note the importance of the 3GHz deep image as I clearly identify the central prior as a radio emitter, which is not clear at 1.4GHz.

In Figure 4.2, I show the super-deblending process between 100μm and 1.1mm centered on the same prior. The cutouts have the same size, the blending appears clearly. In each cutout, I show in white circles the priors position not selected at the current band, the filled one being those subtracted based on the SED fitting. The yellow circles are the fitted priors with their size being proportional to the measured fluxes. Dotted lines are sources with SNR < 2. The SPIRE images are the one with the less yellow circles as they are the most confused ones, yet, thanks to the efficient selection process, I was able to detect a few sources with SNR > 2. In this cutout there are two main FIR sources,

Table 4.1: EGS *"Super-deblended"* Photometry Results

$Band$	F_{cut} (mJy)	$\rho_{fit}{}^{a}$ $(beam^{-1})$	$N_{fit}{}^{b}$	$N_{excl.}{}^{c}$	$N_{detect}{}^{d}$	$1\overline{\sigma}^{e}$ (mJy)	$N_{add.}{}^{f}$
$24\mu m$	...	2.08	41595	0	2773	$6.93e^{-3}$	5
$1.4GHz$	...	1.08	41595	0	213	$13.5e^{-3}$	0
$3GHz$	...	$0.03-0.34$	41595	0	1722	$1.78e^{-3}$	6
$100\mu m$	...	0.56	7061	0	305	1.29	6
$160\mu m$	3.0	0.61	2791	1959	217	2.77	9
$250\mu m$	4.7	1.05	2065	2364	441	2.13	6
$350\mu m$	8.7	1.12	1153	2767	159	3.95	0
$450\mu m$	2.5	0.67	996	1598^{j}	98	1.62	14
$500\mu m$	6.4	1.1	542	2938	48	5.65	0
$850\mu m^{g}$	1.0	0.27	1117	5875^{j}	53	1.04	15
$850\mu m^{h}$	0.4	0.8	707	5001^{j}	125	0.33	13
$850\mu m^{i}$	...	...	1466	...	172	0.38	(28)
$1.1mm$	0.6	0.11	255	2269^{j}	32	0.54	24

Notes.

[a] ρ_{fit} is the number density of prior sources fitted at each band, normalized by the Gaussian approximation beam area, see Table 3.1 for image coverage and Equation 3.1 for a definition of ρ_{fit}.

[b] N_{fit} is the number of prior sources fitted at each band.

[c] $N_{excl.}$ is the number of prior sources excluded from fitting at each band. These sources are subtracted from the original image with their SED-predicted flux density at each band.

[d] N_{detect} is the number of prior sources with S/N $\geq$ 3 (i.e. detected) at each band.

[f] $N_{add.}$ is the number of additional sources that are not in the prior source catalog but blindly extracted from the intermediate residual image product at each band.

[e] $1\overline{\sigma}$ is the median of the flux density uncertainties of all detected sources in each band.

[f] N_{add} is the number of additional priors that were added in each band. They are extracted from the residual map using *SExtractor* and have at least a 2σ detection.

[g] Shallower, Non Matched-filtered map from Geach et al. (2017).

[h] Deeper, Matched-filtered map from Zavala et al. (2017).

[i] Combination of measurements from both maps, see Equations 3.2 and 3.3.

[j] Total number of sources to subtract if the image was covering all the prior positions. The actual number of weak sources removed is smaller.

the central source ID12502 at $z \sim 2$ and the source ID13658 at $z \sim 2.5$ in the upper right corner. In the SPIRE bands, these two sources are blended and look like a single source in the middle, thanks to my “super-deblending" process, I was able to split this blob between the two main contributor (plus 1 or 2 other minor contributors). In the SCUBA2/450μm, the flux can seem to not be coming from the selected prior in the upper right corner, however, the positions plotted here are the HST-based position, but when fitting the images, I allowed the bright source to vary position. For SCUBA2/450μm, I allowed a variation up to 1.5 pixel (3") which allowed to associate this emission to the prior ID13658. I am confident that the emission at 450μm comes from this prior as it is consistent when looking at the SED across all FIR bands and there is no other priors visible in *HST*/IRAC/*JWST* images that could explain this.

Finally, in Figure 4.3, I show the final SED fitting of the central source ID12502 and the upper right source ID13658 and there RGB cutout made using the filters F115-F200-F444 of *JWST*/NIRCam. For ID12502, the SED is very well fitted with a photometric redshift ~ 1.9 and a SFR ~ 186M$_\odot$ yr^{-1}. This galaxy was classified as a Main Sequence galaxy. The blue line is the stellar component, fitting the K_S and IRAC fluxes from Stefanon et al. (2017), the red line is the AGN torus, the green line is the dust continuum emission and the black line is the total. In this galaxy, the AGN torus represents only 4% of the IR-luminosity. For ID13658, the SED is well fitted with a spectroscopic redshift $z_{spec} = 2.47$ and a SFR ~ 364M$_\odot$ yr^{-1}. This galaxy was classified as a Main Sequence galaxy hosting a radio loud AGN. In this galaxy, the AGN torus represents $\sim 8\%$ of the IR-luminosity. The position of the peak in the FIR emission seem to be a bit shifted, this is probably due to the dust temperature, that is not taken into account in the simple SED model used in the “super-deblending" process. Similarly, the two points from the channel 2 and 3 of IRAC are not correctly fitted, they fall between the end of stellar component and the beginning of the dust and AGN components, which might explain the difficulty to retrieve these fluxes.

These galaxies sit in a crowded and blended environment, yet I was able to retrieve their fluxes in each band and obtained a consistent SEDs, demonstrating the high efficiency of the super-deblending technique.

4.2 . CATALOG PERFORMANCES

In this catalog, I have 2749 priors detected with S/N > 3 at the 24μm and/or radio bands, it is $35\times$ less than the 24μm+radio detections in the COSMOS super-deblended catalog (Jin et al. 2018), for an area that is $31\times$ smaller. So I have a similar density of detected priors in 24μm and/or radio. Just like in L18;

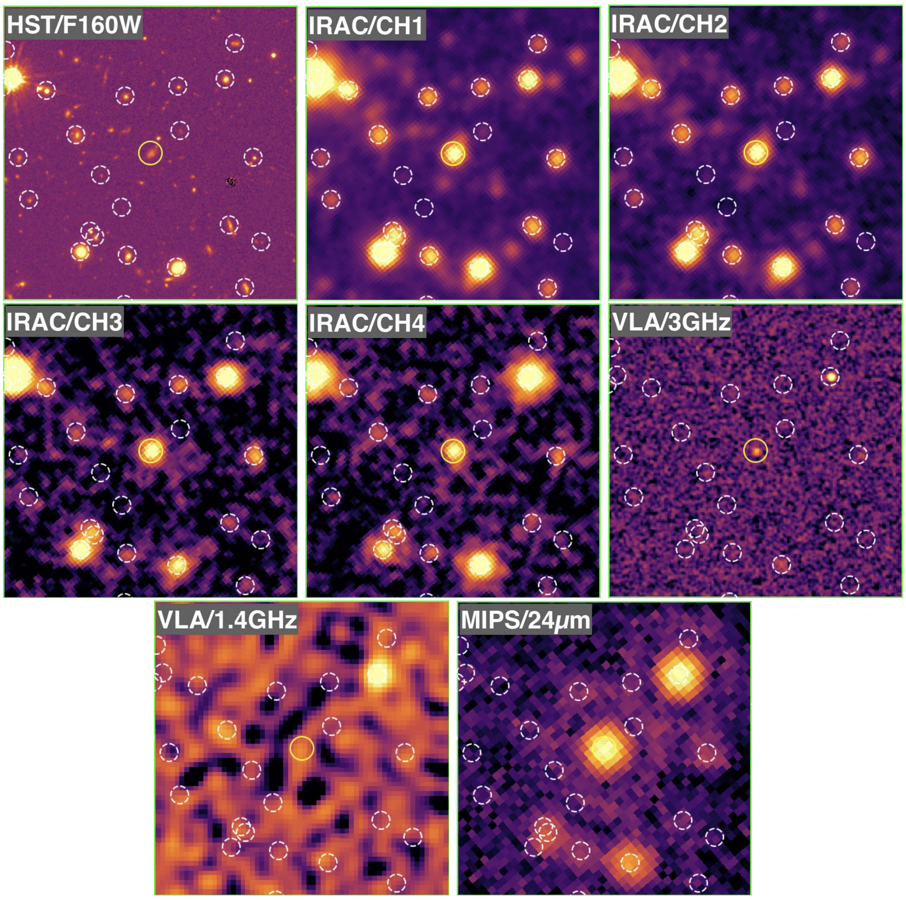

Figure 4.1: Example of the "super-deblending" process. I fit the source ID12502 together with other sources in an image box at each band (see Figure 4.2) and show its finalized SED in Figure 4.3. Here, I show multiband cutouts in a $50" \times 50"$ box of images used to make the prior catalog, the white circles are the priors of the super-deblended catalog, the yellow circle is ID12502. I show the *HST* H-band instead of the K_s band that is used for the SED fitting. The K_s and IRAC photometry is taken from Stefanon et al. (2017).

J18 I defined a FIR signal-to-noise ratio:

$$(S/N)^2_{FIR+mm} = \sum_{\lambda=100\mu m}^{1.1mm} (S/N)^2_\lambda \tag{4.1}$$

I had 480 galaxies detected with $(S/N)_{FIR+mm} > 5$ among 7142 priors, leading to a 6.7% detection rate. In comparison, Jin et al. (2018) super-deblended catalog in the COSMOS field ($\sim 30\times$ larger than EGS) contains 11220 detections for 192249 priors (5.8% detection rate). Hence, I had a prior catalog slightly denser ($\sim 10\%$) and a detection rate 15% more efficient.

As I show in Figure 4.4, I was able to reach possibly $z \sim 6-8$. To compare my catalog with the last super-deblended catalog produced by Jin et al. (2018),

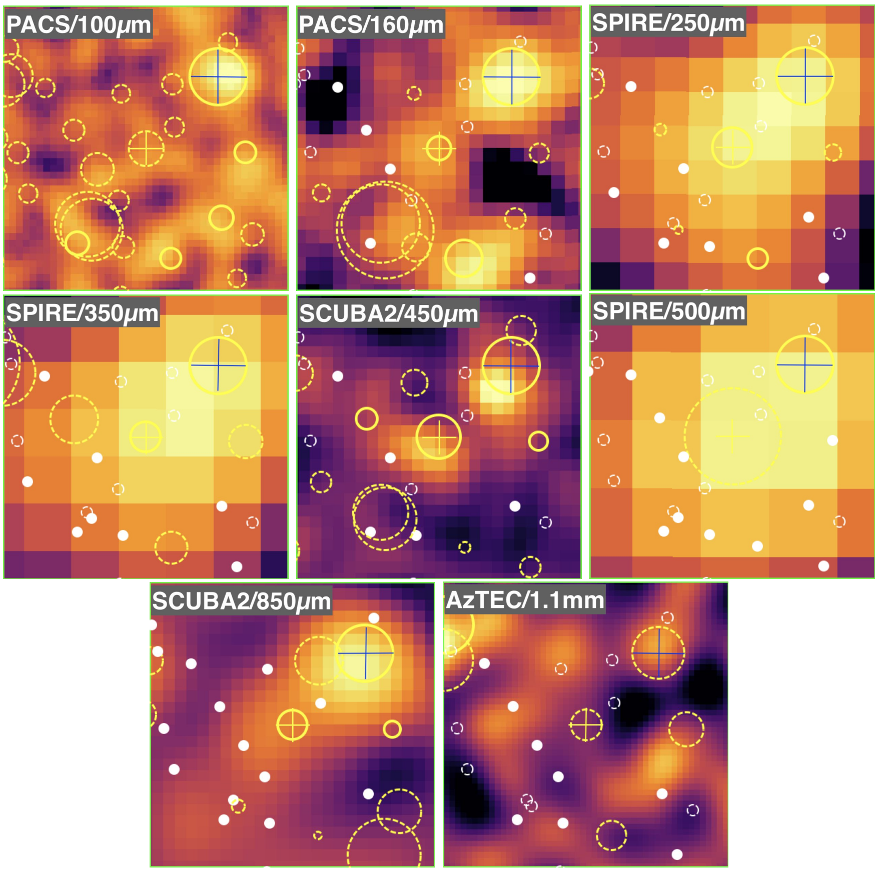

Figure 4.2: Example of the “super-deblending" process. I fit the sources ID12502 and ID13568 together with other sources in an image box at each band and show its finalized SED in Figure 4.3. Here I show multiband cutouts in a $50" \times 50"$ box of the super-deblended maps between $100\mu m$ and $1.1mm$. The white circles are the priors that are not fitted, the filled one are removed from the map. The yellow circles are the fitted priors, with solid contour if $S/N > 2$, their radius is proportional to the their flux or the 2σ upper-limit for the solid or dashed markers respectively. The yellow and blue crosses mark the position of ID12502 and ID13568 respectively.

I calculated the number of starburst galaxies adopting Rodighiero et al. (2011) criterion; a starburst is an abject with sSFR $\geq 4\times$ sSFR$_{MS}$, I used the MS from Schreiber et al. (2015). I found 96 starbursts galaxies at $z < 4$, representing a fraction of 20% of all IR detections. This fraction was larger than the one from Jin et al. (2018) mainly because I had shallower FIR *Herschel*/SPIRE images, hence I didn’t probe the lower part of the MS (at lower SFR) as efficiently as they did.

The fact that overall I detected more IR galaxies than Jin et al. (2018) is mainly driven by high redshift galaxies. Indeed, I had 48 detected galaxies at $z > 3$, this was a detection rate nearly $2\times$ more important than from Jin et al. (2018). This higher efficiency came from the mass-selected galaxies from the

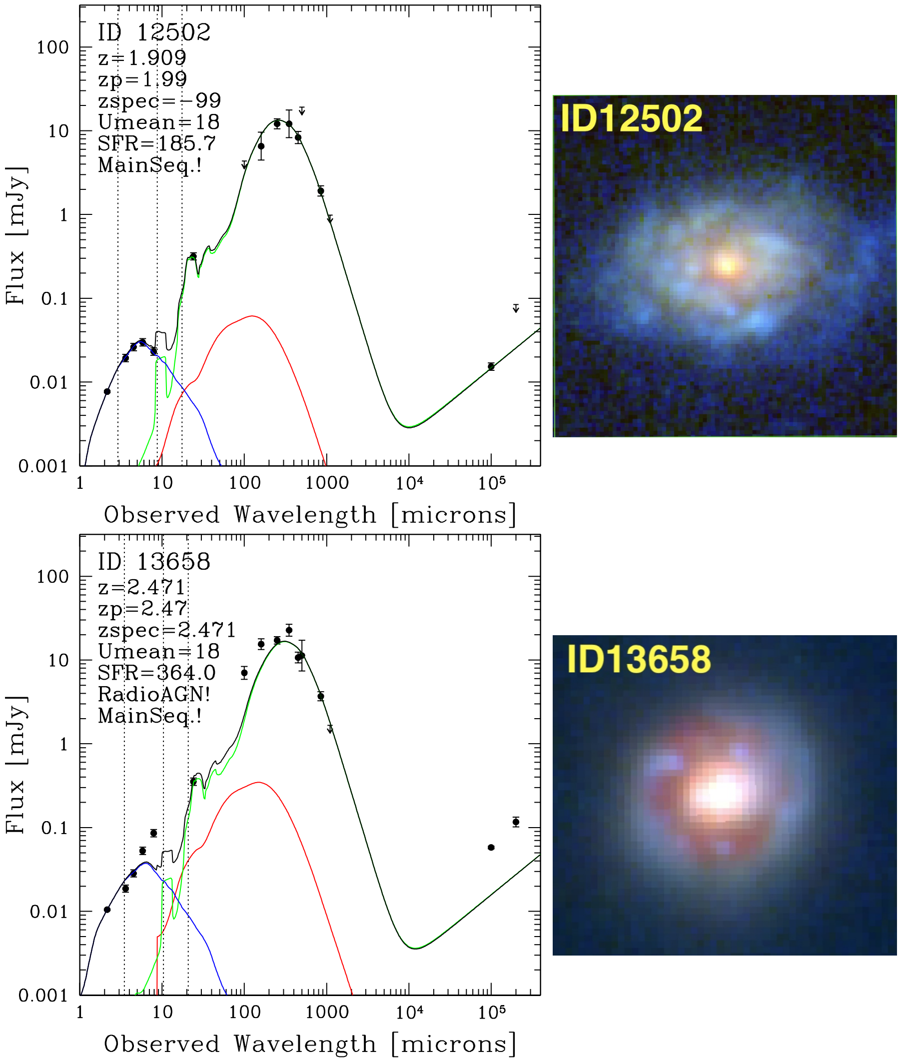

Figure 4.3: Left panels: Example of the “super-deblending" process. I fit the sources ID12502 (left) and ID13658 (right) together with other sources in an image box at each band (See Figures 4.1 and 4.2). Here, I show their finalized SED fitting. Blue, red and green curves show the stellar component (Bruzual & Charlot 2003), the AGN torus emission (Mullaney et al. 2011) and the dust continuum emission (Magdis et al. 2012). The z_p is the near-IR photometric redshift from the Stefanon et al. (2017) catalog; these galaxies were classified as Pure Main Sequence with a $SFR_{IR} = 185.7$M$_\odot$ yr^{-1} and $SFR_{IR} = 364.0$M$_\odot$ yr^{-1}, ID13658 is a radio-loud AGN. The downward arrows show the 2σ upper limit at a given wavelength. Right panels: RGB cutouts of the two sources produced using *JWST*/NIRCam images from filters F115W, F200W and F444W.

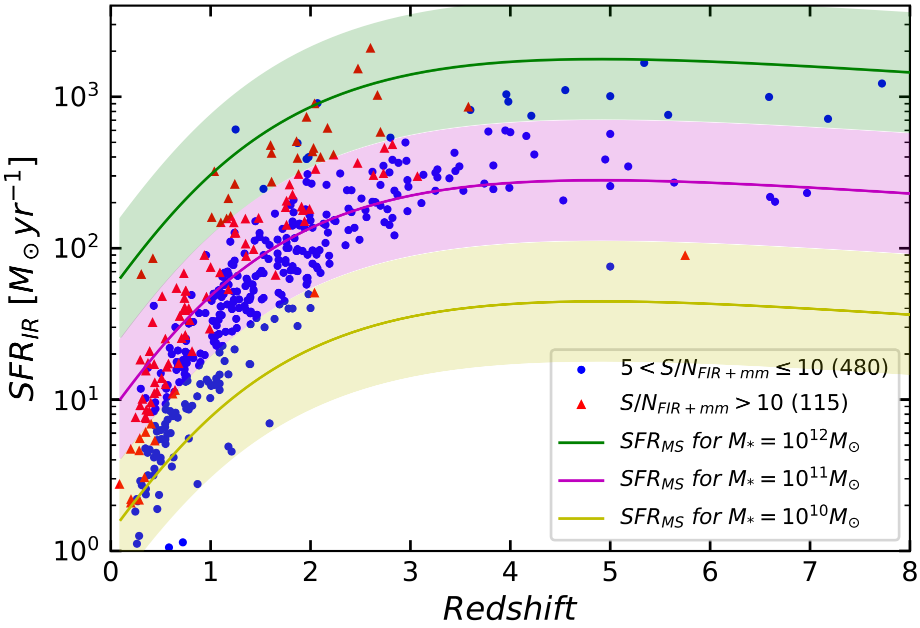

Figure 4.4: SFR vs. redshift for the $S/N_{FIR+mm} \geq 5$ sources. The SFRs are computed from the integrated $8 - 1100 \mu m$ infrared luminosities derived from FIR+mm SED fitting, assuming a Chabrier IMF (Chabrier 2003). Colors indicate the combined S/N over the FIR+mm bands (> 5 for blue and > 10 for red). The colored curves show the empirical tracks of the MS galaxy SFR as a function of redshift at three main sequences in specific stellar masses (Sargent et al. 2014).

highly complete Stefanon et al. (2017) catalog (10% of the $z > 3$ detections) and also to the NIRCam additional sources representing 8% of the $z > 3$ galaxies. NIRCam additional sources were crucial as 80% of IR detected sources were at $z > 3$, allowing a better completeness of the catalog toward the highest redshifts.

In Figure 4.5, I show the redshift distribution of the $S/N_{FIR+mm} > 5$ sources from my catalog. The distribution of the number of detections is nearly flat up to $z \lesssim 2$, followed by an exponential decrease between $z \sim 2$ to $z \sim 7$. To take into account the uncertainties on the photometric redshift estimations, I convolved the redshift distribution with its uncertainty. Practically, I perturbed the photometric redshifts based on their uncertainty taking a random value following a normal distribution centered on the best redshift and with a width equal to the associated uncertainty. By doing that a hundred times, I obtained the mean cumulative number of detected sources in each redshift bin. From this cumulative distribution, shown in red in Figure 4.5, I have $4 - 5\%$ of detected sources at $z > 4$ and only a handful of them are predicted with $z > 6$.

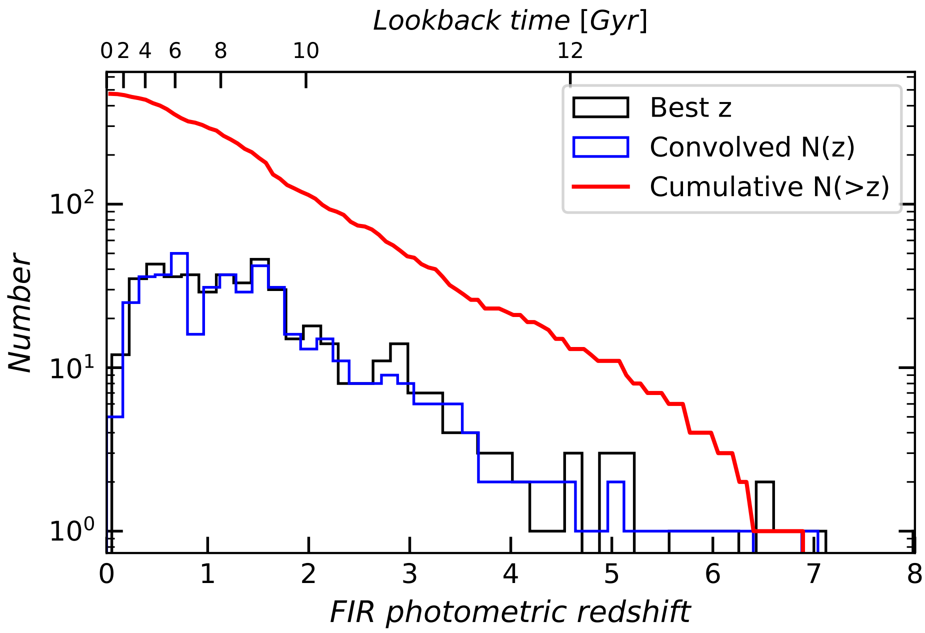

Figure 4.5: Redshift distribution of $S/N_{FIR+mm} > 5$ sources. The black histogram shows the distribution of the best-fit redshifts from SED fitting. The blue histogram shows the uncertainty-convolved redshift distribution, and the red line shows its cumulative distribution $N(> z)$

More quantitatively, in the pool of 480 sources with $S/N_{FIR+mm} > 5$, I had 25 sources with $z > 4$. Among them, 18 were from the Stefanon et al. (2017) priors and had an optical photometric redshift, 2 being mass-selected (i.e. not detected at 24μm or in the radio), 1 was an additional source from NIRCam, 1 was added from the residual of the PACS/160 image and 5 were from the residual image at 1.1mm. None were from the 850μm images, this was because the 850μm image were fitted after the 1.1mm, hence taking advantage of the 1.1mm additional sources, the larger map from Geach et al. (2017) being too shallow to detect any high z additional sources. The FIR-based photometric redshifts were extracted from the SED fitting based on the model giving the lowest χ^2 and I applied the $\Delta\chi^2 = 2.5$ criterion (corresponding to 90% probability confidence) to estimate the uncertainty of the redshift (Avni 1976). For more details on the SED fitting procedure and on the redshift estimation, I refer the reader to Section 3.4 and to Jin et al. (2018).

We can look for dusty star-forming galaxies (DSFG) at high redshift, following the selection criteria of Ivison et al. (2016). I selected them with *Herschel*/SPIRE colors ($S_{500\mu m} \geq 30mJy$, so $S_{500\mu m}/S_{250\mu m} \geq 1.5$ and $S_{500\mu m}/S_{350\mu m} \geq 0.85$). Ivison et al. (2016) detected 35 DSFGs in a $600deg^2$ survey with $z = 4 - 6$. Jin et al. (2018) made a similar selection in the COSMOS field and found a higher space-density thanks to the “super-deblended" catalog, they detected 64 DSFGs in a $2deg^2$ survey with $z = 4 - 6$. In my catalog, I was able to detect only 1 such DSFGs in the same redshift range (ID28834 at $z = 5.0$), for a $0.06deg^2$ survey, leading to a density 50% less important than Jin et al. (2018), this was expected as the *Herschel*/SPIRE images are deeper in the COSMOS field than in the EGS field of view getting smaller, the probability to find a high z DSFG was getting small too.

4.3 . FINAL SED FITTING

At the end of the super-deblending cycle described in the previous section, I applied a final SED fitting to get an optimal estimation of several parameters (fluxes, SFRs, redshifts). To make sure that the extracted information was reliable, I looked at the χ^2 distributions. Since the part of the spectrum that is most affected by blending is the FIR and that the mid-IR could be affected by the level of PAH, which is not taken into account in my SED models, I calculated the χ_r^2 over the $100 - 1100\mu$m range. I had a median reduced χ_r^2 of 1.7 for galaxies with $(S/N)_{FIR+mm} > 10$ and of 1.8 for galaxies with $5 < (S/N)_{FIR+mm} < 10$. Overall, I had $\sim 19\%$ of galaxies with $(S/N)_{FIR+mm} > 5$ that had a $\chi_r^2 > 4$, hence where the SED fit was not of good quality. Different possibilities could explain this high level of failure: first the uncertainties could be underestimated, but the errors have been carefully tuned via extensive Monte-Carlo simulations and compared to literature. It was then highly improbable that error-bars could be responsible of high χ_r^2 values, moreover, I limited the SNR to 5 at best for all individual bands. Another reason could be that the deblending didn't work correctly for some crowded regions and the fluxes haven't been associated to the right prior, but when comparing individual bands to the literature, I never found numerous outliers. On the contrary, we are always consistent. In GOODs-North, Liu et al. (2018) explain that their 2% of failed SED fit were mainly due to a problem of redshift or blending between high and low redshift sources. It is highly probable that I am affected by the same problem here especially since I have shallower images. However, it would not explain why my number was much higher than the one from Liu et al. (2018).

To try and find the origin of the fit failures, I looked at the χ^2 value for each band to see if a specific band was responsible for a systematic effect on the χ_r^2 values. For each sources in my catalog, I calculated the χ^2 at each band band. By looking at all the χ^2 values of a single band, I hoped to detect a systematic effect. In Figure 4.6 I show a box plot. For each band, the box illustrates its χ^2 distribution, the orange horizontal line is the median, the box delimits the first and third quartiles, hence contains 50% of the points and the whiskers delimit the standard deviation of the distribution. The two PACS bands have

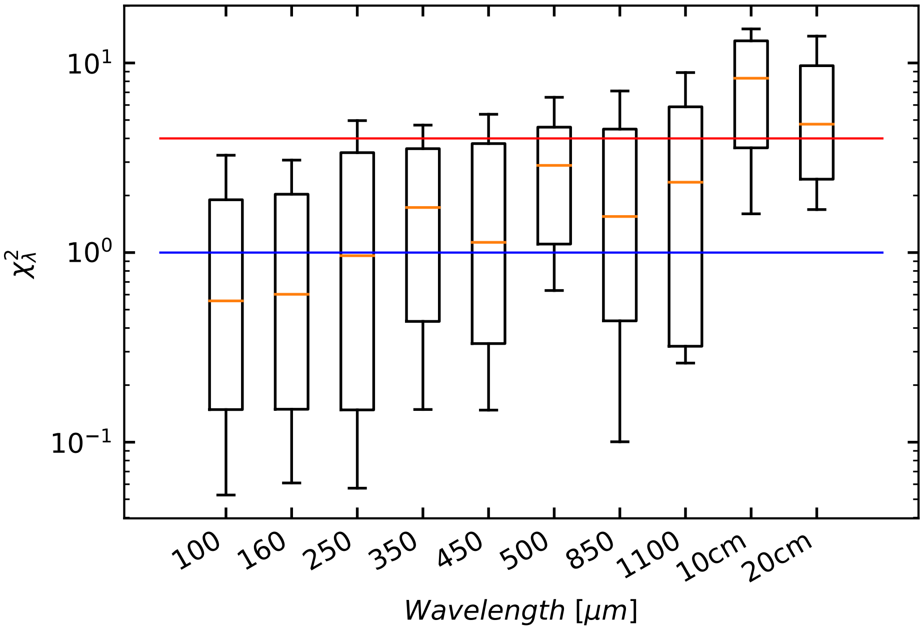

Figure 4.6: Study of χ^2 evolution with the wavelength. For each source, I calculated the χ^2 at all bands, I plot here the distribution of all the individual χ^2 value for single bands. The orange line is the median, the edges of the box represents the first and third quartiles (25% and 75% respectively) and the whiskers correspond to the 1σ distribution. I also plot the $\chi^2 = 1$ line in blue representing the ideal value and the $\chi^2 = 4$ line in red representing the critical value above which the fit is considered a failure.

a median $\lesssim 1$ (blue line in Figure 4.6), which is expected for a good fit. That is also the case for the 250μm and 450μm images. For the other FIR bands, the median oscillates between 2 and 3 with, on average $\sim 70-75\%$ of points with a $\chi^2 < 4$ (red line in Figure 4.6). The two bands with the largest χ^2 are the SPIRE/500μm and the 1.1mm bands. This is somewhat expected as this two bands are shallow, especially the SPIRE/500 which also is the most blended. Finally, I noticed that the χ^2 associated to the radio bands was much larger, this was expected as the SED model didn't take into account radio emission from AGNs, hence, the fact that most radio data points are not consistent with the dust SED means that they probably have an AGN component. This figure does not show a particular FIR band that would be responsible for the failed SED fit. The main difference between Liu et al. (2018) and my catalog is that they use much deeper FIR images, hence, their SED predictions and prior selection wer more accurate than mine, due to the shallowness of my images, especially in the SPIRE bands, there is a possibility, despite extensive Monte-Carlo simulations that my fluxes are boosted. Having all of this in mind, I considered that having $\sim 80\%$ of successful SED fit was a success, understanding better the reason why $\sim 20\%$ of fit failed would require at individual cases and see if I can see a common issue. Due to time constraints, I didn't have time to dig deeper into this.

This study of χ^2 shows that the SED fitting procedure was efficient, and validates the interest of using SED fitting to predict fluxes. I can also be confident with the fitted fluxes and SFR. For the redshift, it is more delicate because of the degeneracy between redshift and dust temperature. For a detailed analysis of the consequences of this degeneracy, I refer the reader to Section 7.2 of Jin et al. (2018).

All of these convinced us that I probed the FIR images as much as I possibly could and the super-deblending process matched the goal of producing the deepest FIR catalog in the EGS field with a little help from newly acquired VLA and NIRCam images.

4.4 . NUMBER COUNT

Finally, it is important to clarify that I did not embark in a direct study of the completeness of my IR photometric catalog. Given the large PSFs in the FIR/(sub-)millimeter bands, the probability of detecting a galaxy of a given flux largely depends on the properties and densities of surrounding galaxies. Estimating this probability would thus require extended simulations to be performed simultaneously in all bands. However, I decided to calculate differential number counts and to compare them to the literature to make sure that we were consistent and not too incomplete. I highlight three bands here, PACS 160μm, SPIRE 350μm and SCUBA2 850μm, this is because both PACS bands gave similar results and so did the three SPIRE bands. The number counts can be found in Table 4.2.

These number counts were calculated from the fitted fluxes. The errors were calculated by perturbing the fluxes to get the uncertainty on the number of sources per flux bin. The shot noise was also taken into account and a small (5%) error was added to take into account the uncertainty on the area coverage of the catalog.

In Figure 4.7, I compare my number counts to the number counts from literature measured in deeper fields. For the PACS band, my differential number counts are in agreement with the literature. For the SPIRE band, my number counts seem to be slightly above previous results but in agreement within error bars. The difference could come from the fact that using my "super-deblending" method, I am able to resolve fainter sources, hence having a better completeness especially around $20-30$mJy. Finally, the shallowness of the SCUBA2 image from Geach et al. (2017) makes it difficult to compare it with the literature because of the large scatter, but my results seem to be in general agreement with previous studies.

Table 4.2: Differential Number Counts

Band (μm)	Bin center (mJy)	$S^{2.5}dN/dS$ ($mJy^{1.5}deg^{-2}$)	Error ($mJy^{1.5}deg^{-2}$)	Bin width (mJy)
160	7.52	38067	7341	2.26
160	10.18	91454	14332	3.06
160	13.78	132596	21360	4.14
160	18.64	159301	28838	5.60
160	25.23	153982	34845	7.58
160	34.14	157000	43657	10.25
160	46.20	137330	51376	13.87
160	62.53	131861	60626	18.78
160	84.62	99989	70025	25.41
350	8.89	25757	7729	1.98
350	11.13	60626	14092	2.48
350	13.92	104142	21919	3.11
350	17.42	164461	32524	3.89
350	21.80	225061	44788	4.87
350	27.28	215459	50835	6.09
350	34.13	157223	51027	7.62
350	42.70	137189	56071	9.53
350	53.44	91801	53751	11.93
850	0.99	1916	299	0.58
850	1.81	4986	728	1.06
850	3.30	9436	1515	1.93
850	6.02	7839	1914	3.52

These number counts comparison allow us to be confident about the completeness of my “super-deblended" catalog, especially for fluxes higher than 5σ. However, for fluxes lower than 5σ my measurements are incomplete in comparison to other studies in deeper fields. This is a logic consequence of the “super-deblending" prior selection process where I select only the sources that are predicted to be above a certain level of flux and subtract the fainter sources. The fact that my number counts are in agreement with those from deeper studies in other fields demonstrates the solidity of the “super-deblending" technique to retrieve fluxes in highly blended images.

4.5 . LOOKING FOR THE MAIN SEQUENCE

In Figures 4.8 and 4.9, I plot for several redshift bins between $z = 0.2$ to $z = 8.0$, the SFR_{IR} versus the $log_{10}(M_*/M_{\odot})$. I choose to plot only the sources that satisfy $SNR_{IR} > 5$ and $SFR_{IR} > 3 \times \sigma_{SFR}$, so a total of 391 sources. I

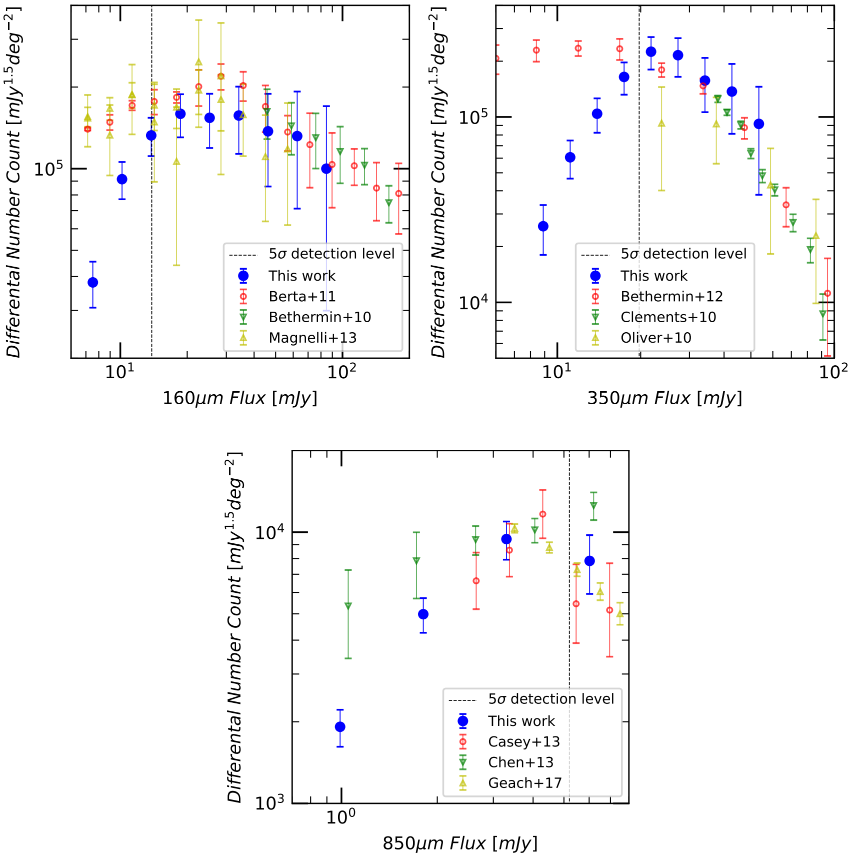

Figure 4.7: Comparison of my differential number counts with the literature. In the upper left panel for $160\mu m$, I compare my results with Berta et al. (2011); Béthermin et al. (2010); Magnelli et al. (2013). In the upper right panel for $350\mu m$, I compare my results with Béthermin et al. (2012); Clements et al. (2010); Oliver et al. (2010). And in the lower panel for $850\mu m$, I compare my results with Casey et al. (2013); Chen et al. (2013); Geach et al. (2017). The black dotted line correspond to the 5σ detection level at the corresponding band in my "super-deblended" catalog.

add the Schreiber et al. (2015) Main Sequence and a color code (green for pure main sequence objects: $SFR - SFR_{MS} < 0.3$dex, red for pure starbursts: $SFR - SFR_{MS} > 0.6$dex and blue for unclassified, see Section 3.4). The distribution of my data shows that it is dominated by main sequence galaxies, they represent 50% of the sample, and 74% if I add the unclassified objects above the main sequence but not enough to be classified as pure starburst. Schreiber et al. (2015) Main Sequence is in Salpeter IMF (Salpeter 1955), while my data is in Chabrier IMF (Chabrier 2003), to stay consistent, I multiply the M_* by 1.23 to convert it to Salpeter IMF, then calculate the corresponding SFR_{MS} and convert it back to Chabrier IMF by dividing it by 1.58.

These Figures show that the population of detected sources ($SNR_{IR} > 5$)

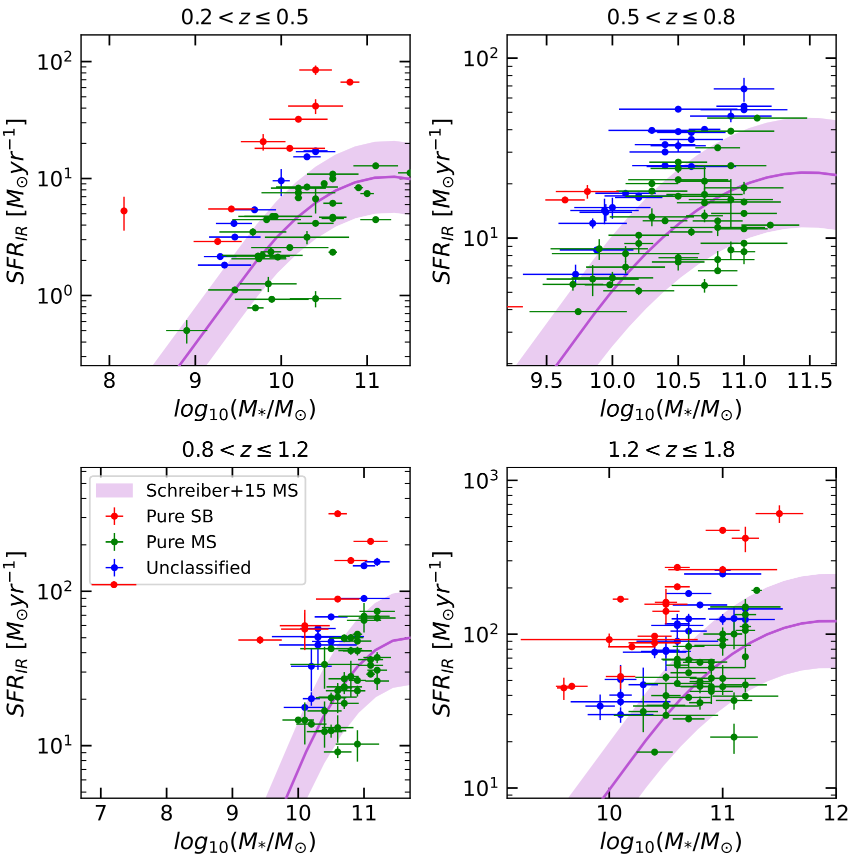

Figure 4.8: SFR_{IR} vs M_* for some of the 391 resolved sources ($SNR_{IR} > 5$) with $SFR_{IR} > 3 \times \sigma_{SFR}$ for several redshift bins. Red dots are sources classified as pure starburst, green dots are sources classified as pure Main Sequence and blue dots are unclassified sources (see Section 4.5). The magenta line and shaded region correspond to the Main Sequence and its scatter as described in Schreiber et al. (2015).

with $SFR_{IR} > 3 \times \sigma_{SFR}$ is biased. Indeed, in this sample, I have 196 pure Main Sequence galaxies, 100 pure starburst galaxies and 95 that remain unclassified. The fact that the fraction of pure starburst galaxies in the sample ($\sim 26\%$) is so high is linked to the selection bias. Due to the confusion of the FIR bands, especially the SPIRE bands, the strongest detections correspond at the highest level of SFR for a given redshift, this mean that the starburst galaxies are over-represented compared to normal MS star-forming galaxies. The sample is also biased in stellar mass, the detections correspond to the most massive galaxies ($M_* > 10^{11} M_\odot$) and most of them have $z < 3$. Nevertheless, I still have some detections at lower masses and higher redshift. Probing less massive galaxies at high redshift would have required higher spatial resolution and longer exposures in the FIR bands. That explain why I didn't have source below $M_*/M_\odot = 10^9$ or with a SFR_{IR} less than a few tens of $M_\odot.yr^{-1}$

at $z > 1.2$.

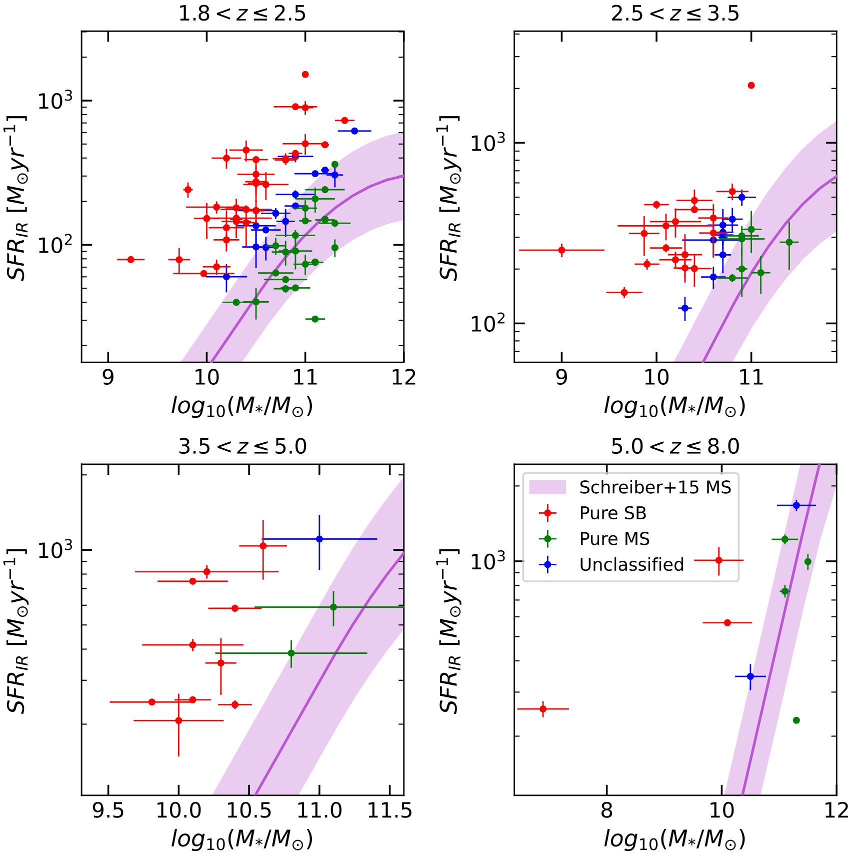

Figure 4.9: SFR_{IR} vs M_{*} for some of the 391 resolved sources ($SNR_{IR} > 5$) with $SFR_{IR} > 3 \times \sigma_{SFR}$ for several redshift bins. Red dots are sources classified as pure starburst, green dots are sources classified as pure Main Sequence and blue dots are unclassified sources (see Section 4.5). The magenta line and shaded region correspond to the Main Sequence and its scatter as described in Schreiber et al. (2015).

It is important to highlight the fact that for sources with $SNR_{IR} < 3$, the SED fitting can be erroneous, and so the computed SFR. Hence, the classification in Main Sequence or starburst must be taken with precaution. Most of the $SNR_{IR} < 3$ sources classified as starburst are badly classified because the computed SFR is more likely to be an upper-limit than the actual SFR.

4.6 . USE OF THE CATALOG

The “super-deblended" catalog has been shared within the CEERS collaboration and appeared to be useful. Indeed, several CEERS papers lean on my work to assert their results (Kocevski et al. 2023, Zavala et al. 2023, Finkelstein et al. (2022)). The super-deblending technique is particularly efficient to detect

DSFGs masquerading as high redshift galaxies as it has been proven that they are or could be (Zavala et al. 2023,Fujimoto et al. 2022), and so, is a mandatory sanity check for any high redshift ($z > 9$) candidates. This is especially true in the EGS field as their is no sub-mm coverage from ALMA or NOEMA. The “super-deblended" catalog was also used in Kirkpatrick et al. (submitted to ApJL) where they compare the *Spitzer*/MIPS and *JWST*/MIRI performances as they probe the same wavelength range. The “super-deblending” technique was also used to deblend LOFAR images for the NICE collaboration (PIs: E. Daddi, T. Wang).

This catalog is also a good tool to select high-z DSFGs, like Cosmic Noon galaxies as I will see in the next chapter.

As a final remark on the catalog, I emphasize that I will publicly release the photometric catalog for all 24μm$+$radio priors and the additional sources extracted from the residual images in an upcoming publication.

This concludes the making and studying of the “super-deblended" catalog. Based on this far-IR catalog, we can easily gather a list of dust-rich galaxies as they will be among the brightest in the far-IR detections. In the following chapters I explain how, using this catalog and the exquisite images of the *JWST*, I studied dusty star-forming galaxies around Cosmic Noon.

5 - DUSTY STAR FORMING GALAXIES AT COSMIC NOON

In the remaining of this manuscript, I will study dusty star-forming galaxies, it is then important to establish what is the current understanding of them. This is what I present in the following section. I also explain in this chapter how I selected the galaxies that I decided to study in detail.

5.1 . WHAT IS THE CURRENT LEVEL OF UNDERSTANDING OF DSFGs AT $z = 2$?

Until recently, the existence of the so-called galaxy Main-Sequence, which I recall is a correlation that the majority of star-forming galaxies observe in the stellar mass (M_*) versus star formation rate (SFR) plane up to redshift 3 (MS, e.g., Daddi et al. 2007; Elbaz et al. 2007; Noeske et al. 2007; Schreiber et al. 2015) and its tight scatter has been interpreted as evidence that star formation in most galaxies is a fairly ordered process (Schreiber & Wuyts 2020). The 'consensus' is that galaxies on the MS are forming stars in a quasi steady state inside gas-rich stellar disks (e.g., Sancisi et al. 2008; Dekel et al. 2009) whereas galaxies above the MS undergo a starburst, driven by stochastic processes such as major mergers, whose typical signature is compact star formation (e.g., Tacconi et al. 2008).

However, recent studies at $z \sim 1-3$ have shown that some massive ($M_* \geq 10^{11} M_\odot$) MS galaxies have a stellar distribution typical of late type galaxies but where the star formation only occurs in a compact nucleus (Elbaz et al. 2018; Puglisi et al. 2019, 2021; Tadaki et al. 2017, 2020; Franco et al. 2020; Gómez-Guijarro et al. 2022a; Jiménez-Andrade et al. 2019, 2021). The origin of these compact SF sub-mm galaxies (SMGs) observed with the *Atacama Large Millimeter Array* (*ALMA*) is yet to be fully understood. Three main scenarios to form the compact sub-mm nucleus are : (1) gas fueled to the core via violent disk instabilities (VDI) and clump migration, (2) a starburst induced by a major merger or (3) accretion and/or minor mergers (e.g. Gómez-Guijarro et al. 2022b). These compact SF nuclei could be an indication of an early quenching phase (Puglisi et al. 2019; Franco et al. 2020; Puschnig et al. 2023).

Besides the compact nucleus, high-*z* SF galaxies are observed to have giant SF clumps (radius ~ 1kpc). The origin of these clumps has been investigated by many studies (Puschnig et al. 2023; Fensch & Bournaud 2021; Hodge et al. 2019; Rujopakarn et al. 2019; Mandelker et al. 2014; Wuyts et al. 2012; Elmegreen 1994, 1989). Mandelker et al. (2014) suggests that they can either be *in-situ* clumps, originating from VDI (e.g. Elmegreen 2011), in this case they are young and star-forming, or they can be *ex-situ* clumps, originating from minor mergers, in that case they will be older and with a low gas fraction and low specific star-formation rate (sSFR). A recent simulation showed that the formation of such long-lived giant clumps is only possible with a gas fraction of at least 50% (Fensch & Bournaud 2021). This large gas fraction is necessary to induce VDI that will produce clumps that will migrate toward the center, creating strong gas nuclear inflow and triggering an evolution of the structure of the galaxy, leading to a morphological evolution (Fensch & Bournaud 2021). This scenario is also favored by some observations (Förster-Schreiber et al. 2011; Guo et al. 2012). More recently, Puschnig et al. (2023) studied a local galaxy as proxy for high-*z* galaxies, confirming that the giant SF clumps mostly originate from a fragmentation of the disk, induced by VDI and not accretion or minor mergers. With its high spatial resolution, the *James Webb Space Telescope*'s (*JWST*) near-IR Camera (NIRCam) is able to better resolve such giant SF clumps and could help constraining this scenario. It is thus becoming clear that the galaxies within the MS scatter are not all largely unperturbed gas-rich disks. The compact SF cores, as well as the giant clumps, independently of their formation history, imply complex phenomenology at play, much different than local SF galaxies in the MS that are typically well behaved spirals.

Recently, emphasis has been brought onto other kind of asymmetries characterising high redshift SF galaxies. Kalita et al. (2022) discovered strong lopsidedness affecting the three massive SF galaxies in a $z = 2.91$ group core. They suggested a link between the lopsidedness of a galaxy in a dense environment to gas accretion and minor mergers. The lopsidedness would then be a marker of the point of impact of the accretion stream, following Bournaud et al. (2005) who investigated the origins of lopsidedness in simulated galaxies. Their conclusion is that it is very unlikely that the lopsidedness is the result of internal mechanisms but is more likely to be linked to the assembly history and the environment of the galaxy, to asymmetric gas accretion and to minor merger and interactions with neighbouring galaxies. This is also the conclusion of studies on lopsidedness of galaxies in the local universe (Jog & Combes 2009; Zaritsky et al. 2013). Rujopakarn et al. (2023) studied a galaxy in a dense environment with SF off-center substructures. They interpreted it as either forming spiral arms following a minor merger, an interaction with a neighbouring galaxy or a lopsided structure resulting from the point of impact of the cold gas accretion stream. Colina et al. (2023) reported *JWST* MIRI observations of GN20, an extremely luminous sub-mm galaxy residing in a $z = 4.05$ protocluster (Daddi et al. 2009). They reveal a massive extended disk surrounding the sub-mm compact nucleus, displaying strong lopsidedness. As of today, the lopsidedness has only been studied in dense environments and serendipitously. Observing lopsided disk in less crowded environment and inferring their prevalence in complete samples could shed further light on their presumed origin from interactions and accretion, and clarify whether a massive hosting dark matter halo is, or not, required.

By probing the rest-frame optical to near infrared (near-IR) at Cosmic Noon, *JWST*/NIRCam has a unique ability to fill the gap between the sub-mm compact nucleus observed with *ALMA* and the larger galactic disk observed in the optical and will help critically examining the competing scenarios. As an example, Rujopakarn et al. (2023) recently studied substructures within a dusty star forming galaxy (DSFG) at $z \sim 3$ imaged with both *ALMA* and *JWST*. From NIRCam images, they showed that the ALMA substructures are also visible at 4μm, demonstrating the direct link that one can draw between near-IR and sub-mm emissions. This suggests that the long wavelength channel of NIRCam might be a good tracer of compact obscured star formation in MS DSFGs.

The present study is part of the Cosmic Evolution and Epoch of Re-ionization Survey (CEERS[1]; ERS 1345, PI: S. Finkelstein) which is one of the Early Release Science (ERS) programs of the *JWST* (Gardner et al. 2023) that observed a part of the EGS *Hubble Space Telescope* (*HST*) field with NIRCam (Rieke et al. 2023). EGS is too far North to be observed with *ALMA* and there is no high resolution imaging with the *Northern Extended Millimeter Array* (*NOEMA*) yet. However, the high sensitivity and exquisite spatial resolution of NIRCam towards 5μm can be used as a surrogate to identify the most obscured and massive regions within galaxies, hence those most likely vigorously star-forming.

Understanding how DSFGs are formed and evolve is crucial to get the larger picture of galaxy formation and evolution, and it could be a key element to explain the quenching of galaxies at and after Cosmic Noon. To this aim, *JWST*/CEERS allows a major step forward. Indeed Kartaltepe et al. (2023) already showed that *JWST* reveals the diversity of morphologies of galaxies at high redshift. *JWST* high spatial resolution and sensitivity is able to detect faint disks that were previously undetectable with *HST*. Moreover, a recent study by Kamieneski et al. (2023) uses *JWST*/NIRCam to probe the dust attenuation and sSFR of a lensed DSFG at $z = 2.3$. They demonstrate the power of *JWST*/NIRCam to precisely measure these properties at sub-galactic scales, allowing them to conclude that despite a more dust attenuated bulge, the color gradient of this galaxy is mainly driven by an early stage of inside-out quenching. This makes *JWST*/NIRCam the best instrument to investigate the morphological evolution of DSFGs around Cosmic Noon, in terms of compact star formation, giant clumps and galaxy structure.

The study is organized as follows. In Section 5.2 I present the data used in this study and the sample selection process. In Chapter 6, I detail the methods used to analyse each galaxy individually. In Chapter 7, I outline the main results of the analysis. Finally, in Chapter 8, I discuss the possible implications of the results in terms of formation and evolution of DSFGs at Cosmic Noon.

---

[1] `https://ceers.github.io`

In this work, I adopted H_0 = 70km s^{-1} Mpc^{-1}, Ω_M = 0.3, Λ_0 = 0.7, and a Chabrier IMF (Chabrier 2003). When necessary, I converted stellar masses and SFR from Salpeter IMF (Salpeter 1955) to Chabrier IMF by multiplying the M_* by 1.23 to convert it to Salpeter IMF and calculating the corresponding SFR_{MS} and converting it back to Chabrier IMF by dividing it by 1.58.

5.2 . USING THE *JWST* AND THE SUPER-DEBLENDED CATALOG TO STUDY DSFGs

5.2.1 . CEERS IMAGING

For the purpose of this study, I used the NIRCam imaging of CEERS, reduced using a customized pipeline by the CEERS collaboration (Bagley et al. 2022). It includes images in 7 filters: F115W, F150W, F200W, F277W, F356W, F410M and F444W for an average 5σ depth of 28.6 AB mag (See Table 3 of Bagley et al. (2022) for more details, each filter/pointing as a slightly different depth). The Point-Spread-Function (PSF) Full-Width at Half-Maximum (FWHM) of those filters range from 0.040" to 0.145" for F115W and F444W respectively[2]. For this study, I used the CEERS imaging from the June 2022 pointings, which represent 40% of the total area covered by NIRCam for CEERS between June and December 2022. I used the background subtracted images as I wanted to measure precise photometry. As I needed to extract galaxy properties based on spectral energy distributions (SEDs), I decided to complement shorter wavelengths by taking advantage of the existing *HST* imaging in the field. I used the publicly available *HST* data products version 1.9, available through CEERS. These mosaics were derived from *HST* archival data, but with improved calibration compared to the default pipeline products, and have astrometry tied to Gaia-EDR3 (Lindegren et al. 2021). As described in the accompanying data release, the mosaics were created from the combination of *HST* programs 10134, 12063, 12099, 12167, 12177, 12547, 13063, and 13792, and the reduction and calibration followed a similar procedure to those described in Koekemoer et al. (2011). I used two filters; F606W and F814W with a PSF FWHM of 0.115" and 0.110" respectively (Koekemoer et al. 2011). I did not use the *HST*/WFC3 images as these bands are redundant for bright galaxies, as they are covered by *JWST*/NIRCam images which are deeper and with better spatial resolution.

5.2.2 . THE "SUPER-DEBLENDED" FAR-IR CATALOG

My goal here is to study the morphology and SF activity of DSFGs. I select galaxies based on their IR detection in the state-of-the-art super-deblended far-IR (FIR) catalog of the EGS field (see Chapter 3 and 4). FIR emission is a secure tracer of star formation (once the AGN components are removed), while

---

[2] `https://jwst-docs.stsci.edu/jwst-near-infrared-camera/nircam-performance/nircam-point-spread-functions`

optical/near-IR classification of SF galaxies is subject to larger uncertainties especially in the presence of dust. Hence, my FIR selection ensures the galaxies under scrutiny are truly highly SF.

I recall that the super-deblending is based on a well-established technique (Liu et al. 2018; Jin et al. 2018). It is a multi-wavelength fitting technique meant to optimize the number of priors fitted at each band to extract the deepest reachable information. I used images from *Spitzer*, *Herschel*, SCUBA2 and AzTEC. The key was to obtain an adaptive balance as a function of wavelength between the density of priors fitted, the quality of the fit, and the achievable deblending given the PSF sizes. I started with the deepest images and fitted band after band toward shallower images. Extensive Monte-Carlo simulations ensured that the uncertainties associated to the flux measurements were "quasi-Gaussian" (for more details see Chapter 3 and 4 as well as Liu et al. 2018; Jin et al. 2018).

5.2.3 . SAMPLE DEFINITION

I selected all sources securely detected in the FIR catalog (see Section 5.2.2) that fell in the CEERS/NIRCam regions observed in June 2022. Since short wavelength channels have a slightly different field of view than long wavelength channels, I checked that the sources are observed in all of them and that they were not too close to the edge of the images so that there were not partially cut. In detail, I require the galaxies to have SNR$_{FIR} > 5$, where SNR$_{FIR}$ is the signal-to-noise ratios (SNR) added in quadrature from 100μm to 1.1mm (see Chapter 4, Equation 4.1) and have at least one detection (SNR> 3) in a *Herschel*/SPIRE band after deblending (required to reliably measure SF components in case of AGNs). The implication of the IR selection is that I don't have a stellar mass complete sample of SF galaxies (e.g., complete above some mass threshold), and I have instead something closer to a (redshift-dependent) SFR limit. I am aware that I am missing SF galaxies below my IR detection threshold, as I wish to focus to highly (and securely) star-forming galaxies.

I also limited the sample to galaxies within $1.5 < z < 3.0$, as I am willing to focus on galaxies at "Cosmic Noon", as recalled in the Introduction. To get accurate redshift estimates, I used the recent redshift compilation produced by Kodra et al. (2022), which includes photometric redshifts based on CANDELS (Grogin et al. 2011; Koekemoer et al. 2011) as well as grism-based redshifts from 3D-HST (Momcheva et al. 2016) and spectroscopic redshifts from the MOSDEF survey (Kriek et al. 2015).

This sample comprised a total of 26 IR-detected sources. From these, 4 had to be rejected after a clean up. After close inspection, three galaxies were in a blended region and/or close to a much brighter IR source, making the *Herschel* measurements less reliable. The last rejected source hosted an AGN (clear radio excess, $\sim 10\times$ brighter than what is expected for the radio continuum based on IR emissions, and X-ray detected: ID15327, RA = 215.82825, Dec = 52.80844, $z_{phot} = 1.61$, $log_{10}(L_{AGN}/L_{\odot}) \gtrsim 11.3$), hence the majority of its IR luminosity does not come from SF regions which are the main objects of this study.

This left us with a clean sample of 22 FIR-bright DSFGs around Cosmic Noon. I illustrate in Figure 5.1 the distribution of the sample in terms of stellar mass estimated in the pre-*JWST* era (Stefanon et al. 2017) and total IR luminosity from my super-deblended catalog (calculated based on the equations in Press et al. (1992)) versus redshift (Kodra et al. 2022). I also show the distance from the MS (Schreiber et al. 2015) with a 0.6 dex total scatter (Rodighiero et al. 2011) defined as $\Delta_{MS} = SFR_{IR}/SFR_{MS}$. Schreiber et al. (2015) uses a Salpeter IMF (Salpeter 1955), I converted stellar masses and SFRs from Salpeter IMF to Chabrier IMF by subtracting 0.24 dex. The red shaded region corresponds to the pure starburst region as defined in Liu et al. (2018) ($log_{10}(SFR_{IR}/SFR_{MS}) > 0.6$ dex), I have two galaxies in my sample classified as pure starburst. The rest is mostly either within the scatter of the MS, but above its average trend, i.e. above the MS but below the starburst regime.

In Figures 5.2, 5.3 and 5.4, I show RGB cutouts of my sample of galaxies using the F115W, F200W and F444W filters of NIRCam. The galaxies are separated in three classes, as discussed in detail in the next Section.

We have now a sample of DSFGs ready to be studied. I explain in the next chapter how I probed their properties.

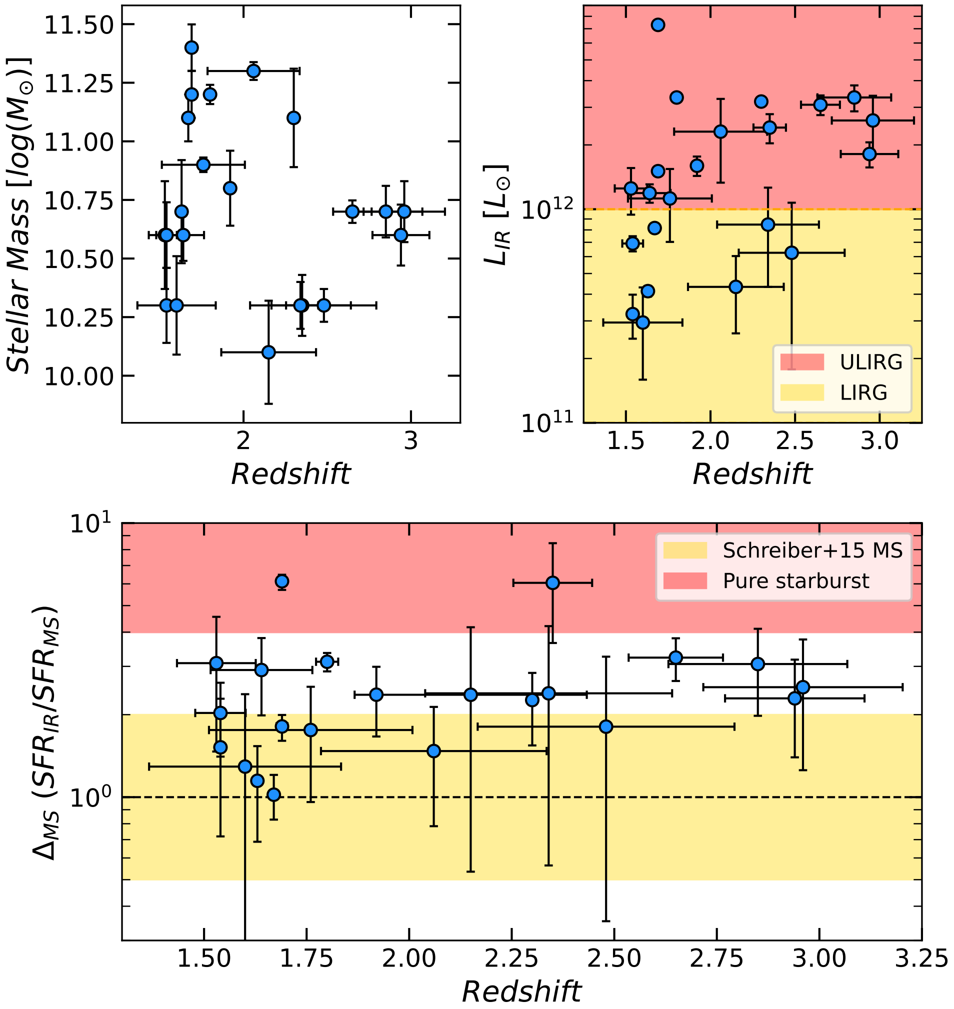

Figure 5.1: Stellar Mass (upper-left panel), total IR luminosity from the super-deblended catalog (upper-right panel) and distance from the Main Sequence (MS, lower panel) of the galaxies in the selected sample versus their redshift. The colors on the upper-right panel delimits the luminous IR galaxies (LIRG, in yellow) and ultra-LIRG (ULIRG, in red) local regimes for information. On the lower panel, the yellow shaded region illustrates the MS from Schreiber et al. (2015) while the red shaded region illustrates the pure starburst regime (Liu et al. 2018).

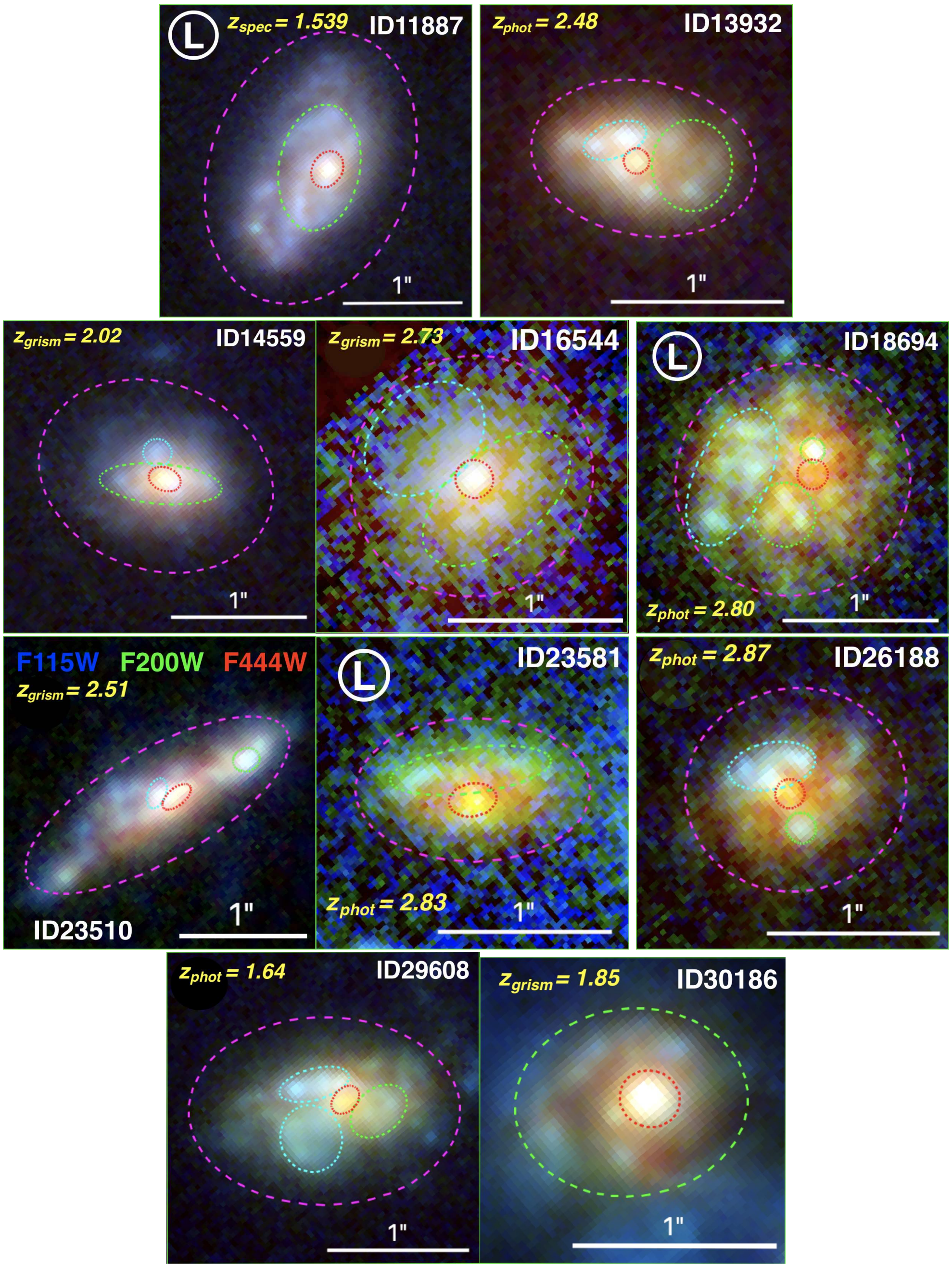

Figure 5.2: Type I: *SF disks with a red SF core* (see Section 6.7). RGB (F115W, F200W, F444W) non PSF-matched cutouts. In each cutouts the white bar defines the scale of the image. The dotted regions correspond to the different studied components, the core/bulges are shown in red, the rest are the different parts of the disks (blue or green show patches when present, magenta is the remaining of the disk) see Section 6.5. The galaxies with a circled L are the most lopsided galaxies of my sample, see Section 7.1.3.

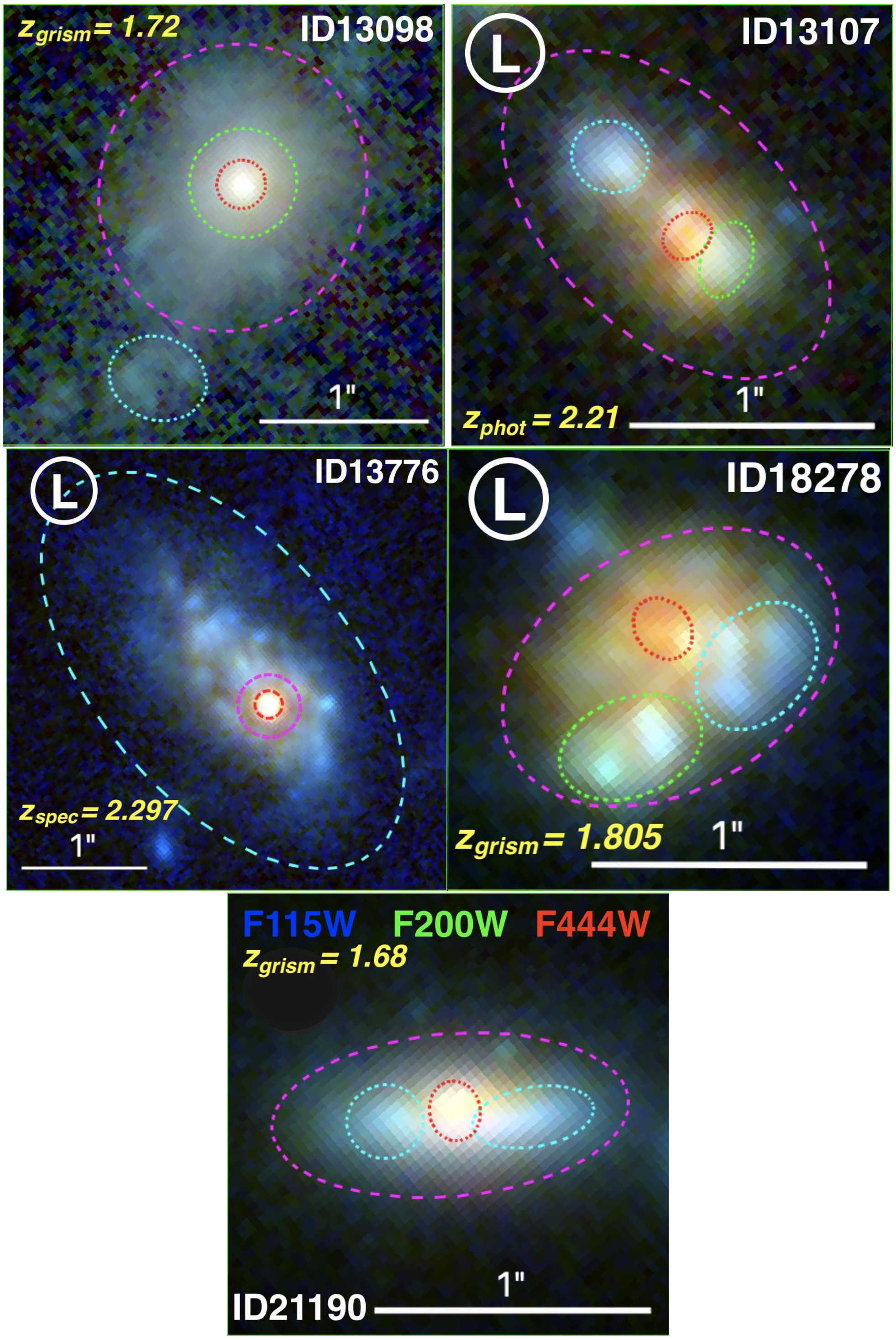

Figure 5.3: Type II: *Quenched disks with a SF core* (see Section 6.7). Similar to Figure 5.2.

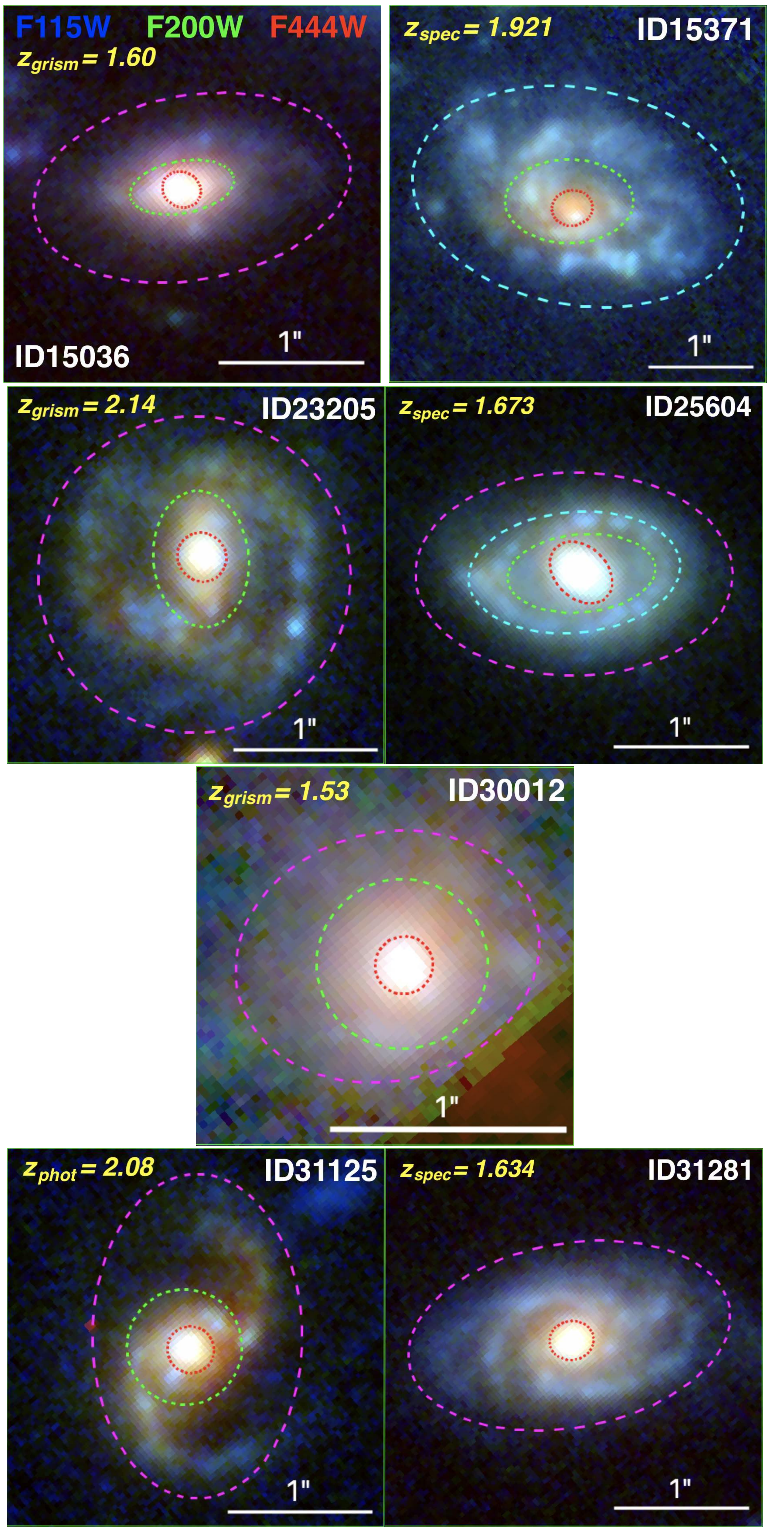

Figure 5.4: Type III: *SF disks with a quenched bulge* (see Section 6.7). Similar to Figure 5.2 and 5.3.

6 - PROBING THE PROPERTIES OF DSFGs AT COSMIC NOON

In this chapter, I detail the methods used to analyze each galaxy, taking one of the objects (ID15371) as an example, to better clarify the procedure that I applied to all galaxies. For each galaxy, I started by creating cutouts in each band (*HST*/ACS F606W, F814W and *JWST*/NIRCam F115W, F150W, F200W, F277W, F356W, F410M, F444W). I show the cutouts of a DSFG in Figure 6.1 where one can already see by eye a difference between the disk visible in all bands and the center of the galaxy invisible in the *HST* images but getting brighter at longer wavelengths, justifying the need to study each component individually rather than the galaxy as a whole. One of the first steps was to see if I could identify a bulge and a disk in each galaxies just like for ID15371, as discussed below.

JWST/NIRCam images have a spatial resolution ranging from $0.040''$ at 1.15μm up to $0.145''$ at 4.4μm. The larger 4.4μm PSF allows a resolution in physical size down to 1.23 (1.12) kpc for a galaxy at redshift 1.5 (3). This means that I was able to spatially resolve galaxy substructures down to a radius ~ 0.6kpc. This made the resolution of F444W perfect for this study as we know the sizes of compact SF regions and giant clumps to be ~ 1kpc (Gómez-Guijarro et al. 2022a; Rujopakarn et al. 2019; Förster-Schreiber et al. 2011).

6.1 . MEASURING GALAXY SIZES

Several studies have shown that the regions of star-formation, either traced by the dust emission at 1.1mm observed with *ALMA* or by the radio continuum emission detected by the *Very Large Array* (VLA), are more compact than the optical size of the galaxy (Puglisi et al. 2019; Gómez-Guijarro et al. 2022a; Fujimoto et al. 2017; Jiménez-Andrade et al. 2019, 2021).

JWST, with its sensitivity of the near and mid-IR, can detect both the obscured star-forming central part of each galaxy invisible with *HST* and the less obscured larger system, invisible with ALMA or *VLA* and bridge the gap.

To investigate this, I measured the total near-IR half-light radius ($R_{e,NIR}$) of each galaxy in the closest band to 1.6μm rest-frame (F410M or F444W filter depending on the redshift). This rest-frame wavelength was chosen as it is a known tracer of the stellar mass of galaxies and is not affected by dust attenuation (Hainline et al. 2011; Casey et al. 2014). Moreover a recent study using NIRCam/CEERS data showed the excellent agreement between the near-IR size and the stellar mass size of galaxies around Cosmic Noon (van der Wel et al. 2023). I measured $R_{e,NIR}$ from a curve of growth method, given that

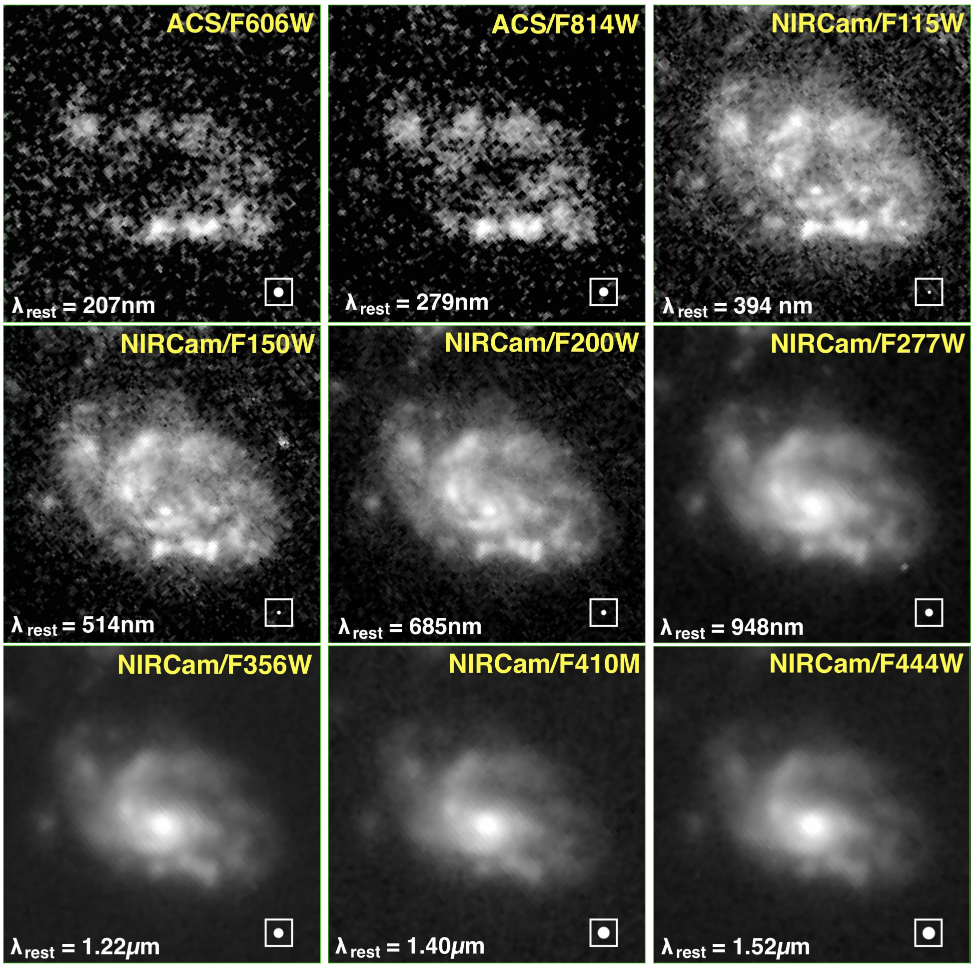

Figure 6.1: Cutouts of *HST*/ACS and *JWST*/NIRCam images of the DSFG ID15371 at $z_{spec} = 1.921$. Cutout size: $3.6'' \times 3.6''$. I also indicate the rest-frame wavelength corresponding to each filter (white label). The filled circle in the white box illustrate the PSF size for each filter.

in all cases the PSF has a negligible effect (much smaller than any $R_{e,NIR}$). The $R_{e,NIR}$ was defined as the radius of a circular aperture, centered at the center of mass (barycenter) of the galaxy, which encompassed half of the total flux density of the galaxy at the considered wavelength. To estimate the uncertainty, I used the fact that I typically have a 5% uncertainty on the measurement of the total flux of the galaxy (see Section 6.5 for more details on the photometry measurements). I also measured the bias introduced when using a circular aperture for edge-on galaxies (like ID23510 in Figure 5.2) by comparing the fluxes encompassed in an elliptical aperture and a circular aperture. The difference is about 5%. Hence, by changing the total flux of the galaxy within 10% I can estimate the uncertainty on $R_{e,NIR}$ for which 50% of the total flux is encompassed.

I also measured the total optical half-light radius ($R_{e,O}$) of each galaxy in the closest band to 550nm rest-frame following the same procedure to compare it with $R_{e,NIR}$.

6.2 . IDENTIFICATION OF CORES/BULGES

Depending on the redshift, the F444W filter of NIRCam probes the rest frame near-IR between 1.1μm and 1.8μm which is a good tracer of stellar mass (van der Wel et al. 2023). Hence, inspection of galaxy morphologies in this filter allowed us to search for the center of mass of each galaxy in my sample, or lack there-of, as a well defined peak in the F444W images. I was able to clearly identify a peak in the flux distribution of this filter for every galaxy. Depending on the galaxy, the peak was more or less pronounced, but always confidently there. I then defined a region in each galaxy encompassing the peak, as the core or the bulge of the galaxy. The regions are defined by eye as the peak is easily identifiable in every galaxies, the limit of the core is where the flux coming from the red F444W filter doesn't dominate anymore the RGB (F115W, F200W, F444W) color. Generally, a bulge is often defined in the literature as a quiescent central component with a high Sersic index (e.g., $n \sim 4$), and is a common component in local massive galaxies. In my study I did not attempt obtaining Sersic fits of separate components, and, more importantly, I anticipated that in many cases the central concentrations would not be quiescent, actually, most of them were highly SF and attenuated. I decided thus to call the central concentrations as cores when they were SF and bulges when they were quiescent. They are represented by the regions delimited by the red dotted lines in all galaxies in Figure 5.2, 5.3 and 5.4.

I emphasize that for most of my sample, it would not have been possible to identify the center of mass only based on *HST* images (see e.g. ID15371 in Figure 6.1 as an obvious example). This demonstrates once again the power of *JWST* when it comes to studying high-*z* DSFGs.

6.3 . LOPSIDEDNESS

Having defined the core/bulge of each galaxy, I considered the rest to be the disk. Hence, I could obtain an evaluation of the lopsidedness for each galaxy. I considered it to be an important property to investigate because a lot of galaxies in my sample are obviously highly lopsided already by visual inspection (see for example ID11887, ID13776, ID18278, ID18694 in Figure 5.2 and 5.3). To quantitatively study this phenomenon, I defined two parameters:

the eccentricity, defined as:

$$E = \sqrt{\frac{(X_{core} - X_{disk})^2 + (Y_{core} - Y_{disk})^2}{R_{disk}^2}}, \tag{6.1}$$

where (X_{core}, Y_{core}) and (X_{disk}, Y_{disk}) are the coordinates of the central core of the galaxy and of its disk respectively, while R_{disk} is the radius of the disk. The center of the core was simply defined as the pixel with the maximum flux density in the F444W filter. The center of the disk was defined as the barycenter of the disk measured in the rest-frame optical band (F150W or F200W depending on redshift). I measure it in the optical and not in the near-IR because the disk is less attenuated than the core, hence brighter than the core at these wavelengths. To not be biased by the core, I applied a circular mask centered on (X_{core}, Y_{core}) with a radius defined by the closest pixel to the center that has a F444W flux density less than half the core center flux density. Finally, R_{disk} was calculated using a circular aperture centered on (X_{disk}, Y_{disk}) encompassing half of the disk flux density. This quantifies the eccentricity of the disk with respect to the core/bulge compared to its size and is a-dimensional.

The other quantity that I defined to probe the lopsidedness of the galaxies is the asymmetry. The asymmetry was calculated for the F444W NIRCam filter as I am trying to probe the mass distribution asymmetries and, as previously mentioned, F444W is the best tracer of the stellar mass distribution. I calculated the asymmetry by rotating each image by $180°$ and subtracting it from the original image, the center of rotation was (X_{core}, Y_{core}) from Equation 6.1. The asymmetry is defined as:

$$A = \frac{\sum_{i=0}^{N} |F_i - F_i^{180°}|}{F_{tot}}, \tag{6.2}$$

where F_i and $F_i^{180°}$ are the flux of the i-th pixel and its $180°$ symmetric counterpart with respect to the center of the central core/bulge as defined in Equation 6.1. F_{tot} is the total flux of the galaxy. Since I worked on background subtracted images, I considered the background asymmetry to be negligible. This quantity describes how smoothly and how symmetrically the stellar mass is distributed around the central core/bulge of the galaxy and is also a-dimensional. Usually, the lopsidedness is probed using a Fourier decomposition (e.g. Dolfi et al. 2023; Kalita et al. 2022; Jog & Combes 2009; Bournaud et al. 2005). I decided to use a different, simpler method; the asymmetry, that has already been used in gas velocity space and was found to correlate well with the Fourier analysis of stars (Bournaud et al. 2005; Matthews et al. 1998).

6.4 . CLUMPINESS

After identifying the core or bulge of each galaxy, I investigated the surrounding disk-like structures. Some of the galaxies have a smooth disk, others have a much more perturbed/complex disk morphology showing a large number of clumps (see Figure 5.2, 5.3 and 5.4).

I did not embark in a physical study of the clumps in this work. My goal for this paper is to assess the presence or not of clumps in the disks and have an idea of how fragmented the disks are. Hence, I did not try to derive any physical properties of the individual clumps. I decided to measure a clumpiness index, defined as the number of clumps in the disk of each galaxy. I counted the number of clumps visually identifiable in the RGB (F115W, F200W, F444W) image, making sure that the bulge/central concentration was not counted as a clump. This number varies from 0 up to 7 for the clumpiest galaxy. To be counted as a clump, the feature had to be compact compared to the galaxy size, and either had to have a different RGB color from the surroundings and/or appear as a local brighter spot. The clumps appear most clearly at the shortest wavelength (F115W or F200W filters), as expected (Wuyts et al. 2012). For ID15371, I identify 4 clumps, there are shown by the white ellipses in the left panel of Figure 6.2.

6.5 . SPATIALLY RESOLVED PHOTOMETRY

To quantitatively study my galaxies, I needed photometry measurements. I decided to divide my galaxies in several components. For the simplest cases I only had the core/bulge and the disk, and when the disk had several clump/patches with different colors in the RGB image, I broke it down to several circular or elliptical regions. Each region was designed so that it had, qualitatively, a homogeneous (F115W, F200W, F444W) color. The division of the disk is once again done by visual inspection. I emphasize that I seek to study each region that has a different color, hence, if several clumps are close and with a similar RGB color, I consider them to be part of the same disk component. Moreover, due to the spatial resolution of the PSF-matched images, I did not want to design too small regions that could lead to biased flux measurements. I tried to respect a balance between the size of the component I defined (not too close to the PSF size) and the homogeneity of the RGB color inside it. I emphasize that the components are not necessarily concentric as most of the galaxies are not radially symmetric and are not limited in number. If I observed, for example, two blue disconnected patches in a galaxy, I defined them as two different components and fitted them individually. In the case of ID15371, I divided the galaxy in three regions, the red central core/bulge, the bluer disk and an intermediate region, that is still part of the disk but close to the red core and with intermediate colors (see Figure 6.2).

In terms of rest-frame colors, since my sample of galaxies is distributed across $z \sim 1.5$ to $z \sim 3$, F115W probes the rest-frame near-UV/blue ($300-460$nm), F200W probes the rest-frame green/red ($500-800$nm) and F444W probes the rest-frame near-IR ($1110-1780$nm). The scatter in rest-frame wavelength is less or equal to the band-width of each filter. This means that I globally probed consistent colors between galaxies.

By dividing each galaxy in sub-galactic regions, there was a risk that small regions get close to the PSF FWHM of some filters. Hence, leading to an underestimation of the flux at the longest wavelengths, and an artificial deformation of the SED. To avoid this, I decided to work on PSF-matched images using the broader PSF of the F444W filter. In Figure 6.2, I show RGB images of the DSFG ID15371 using (F115W, F200W, F444W) before and after PSF-matching. To make sure that I didn't underestimate stellar masses and SFR when running the SED fitting, I chose regions larger than the PSF FWHM (0.145"). In Figure 5.2, 5.3 and 5.4, for each galaxy I overlay the delimitation of the different components I decided to study separately based on their color (those RGB images are showed before PSF-matching).

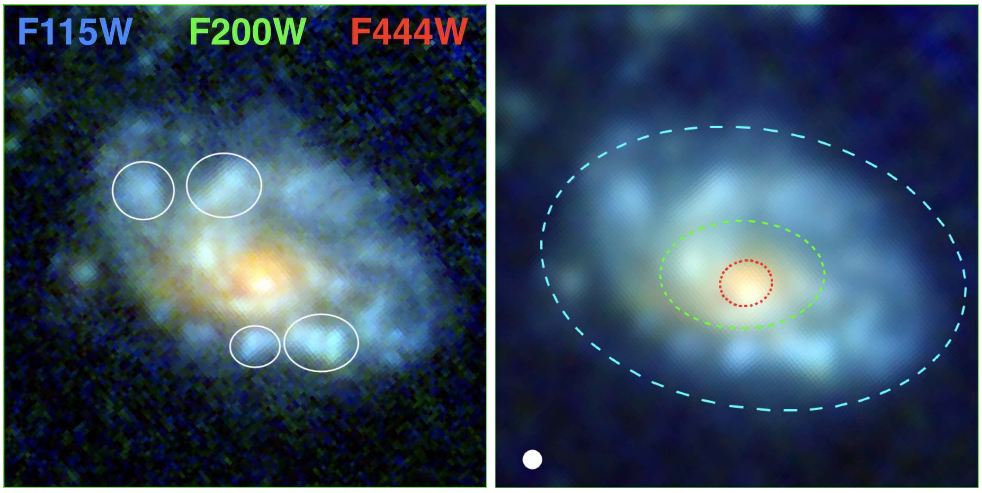

Figure 6.2: RGB (F115W, F200W, F444W) image of the galaxy ID15371 ($3.6" \times 3.6"$) at $z_{spec} = 1.921$ before (left panel) and after (right panel) PSF-matching. In the left panel, the white ellipses show the features I identified and counted as clumps. In the right panel, the colored dotted lines correspond to the division of the galaxy in homogeneously colored regions and the white filled circle to the PSF size.

After having defined the regions to study, I measured the flux in each band for each region. To do so, I summed the value of each pixel in each region of the science image. The pixels were counted only once, meaning that the flux in the smaller regions (like the red ellipse for ID15371) was not included when calculating the flux of larger regions (like the green ellipse for ID15371, see Figure 6.2).

Our goal was to fit the SED of the different components of each galaxy. For the properties that I later extracted from these SEDs to be reliable, it was crucial that I had reliable uncertainties on the fluxes. To estimate the flux uncertainties, I re-normalized the errors propagated via the Root Mean Square (RMS) images. The uncertainty was defined as:

$$df = f_{\lambda,N} \times \sqrt{\sum_{i=0}^{N} \sigma_i^2}, \tag{6.3}$$

where the sum was made on all pixels in the region, σ_i is the RMS of the pixel i, and N the total number of pixel in the region. I decided to define $f_{\lambda,N}$, a normalisation factor that takes into account extra noise, e.g. from the correlated signal between pixels that is particularly important for the long wavelength filters that were drizzled from a pixel size of 63mas to 30mas. To calculate this factor, I measured the flux dispersion in ~ 20 empty regions of the science image for several apertures in each band. I then compared this value to the RMS calculated from the RMS image in apertures of the same size and the normalisation factor is defined as their ratio. To be conservative, I never applied a factor leading to lower uncertainties. These factors are generally small, ($f_{\lambda,N} \sim 1.5$ at most).

6.6 . SED FITTING

To characterize my sample of galaxies, I needed to have access to their resolved M_* and SFR. To this aim, I fitted each galaxy component SED using the Code Investigating GALaxy Emission (CIGALE, Boquien et al. 2019). I used a single declining exponential model also known as "τ model" to model the star formation history of each galaxy. I adopted the Bruzual & Charlot (2003) model for computing the spectral evolution of single stellar populations with a fixed solar metallicity of Z = 0.02 which is reasonable for $M_* \sim 10^{10-12} M_\odot$ DSFGs following the Mass-Metallicity relation (Ma et al. 2016). After testing with and without including nebular emissions, I decided not to include them as, for my sample, they lead to higher χ^2 with no noticeable effect on the extracted properties (A_V, SFR, M_* and redshift).

Some galaxies showed possible signature of strong emission lines, visible as green patches/clumps in Figures 5.2, 5.3 and 5.4. However, including them had a negligible effect on the estimation of the SFR since it usually had a 50% uncertainties. I discuss this in more detail in Section 8.1.

I used a modified Charlot & Fall (2000) dust attenuation law and the Draine et al. (2007) dust emission models update from 2014 to predict FIR flux densities. The idea behind the modification of Charlot & Fall (2000) model is that young stars embedded in their birth cloud suffer from additional attenuation compared to stars that have broken out and escaped into the ISM, and that the attenuation curves associated to the birth cloud and the ISM must be different. In practice, this is modelled by assuming two different power-law attenuation curves of the form $A(\lambda) \propto \lambda^{\delta}$: one for the birth cloud with a slope of $\delta_{BC} = -1.3$, and one for the ISM with a slope of $\delta_{ISM} = -0.7$. Because radiation from young stars has to travel through both the birth cloud and the ISM to escape the galaxy, the spectrum of stars younger than 10Myr are attenuated by both the birth cloud and ISM curves. Stars older than 10Myr are only attenuated by the ISM curve (Boquien et al. 2019).

For the redshift, I used the Stefanon et al. (2017) catalog, as well as the latest redshift catalog published by Kodra et al. (2022). I encountered three different cases:

- If I had a high-quality spectroscopic redshift, then I used it and fixed it. I have 5 galaxies with a spectroscopic redshift.

- If I had a grism-based redshift from 3D-HST, I downloaded the spectrum and examined its quality, actual features detected, the redshift probability distribution and defined the redshift and its uncertainty accordingly. I have 10 galaxies for which I find a high-quality grism-based redshift.

- If I only had photometric data, I allowed $(1+z)$ to vary within $\pm 10\%$. I have 7 galaxies with a photometric redshift.

In Figure 6.3, I show the best SED models corresponding to each region of my example galaxy defined in Figure 6.2.

To be able to extract reliable information from the SED fit, it was crucial to check the fit quality. To be conservative and have reasonable χ^2, I decided to limit the photometric accuracy of each band to $S/N = 20$. However, if the CIGALE fit returns high χ^2 values, there is a possibility that the input flux uncertainties are still underestimated. In that case, I increased the uncertainties by adding up 10% of the flux to the error in each band. To consider the fit acceptable, I want the reduced χ^2 such as $\chi^2_{red} \leq 1.67$, which is the reduced critical value corresponding to a significance level of 10% in the χ^2 test for 8 degrees of freedom.

To estimate the robustness of the best model, I studied the χ^2 distributions associated to the 3 main free input parameters: the dust attenuation, the age of the stellar population and the e-folding time. In Figure 6.4, the upper-left panel shows the χ^2 distribution associated with the different values of the dust V-band attenuation A_V of the stellar continuum used to fit the SED of the red core of the DSFG ID15371. The upper-right panel shows the same information for t/τ with t and τ being the age of the oldest stars and e-folding time of the stellar population used to define the star formation

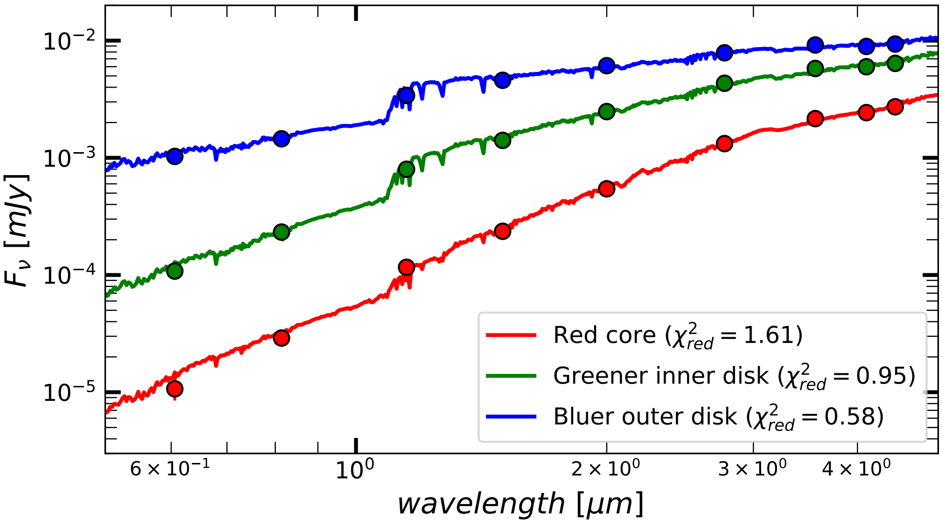

Figure 6.3: Best SED models computed by CIGALE (Boquien et al. 2019) for the red core (in red), the blue disk (in blue) and the intermediate region (in green) of the DSFG ID15371 at $z_{spec} = 1.921$ (the same example galaxy shown in Figures 6.1 and 6.2). I show in the legend the value of the reduced χ^2 (χ^2_{red}) for each SED fit.

history of the galaxy. Taking the width of these distribution at $\chi^2_{min} + 1$ and $\chi^2_{min} + 2.7$ give us the 68% and 95% confidence interval respectively (Avni 1976), illustrated by the horizontal thick and thin dashed lines in Figure 6.4. The fact that I see only a portion of the distribution for t/τ comes from the fact that the age is getting close to the age of the Universe, allowing larger t would not make physical sense.

I can use the same reasoning for the properties extracted from the SED like the M_* or the SFR averaged over the last 10Myrs. I show an example in the lower panels of Figure 6.4.

Just by looking at Figure 6.4, I can already conclude that the red core of the DSFG ID15371 is dusty ($A_V \sim 2.73$) and weakly star-forming (SFR $\sim 18 - 40$ $M_\odot/yr$ and $t/\tau \gg 1$).

As a sanity check, I estimated the SED of the whole galaxy by summing up the SEDs of all the components. I then compared this SED with the near-IR and FIR flux densities measured in my super-deblended catalog (K$_S$ and IRAC fluxes are from Stefanon et al. 2017, see Chapter 3 for the far-IR flux extraction) to make sure that they were consistent. If the FIR flux densities are brighter than predicted by the SED fitting, it can be a hint that this galaxy is in a starburst episode and/or that there is a deeply attenuated component that is not visible even at 4.44μm. It can also be due to the presence of an AGN that boosts the FIR flux, this can be confirmed by a radio excess detected in

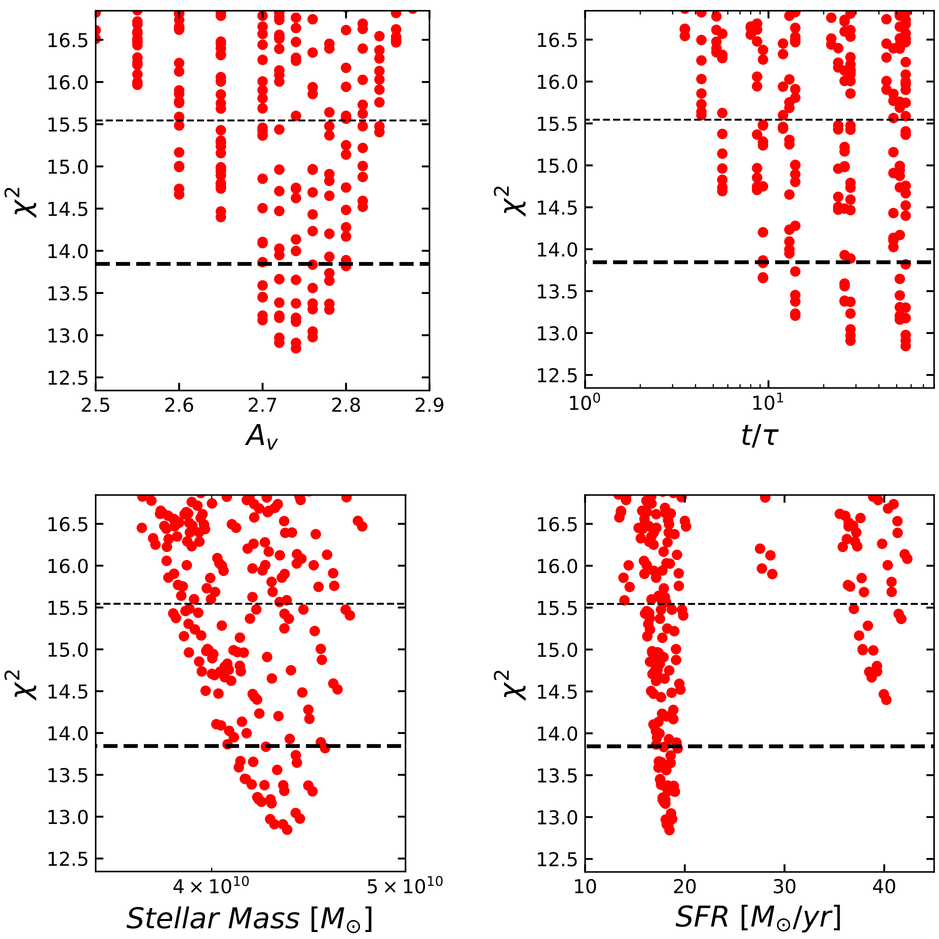

Figure 6.4: χ^2 distributions associated with the dust attenuation (upper-left panel), t/τ (upper-right panel), the stellar mass (lower-left) panel and SFR averaged over the last 10Myrs (lower-right panel) produced by CIGALE (Boquien et al. 2019) for the fit of the red core SED of the galaxy ID15371 at $z_{spec} = 1.921$. The thick and thin black dashed lines corresponds to the 68% and 95% confidence interval respectively.

my super-deblended catalog or an X-ray detection (Stefanon et al. 2017; Nandra et al. 2015). I recall that I removed from the sample only one galaxy where I knew that the FIR luminosity was dominated by the AGN luminosity (see Section 5.2.3) but kept those where the AGN luminosity didn't dominate the FIR luminosity. On the contrary, if the SED predicts a FIR flux density brighter than the one measured, it means that there is a problem in the fitting possibly linked to the grid of the input parameters. In Figure 6.5, I show the comparison between the total SED of the galaxy ID15371 and the FIR flux densities. For this galaxy, the flux densities are consistent with the predicted FIR SED meaning that there is no hidden component. This is the case for all the galaxies in my sample except one (ID13107 for which I have a FIR detection brighter than the SED model, pointing toward either a deeply attenuated component or an AGN even though there is no AGN signature in X-ray or radio). However for 3 galaxies (ID13098, ID13776 and ID31281), the measured 100μm flux is boosted compared to the SED predicted flux, possibly a signature of a hot AGN, 2 of them have an X-ray detected AGN (Nandra et al. 2015). By observing Figure 6.5, one can notice that the predicted IRAC fluxes are fainter than the actual measurement. This observation is not true for every galaxy, I measure the flux in the NIRCam F356W and F444W which probe the same wavelength as IRAC channel 1 and 2 to be fainter for this galaxy. This is mostly a sign of blending in the earlier IRAC imaging.

A caveat of this SED fitting method is that I used the same SFH and parameters for all regions, some with very different properties. I chose to use the simple tau model because of the meaning of t/τ regarding the star-forming activity of the galaxy. I decided to make a two-pass SED fitting, in the first pass, the goal was to separate the star-forming from quiescent regions. In the second pass, I fitted the star-forming regions with a nearly constant SFR (by imposing $\tau \gg t$). This allowed to have a good estimate of the recent SFR. Moreover, by comparing it to the far-IR SFR from my super-deblended catalog and to the relative position of each component with respect to the Main Sequence or the quiescent quadrant of the UVJ color-color diagram (see Section 6.7 for more detail on these last two points), I had a confirmation of the star-forming activity of each galaxy component. For the quiescent regions, there can be a degeneracy between the age and the dust attenuation, to tackle this, I imposed $t \gg \tau$. I estimated that the good quality of the photometry in the rest-frame near-IR and the two-pass SED fitting procedure allowed us to get robust estimates of both the stellar mass and the SFR of each component.

To tackle the great diversity of galaxies, I decided to divide them into several classes as defined in the next Section.

6.7 . CLASSIFICATION

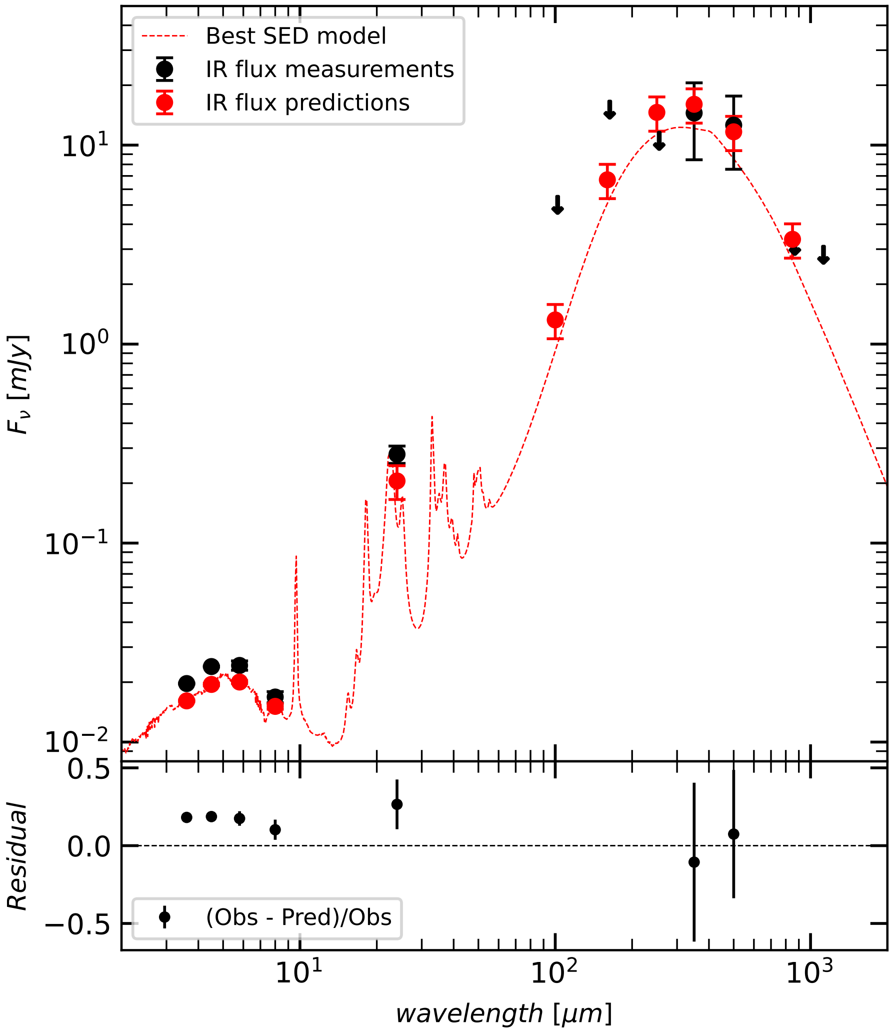

Figure 6.5: Total SED of the galaxy ID15371 at $z_{spec} = 1.921$ in red. It was calculated by adding up the CIGALE best SED model of each component. The black points are the near-IR and FIR fluxes with their uncertainties or upper limits (arrows) from my super-deblended catalog. From the FIR data points, I have $SFR_{IR} = (150 \pm 15)$M$_\odot$ yr^{-1}, the CIGALE fits give a consistent total $SFR_{10Myrs} = (197 \pm 125)M_\odot$ yr^{-1}. Given its stellar mass ($M_* = 10^{11}$M$_\odot$), this galaxy is on the main sequence.

From the CIGALE SED fitting, I derived an estimation of the M_*, the SFR and the dust attenuation (A_V) of each component of the galaxies. For the galaxy ID15371, in the upper panel of Figure 6.6, one can see the three components respective M_* and SFR plotted on the MS (Schreiber et al. 2015; Huang et al. 2023). All the components of the DSFG ID15371 have some ongoing star-formation, with the red core being on its way to quenching but still slowly star-forming.

Using the best SED models provided by CIGALE, I also estimated the rest-frame U, V and J AB magnitudes. I used Apellániz (2006) U and V filters, and for the J band, I used the 2MASS J relative spectral response curve. In Figure 6.7, I display all the regions of my galaxies on the $(V-J, U-V)$ plane. I recover the sSFR effect: when moving from the lower right corner to the upper left corner, the sSFR decreases (Wang et al. 2017). This makes the UVJ color-color diagram ideal to separate SF galaxies from quiescent galaxies. I note that the galaxies with sSFR $\lesssim 0.1$Gyr^{-1} are all in the quiescent region defined by Whitaker et al. (2011) and delimited by the black dashed line in the Figure. The colored dotted lines delimit the regions defined by Zick et al. (2018).

For the DSFG ID15371, I have confirmation in the UVJ diagram that all the components are star-forming (lower panel of Figure 6.6). Moreover, the three components are aligned on the diagonal of the diagram which is the signature of a gradient of dust attenuation from the center towards the outer parts (Calzetti et al. 2000). Indeed, from the SED fitting, I had $A_{V,red} = 2.70 \pm 0.11 > A_{V,green} = 2.09 \pm 0.23 > A_{V,blue} = 0.75 \pm 0.11$.

Generally, to estimate if a region was SF or quiescent, I used the UVJ color-color diagram (is the component in the quiescent quadrant or not ?), the position relative to the MS (is the component on/above the MS or well below it ?, what is its position compared to the other regions of the same galaxy ?) and, as I used a simple exponential model for the star-formation history, the value of t/τ is also an indicator of the star-formation activity. If $t/\tau \gg 1$, then the peak of star-formation is firmly in the past, and the component is on its way to quenching. On the contrary, if $t/\tau \lesssim 1$, the galaxy is still actively star-forming. Based on these three pieces of information, I was able to discriminate between SF and quiescent regions. Here, I defined a region as quiescent if below the Main Sequence and the other galaxy components (by ~ 0.6dex). Hence, some regions that I classified as quiescent are not completely passively evolving and could still be slowly star forming. Most of the time, the three indicators are in agreement, however, in some cases the results were ambiguous: the regions where all three indicators where not in agreement represent less than 5% of all the studied regions. In that case, I first looked at their position relative to the MS to see if it was consistent with the t/τ values from the best models and it always was. The inconsistency of the UVJ color-color diagram can be explained in several ways: the UVJ dia-

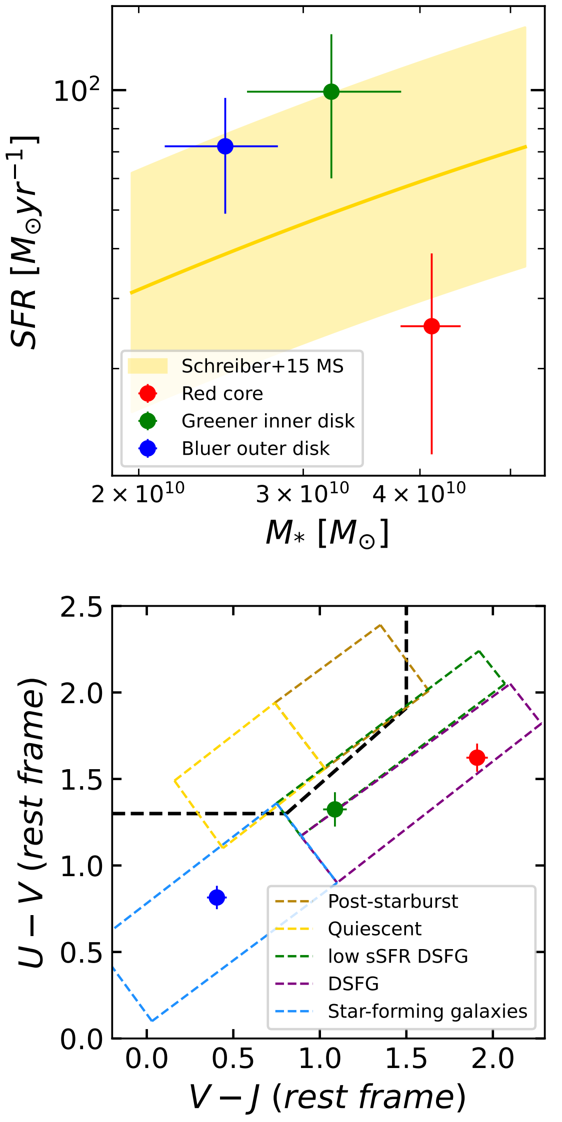

Figure 6.6: Upper panel: Galaxy ID15371 components plotted over the Main Sequence (Schreiber et al. 2015; Huang et al. 2023). Lower panel: Galaxy ID15371 components in the UVJ color-color diagram, the black dotted line delimits the quiescent region (Whitaker et al. 2011) and the colored ones, the regions defined by Zick et al. (2018). See Figure 6.2 for the definition of the components.

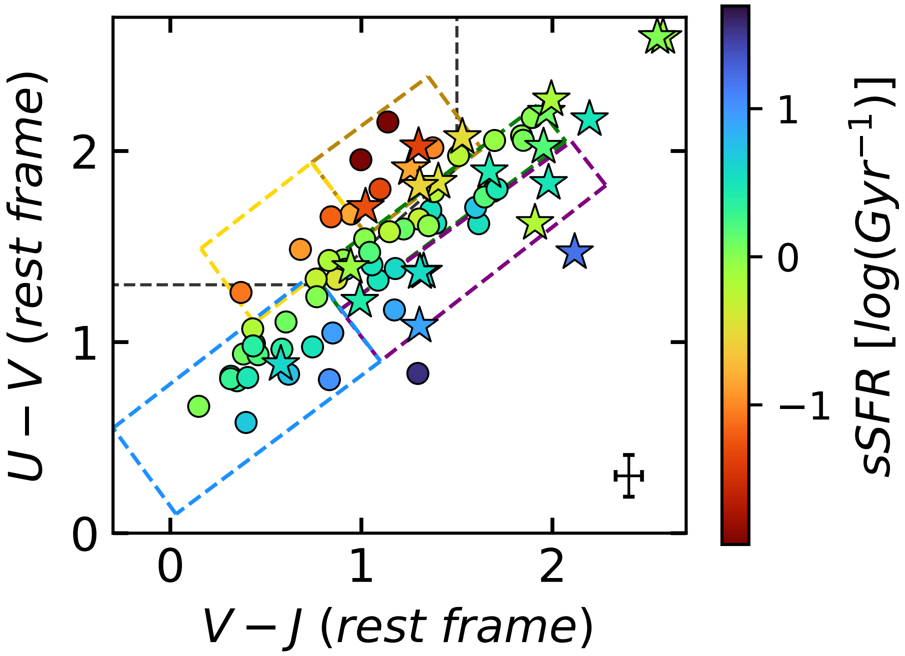

Figure 6.7: UVJ color-color diagram. Each marker represents a region of a galaxy. The star-shaped markers are cores/bulges and circular markers are disk components. The color of the marker depends on the sSFR of the considered region. The error-bar in the lower right corner shows the average uncertainty. The black dotted line delimits the quiescent region (Whitaker et al. 2011) and the colored ones, the regions defined by Zick et al. (2018). The orange region corresponds to *Post-starbursts*, the yellow one to *Quiescent*, the green one to *low sSFR DSFG*, the magenta one to *DSFG* and the blue one to *Star-forming galaxies*.

gram uses only a part of the information (3 rest-frame bands) contrary to the other probes that uses the full SED. More importantly, real situations exist where the UVJ diagram characterizes correctly the presence of star formation but this star formation is suppressed as exemplified by the sub-MS location (suppressed with respect to the ensemble average given the mass) and by the t/τ (suppressed with respect to the past star formation history of this galaxy). That is the case for the central region of ID15371 (see Figures 6.4 and 6.6). In the rare cases where the t/τ value didn't allow any conclusion ($t/\tau \sim 1$), I decided based on the MS and the UVJ color-color diagram that were consistently pointing either toward star-formation or quiescence. In all the cases, I was able to classify the regions as quiescent or star-forming.

As a result of this analysis, I had 22 vastly different galaxies with various morphologies, colors (see Figures 5.2, 5.3 and 5.4) and star-formation activity. I found that the variety of features could be meaningfully re-conducted to three galaxy groups:

- Type I: *SF disks with a red SF core*, characterized by the fact that all their regions are SF. Some have a complex multi-color clumpy disk morphology in the RGB (F115W, F200W, F444W) image. They all have a dust attenuated red SF core.
- Type II: *Quenched disks with a SF core*, characterized by a dust attenuated red SF core and a quenched disk (in one case, partially quenched).
- Type III: *SF disks with a quenched bulge*, characterized by a quenched central bulge while the disk is still star-forming. These are similar to local spirals.

For the disks with several components, they usually were all either SF of quiescent. There was only one galaxy (ID18278) where only a fraction of the disk was quiescent (green region in Figure 5.3), I decided to include it to the Type II as the quiescent part encompasses 16% of the disk stellar mass and could be considered as an early stage of quenching. 4 galaxies hosts X-ray AGNs that do not dominate the FIR emissions; 1 is a Type I galaxy (ID30186), 2 are Type II galaxies (ID13098 and ID13776) and the last one is a Type III galaxy (ID23205) (Nandra et al. 2015).

After having classified my sample of 22 galaxies, I had 10 Type I galaxies, 5 Type II and 7 Type III. The RGB cutouts of my sample are separated following the three Types, with Figures 5.2, 5.3 and 5.4 showing the Type I, II and III galaxies respectively. This is summarized in the top panel Figure 6.8 where each wedge size is proportional to the number of galaxies of the considered Type. I illustrate each Type with a pictogram, the color red representing quiescent regions and the color blue representing star-forming regions. The color of each wedge is linked to the Type, in all Figures in the rest of this manuscript, the red markers will represent Type I galaxies, green markers Type II and blue markers Type III. The lower panels of Figure 6.8 summarize the properties of each Types by looking at the connection between sSFR and A_V and color (in mag AB) gradients. The first observation is that cores/bulges are systematically redder than disks and there is a strong correlation between A_V gradient and color gradient (Pearson coefficient = 0.83, p-value = $2e{-6}$) while there is no correlation between sSFR gradient and color gradient (Pearson coefficient = 0.27, p-value = 0.23). This means that the color differences that I observe in Figures 5.2, 5.3 and 5.4 trace dust density in-homogeneities and not older/younger stellar population. The Type I galaxies (in red) do not have a noticeable sSFR gradient ($sSFR_{core} \sim 1.2 \times sSFR_{disk}$), but have a strong A_V gradient, hence, the fact that the cores of Type I galaxies appear much redder than the disks in Figure 5.2 is due to their high dust density; the blue regions are low A_V regions. For the Type II galaxies, I observe the sSFR gradient I expected, the core is star-forming while the disk is quenched ($sSFR_{core} \sim 6.5 \times sSFR_{disk}$), they have the strongest dust gradient because of their highly dust attenuated core and their quenched disk that has low level of dust attenuation. I note that the sSFR gradient should make the core appear bluer than the disk (because of the younger stellar population in the core), however I observe the exact opposite. The color gradients I observe in Figure 5.3 are dominated by the dust attenuation gradient. Eventually, Type III galaxies have low attenuation both in their quenched bulge and star-forming disk, hence have a weak A_V gradient. Their sSFR gradient is however strong, as expected of the opposite sign compared to Type II (quenched bulge and star-forming disk, $sSFR_{core} \sim 0.2 \times sSFR_{disk}$). In Figure 5.4 the color gradients mostly trace the age difference between the stellar populations of the (redder) bulge and the (bluer) disk.

I note that, the strong gradients I observe, both in sSFR and A_V justify the need to divide my galaxies in three Types to illustrate the three possible sSFR gradient and to divide them in several sub-galactic regions because of the huge dust gradient. Moreover, as expected by the selection criteria detailed in Section 5.2.3, I did not have any fully quiescent galaxy in my sample.

In this chapter, I detailed all the properties I decided to study to attempt to better understand DSFGs at Cosmic Noon. In the next chapter, I present the main results of this analysis.

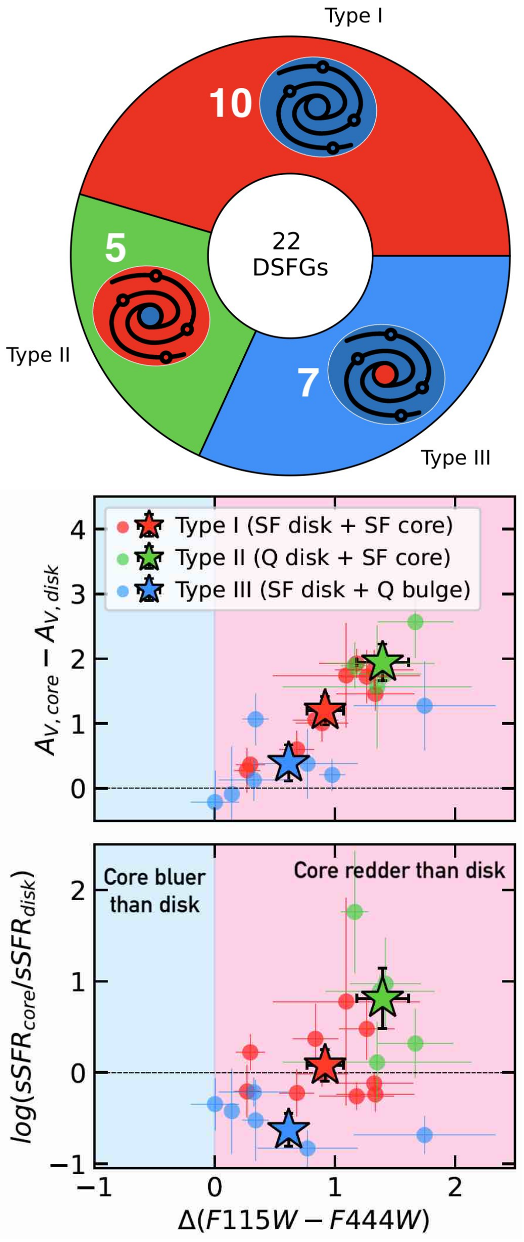

Figure 6.8: Upper panel: Distribution of the galaxy sample in the different groups based on their resolved SF activity. Each region size is proportional to the number of galaxies in the group, written in white. The pictograms illustrate the properties of each Type, the blue and red colors representing SF and quiescent regions respectively. I link each Type of galaxy to a color as defined by the wedges color. Middle panel: A_V gradient vs color gradient (in AB mag), red, green and blue markers are linked to the Types defined in the top panel. Lower panel: sSFR gradient vs color gradient (in AB mag), red, green and blue markers are linked to the same Types as in the middle panel. Circular markers are individual galaxies, star markers are the mean value for each Type of galaxy with their associated error bar indicating the error of the mean.

7 - PROPERTIES OF DSFGs AT COSMIC NOON

In this chapter, I present the results of the analysis of the 22 galaxies in my sample, distinguishing among the three classes I just defined in the previous Chapter. I first looked at the properties of the whole galaxies in Section 7.1 and then at the resolved properties at a sub-galactic level in Section 7.2. In Table 8.1, I give the main properties of my sample of 22 galaxies.

In the following, I compared the behaviour of the different Types of galaxies. To assess the significance of the trends, I compared the difference between the mean of a property for each Type with the error on the mean. I emphasis that I also checked the median value and that it doesn't affect the observed trends. In the Figures, each star-shaped marker is the mean and the error bar is the error of the mean (defined as $err_{mean} = rms/\sqrt{N}$ with rms the root mean square of the distribution and N the number of galaxy in each Type).

7.1 . GENERAL PROPERTIES

7.1.1 . MAIN SEQUENCE GALAXIES

To characterize the different Types of galaxies, I first looked at their typical redshift, M_* and $sSFR_{IR}$. The redshifts and M_* were extracted from the SED fitting procedure described in Section 6.6 while the $sSFR_{IR}$ was computed by dividing the SFR_{IR} of each galaxy by the sum of the M_* of each component with the SFR_{IR} taken from my super-deblended catalog.

In Figure 7.1, a redshift trend is appearing: the Type I galaxies with their SF core and SF disk are on average at higher redshift ($z = 2.32 \pm 0.15$) than the Type II galaxies with their SF core and quiescent disk ($z = 1.94 \pm 0.11$), that are themselves at a slightly higher redshift than the Type III galaxies ($z = 1.80 \pm 0.09$), analogs to the spiral galaxies I observe in the local universe with a quiescent bulge within a SF disk. The difference in redshift is 2σ between the Types I and II and 3σ between Type I and III. This suggests that this redshift trend is real and opens the possibility of an evolutionary link between class I and II/III.

All of my galaxies have a $M_* > 10^{10}$M$_\odot$ with an average of $M_* = 8.2^{+2.2}_{-1.7} \times 10^{10}M_\odot$ (left panel of Figure 7.1). There is no correlation between the Types and the M_*, all Types have a similar average M_*. By comparing the $sSFR_{IR}$ of my galaxies with the MS of Schreiber et al. (2015) (right panel of Figure 7.1), I confirmed that typically these galaxies are MS galaxies, consistently with Figure 5.1 and Section 5.2.3. The MS sSFR at a fixed redshift was calculated by taking the mean M_* of my sample which is $< M_* > = 10^{10.92}$M$_\odot$. Moreover, the typical $sSFR_{IR}$ is observed to decrease at lower redshift, as expected from the cosmic trend.

The Type III galaxies, which have a quenched bulge, have the weakest $sSFR_{IR}$ on average ($sSFR_{IR} = 0.75^{+0.18}_{-0.14}$Gyr^{-1} for quenched bulges versus $sSFR_{IR} = 2.01^{+0.81}_{-0.56}$Gyr^{-1} for SF cores). They also are at lower redshift than the others. This suggests that they are more evolved than other classes.

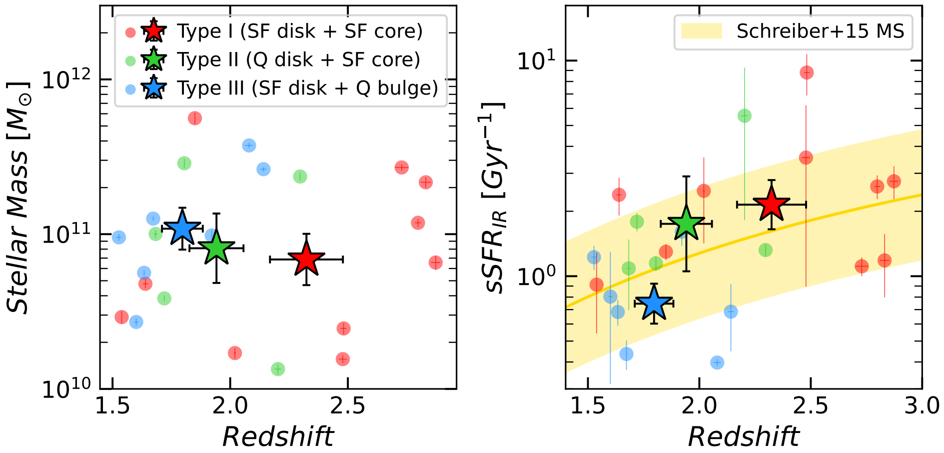

Figure 7.1: Left panel: M_* versus redshift. Right panel: $sSFR_{IR}$ versus redshift, the yellow shaded region is the MS (Leslie et al. 2020; Huang et al. 2023). I show the error-bars for individual galaxies, when not visible, they are smaller than the marker. Circular markers are individual galaxies, star markers are the mean value for each Type of galaxy with their associated error bar indicating the error of the mean.

7.1.2 . GALAXY NEAR-IR SIZES

The presence of highly obscured cores at the center of galaxies, like for ID15371 (see Figure 6.1), can let us believe that I am studying the counterparts of the *ALMA* compact SF SMGs. Indeed, SMGs are known to be compact, dust obscured and with a high star formation efficiency.

The galaxies hosting a SF region at their center (Type I and II) tend to be slightly more compact in the near-IR, with $R_{e,NIR} = 2.34 \pm 0.37$kpc, than the galaxies with a quenched bulge (Type III), with $R_{e,NIR} = 2.93 \pm 0.42$kpc (this is tentative as there only is a 1σ difference, see Figure 7.2). The Type II galaxies and their quiescent disk are on average the most compact galaxies in the near-IR with a typical size of 2.19 ± 0.30kpc.

In Figure 7.2, I compare the $R_{e,NIR}$ to the $M_* - R_e$ relation from van der Wel et al. (2014) based on rest-frame optical measurements. Most of my 22 galaxies are more compact in the near-IR than in the optical, with $\sim 40\%$ being below the $M_* - R_e$ relation scatter. I also checked that the optical sizes of my galaxies are compatible with the $M_* - R_e$ relation. This demonstrates than in my galaxies, the dust, traced by the near-IR emissions, is more concentrated than the stellar light, traced by the optical emissions. This is a confirmation of an already well established fact (van der Wel et al. 2023; Gómez-Guijarro et al. 2022a; Jiménez-Andrade et al. 2021; Puglisi et al. 2019; Jiménez-Andrade et al. 2019; Fujimoto et al. 2017).

However, I note that the Type I galaxies have very comparable optical and near-IR sizes ($\sim 15\%$ difference in size on average), their star-forming core is not as concentrated as for the other galaxies of the sample.

I discuss in Section 8.4 how the Type I and II galaxies might relate to the *ALMA* SMGs.

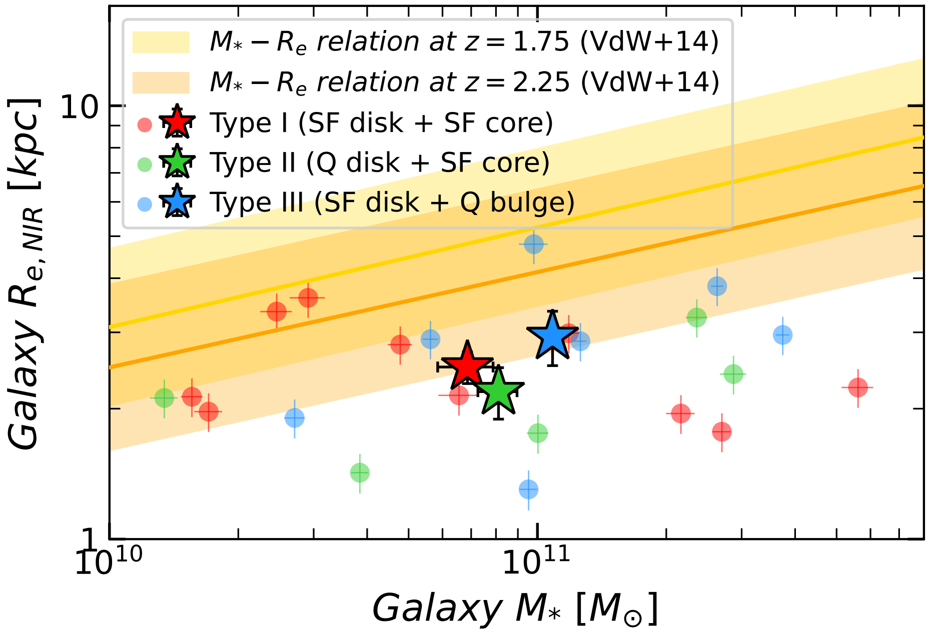

Figure 7.2: Optical ($R_{e,O}$, left panel) and near-IR ($R_{e,NIR}$, right panel) half-light radius measured in the closest band to 550nm and 1.6μm rest-frame respectively versus the total M_* of the galaxy. Circular markers are individual galaxies, star markers are the mean value for each Type of galaxy with their associated error bar indicating the error of the mean. The yellow and orange shaded regions illustrate the Mass-Size relation derived by van der Wel et al. (2014) at the redshift of my sample.

However, studying the half-light radius is not enough as a large fraction of the galaxies in my sample are not symmetric (see Figures 5.2, 5.3 and 5.4).

7.1.3 . WIDESPREAD LOPSIDEDNESS

As one can see in Figures 5.2, 5.3 and 5.4, some galaxies are strongly lopsided (marked with a circled L). They are asymmetric and/or their red central region is off-centered with respect to the disk. This lopsidedness appears to be quite common among Type I and II galaxies. In Figures 5.2, 5.3 and 5.4, the marked galaxies are the 6 most lopsided galaxies, 3 are Type I (30% of the sample) and 3 are Type II (60% of the sample). The Type III galaxies look much more symmetric, these galaxies have a quenched bulge and are on average at lower redshift, they had presumably more time to evolve and stabilize their disk. To verify this, I investigate the lopsidedness of each galaxy.

As explained in Section 6.3, for each galaxy I calculated its asymmetry (A) and eccentricity (E). Type III galaxies appear to be much less lopsided, they have a low eccentricity ($9.8 \pm 2.5\%$) and asymmetry ($22.8 \pm 3.0\%$) while Type I and II galaxies, which show comparable lopsidedness, tend to be much more asymmetric ($33.0 \pm 3.5\%$) and off-centered ($30.3 \pm 4.0\%$) (see upper panel of Figure 7.3). The difference has a 4.3σ and 2.2σ significance for the eccentricity and asymmetry respectively. In the upper panel of Figure 7.3, I show the eccentricity vs the asymmetry. I considered the Type III galaxies as not lopsided, and used their typical eccentricity and asymmetry as a proxy for measurement errors and systematic effects. The thin black dotted line shows the threshold to define a galaxy as weakly lopsided ($A+E > 0.37$, this value corresponds to the average $[A+E]+1\sigma$ of Type III galaxies). I have 14 galaxies that are at least weakly lopsided, representing 64% of the sample. If the galaxies are above the thick black dashed line, meaning that $A + E > 0.70$ (this value corresponds to the average $2 \times [A + E] + 1\sigma$ of Type III galaxies), I consider them as strongly lopsided, I encircled them in Figure 7.3 and they are visible in Figures 5.2, 5.3 and 5.4 with a circled L. I have 6 strongly lopsided galaxies, representing 27% of the sample. Usually, a strong asymmetry is linked to a strong eccentricity, however I have galaxies with a low level of asymmetry but with a highly off-centered disk. All the strongly lopsided galaxies (circled in black) have high eccentricity. In other words, I observe a lack of strong asymmetry with low eccentricity.

The position of the average lopsidedness of Type I and II galaxies in Figure 7.3, indicates that being lopsided might be a typical property of these galaxies.

In the lower panels of Figure 7.3, Type III galaxies, which are more evolved and have a quiescent bulge have low level of asymmetry. On the contrary, Type I and II galaxies have a higher level of asymmetry. I observe (1) a lack of galaxies with a compact disk and high asymmetry and vice-versa, (2) a lack of galaxies with a high core mass fraction and high asymmetry and vice-versa and (3) the galaxies with a quiescent bulge with high mass fraction have low asymmetry. This is consistent with the observation of galaxies in the local universe, indeed, present-day late-type galaxies with more extended disks and lower central stellar mass density are typically more lopsided than early-type galaxies with smaller disks and higher central stellar mass density (Dolfi et al. 2023; Varela-Lavin et al. 2023). It seems that as the core grows in mass from accretion, the disk gets smaller and loses its lopsidedness, leading to Type I spiral-like galaxies.

Thanks to the spatial resolution of *JWST*, I had access to sub-galactic scales, which is crucial to understand the morphology and evolution of DSFGs.

7.2 . RESOLVED PROPERTIES

For each galaxy, each component has been classified either as star-forming or quiescent (see Section 6.7). In Figure 7.4, I show that the quiescent regions are massive ($M_* \gtrsim 10^{10} M_\odot$) and have a relatively low dust attenuation with an average of $A_V \sim 1.6$ and maximum at $A_V \sim 3$ while SF regions have an average of $A_V \sim 2.3$ maximum at $A_V \sim 5.4$. The SF regions follow a correlation (with a Pearson coefficient of 0.62, p-value = $9e-8$), the more massive components are more attenuated. This is consistent with the idea that the stellar mass is the main driver of dust attenuation in SF galaxies (Lorenz et al. 2023).

In the following Sections, I present the results regarding the core/bulge and disk of my galaxies.

7.2.1 . CORES AND BULGES PROPERTIES

I first looked at the red central region of each galaxy, as defined in Figures 5.2, 5.3 and 5.4. In the left panel of Figure 7.5, I show the dust attenuation versus the M_* of the red star-forming cores (in red and green) and quiescent bulges (in blue). As mentioned above, the dust attenuation of SF cores (Type I and II) correlates with its M_*: the more massive the core, the more dust attenuated (with a Pearson coefficient of 0.75, p-value = 0.001). Also, the bulges are less attenuated than SF cores, consistent with the fact that they are quiescent and host an evolved stellar population where the dust might have been consumed/destroyed.

Figure 7.5 also shows a trend in redshift. On average, the bulges are slightly more massive (M_*^B) than the SF cores (M_*^C) but with only a 1.5σ significance. The SF cores of Type II galaxies (M_*^{II}) and those of Type I galaxies (M_*^I) are consistent within errors.

$$M_*^B = 3.75^{+1.04}_{-0.81} \times 10^{10} M_\odot \gtrsim M_*^C = 1.81^{+1.19}_{-0.65} \times 10^{10} M_\odot \tag{7.1}$$

$$M_*^{II} = 2.60^{+2.19}_{-1.19} \times 10^{10} M_\odot \approx M_*^I = 1.26^{+0.92}_{-0.53} \times 10^{10} M_\odot \tag{7.2}$$

The weak trend between the M_* of higher-*z* SF cores and lower-*z* bulges is consistent with the idea of a bulge that grows in mass with time, fed by accretion from the disk, clump migration or minor/major mergers.

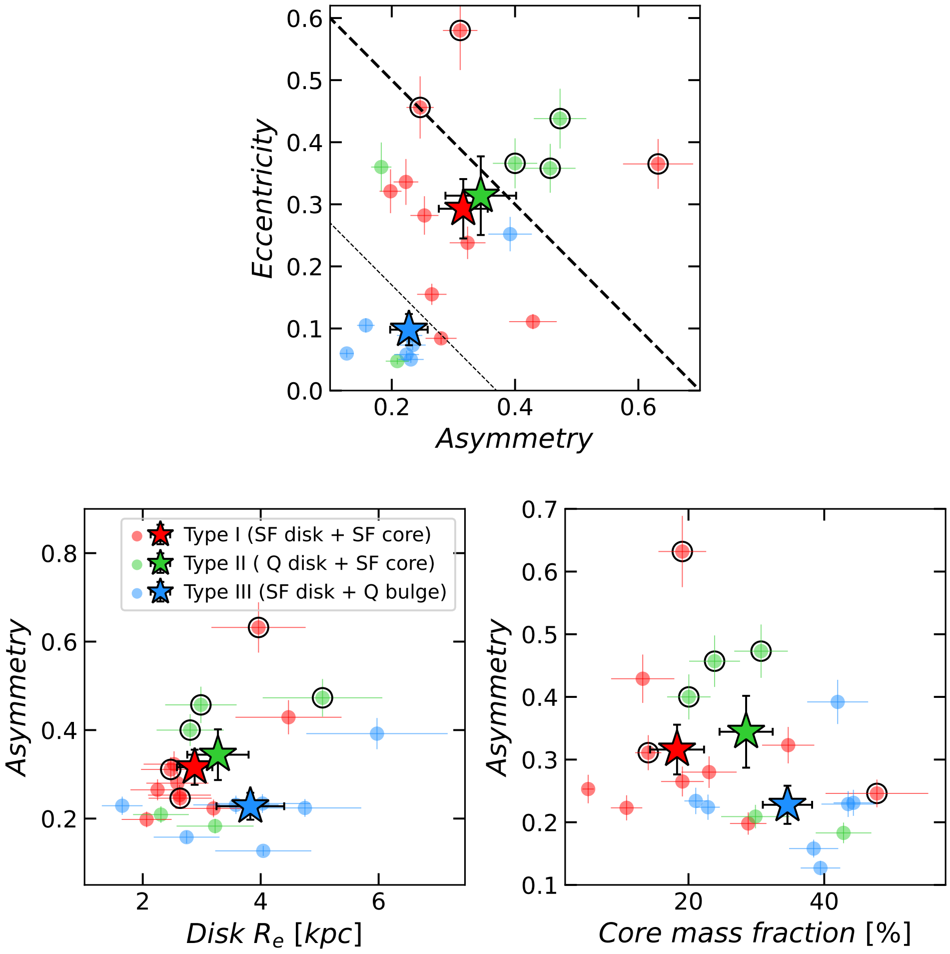

Figure 7.3: Eccentricity and Asymmetry. Upper panel: Eccentricity versus Asymmetry, markers with a black circle are the strongly lopsided galaxies (see Figures 5.2, 5.3 and 5.4), thin black dotted line delimits weakly lopsided galaxies, thick black dashed line delimits strongly lopsided galaxies. Lower left panel: Asymmetry versus Disk half-light radius as defined in Section 6.3. Lower right panel: Asymmetry versus mass fraction in the core/bulge of the galaxy, asymmetry is calculated using the F444W filter. Circular markers are individual galaxies, star markers are the mean value for each Type of galaxy with their associated error bar indicating the error of the mean.

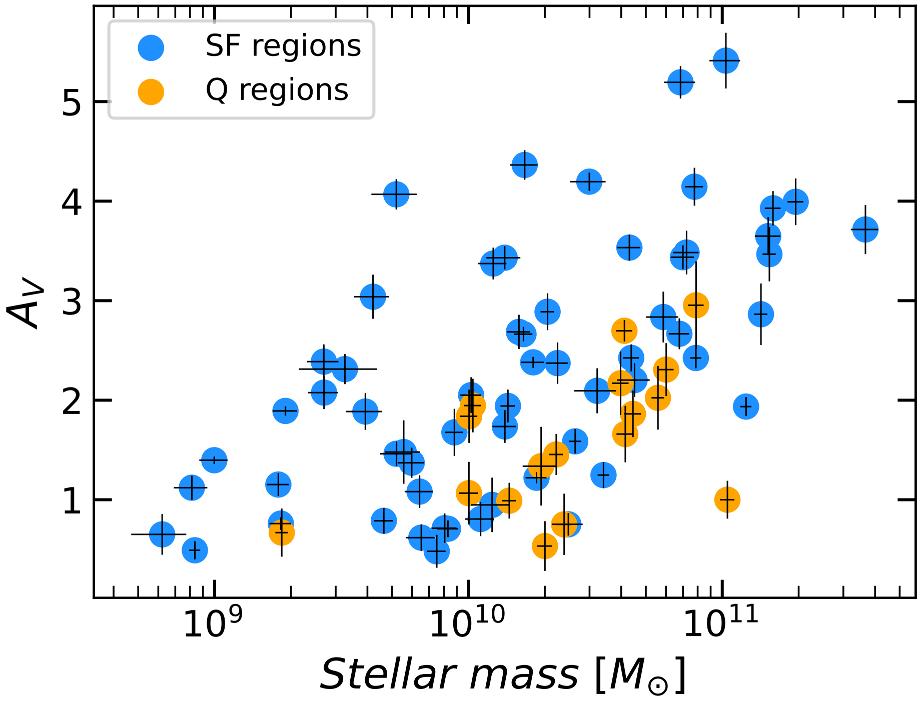

Figure 7.4: A_V versus M_* for each regions identified in Figures 5.2, 5.3 and 5.4. Quiescent regions are in orange and Star-forming regions in blue. At fixed stellar mass, star-forming regions are more attenuated, on average.

I compared the M_* and SFR fraction of the red cores and bulges with respect to the host galaxy (right panel of Figure 7.5). For Type I galaxies, the red core M_* represents only $21.6 \pm 4.0\%$ of the M_* of the galaxy. This fraction is smaller than for the other galaxies of the sample where the red core represent $34.4 \pm 6.2\%$ for Type II ($\sim 2\sigma$ difference) and $35.9 \pm 3.6\%$ for Type III ($\sim 3\sigma$ difference) of their total M_*. This can be linked to the redshift trend, the Type I galaxies being at higher redshift, their core could still be at an early stage of growth. It also explains their lowest $R_{e,IR}/R_{e,O} = 0.89 \pm 0.14$, as their M_* is much less concentrated in the central region that the other two Types.

As expected from the definition of my Types of galaxies, the Type II galaxies have a red core with a SFR fraction $(64 \pm 18\%)$ significantly greater than the M_* fraction $(34.4 \pm 6.2\%)$ since the disk is mostly quenched, while the Type III galaxies have a red bulge M_* fraction $(35.9 \pm 3.6\%)$ significantly more important than the SFR fraction $(9.8 \pm 3.4\%)$ as the bulge is quenched.

Some of these cores/bulges appeared to be compact, I decided to investigate them further in the next Section.

7.2.2 . COMPACT CORES AND BULGES

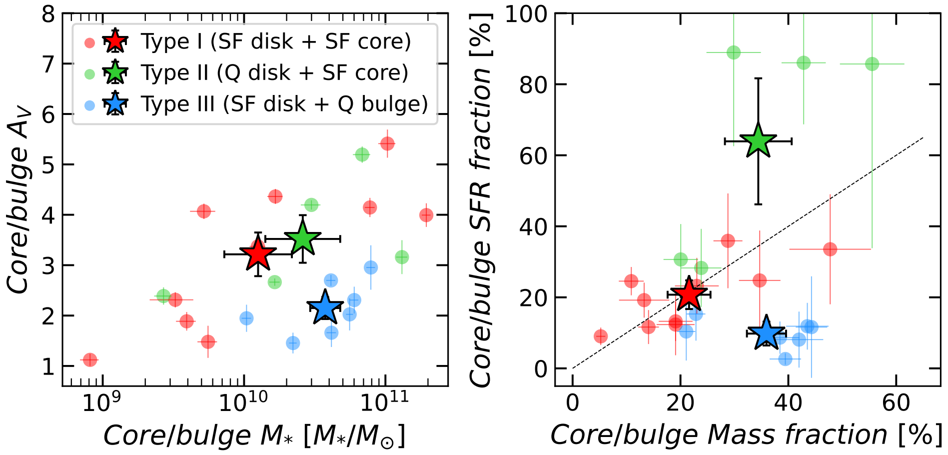

Figure 7.5: Red regions properties. Left panel: Dust attenuation versus Stellar Mass. Right panel: SFR fraction versus M_* fraction in the red region. The black dotted lines is the $1{:}1$ correlation. Circular markers are individual galaxies, star markers are the mean value for each Type of galaxy with their associated error bar indicating the error of the mean.

All of my galaxies have a central core/bulge appearing in the near-IR (filter F410M or F444W). For some galaxies, the core/bulge has a clear clump-like morphology, is much brighter than the surroundings and is clearly delimited (e.g. ID13776 and ID23205 in Figure 7.6). I identified compact cores in 17 galaxies out of 22: 6 Type I galaxies with a compact core (60% of my sample), 4 Type II (80% of my sample) and all 7 Type III galaxies of my sample have a compact bulge. I decided to investigate further these compact cores/bulges by dividing the in two categories, the SF cores (from Type I and II) and the quiescent bulges (from Type III).

To do so, I measured the half-light radius of the compact cores and bulges defined as the radius of a circular aperture encompassing half of the flux of the core, I applied a similar technique as described in Section 6.1. The SF cores tend to be slightly more compact than the quiescent bulges (0.76 ± 0.03kpc vs 0.84 ± 0.04kpc, with a $\sim 1.5\sigma$ significance, see Figure 7.7). The markers with a black circle are the compact core with an X-ray detection, possibly tracing an AGN. 3 of them are found in SF cores, and 2 are in the most massive galaxies with the largest SF cores. Even if the definition of the compact core is somehow arbitrary, and that there could be some level of contamination from the disk, this goes in the same direction as Cochrane et al. (2023) simulations. They found that without AGN feedback, the SF core would undergo a compaction event while the presence of AGN winds would prevent such compaction by evacuating the gas and precipitate the quenching of the core.

I also note that the quiescent bulge tends to be larger in more massive

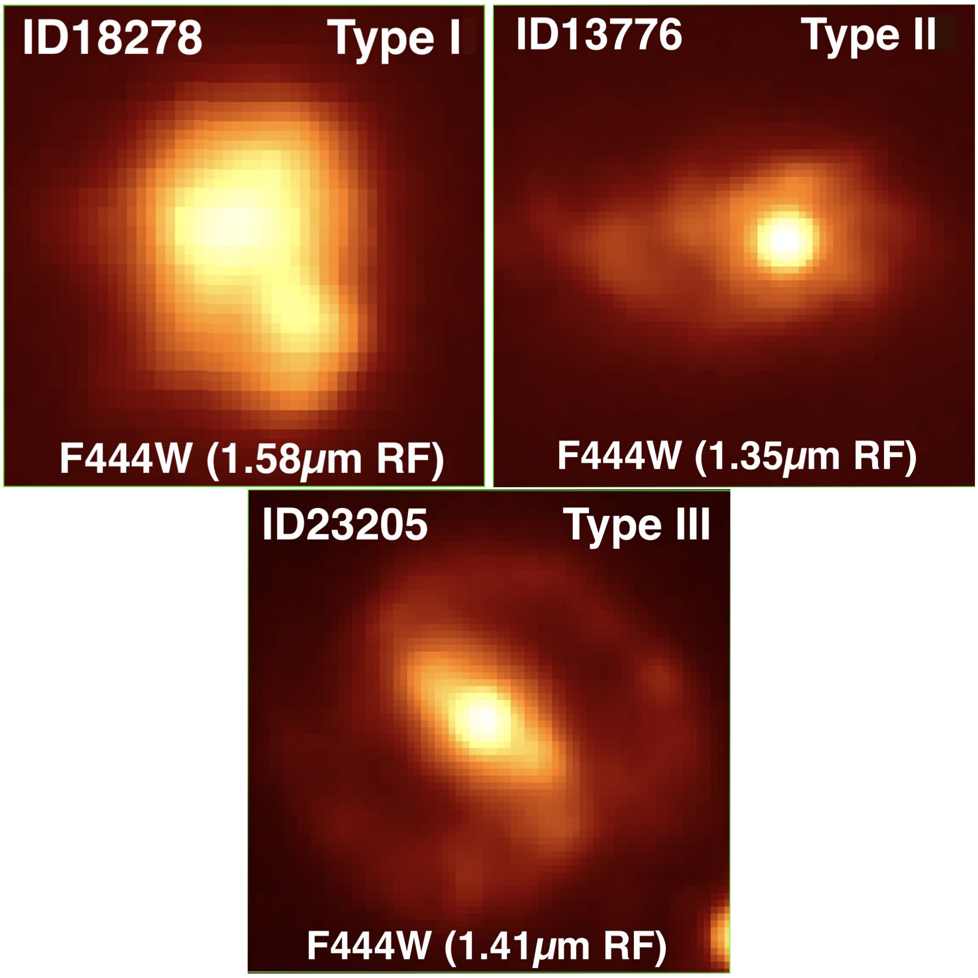

Figure 7.6: Cutouts of a galaxy of each Type with the F444W filter. While a central clump-like core is clearly apparent for the ID13776 and ID23205, it is less clear in ID18278. I indicate the rest-frame central wavelength of the filter in parenthesis.

galaxies. Ikarashi et al. (2017) found that the most compact cores of SMGs are those where there is both star formation and an AGN. This is not what I observe for two of the SF cores hosting an X-ray AGN (showed with the encircled markers in Figure 7.7), it is possible that in these galaxies the AGN has strong feedback and the system is quite evolved and ready to quench. The third SF core hosting an X-ray AGN is however compact and the presence of the AGN could facilitate this compaction.

The sizes of the SF compact cores are compatible with those measured in the sub-mm (See Section 8.4 for more details).

After analyzing the cores of my galaxies, I decided to investigate their differences with respect to the disk, especially the reasons of the redness of the

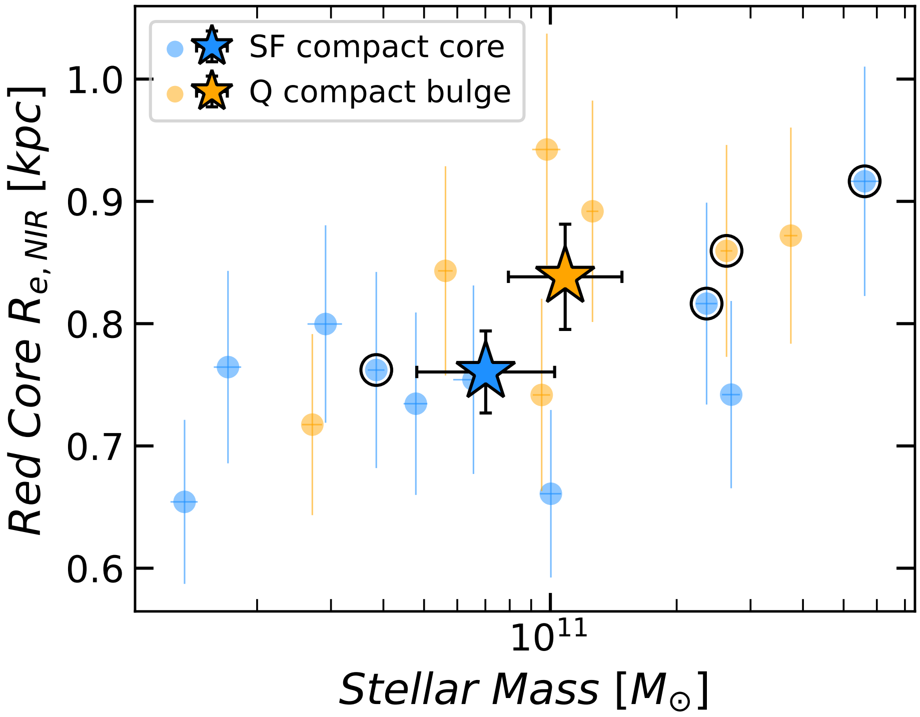

Figure 7.7: Compact red cores and bulges half-light radius versus the stellar mass of the galaxy. Circular markers are individual galaxies, star markers are the mean value for each group of galaxy with their associated error bar indicating the error of the mean. Markers with a black circle are cores hosting an X-ray AGN (Nandra et al. 2015).

core compared to the surroundings.

7.2.3 . NIRCAM COLOR VARIATIONS WITHIN THE DISK

In Section 6.7, I showed that the main driver of the color gradient between the cores and disks is the dust attenuation.

When looking at Figures 5.2, 5.3 and 5.4 I noticed that some disks are also highly in-homogeneous in terms of color. To investigate the physical processes responsible for the color variations I observed in the disks, I compared the color variations with the dust attenuation and sSFR variations in a similar way I did in Section 6.7 when I investigated the gradients between the cores and the disks. When measuring the variations, I always measured the differences between a redder part of the disk and a bluer part (in other words $\Delta(F115W - F444W) > 0$ in AB mag). I compared all the components of the disks, meaning that if a disk was divided in 3 patches, there are 3 markers in Figure 7.8 comparing the first and second, second and third and first and third component respectively. In the two upper panels of Figure 7.8, I first clearly identify a correlation between the color variations and the dust extinction variations (Pearson coefficient = 0.78, p-value = $6e-11$) consistent with the expectation that the redder regions are those with the greatest A_V (Calzetti et al. 2000). However, I do not identify any correlation between color variations and sSFR variations (Pearson coefficient = 0.16, p-value = 0.29), some color variations are even inconsistent as when $sSFR_{redder} > sSFR_{bluer}$, I am comparing a red patch hosting a younger stellar population (more star-forming) with a bluer patch hosting an older stellar population (less star-forming), hence the colors should be the other way around. This two observations demonstrate that the color variations I observe within the disks in Figures 5.2, 5.3 and 5.4 are driven by dust. NIRCam colors at $z \sim 2$ trace dust, red spots are highly extinct while blue spots are weakly dust attenuated. This is consistent with previous studies based on NIRCam images (e.g. Miller et al. (2022)) .

As the clumps could play an important role in the color variations, it is important to investigate their abundance.

7.2.4 . CLUMPY DISKS

As one can see in Figures 5.2, 5.3 and 5.4, some galaxies are very clumpy. The clumpiness does not seem to be linked to a particular Type of galaxy. Most of the clumps are observed in the shortest wavelength, consistent with Wuyts et al. (2012) who state that the number of clumps decrease when moving toward longer wavelength. In Figure 7.9, I investigate the the possible link between the clumpiness and the disk and the core of the galaxy. In the left panel,I show the distribution of the number of clumps observed in each disk versus the SFR of the disk (defined as the sum of the SFR of the regions delimited in Figures 5.2, 5.3 and 5.4) separating the SF disks from the quiescent disks. There is no apparent correlation between the star-forming activity of the disk and the number of clumps. The fact that I observe clumps in quiescent disks is quite surprising as they usually are supposed to be place of local starburst (Wuyts et al. 2012). I discuss the implication of this result in Section 8.3.

In the left panel of Figure 7.9, I study the impact of the fraction of stellar mass in the core (in blue) or bulge (in red) on the number of clumps. The galaxies with a quiescent bulge, that I know to be at lower redshifts (see Section 7.1.1 and Figure 7.1), have a higher fraction of their mass in their bulge ($35.9\% \pm 3.6\%$) than the galaxies with a star-forming core have in their core ($25.8\% \pm 3.7\%$) with a $\sim 2\sigma$ significance. They also tend to have a smaller number of clump: 1.7 ± 0.8 clumps on average for a galaxy with a bulge and 2.8 ± 0.6 clumps on average for a galaxy with a star-forming core (1.1σ significance). The plot also shows that by looking at galaxies with a star-forming core (in blue in Figure 7.9), the ones with the smallest M_* fraction at their core are also the clumpiest. I see here both the effects of the redshift, lower red-

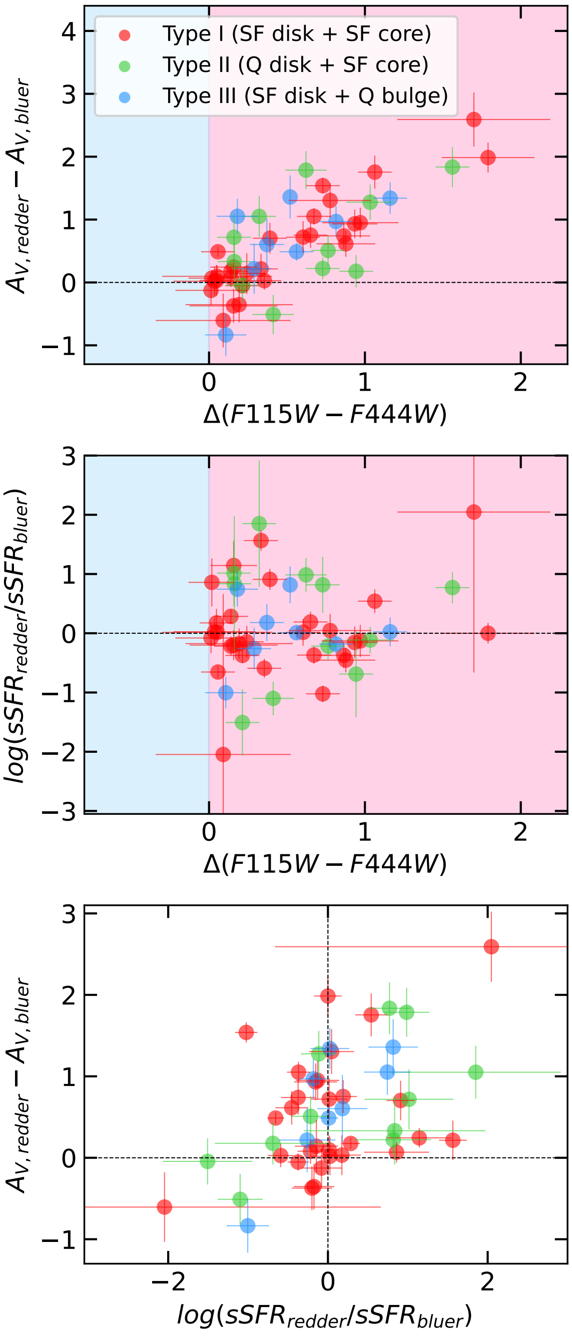

Figure 7.8: Top panel: Comparison between the A_V and the F115W - F44W AB mag color between redder and bluer patches within the disks (if the disk has been divided in at least two components in Section 6.5). Middle panel: Comparison between the sSFR and the F115W - F44W AB mag color between redder and bluer patches within the disks. Lower panel: Comparison between the A_V and the sSFR between redder and bluer patches within the disks. Only variations are probed, not gradients, I do not look for radial effects has my galaxies have highly asymmetrical disks.

shift galaxies have less clumps and of the central M_* fraction, higher fraction leads to less clumps.

One could argue that the fact that galaxies with a star-forming core are at higher redshift than those with a quiescent bulge (Type III) means that I probe shorter rest-frame wavelength, hence, I have a higher probability of observing clumps in their disk (Wuyts et al. 2012). However, the range of redshift that I am probing here is quite narrow, and the clumps that I count are the brightest and visible in several filters. These galaxies actually are clumpier.

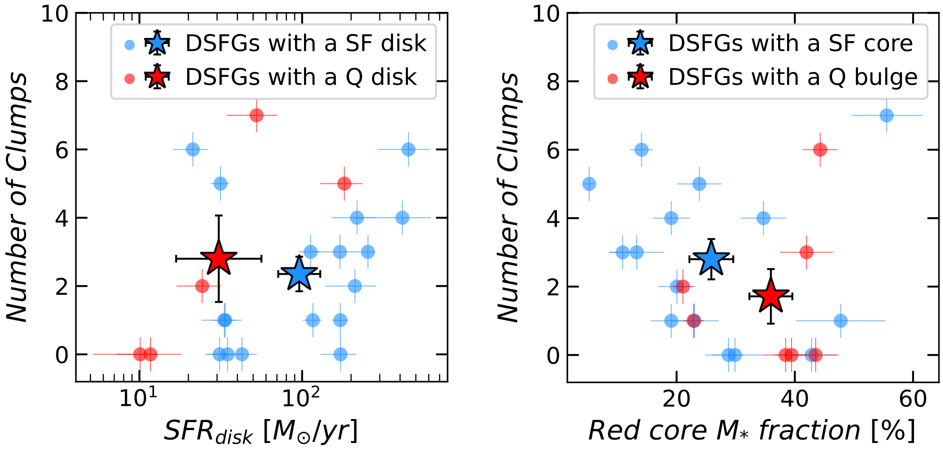

Figure 7.9: Number of clumps in the disk versus its SFR. Circular markers are individual galaxies, star markers are the mean value for each Type of galaxy with their associated error bar indicating the error of the mean.

In this chapter, I presented the results of my analysis of DSFGs at Cosmic Noon. These interesting results raised some important scientific questions that I decided to address in the next chapter.

8 - ON THE EVOLUTION OF DSFGs AT COSMIC NOON

In this Chapter, I first discuss the green patches/clump that are visible in the RGB cutouts in Figures 5.2, 5.3 and 5.4 in Section 8.1. Then, I discuss the presence of blue clumps inside quiescent disks in Section 8.3. I investigate the possible link between the compact SMGs observed with *ALMA* and my DSFGs in Section 8.4. In Section 8.6, I discuss the origin and consequences of lopsidedness and its abundance. Eventually, in Section 8.7, I discuss two possible evolutionary paths that could lead to the formation of Type II galaxies.

8.1 . BRIGHT EMISSION LINES

When looking at Figures 5.2, 5.3 and 5.4, one can notice that some of the disks have different colors, with a blue and a green part. The green clumps/patches are visible in all Types of galaxies. Considering their redshift, they probably are due to bright H_α or $[O_{III}]$ emission lines which are known tracer of star-formation. The H_α line will fall in the green filter (F200W) for galaxies with a redshift between 1.67 and 2.39 and the $[O_{III}]$ emission line will fall in the green filter for galaxies with a redshift between 2.52 and 3.47. On the 7 galaxies where I identify green patches, 2 are consistent with H_α emission from a star-forming region (ID15371 and ID29608) and 3 are consistent with $[O_{III}]$ emission from a star-forming region (ID18694, ID23510 and ID23581). For the 2 remaining galaxies, it is more surprising, as the green patches/clump are observed in the quiescent disks of Type II galaxies.

For the ID13107 galaxy ($z = 2.21 \pm 0.02$), the green patch is close to the center of the galaxy, it is then possible that the H_α line is produced by the accretion disk of an AGN sitting at the center of the galaxy that becomes bright in this region because of a much weaker dust attenuation than in the core. Even though I have no radio or X-ray signature of an AGN in this galaxy, as mentioned before, the predicted SFR from the SED fitting is not enough to explain the FIR flux density observed with *Herschel* for this galaxy. This convinced us that there could be an AGN at the core of this galaxy.

For the ID18278 galaxy ($z = 1.805$), the situation is different, the green patch is in the outer region and composed of clumps. These clumps could have actually been ionized by the hot evolved low-mass stars (Cid Fernandes et al. 2011; Belli et al. 2017) with an enhanced H_α line due to shocks from the minor merger. Indeed, these clumps are old (age of oldest stars $= 2.5 \pm 0.5 Gyr$) and have a very low sSFR, consistent with the *ex-situ* clumps defined in Mandelker et al. (2014).

8.2 . ORIGIN OF DUSTY PATCHES WITHIN DISKS

In Section 6.7, I demonstrated that the color gradient is linked to the strong A_V gradient. The fact that the core is much more attenuated than the disk is expected because the SFR surface density is higher in the core than the disk, hence is the dust surface density and the dust column density.

However, the patchy distribution of dust within the disks is more surprising. From the lower panel of Figure 7.8, I observe a correlation between dust density and sSFR for Type II and Type III galaxies (Pearson coefficient = 0.62 and 0.83 with p-value = 0.04 and 0.01 respectively). Meaning that for these galaxies, the patches could be linked to not yet quenched regions in the disks of Type II galaxies and partly quenching disk for Type III. The patches could then find their origin in internal instabilities, or interactions with the local environment. For Type I galaxies, I do not observe this correlation (Pearson coefficient = 0.35, p-value = 0.07). For these galaxies, the patches could be correlated either to metallicity, higher metallicity leading to higher dust column, or to geometry.

I investigated the origins of the patchy distribution by looking for correlations between the greatest difference in A_V in each disk and the redshift, the fraction of stellar mass in the core/bulge, the fraction of SFR in the core/bulge, the lopsidedness and the environment. I found no correlation (all p-value > 0.2). I then looked for a correlation between the number of patches/components of each disk (as defined in Figures 5.2, 5.3 and 5.4) and the same parameters. The only correlation I found, that is visible in Figure 8.1, is with the mass fraction in the core (Pearson coefficient of -0.60, p-value = 0.003), the number of patches/components gets smaller when the mass is more concentrated in the core of the galaxy. This is especially true for the galaxies with a star-forming core (Type I and II, with a Pearson coefficient of -0.67 and a p-value of 0.006, while Type III have a Pearson coefficient of 0.14 with p-value of 0.76). This correlation is expected from Hopkins et al. (2023); when the central gravitational potential well is deep enough, it stabilizes and homogenizes the disk. This correlation is consistent with the one I observed for the clumps (See Section 7.2.4 and Figure 7.9). However, if this (anti-)correlation justify why I do not see patches in Type III galaxies, it doesn't clear up the mystery of their origin.

I would need spectroscopy to understand better what is happening in those disks, and even there the mystery would remain of why the disks are so in-homogeneous in dust attenuation, whether it is due to metallicity or geometry differences (and why these would persist over homogeneous patches within a disk, as opposed e.g. to simple radial gradients).

8.3 . CLUMPS IN DSFGs

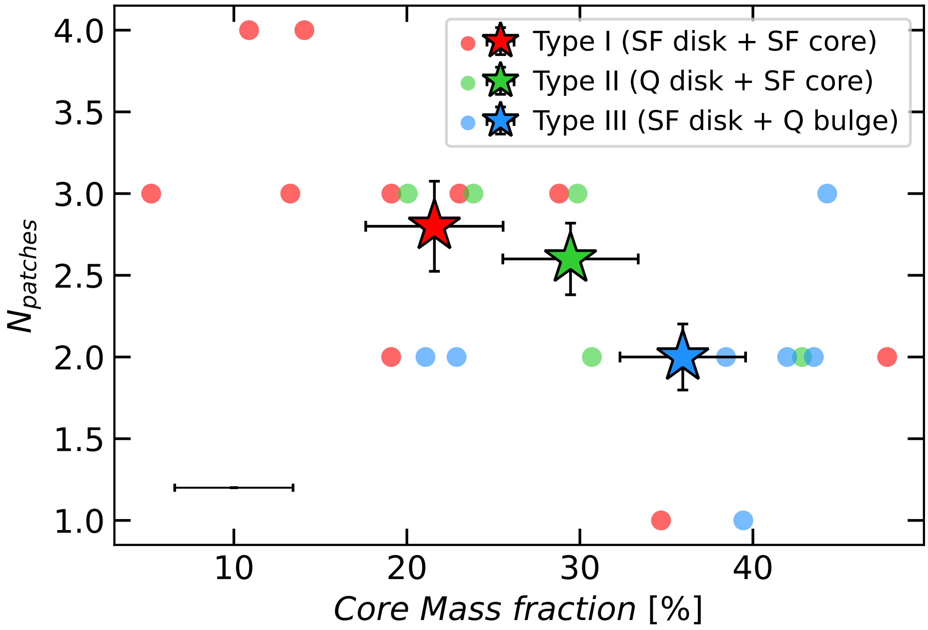

Figure 8.1: Number of patches/component of each disk versus the stellar mass fraction in the core/bulge. In the lower left corner, I show the average error bar for individual galaxies. Circular markers are individual galaxies, star markers are the mean value for each Type of galaxy with their associated error bar indicating the error of the mean.

In all the Types of galaxies, I identified the presence of clumps. I observed that galaxies at lower redshift tend to have less clumps, this suggests that the clumps either get destroyed within the disk and are not replaced by new clumps, or migrate toward the core and participate to its mass growth possibly triggering enhanced star formation. They might also be lower mass/less luminous, hence below my detection threshold. I do not see any evidence of recent major mergers in my galaxies, suggesting that most of the clumps I observe are originating from a fragmentation of a gas rich unstable SF disk, consistently with Puschnig et al. (2023) and Fensch & Bournaud (2021) that showed that large scale instabilities in gas-rich galaxies can create such star-forming giant molecular clumps.

I also noted that the most clumpy high-redshift galaxies also have the least concentrated cores, with less than 20% of their stellar mass at the center of the galaxy (see Figure 7.9) and, on the contrary, the least clumpy galaxies at lower redshift have nearly 40% of their stellar mass in the quiescent bulge. I also showed in Figure 7.5 that galaxies at later times have higher core mass fractions. This suggests that either, as the clumps migrate through the disk, they feed the central core, making it grow in mass or that, as the central gravitational potential well gets deeper, the disk is stabilized, the VDI are destroyed, and the galaxy can have a smoother spiral-like disk. My observation are consistent with the simulations from Hopkins et al. (2023) that showed a well defined dynamical center is necessary to stabilize the disk and put an end to bursty star-formation. Also, my results are in agreement with the new JWST results from Kalita et al. (2022), pointing to an increased galaxy fragmentation with decreasing bulge/core mass fraction.

When looking at Figure 5.3, one can clearly identify clumps in the Type II galaxies. The blue clumps of these quiescent disks (ID13107, ID18278 and ID13776 in Figure 5.3) are due to a low dust attenuation and not a high sSFR. Indeed, the disk has $A_V = 1.0{\pm}0.2$ while the central SF core has $A_V = 3.5{\pm}0.2$. I recall that the blue colors in NIRCam color cutouts for these redshifts are typically a signature of low dust attenuation. This could indicate that clumps are not only formed in highly star-forming regions.

8.4 . AM I OBSERVING COMPACT SMGs COUNTERPARTS ?

In most of my IR-luminous galaxies, a central compact clump-like highly dust attenuated SF red core is present. While it is nearly invisible in the optical rest-frame, it becomes bright in the near-IR (see Figures 6.1 and 7.6). As I showed in Section 7.2.3, they are surrounded either by a SF (Type I) or a quiescent (Type II) disk with much lower dust attenuation. I identify 10 of those (see Table 8.1 and Section 7.2.2) in my sample.

When I measured the size of these red compact SF cores, I found that the average $R_{e,NIR}$ was about 0.76kpc (Figure 7.7). This size is compatible with the sizes measured with *ALMA* for the compact SMGs : 0.6 ± 0.2kpc in Zavala et al. (2022), ~ 0.73kpc in Gómez-Guijarro et al. (2022b) or $1-2$kpc across in Rujopakarn et al. (2019). The NIRCam sizes tend to be slightly larger than the *ALMA* sizes, this is not due to a spatial resolution issue, but to the heavy dust obscuration of the core.

Moreover, compact SMGs at $z \sim 2-3$ are characterized by a SFR ≥ 100M$_\odot$ yr^{-1} (Gómez-Guijarro et al. 2022b; Jiménez-Andrade et al. 2021, 2019; Hodge et al. 2019). 7 out of the 10 galaxies where I identified a compact star-forming core have a total SFR compatible with this criteria (see Table 8.1). 5 of them having SFR $\gtrsim 100$M$_\odot$ yr^{-1} in the core alone, 1 has SFR ≥ 50M$_\odot$ yr^{-1} in the core and the remaining galaxy has a lower SFR in their core.

To confirm the possibility of SMGs counterpart, I can use my FIR super-deblended catalog in the EGS. 6 out of the 10 galaxies are detected at 2σ in SCUBA2/850μm among which 3 are 3σ detected. 3 out of the 4 undetected galaxies at 850μm are in the shallower part of the FIR catalog. Moreover, if I look at the predicted flux at 1.1mm for these galaxies, the mean predicted flux is 0.80mJy, and 4 of them are predicted to be brighter than 1mJy at 1.1mm. A total of 5 galaxies have either a 3σ detection in SCUBA2/850μm or a prediction > 1.1mJy at 1.1mm (ID13776 and ID21190 from the Type II class and ID16544, ID29608 and ID30186 from the Type I class). They correspond to the 5 galaxies measured with a SFR$\gtrsim 100$M$_\odot$ yr^{-1} in their core.

All these elements convinced us that I have at least 5 or 6 galaxies that are good candidates of compact SMGs counterparts, they are equally distributed between Type I and II.

Contrary to what is observed with *ALMA*, these compact cores are not isolated, they all are surrounded by a larger disk. The fact that their is a huge dust gradient between the core and the disk, as I showed in Section 6.7 might explain why I do not this the latter in sub-mm surveys: the core is bright in the rest-frame near-IR while the disk is bright in the rest-frame optical. The presence of a disk confirms Hodge et al. (2019) and Puglisi et al. (2019) who both stated that the compact SMGs are obscured part of a larger system.

The fact that some galaxies in my sample have highly extinct cores could link them the so-called *HST*-dark galaxies. I compared my sample with the *HST*-dark and *HST*-faint galaxies in the same field from Pérez-González et al. (2023). My galaxies are in general agreement with the SFG at $z < 4$ in Pérez-González et al. (2023), especially with the fact that I observe highly dusty patches out to large radii. Four of the galaxies in my sample are classified as *HST*-faint (ID16544, ID18694, ID23581 and ID26188). All are Type I galaxies, which seems logical because quiescent regions have lower A_V, hence are brighter in *HST*. One of them (ID23581) has $A_{V,min} > 3$, hence expected to be *HST* faint/dark, while the remaining three galaxies have $A_{V,min} \sim 1.5$, which is the average $A_{V,min}$ of the sample. It is more surprising that those three galaxies are *HST* faint/dark. However, these 4 galaxies are actually the galaxies at the highest redshift of the sample ($2.7 < z < 2.9$), with photometric redshift from my SED fitting procedure consistent with the ones from Kodra et al. (2022) and the ones from my super-deblending catalog. There is a chance that their HST faintness comes more from their higher redshift than their high level of dust (at least for 3 of them).

8.5 . RELATION TO BLUE NUGGETS SIMULATIONS

In the cosmological simulations from Lapiner et al. (2023), the typical high-redshift and low-mass galaxy is a gas-rich, star-forming, highly perturbed, and possibly rotating system, fed by intense streams from the cosmic web. When the stellar mass is in the ballpark of $\sim 10^{10}$M$_\odot$, the galaxy undergoes a major, last, wet compaction into a 'Blue Nugget', starting with a compact gaseous star-forming system that rapidly turns into a compact stellar system. The galaxies that I observe are all above this $\sim 10^{10}$M$_\odot$ threshold. However, non of them look like a blue nugget except possibly ID13098. I discuss the specific case of ID13098 in Section 8.7. The other ones that are in the range of mass where the wet compaction should happen do have a compact dusty star forming core, but they also have a much larger star-forming disk. Moreover, the more massive galaxies could be undergoing a rejuvenation event after blue nugget phase as it is suggested by Lapiner et al. (2023). However, when comparing the t_{50} of the disk and core, I find no evidence that the star-forming disks are younger than the cores. The fact that I do not observe any blue nuggets (or a single one) might be due to their low-mass, or low SFR, or that the previous observations were not deep enough to detect the low-luminosity disks. It may be possible that the most massive galaxies undergo a different quenching mechanism that lower-mass galaxies.

8.6 . INVESTIGATING THE LOPSIDEDNESS

Galaxy lopsidedness has not so far attracted much attention at high redshift, probably because of a lack of spatial resolution and/or incomplete data since the most obscured part of the galaxies are not visible with pre-*JWST* telescopes. However, the spatial resolution of NIRCam shows that it is a common features of DSFGs around the Cosmic Noon. Indeed, I showed in Section 7.1.3 that being lopsided seem to be the typical morphology of Type I and II galaxies (see Figures 5.2, 5.3 and 7.3). Bournaud et al. (2005) investigated the origins of lopsidedness in field galaxies and concluded that it is very unlikely the result of internal mechanisms but rather linked to the history and environment of the galaxies. With the NIRCam images, I have access to the spatially resolved morphology of these galaxies, and can try to better understand the causes of the lopsidedness.

Among the lopsided galaxies showed in Figures 5.2 and 5.3, some have a clear compact central core and a rather homogeneously colored disks (e.g. ID11887, ID13776), others are mostly clumpy galaxies with a less compact core (e.g. ID18694, ID18278).

For the first category, even if I don't have the kinematics to confirm it, it seems that the galaxies have a stable disk, with no major merger features. This means that the lopsidedness of these galaxies, is probably due to accretion and minor mergers. This accretion would be happening via streams of cold gas that asymmetrically feed more generously one side of the galaxy making it grow larger than the opposite side. Moreover, the fact that these galaxies are clumpy (see Section 7.2.4) and that their disk is highly heterogeneous (see Section 7.2.3) favors the idea of accretion or minor mergers that could create clumps or patches in the disks with different SFRs or A_V. However, the fact that Type I galaxies have a star-forming disk and Type II a quiescent disk means that the properties of gas transport in Type I and Type II galaxies are different.

In Type I galaxies, the disk acquires its gas via accretion streams or minor mergers and forms stars, but the gas also goes to the core, which is SF as well. Bournaud et al. (2005) showed via simulations that the strong lopsidedness could be the result of gas accretion if it as asymmetric enough and that the lopsidedness from accretion is relatively long-lived (~ 3Gyr), hence easily observable. This has also been confirmed by a recent study based on the TNG50 simulation (Dolfi et al. 2023) where they conclude that the lopsidedness in local galaxies originates from accretion over several Gyr while symmetric galaxies formed earlier and within a shorter timescale.

In Type II galaxies, on the other hand, while the gas keeps going to the core and keeps it SF, the disk is quenched. This would seem to suggest that the gas does not stay in the disk, but goes straight to the center. A possible explanation would be that Type II galaxies have larger inflows or very powerful outflows that blow away and/or shock the gas in the disk (confirming this would require spectroscopy). It could also be that in Type II galaxies the accreted gas has a more radial accretion, with little angular momentum and goes straight into the central regions. Or, for some reason, the gas rapidly looses its angular momentum and abandon the disk and falls into the center. This would, depending on the direction of accretion, feed the lopsidedness. This effect has already been suggested by Kalita et al. (2022) where they were able to link the lopsidedness of 3 galaxies at $z \sim 3$ in a dense environment to cold gas accretion using Lyman-α emissions. The strong lopsidedness of these galaxies, would then be a tracer of the point of impact of the accretion streams.

For the clumpier galaxies, the disk is star-forming and not homogeneous. Kannan et al. (2015) showed with simulations that gas-rich disks are able to survive major mergers and that the following enhanced star-formation is not entirely happening in the core of the galaxy, but a substantial fraction takes place in the disk too. This is compatible with my Type I galaxies, the fact that their SF disks are clumpy and heterogeneous in terms of dust and sSFR could be a signature of a recent major merger (Calabrò et al. 2019). Moreover, Kannan et al. (2015) mention that the presence of a gas-rich disk contributes to reducing the efficiency of bulge formation, which is compatible with the non-compact core observed in some of these galaxies. Usually major mergers features are short lived, but the clumps I observe could be preserved due to Toomre instabilities. Indeed Fensch & Bournaud (2021) showed, via simulations, that a galaxy with a gas fraction greater than 50% will have strong disk instabilities leading to the formation of long-lived giant clumps and strong nuclear inflow affecting the structure of the galaxy and possibly introducing lopsidedness. It has already been observed in a local galaxy used as proxy for high redshift galaxies (Puschnig et al. 2023). A major merger could then result in a clumpy galaxy with a perturbed structure, which is what I have in Figure

5.2 for some Type I galaxies. The color variations between clumps/regions in the galaxies could be tracers of the original galaxy they were a part of before the merging as they trace the dust attenuation. However, a major merger is not necessarily required, indeed, Rujopakarn et al. (2023) studied a lopsided galaxy at $z \sim 3$ and concluded that its lopsidedness did not originate from interaction with the environment but from internal, large scale instabilities, that could, in the end, form bars or spiral arms.

The lopsidedness of these galaxies could also be the signature of the bulge angular momentum build-up. Indeed, either via accretion, minor mergers, major mergers, internal instabilities and tidal effects, the lopsidedness will break the disk balance, consequently creating a torque on the bulge of the galaxy resulting in an angular momentum loss.

The significance of the difference of lopsidedness between Type III galaxies and the rest of the sample means that, by some mechanism, the galaxies become much more symmetric after the Cosmic Noon. Indeed, I recall that my Type III galaxies have $z = 1.80 \pm 0.09$ while Types I and II have $z = 2.19 \pm 0.14$. This could be due to increasing virialization with passing of time, also due to the stabilising effect of the larger bulge mass fraction (see lower right panel of Figure 7.3).

8.7 . WHERE DO TYPE II GALAXIES COME FROM ?

The Type II galaxies (see Section 6.7 and Figure 5.3) have an unusual behavior. They have a compact star-forming core embedded in a quiescent disk, and represent $\sim 23\%$ of the galaxies of my sample, so are relatively common. Kalita et al. (2022) studied such galaxies in a crowded environment at $z \sim 3$ and linked the quiescence of the disk to its strong lopsidedness which rapidly fuels the gas to the core of the galaxy. In my sample of Type II galaxies, 3 have a strong lopsidedness, 1 is only weakly lopsided and has an off-center core while 1 is not lopsided at all. This means that even if lopsidedness can be a driver of outside-in quenching, it is not the only one.

Based on my observations, I have three possible scenarios that could explain the observed suppression of star-formation in the disk.

The first scenario is the one developed by Kalita et al. (2022) with the lopsidedness either coming from a major merger strong enough to result in this off-centered core or from asymmetric accretion of gas via streams and minor mergers, feeding the disk preferentially on one side. The strong lopsidedness resulting from this is enough to explain the quenching of the disk as it greatly facilitates the transportation of the gas toward the core (Fensch & Bournaud 2021).

The second scenario is a wet compaction event leading to an apparent outside-in quenching. ID13098 is in the correct range of stellar mass and redshift to be in a ‘blue nugget’ phase (Lapiner et al. 2023; Dekel et al. 2009; Tacchella et al. 2016) where the galaxy undergo a wet compaction caused by gas-rich mergers or smoother gas streams, leading to an episode of high central star-formation and outside-in quenching. The presence of the low-luminosity quiescent disk might indicate that the compaction is not completely done yet. If it is a blue nugget, the outside-in quenching may not be final as when the gas has been consumed at the center and the bulge has grown, a star-forming ring can form in the disk via accretion of new gas-reach material from the intergalactic medium leading to an inside-out quenching in the post-blue nugget phase.

The last scenario is an actual outside-in quenching linked to the strong lopsidedness but not resulting from a major merger. In Figure 7.1, I show that the Type I galaxies are the most star-forming and at the higher redshift on average. They also have a stellar mass consistent with the Type II galaxies. This means that there could be an evolutionary path between Type I and Type II galaxies driven by VDI and lopsidedness. The idea is that the star-forming clumps of the Type I galaxies will migrate toward the center of mass of the galaxy (Mandelker et al. 2014). By doing so, they will fuel strong gas nuclear inflow creating a compact SF core (Fensch & Bournaud 2021). On their way to the center of the galaxy, the clumps will accrete the gas of the disk and could leave a completely gas deprived disk and a compact SF core. When growing, the SF core will prevent the formation of new clumps in the disk by stabilizing it (Hopkins et al. 2023) while the lopsidedness could be conserved due to the large scale instabilities. In this scenario, Type II galaxies are observed in a process of outside-in quenching.

Chandar et al. 2023 demonstrated that the local ULIRG Arp220 is composed of a central starburst and a larger quiescent disk. The starburst has been triggered by a major merger. The galaxy is classified as shocked post-starburst galaxy which is a stage prior to post-starburst. In that case, it appears that shocks induced by the merger forced the outer disk in this galaxy to turn quiescent. This is close to first scenario I described with the outside-in quenching originating from a major merger.

In my case, in the four remaining galaxies, two have clumpy heterogeneous disks (ID13107 and ID18278, see Figure 5.3), the different properties of the patches, either linked to dust or sSFR (see Section 7.2.3) favors the idea of asymmetric accretion streams and minor mergers as the source of lopsidedness for these two galaxies. The ID13776 has a clumpy but more homogeneous disk, but highly off-centered. The eccentricity of this galaxy can both originate from asymmetric accretion making the disk grow on one side or from a major merger strong enough to shift the disk. In the same way, it is hard to conclude for the last galaxy (ID21190) which is not lopsided and seem to have a smooth homogeneous disk.

8.8 . THE ROLE OF ENVIRONMENT

A way to discriminate between the scenarios of outside-in quenching and the origin of the lopsidedness of galaxies is to look at their local environment. To this aim, I use the environment density measurements from Chartab et al. (2020). They measure the density contrast of galaxies with a magnitude brighter than 26 AB mag in the H-band. The density contrast is defined as the number density enhancement with respect to the average density in the vicinity of the galaxy (local density/background density). In Figure 8.2, I compare the local density contrast of my sample with the general population of galaxies in the EGS field.

The star markers in Figure 8.2 are the Type II galaxies. They do not sit in any particular kind of environment, they are relatively close to the median of the general population showed by the blue dotted line. This suggest that outside-in quenching can happen both in dense environment via major mergers but also in lighter environment via internal effects. The galaxy at lower density is ID13098 that I discuss in Section 8.7. The fact that this galaxy is relatively isolated favors the scenario of wet compaction as the origin of its outside-in quenching. For the other galaxies, the local density is insufficient to discriminate between scenarios as they do not sit in strongly over/under crowded environments but show that they all are likely.

The color of the markers trace the lopsidedness of the galaxies. There is no obvious difference between the lopsided galaxies and the general population. I do not see any signature that could link the environment to the lopsidedness. The fact that I see lopsided galaxies not only in dense environment and that most of them have a regularly looking disk favors the idea that lopsidedness originates from accretion and/or VDI. However, this is only a tentative explanation, these measurements are not strong enough to say if environment could be a driver of lopsidedness. The circular marker showing a weakly lopsided galaxy in a high density environment is ID30186. This galaxy is the brightest galaxy of a group of ~ 16 members at $z_{spec} = 1.85$, is undergoing a major merger and is surrounded by quiescent intra-halo light (Coogan et al. 2023).

Discriminating further between the different scenarios would require spatially resolved spectroscopy to study the kinematics of each of these galaxies, and especially of the disk of each of them, to see if their disk is rotating, which would favor accretion and minor mergers, or if they are dominated by dispersion velocity favoring the scenario of major mergers and VDI.

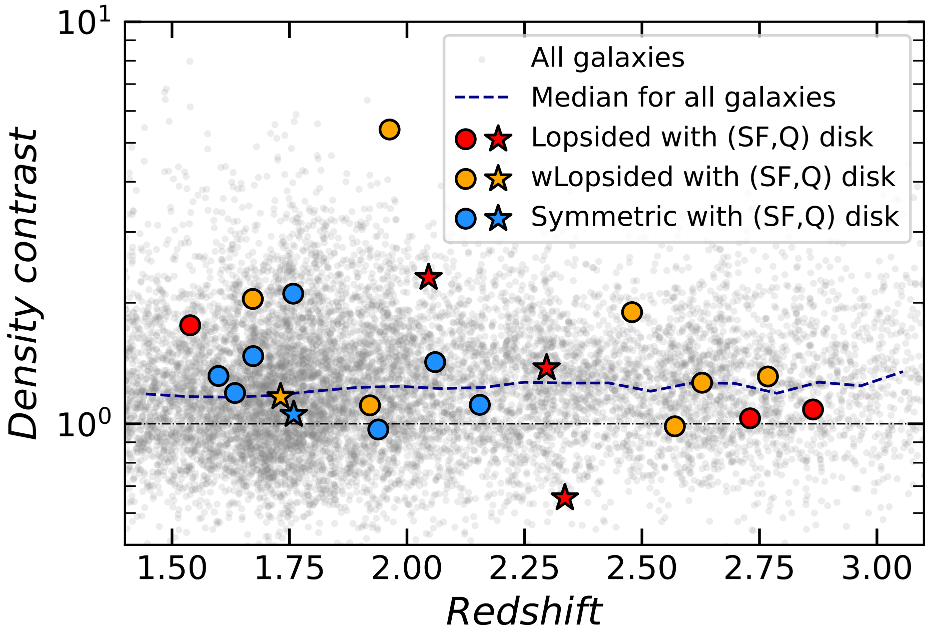

Figure 8.2: Density contrast of galaxies versus their redshift. Density contrast is defined as the number density enhancement with respect to the average density in the vicinity of the galaxy (Chartab et al. 2020). Grey scatter is the general population of H-band mag AB ≤ 26, the black dotted line is 1, the blue dashed line is the median density contrast of the general population in redshift bins. Star-shaped markers are galaxies undergoing outside-in quenching (Type II). Circular marker are the Type I and III galaxies. The colors of the markers trace the lopsidedness.

Table 8.1: Main properties of my sample of 22 DSFGs. See Section 6.7 for Type definitions.

ID (CANDELS)	Redshift	Mass $log_{10}(M_*/\mathrm{M}_\odot)$	Mass$_{core}$ $log_{10}(M_*/\mathrm{M}_\odot)$	SFR $\mathrm{M}_\odot$ yr^{-1}	SFR$_{core}$ $\mathrm{M}_\odot$ yr^{-1}	Type	Morphology
11887	1.539^b	10.5 ± 0.1	9.59 ± 0.07	38 ± 24	5 ± 3	Type I	cSFC+Lop
13098	1.720^a	10.6 ± 0.1	10.22 ± 0.04	73 ± 63	62 ± 9	Type II	cSFC^c+wLop
13107	2.21 ± 0.02	10.1 ± 0.1	9.43 ± 0.06	29 ± 21	10 ± 2	Type II	cSFC+Lop
13776	2.297^b	11.4 ± 0.1	10.86 ± 0.05	340 ± 214	114 ± 64	Type II	cSFC^c+Lop
13932	2.48 ± 0.02	10.2 ± 0.1	8.91 ± 0.07	35 ± 20	3 ± 1	Type I	wLop
14559	2.020 ± 0.004^a	10.2 ± 0.1	9.59 ± 0.07	44 ± 25	10 ± 3	Type I	cSFC^c
15036	1.60 ± 0.01^a	10.5 ± 0.1	10.02 ± 0.03	36 ± 22	3 ± 2	Type III	...
15371	1.921^b	11.0 ± 0.1	10.61 ± 0.03	197 ± 125	26 ± 13	Type III	wLop
16544	2.73 ± 0.03^a	11.4 ± 0.1	10.89 ± 0.03	269 ± 186	97 ± 31	Type I	cSFC^c+wLop
18278	1.805^a	11.5 ± 0.1	10.84 ± 0.06	254 ± 168	72 ± 23	Type II	Lop
18694	2.80 ± 0.01	11.1 ± 0.1	10.22 ± 0.05	415 ± 244	52 ± 9	Type I	Lop
21190	1.68 ± 0.01^a	11.0 ± 0.1	10.48 ± 0.07	106 ± 95	94 ± 20	Type II	cSFC^c
23205	2.14 ± 0.01^a	11.40 ± 0.05	10.78 ± 0.03	138 ± 87	21 ± 10	Type III	...
23510	2.51 ± 0.02^a	10.4 ± 0.2	9.51 ± 0.15	141 ± 106	27 ± 6	Type I	wLop
23581	2.83 ± 0.02	11.3 ± 0.1	11.01 ± 0.06	259 ± 152	87 ± 38	Type I	Lop
25604	1.673^b	11.1 ± 0.1	10.75 ± 0.02	24 ± 18	3 ± 4	Type III	...
26188	2.87 ± 0.02	10.8 ± 0.1	10.10 ± 0.05	257 ± 178	34 ± 11	Type I	cSFC+wLop
29608	1.64 ± 0.03	10.7 ± 0.1	9.72 ± 0.09	342 ± 181	84 ± 11	Type I	cSFC^c+wLop
30012	1.53 ± 0.01^a	11.0 ± 0.1	10.62 ± 0.03	49 ± 42	6 ± 3	Type III	...
30186	1.85^a	11.7 ± 0.1	11.29 ± 0.03	550 ± 436	136 ± 57	Type I	cSFC^c+wLop
31125	2.08 ± 0.02	11.60 ± 0.05	10.90 ± 0.03	237 ± 156	25 ± 18	Type III	...
31281	1.634^b	10.80 ± 0.05	10.35 ± 0.03	36 ± 35	0.9 ± 0.5	Type III	...

Notes.
^{a}Grism based redshift.
^{b}Spectroscopic redshift.
^{c}SMGs analog candidate (see Section 8.4).
'cSFC' and '(w)Lop' stand for *compact star-forming core* and *(weakly) lopsided* respectively.

9 - CONCLUSIONS AND PERSPECTIVE

During this thesis, I have brought together years of observations in the far-IR and the newest images for the *James Webb Space Telescope* in an attempt to understand to a deeper level the formation and evolution of galaxies at the Cosmic Noon. This was achieved by producing the deepest far-IR catalog in the EGS field. In the following sections, I summarize the main results of these three years of work and open some perspective for continuing this work.

9.1 . THE DEEPEST FIR CATALOG IN THE EGS FIELD

In the first half of this manuscript, I presented a detailed "super-deblended" photometry catalog for FIR-to-(sub-)millimeter imaging data sets in the EGS full $209 arcmin^2$ field. In an attempt to overcome the blending problem due to the large PSF in the SPIRE bands especially, I adopted the "super-deblending" technique that has been developed by Liu et al. (2018) in the GOODS-North field and improved by Jin et al. (2018) in the COSMOS field. My images have a similar depth as the images from Jin et al. (2018), nonetheless, I still had to improve and adapt the method to the EGS field.

Using Stefanon et al. (2017), I built a highly complete set of 7061 priors for deblending the images. I have 2773 detections in the MIPS/24μm image and 1722 in the VLA/10cm one.

In the deblending of the FIR/(sub)mm images, I made a few changes, I added a systematic analysis of the effect of the background level chosen when running GALFIT (Peng et al. 2010) allowing to choose the level that will minimize the uncertainties. In the simulations, I also made sure that a simulated source would be at a reasonable distance from an actual prior, this allowed to avoid unrealistic outliers and bias.

Unfortunately, some images do not cover the full EGS field, it is the case for the SCUBA2 and AzTEC maps. For SCUBA2, I fitted two images, one deeper but covering a smaller area than the other.

A total of 480 galaxies are individually detected with a combined $S/N > 5$ over the FIR/(sub)mm wavelengths, including 48 detections at $z \geq 3$ (mostly photometric). I compared my results with publicly available catalogs for each wavelength. My results are in agreement with the literature, my estimations of uncertainties are mostly in agreement. For the SPIRE bands, I find that some uncertainties may have been under-estimated in previous work as they don't take the blending into account as well as I did. Overall, this catalog is the deepest far-IR catalog in the EGS field.

This catalog will be published and publicly released soon but has already proven to be useful to confirm the possibility of very high photometric redshift candidates detected with *JWST*.

9.2 . *JWST* SHEDS LIGHT ON DSFGs

In the other half of this manuscript, I used the new set of images in the near-IR from *JWST*/NIRCam in the EGS field from the CEERS collaboration to investigate the formation and evolution of DSFGs at Cosmic Noon. To start with, I selected a sample of DSFGs based on their FIR emissions and around Cosmic Noon ($1.5 < z < 3.0$) using my super-deblended catalog. I ended up with 22 galaxies in the CEERS field.

I studied each galaxy on a sub-galactic scale by dividing them in different regions based on their NIRCam (F115W, F200W, F444W) colors, taking advantage of the spatial resolution. Using the available photometry from *HST* and *JWST*, I ran SED fitting and derived physical parameters for each galaxy component and classified them as star-forming or quiescent. I classified the galaxies in different Types based on the star-forming activity in their core and disk. The Type I have a star-forming disk with a red star-forming core, the Type II are quiescent disks with a SF core and the Type III are star-forming disks with a quenched bulge. The main results of my study are:

- $\sim 70\%$ of the DSFGs in my sample have a red deeply dust attenuated compact star-forming core that can represent up to 80% of the total SFR of the galaxy but only 20-30% of its stellar mass. Contrary to the simulations that predict blue nuggets, these compact red cores are surrounded by large less obscured disks. Most of these cores are measured or predicted to be SMGs. However, telescopes like *ALMA* or *NOEMA* would only be sensitive to the most obscured part of the galaxy. This study demonstrates the necessity to combine near-IR imaging to sub-mm data to fully grasp the nature of DSFGs.

- 64% of my galaxies are at least weakly lopsided, and 27% strongly lopsided. The lopsidedness could be caused by asymmetric cold gas accretion and minor mergers feeding preferentially one side of the disk, which would, depending on the orientation of the accretion favor a star-forming or quiescent disk. Lopsidedness could also be triggered by a major merger disrupting the disk, and/or via large scale instabilities even if my study favors accretion. The fact that lopsidedness is so common among my sample means that most DSFGs have a complex SFH and do not calmly evolve without any interaction with their environment.

- 23% of the galaxies of my sample have a quiescent disk but a star-forming core. If one of them is compatible with a blue nugget, the others are not. Their observed outside-in quenching could then find its origins in their strong lopsidedness that favors VDI and rapid transportation of gas towards the center or from large scale instabilities and clump migration accreting the gas from the disk to feed it to the core.

- Most of the galaxies have a disk with patches/clumps of different RGB color that are not radially symmetric. The color variations within the disks are mostly driven by dust attenuation. These variations are another indicator that Main Sequence DSFGs have a complex SFH.
- Interestingly, among the quiescent disks, I find evidence of clump-like structures. These clumps are not (or very weakly) star-forming, they are mostly populated by old stars but seem to be to massive to be compared to the globular clusters we observe in the local universe.

This work demonstrates the power of the *JWST* in probing for the first time spatially resolved galaxies in the near-IR at Cosmic Noon, where the only available data was the unresolved images from *Spitzer*/IRAC. This allows reliable studies of quenching and dust attenuation at sub-galactic scales in DSFGs, facilitating the understanding of their morphologies and formation and evolution mechanisms that appear to be more complex than previously thought.

9.3 . PERSPECTIVE AND FOLLOW-UP

This work is the first step toward a deeper understanding of massive galaxy evolution, however, these results are extrapolated from a small population of galaxies. In order to confirm them, it could be useful to exploit the remaining part of the CEERS field observed in December 2022 that I didn't used. To go further, the “super-deblended" catalog in the COSMOS field could be used Jin et al. (2018) to select DSFGs to study using the *JWST* COSMOS-Web survey (PI: Jeyan S. Kartaltepe & Caitlin M. Casey, Casey et al. (2023)). Having a much larger area (about $30\times$ larger than the EGS field), it would allow to have enough statistics to confirm the trend I observed, as well as discover new more subtle trends that are undetectable at low statistics. To analyze such a great number of galaxies would require to render the analysis automatic, the division of galaxies in regions could be made by defining sections in a NIRCam color-color plots for instance, it also could be done using machine learning. It could also be possible to improve the SED fitting, either by using a more physically driven model or a non-parametric fitting. Using the exquisite NIRCam spatial resolution, it could also be possible to fit pixel by pixel instead of patches, this would allow to build attenuation maps, age maps or SFR maps that could be used to better understand what is driving the evolution of the DSFGs, evidence could be found in these maps that could favor a evolution scenario (major merger, cold gas accretion, disk instabilities).

9.3.1 . NOEMA PROPOSALS

Since the EGS field is too North to be observable with ALMA, the only way to get spatially resolved sub-mm maps of my sample of DSFGs would be to use NOEMA. The prime objective of the NOEMA observations would be to probe with a high resolution the star forming region inside these galaxies by localizing the position of the sub-mm emissions in the galaxies accurately ($1-2$kpc accuracy) and by measuring the size of the sub-mm emission to the same accuracy. The *JWST*/NIRCam observations allowed us to have a high resolution view of the galaxies by probing stellar emissions. Having these two sets of images, in the near-IR and millimeter wavelengths would allow to accurately compare the distribution of stellar mass in the IR luminous galaxies (including the very obscured mass that shows up towards $4-5\mu$m in NIRCam) to the SFR spatial distribution, to unveil if they come from the same regions. The same exercise could be done for dust attenuation distributions (from NIRCam colors) and young stars distributions (from 1μm NIRCam imaging and HST already existing). Also, the very large wavelength range at exquisite spatial resolution could allow to classify pixel-by-pixel the stellar emission as quiescent or star forming. All these spatially resolved observations would give a unique opportunity to understand how these sub-mm compact sources are formed, what physical processes could lead to such morphology and test the validity of existing theories on their formation and evolution. In recent work, a direct connection between accretion streams and the morphological transformation of galaxies driving compact star-formation has already been observed in a dense environment (Kalita et al. 2022). This connection shows that galaxies can build-up compact highly star-forming cores without major-mergers, therefore preserving their stellar disks. The aim of the sub-mm observations would be to understand if a similar evolutionary pathway is possible for field galaxies. How could these compact hidden star-forming cores formed ? What processes could drive the apparent 'outside-in' quenching of those galaxies ? Being able to accurately trace the star-forming regions with NOEMA is crucial to answer these questions.

I submitted two proposals, the first one during the summer 2022 Cycle, the proposal was rated B and was not observed due to lack of available telescope time. The other proposal was a re-submission of the the first one, for the winter 2022, it was also rated B, but I got the time and the 14 galaxies in the proposal were observed. I will work on this data in the near future. The proposals can be found in the Appendix 10.2.

9.3.2 . *JWST*/NIRSpec PROPOSAL

As mentioned previously, spatially resolved spectroscopy would allow to discriminate between the several evolution scenarios. NIRSpec is a perfect candidate for the job, this why I decided to submit a proposal for the Cycle 2 of *JWST*.

I proposed to use the NIRSpec in the Multi-Object Spectroscopy (MOS) mode with the G235H disperser to probe and spatially resolve the Hα emission lines of 9 of the galaxies in my sample that could all be observed in a single pointing. The idea was to scan each of these galaxies in order to get a spatially resolved 3D spectrum for each of them. To do that, I would have used large slitlet to cover the disks, and scanned over $5 \times 0.2_{\mathrm{J}} = 1_{\mathrm{J}}$ in the direction of dispersion by step of 0.1_{J}, to obtain full, 3D spectroscopy of each galaxy. I preferred MOS rather than IFU spectroscopy because MOS has a limiting sensitivity $2\times$ lower than IFU spectroscopy. Moreover, the latter can only observe 1 target at a time.

The main goals of my proposal were:

(i) From the Hα Equivalent Width (EW), I could probe the sSFR and spatially resolve it for each galaxy. This is crucial to confirm the star-forming activity or the quiescence of the galaxies as inferred by NIRCam imaging. All of these galaxies are in the upper part of the MS or above it, meaning they are actively star-forming. However, when fitting the SED of different components based on NIRCam imaging, I noticed that some galaxies seem to have quiescent regions. Some of them in the classical inside-out quenching mode, ie a star-forming disk and a quiescent nucleus. Others, as mentioned above are the other way around, with what looks like an outside-in quenching mode. Having access to a spatially resolved direct tracer of star formation would allow me to confirm or not the activity of each component of each galaxies. Hence, confirming the existence of field galaxies having high star-forming activity in a compact nucleus within a quiescent disk, validating the possibility of an outside-in quenching mechanism for field galaxies.

(ii) From the Hα line, I could have access to the kinematics, allowing a better understanding of the morphology and dynamics of each galaxy. The spectral resolution of NIRSpec would make it possible to study the kinematics of these galaxies. Most of the targets have a complex morphology, often lopsided. However, they all seem to have a disk. The kinematics would be able to confirm the presence of a rotating disk, or, in the contrary, kinematic distortions would signal the effect of an ongoing merger, presumably at coalescence (e.g. Shapiro et al. 2008). If there is a rotation, I would be able to see if the center of rotation coincides with the peak in the mass surface density distribution, located at the position of the central starburst, traced by the F444W flux density. This kinematic analysis would be the key to deeply understand the possible formation of these lopsided galaxies with a compact nucleus, possibly lifting the veil on a new quenching mechanism.

(iii) From the detected lines in the spectra, I could put constraints on the metallicity of each galaxy. This information is important for the SED fitting and the accuracy of the derived quantities. Moreover, using the $[N_{II}]/H\alpha$ ratio, I could also probe the presence of an AGN in the nucleus of each galaxy that would be a useful complement to the information I have from radio and X-ray surveys. With the IR catalog, I have access to the IR luminosity of these galaxies, with NIRSpec, I would be able to resolve the degeneracy between star-formation and AGN activity.

To put it in a nutshell, NIRSpec observations of these dusty star-forming galaxies would be a milestone in the understanding of FIR-bright field galaxies evolution in terms of morphology and star forming activity.

Unfortunately, the proposal was rejected. However it could be improved and re-submitted for a later Cycle.

10 - APPENDIX

10.1 . CONTRIBUTIONS TO OTHER PAPERS AS CO-AUTHOR

During the course of my thesis, I had the opportunity to participate to several papers as a co-author. My contributions are mainly linked to my work on the super-deblending catalog that I shared within the CEERS collaboration. I list here these papers and summarize my contributions.

A Long Time Ago in a Galaxy Far, Far Away: A Candidate $z \sim 12$ Galaxy in Early JWST CEERS Imaging. This paper describes one of the most distant galaxies ever observed. I used the Super-deblending to check that there was no FIR emission for this galaxy, hence excluding the possibility of a lower redshift DSFG. Finkelstein et al. 2022, The Astrophysical Journal Letters.

Dusty starburst masquerading as an ultra-high redshift galaxy in JWST CEERS observations. As the title implies, this paper demonstrates how galaxies observed with NIRCam were believed to be at $z > 10$ while they actually were DSFGs at $z \sim 5$ with a similar SED. Sub-mm emission were used to demonstrate this. I used the super-deblending technique to extract FIR fluxes, hence helping proving the point of the paper. Zavala et al. 2023, The Astrophysical Journal.

A $z = 1.85$ galaxy group in CEERS: evolved, dustless, massive intra-halo light and a brightest group galaxy in the making. This paper studies the properties of galaxies and inter-galactic medium of a group of galaxies in the EGS field. The study is based on both *JWST*/NIRCam imaging and my super-deblending catalog. I provided the necessary data and far-IR SED fit. Coogan et al. 2023, Astronomy & Astrophysics.

CEERS Key Paper I: An Early Look into the First 500Myr of Galaxy Formation with JWST. This paper focuses on studying galaxy candidates at $z > 10$. I used the super-deblending technique to check that there was no FIR emission for these galaxies, for the same reason as above. Finkelstein et al. 2023, The Astrophysical Journal Letters.

CEERS Key Paper II: A First Look at the Resolved Host Properties of AGN at $3 < z < 5$ with JWST. This paper is using the NIRCam images from CEERS to study the properties of galaxies hosting an AGN. In this paper I investigated whether any of these sources were dusty starburst galaxies masquerading as quiescent systems by examining their far-IR emission using the super-deblending technique. Kocevski et al. 2022, ApJ.

10.2 . ACCEPTED PROPOSALS

I insert here the two NOEMA proposals that were accepted, even if only one of them was observed. The two proposal are linked as the second one is a re-submission of the first one.

I decided not to insert the NIRSpec proposal as it was rejected.

See Section 9.3.1 and 9.3.2 for more details on these proposals.

IRAM
300, rue de la Piscine
38406 Saint-Martin-d'Hères (France)
Fax: (33/0) 476 42 54 69

Registration n°: **P416057**
Date: **17-MAR-2022**

PROPOSAL FOR THE NOEMA INTERFEROMETER

Title: JWST and NOEMA unveil the nature of submm-compact galaxies in the distant Universe

PIs: Aurelien Le Bail (FR)
CoIs: Mark Dickinson (US), David Elbaz (FR), Emanuele Daddi (FR), Steven Finkelstein (US), Carlos Gomez-Guijarro (FR), Shuowen Jin (DK), Boris Sindhu Kalita (FR), Lucas Leroy (FR), Benjamin Magnelli (FR), Casey Papovich (US), Qinghua Tan (CN-PMO)

Proposal category: Standard
Scientific category: Surveys of galaxies, Merging and interacting galaxies, Luminous and Ultra-Luminous Infra-Red Galaxies (LIRG & ULIRG)

Total requested time: 14.0 (PolyFiX)

Abstract:
In the last few years it has been revealed that a large fraction of IR-luminous sources in the distant Universe (many of which typical Main Sequence galaxies) are ultra-compact (<1kpc size) in their submm emission (hence SFR) but relatively extended in the optical (hence stellar mass). The reason for this dichotomy remains enigmatic as it might be linked to mergers, dynamical instabilities due to cold accretion or pre-quenching phases. We will be obtaining some of the earliest JWST observations, which hold the key to unveil the nature of these galaxies, in the EGS field as part of the CEERS survey. Unfortunately the EGS field lacks high-resolution submm observations as it cannot be seen by ALMA. We propose a pilot project to observe 7 mm-bright sources with NOEMA at 1.25mm in order to measure their SFR sizes, verify their compactness and identify the spatial location of the SFR. The timely NOEMA allocation would enable critical science to for french-led team ahead of competition.

Sources:

Id	Epoch	RA	DEC	z (redshift)	Setups
9333	J2000	14:19:42.643	52:50:52.656	1.68	1
11526	J2000	14:19:47.299	52:52:34.104	1.87	1
11800	J2000	14:19:24.187	52:48:34.668	4.24	1
11903	J2000	14:20:26.086	52:59:33.936	4.61	1
13088	J2000	14:19:07.670	52:45:58.068	1.79	1
14789	J2000	14:20:22.726	52:59:53.664	3.88	1
31125	J2000	14:19:16.675	52:52:22.404	2.15	1

Technical sheet "Continuum 1.25mm":

Summary

Point source detection with only continuum on 7 source(s).
Total observing time: 14.00(2.00 * 7) hours
Track fractions:
C: 100.0%

Instrumental tuning

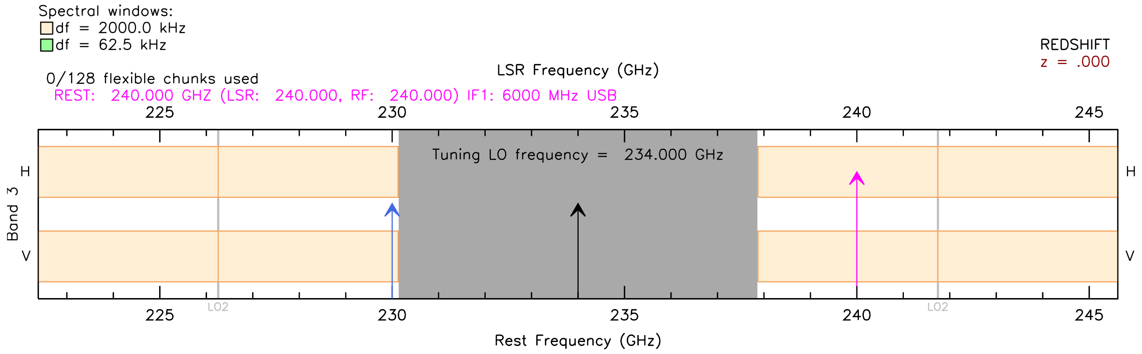

Half the most narrow SPW is equivalent to an offset of 2418.326 km/s in source LSR velocity

Source properties for continuum

Expected signal: 1.1 mJy/beam
Sensitivity: 111.2microJy/beam
(15488.0 MHz x 2 polar)
→ SNR: 10

PI note:
The proposed observations are an essential part of the PhD thesis of the PI, Aurelien Le Bail, carried out at CEA Paris-Saclay (2020-2023).

Justification for NOEMA time:
The EGS field at 52deg declination cannot be observed by ALMA. Timely observing our targets would enable critical science for our NOEMA project with the CEERS JWST observations.
We are aware of an other proposal from the CEERS collaborations (PI: Zavala J.), but we have no overlapping sources and complementary objectives

JWST and NOEMA unveil the nature of submm-compact galaxies in the distant Universe

P.I.: Aurélien LE BAIL

1 Scientific context

The majority of star-forming galaxies are observed to follow a correlation in the stellar mass versus star formation rate plane (e.g., Schreiber et al. 2015). Until recently, the existence of this so-called Main-Sequence (e.g., Daddi et. al. 2007) and its tight scatter was interpreted as evidence that star formation in most galaxies is a fairly ordered process. The 'consensus' had that galaxies on the main sequence are forming stars in a quasi steady state inside gas-rich stellar disks (e.g., Dekel et al. 2009) whereas galaxies above the main sequence undergo a starburst mode driven by stochastic processes such as major mergers, which the typical signature is compact start formation (e.g., Tacconi et al. 2008).

Recent studies at z ≈ 1–3 have shown that some massive ($M_* \geq 10^{11} M_\odot$) Main-Sequence galaxies have a stellar distribution typical of late type galaxies but where the star formation only occurs in a compact nucleus (Elbaz et al. 2018; Puglisi et al. 2019, 2021; Tadaki et al. 2017a, 2020; Franco et al. 2020; Gomez-Guijarro et al. 2022a; Jimenez-Andrade et al. 2019,2021). In fact, these compact submm galaxies comprise the majority of submm-luminous galaxies (e.g., Puglisi et al. 2021). This is incompatible with the 'consensus' expectations for MS galaxies and opens up the mystery of the nature of these galaxies, which could be a crucial phase in galaxy formation and evolution (Puglisi et al. 2021; Gomez-Guijarro et al. 2022b).

This implies that the galaxies within the main sequence scatter are not all largely unperturbed gas-rich disks. The diversity can be associated with the compactness of the gas reservoir which traces the interstellar medium properties of the galaxy. An hypothesis is that sub-mm/mm compact massive galaxies within the main sequence represent transient objects in an early post-starburst phase, following a merger driven starburst episode. We are part of the JWST/CEERS Early Release Science (ERS) observations that will be observed as one of the very earliest JWST projects in June targeting the EGS field. JWST NIRCAM will provide imaging of the 1–5μm galaxy continuum to unprecedented sensitivity and resolution (2.5× better than HST at fixed wavelenhgth). CEERS can provide essential information on the nature of submm-compact galaxies. The only problem is that no sub-arcsec imaging in the submm is available in the EGS (too north to be observed by ALMA), and we are starting to remedy this with this proposal that also builds on the construction, by our team, of a superdeblended IR catalog in EGS (Le Bail et al. in prep).

2 Targets selection

Because sub-mm-compact galaxies are widespread in IR-luminous sources at high-z, our primary selection is a bright flux at 1mm to make NOEMA observations easy and rewarding. Still, this require accurate mm photometry. We have embarked in a 1.5-yr project (as part of the PhD project of the PI) to build a state of the art superdeblended catalog to have the best IR photometry for galaxies in the JWST/CEERS survey field (EGS). This effort is now completed. The targets have been selected in the photometric catalog, including MIPS 24μm, PACS 100μm and 160μm, SPIRE 250μm, 350μm and 500μm, SCUBA-2 450μm and 850μm, AzTEC 1.1mm and VLA 20cm bands. The photometry is measured using the superdeblending technique (Liu et al. 2018; Jin et al. 2018) which is based on a SED fitting of each source between each band to predict the flux in the next band, Figure 1 shows an example of one SED at the end of the procedure while Figure 2 shows cutouts at each band around the same source. To be selected, the targets must fulfill several criteria. (1): the target must have a flux at 1.1mm greater than 1mJy with a signal-to-noise ratio (SNR) greater than 10 (hence, highly secure). If no observation is available at 1.1mm for a target, we use predicted values using SED fitting for the flux and SNR. Previous work show that above this threshold, the compactness can be considered quasi-systematic (Gomez-Guijarro et al. 2022a). (2): the target is required to have an IR signal-to-noise ratio (calculated as the square root of the sum of the signal-to-noise ratios of fluxes measured between 100μm to 1.1mm squared) greater than 5. At the end, **we selected 7 targets probing redshifts from 1.7 to 4.6** (Figs.1, 2, 3), Table 1 details the properties of these targets. We are confident that at least half of the targets are on the Main Sequence, although starburst galaxies are equally relevant. The photometric redshifts are from Stefanon et al. 2017. The error on these redshifts is estimated to be around 5 to 7 percent.

3 This proposal

The prime objective of the NOEMA observations is to probe with a high resolution the star formation region inside these galaxies by localizing the position of the sub-mm emissions in the galaxies accurately, to better than 1-2kpc and by measuring the size of the sub-mm emission to the same accuracy (or a comparably stringent upper limit). In parallel, we will have JWST/CEERS observations in the near-IR between $1\mu m$ and $5\mu m$. The JWST observations we allow us to have a high resolution view of the galaxies by probing stellar emissions. Having these two set of images, in the near-IR and millimeter wavelengths will allow us to accurately compare the distribution of stellar mass in the IR luminous galaxies (including the very obscured mass that will show up towards 4-$5\mu m$ in NIRCam) to the SFR spatial distribution, to unveil if they come from the same regions. We will also be able to do the same exercise for dust attenuation distributions (from NIRCam colors) and young stars distributions (from $1\mu m$ NIRCam imaging and HST already existing). Also, the very large wavelength range at exquisite spatial resolution will allow to classify pixel-by-pixel the stellar emission as quiescent or star forming. All these spatially resolved observations will give us a unique opportunity to understand how these sub-mm compact sources are formed, what physical processes could lead to such morphology and test the validity of existing theories on their formation and evolution. Figure 4 illustrates the improvement in terms of spatial resolution that we can expect from JWST/NIRCam observations between $1.4\mu m$ and $4.5\mu m$. It appears clearly that we should be able to resolve the galaxy and study its morphology in detail while being able to differentiate it from any foreground-galaxy contamination. In recent work, a direct connection between accretion streams and the morphological transformation of galaxies driving compact star-formation has already been observed in a dense environment (Kalita et al. 2022). This connection shows that galaxies can build-up compact highly star-forming cores without major-mergers, therefore preserving their stellar disks. The aim of our observations is to see if a similar evolutionary pathway is possible for field galaxies.

One important point is that the CEERS observations are planned in June if everything goes smoothly with the telescope. If something goes wrong and the science observations are delayed, there is a second window in December for EGS field observations. In this case, the JWST/CEERS configuration is different with the June and December configurations having 50% of their field in common. In any case, we will know which configuration will be chosen soon enough (before the NOEMA observations are executed) which means that if we have to swap to December configuration, we will be able to adapt the NOEMA targets to stay consistent with the CEERS observations.

4 Technical justification

The primary aim of these observations is to detect our targets in their mm dust continuum with sufficiently high SNR to allow an accurate size measurement and their precise spatial position. In case of very compact sources, following Puglisi et al. 2021, we need to have a 1σ uncertainty in the size of about 1 kpc ($0.13''$), so that the relative 1σ upper limit for unresolved sources will be of the same order. The implied positional accuracy will be of the same order of magnitude, that is of order of 1 pixel in HST WFC3, fully sufficient for our science. We will be observing at 240 GHz where the dust continuum is brightest, with fluxes $\geq 1mJy$. Using simulations, we find that observing in Configuration C ($0.8''$ beam) we can reach the required precision with an rms sensitivity of 110μJy/beam. Observing the seven targets in track sharing we can substantially reduce overheads, and we find that 14hrs of total time request are sufficient to reach our goal. Some of our targets are brighter than the limit and the detection and size measurement accuracy will be even higher (Table 1).

We are aware that 1 mm observations are better suited for the winter semesters. However, our relatively short request can be accommodated in the summer during C-configuration, and we believe that the urgency of these NOEMA observations being available when JWST observes our field in order to enable the described crucial science investigations, warrant the effort. If this pilot project is successful, we will be able to request observations of fainter sources in the coming winter semester to enlarge the sample.

5 Supporting material

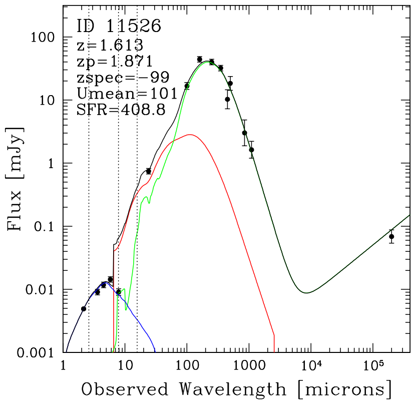

Figure 1: SED of one of the target from the superdeblended catalog. Blue and red curves show the stellar component and AGN torus emission, and the dust continuum emission is shown in green. Umean = 101 is a code to mark that the source was fitted by a starburst-like template. z is the redshift obtained from the fit while zp is the photometric redshift from Stefanon et al. (2017)

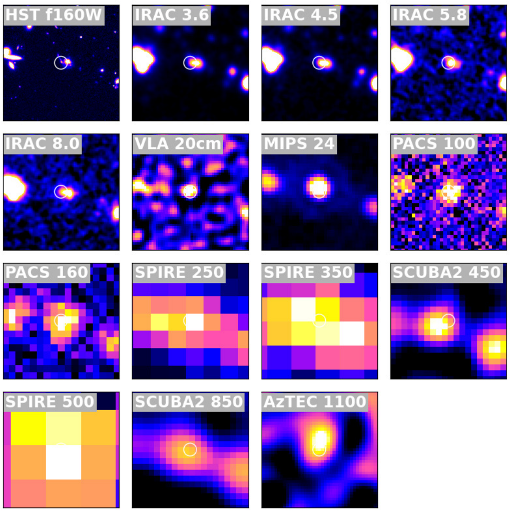

Figure 2: Multi-wavelength cutouts centered on the source 11526 in the bands use for the photometric superdeblending, the field of view is 80”

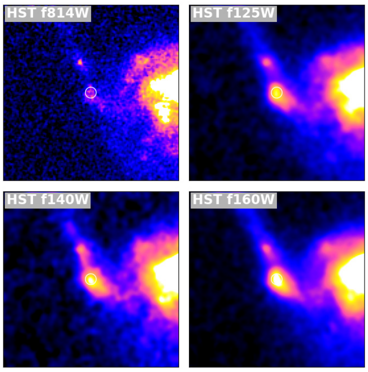

Figure 3: Multi-wavelength cutouts centered on the source 11526 in different CANDELS bands. Field of view is 8”

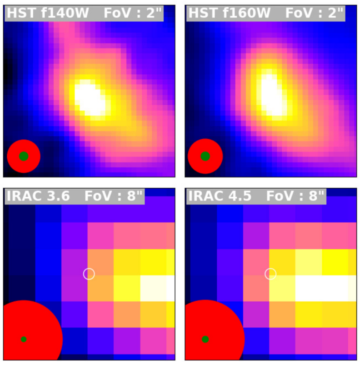

Figure 4: Multi-wavelength cutouts centered on the source 11526 in different HST and IRAC bands. The red circle is the current PSF and the green circle is the expected PSF for JWST/NIRCam filters. White circle is the source 11526 position

ID	z_{phot}	$\log(M_*)$ $[\log(M_\odot)]$	SFR $[M_\odot.yr^{-1}]$	$F_{1.25mm}$ [mJy]	SNR
9333	1.68	11.0	530	1.29 ± 0.05	≈ 12
11526	1.87	10.5	409	1.057 ± 0.015	≈ 10
11800	4.24	9.88	648	2.3 ± 0.2	≈ 21
11903	4.61	9.55	1500	5.40 ± 0.43	≈ 49
13088	1.79	10.9	263	1.21 ± 0.07	≈ 11
14789	3.88	11.2	1263	2.5 ± 0.2	≈ 23
31125	2.15	11.2	368	1.24 ± 0.10	≈ 11

Table 1: List of the 7 selected targets and their properties.

References

Daddi E., et al., 2007, *ApJ.* 670, 156 • Dekel A. Sari R., Ceverino D., 2009, *ApJ.* 703, 785 • Elbaz D., et al., 2018, *A&A.* 616, A110 • Franco M., et al., 2020, *A&A.* 643, A30 • Gomez-Guijarro C., et al., 2022a, *A&A.* 658, A43 • Gomez-Guijarro C., et al., 2022b, *A&A.* Submitted • Jimenez-Andrade E. F., et al., 2019, *A&A.* 625, A114 • Jimenez-Andrade E. F., et al., 2021, *ApJ.* 910, 106 • Jin S. et al., 2018, *ApJ.* 864, 56 • Kalita B. S., et al., 2022, *A&A.* in prep. • Liu D. et al., 2018, *ApJ.* 853, 172 • Puglisi A., et al., 2019, *ApJ.* 877, L23 • Puglisi A., et al., 2021, *MNRAS.* 508, 5217 • Schreiber C., et al., 2015, *A&A.* 575, A74 • Stefanon M., et al., 2017, *ApJ Supplement Series.* 229, 32 • Tacconi L. J., et al., 2008, *ApJ.* 680, 246 • Tadaki K.-I., et al., 2017a, *ApJ.* 834, 135 • Tadaki K.-I., et al., 2020, *ApJ.* 901, 74

IRAM

300, rue de la Piscine
38406 Saint-Martin-d'Hères (France)
Fax: (33/0) 476 42 54 69

Registration n°: **P429953**
Date: **14-SEP-2022**

PROPOSAL FOR THE NOEMA INTERFEROMETER

Title: JWST and NOEMA unveil the nature of submm-compact galaxies in the distant Universe

PIs: Aurelien Le Bail (FR)
CoIs: Emanuele Daddi (FR), David Elbaz (FR), Mark Dickinson (US) (invited), Benjamin Magnelli (FR), Casey Papovich (US), Qinghua Tan (CN-PMO), Steven Finkelstein (US), Shuowen Jin (DK), Carlos Gomez-Guijarro (FR), Boris Sindhu Kalita (FR) (invited), Lucas Leroy (FR), Denis Burgarella (FR), Jorge Zavala (JP), Laure Ciesla (FR), Veronique Buat (FR) (invited)

Proposal category: Standard
Scientific category: Starbursts, star formation, Galactic centres/nuclei, Surveys of galaxies, Luminous and Ultra-Luminous Infra-Red Galaxies (LIRG & ULIRG), Merging and interacting galaxies

Total requested time: 14.0 (PolyFiX)

Abstract:
In the last few years it has been revealed that a large fraction of IR-luminous sources in the distant Universe (many of which typical Main Sequence galaxies) are ultra-compact (<1kpc size) in their submm emission (hence SFR) but relatively extended in the optical (hence stellar mass). The reason for this dichotomy remains enigmatic as it might be linked to mergers, dynamical instabilities due to cold accretion or pre-quenching phases. We obtained some of the earliest JWST observations, which hold the key to unveil the nature of these galaxies, in the EGS field as part of the CEERS survey. Unfortunately the EGS field lacks high-resolution submm observations as it cannot be seen by ALMA. We propose to pursue the pilot project S22BY to observe 15 mm-bright sources with NOEMA at 1.25mm in order to measure their SFR sizes, verify their compactness and identify the spatial location of the SFR. The timely NOEMA allocation would enable critical science to for french-led team ahead of competition.

Resubmission: S22BY
Proposal history:
This is a resubmission of the B-rated S22BY proposal from summer 2022, for which no observations have been taken yet. We re-defined and somewhat enlarged the sample using the JWST NIRCAm data already in hand in the CEERS survey.

Sources:

Id	Epoch	RA	DEC	z (redshift)	Setups
2579	J2000	14:19:26.846	52:45:54.072	2.44	1
4581	J2000	14:20:29.515	52:57:39.528	1.51	1
6118	J2000	14:19:27.804	52:47:22.164	6.12	1
6422	J2000	14:20:30.329	52:58:31.692	5.42	1
9333	J2000	14:19:42.643	52:50:52.656	1.68	1
11526	J2000	14:19:47.299	52:52:34.104	1.87	1
13776	J2000	14:19:35.724	52:51:09.036	2.27	1
16017	J2000	14:19:39.082	52:52:32.664	2.58	1
18278	J2000	14:19:17.450	52:49:21.612	2.0	1
18307	J2000	14:19:39.972	52:53:26.772	2.78	1
20341	J2000	14:19:26.359	52:51:38.376	6.36	1
24433	J2000	14:19:04.361	52:48:59.580	4.22	1
30186	J2000	14:19:00.271	52:49:48.180	1.92	1
31125	J2000	14:19:16.675	52:52:22.404	2.15	1

Technical sheet "1":

Summary

Point source detection with only continuum on 14 source(s) in track sharing mode.
Total observing time: 14.00hours
Track fractions:
Any: 100.0%
from: B, C

Instrumental tuning

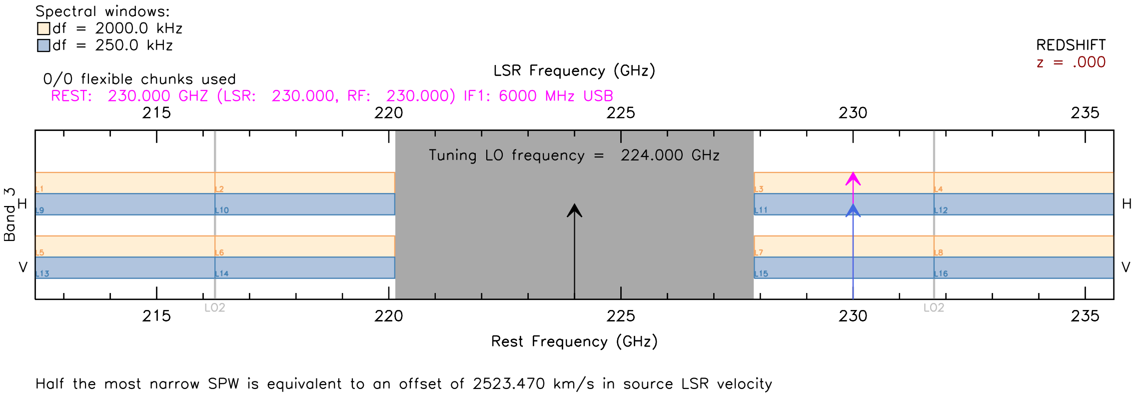

Source properties for continuum

Expected signal: 0.8 mJy/beam Sensitivity: 79.1microJy/beam (15488.0 MHz x 2 polar) → SNR: 10

PI note:
The proposed observations are an essential part of the PhD thesis of the PI, Aurelien Le Bail, carried out at CEA Paris-Saclay (2020-2023).

Justification for NOEMA time:
The EGS field at 52deg declination cannot be observed by ALMA. Timely observing our targets would enable critical science for our NOEMA project with the CEERS JWST observations.

JWST and NOEMA unveil the nature of submm-compact galaxies in the distant Universe

P.I.: Aurélien LE BAIL

1 Scientific context

The majority of star-forming galaxies are observed to follow a correlation in the stellar mass versus star formation rate plane (e.g., Schreiber et al. 2015). Until recently, the existence of this so-called Main-Sequence (e.g., Daddi et. al. 2007) and its tight scatter was interpreted as evidence that star formation in most galaxies is a fairly ordered process. The 'consensus' had that galaxies on the main sequence are forming stars in a quasi steady state inside gas-rich stellar disks (e.g., Dekel et al. 2009) whereas galaxies above the main sequence undergo a starburst mode driven by stochastic processes such as major mergers, which the typical signature is compact start formation (e.g., Tacconi et al. 2008).

Recent studies at z ≈ 1–3 have shown that some massive ($M_* \geq 10^{11} M_\odot$) Main-Sequence galaxies have a stellar distribution typical of late type galaxies but where the star formation only occurs in a compact nucleus (Elbaz et al. 2018; Puglisi et al. 2019, 2021; Tadaki et al. 2017a, 2020; Franco et al. 2020; Gomez-Guijarro et al. 2022a; Jimenez-Andrade et al. 2019,2021). In fact, these compact submm galaxies comprise the majority of submm-luminous galaxies (e.g., Puglisi et al. 2021). This is incompatible with the 'consensus' expectations for MS galaxies and opens up the mystery of the nature of these galaxies, which could be a crucial phase in galaxy formation and evolution (Puglisi et al. 2021; Gomez-Guijarro et al. 2022b).

This implies that the galaxies within the main sequence scatter are not all largely unperturbed gas-rich disks. The diversity can be associated with the compactness of the gas reservoir which traces the interstellar medium properties of the galaxy. An hypothesis is that sub-mm/mm compact massive galaxies within the main sequence represent transient objects in an early post-starburst phase, following a merger driven starburst episode. We are part of the JWST/CEERS Early Release Science (ERS) observations that have partially been observed (40%) as one of the very earliest JWST projects in June targeting the EGS field. The 60% remaining will be observed in December 2022. JWST/NIRCAM will provide imaging of the 1–5μm galaxy continuum to unprecedented sensitivity and resolution (2.5× better than HST at fixed wavelenhgth). CEERS can provide essential information on the nature of submm-compact galaxies. The only problem is that no sub-arcsec imaging in the submm is available in the EGS (too north to be observed by ALMA), and we are trying to remedy this with this follow-up proposal (after the S22BY proposal that was B-rated for the Summer 2022) that also builds on the construction, by our team, of a superdeblended IR catalog in EGS (Le Bail et al. in prep).

2 Targets selection

Because sub-mm-compact galaxies are widespread in IR-luminous sources at high-z, our primary selection is a bright flux at 1.25mm to make NOEMA observations easy and rewarding. Still, this require accurate mm photometry. We have embarked in a 1.5-yr project (as part of the PhD project of the PI) to build a state of the art superdeblended catalog to have the best IR photometry for galaxies in the JWST/CEERS survey field (EGS). This effort is now completed. The targets have been selected in the photometric catalog, including MIPS 24μm, PACS 100μm and 160μm, SPIRE 250μm, 350μm and 500μm, SCUBA-2 450μm and 850μm, AzTEC 1.1mm and VLA 20cm bands. The photometry is measured using the super-deblending technique (Liu et al. 2018; Jin et al. 2018) which is based on an active selection of priors at each band using predictions from the SED fitting of each individual source, Figure 1 shows an example of an SED at the end of the procedure. To be selected, the targets must fulfill several criteria. (1): The target must be detected in Herschel (combined Signal-to-Noise ratio > 5 for SPIRE+Herschel). (2): The target must be in the NIRCam field of view (June or December). (3): The target must have a predicted upper limit (flux + 2*error with the error being the prediction uncertainty) at 1.25mm greater than 0.8mJy. Previous work show that above this threshold, the compactness can be considered quasi-systematic (Gomez-Guijarro et al. 2022a). (4): The target must have $SFR_{IR}/SFR_{opt} > 3$ and $t/\tau > 1.5$. Based on the NIRCam images we already have, we add that $SFR_{IR}/SFR_{opt} < 50$ and $t/\tau \leq 3$. At the end, **we selected 14 targets probing redshifts from 1.7 to 6.4**. This selection, based on the data we have at hand gives us confidence that those targets are main sequence galaxies that should be mainly quiescent but with a hidden compact star forming core as illustrated in Figure 3 and 4. Table 1 details the properties of these targets. The photometric redshifts are from Stefanon et al. 2017.

3 This proposal

The prime objective of the NOEMA observations is to probe with a high resolution the star formation region inside these galaxies by localizing the position of the sub-mm emissions in the galaxies accurately, to better than 1-2kpc and by measuring the size of the sub-mm emission to the same accuracy (or a comparably stringent upper limit). In parallel, we will have JWST/CEERS observations in the near-IR between $1\mu m$ and $5\mu m$. The JWST observations we allow us to have a high resolution view of the galaxies by probing stellar emissions (Fig. 2). Having these two set of images, in the near-IR and millimeter wavelengths will allow us to accurately compare the distribution of stellar mass in the IR luminous galaxies (including the very obscured mass that will show up towards 4-$5\mu m$ in NIRCam) to the SFR spatial distribution, to unveil if they come from the same regions. We will also be able to do the same exercise for dust attenuation distributions (from NIRCam colors) and young stars distributions (from $1\mu m$ NIRCam imaging and HST already existing). Also, the very large wavelength range at exquisite spatial resolution will allow to classify pixel-by-pixel the stellar emission as quiescent or star forming. All these spatially resolved observations will give us a unique opportunity to understand how these sub-mm compact sources are formed, what physical processes could lead to such morphology and test the validity of existing theories on their formation and evolution. In recent work, a direct connection between accretion streams and the morphological transformation of galaxies driving compact star-formation has already been observed in a dense environment (Kalita et al. 2022). This connection shows that galaxies can build-up compact highly star-forming cores without major-mergers, therefore preserving their stellar disks. The aim of our observations is to understand if a similar evolutionary pathway is possible for field galaxies. How could these compact hidden star-forming cores formed ? What processes could drive the apparent 'outside-in' quenching of those galaxies ? Being able to accurately traces the star-forming regions with NOEMA is crucial to answer these questions.

4 Technical justification

The primary aim of these observations is to detect our targets in their mm dust continuum with sufficiently high SNR to allow an accurate size measurement and their precise spatial position. In case of very compact sources, following Puglisi et al. 2021, we need to have a 1σ uncertainty in the size of about 1 kpc ($0.13''$), so that the relative 1σ upper limit for unresolved sources will be of the same order. The implied positional accuracy will be of the same order of magnitude, that is of order of few pixel in JWST NIRCAm, fully sufficient for our science. This will be achieved with the beams from B or C configurations (0.5" to 0.9"). We will be observing at 230 GHz where the dust continuum is brightest, with target fluxes $\geq 0.8mJy$ ensuring SNR> 10. Using PMS, we find that we can reach the required precision with an rms sensitivity of 80μJy/beam with 1h per target on average, observing the fourteen targets in track sharing. We find that 14hrs of total time request are sufficient to reach our goal. Some of our targets are brighter than the 0.8mJy limit and the detection and size measurement accuracy will be even higher (Table 1).

5 Supporting material

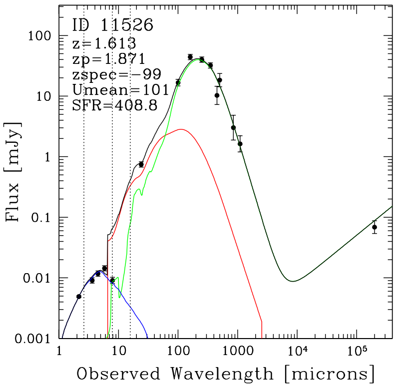

Figure 1: SED of one of the target from the superdeblended catalog. Blue and red curves show the stellar component and AGN torus emission, and the dust continuum emission is shown in green. Umean = 101 is a code to mark that the source was fitted by a starburst-like template. z is the redshift obtained from the fit while zp is the photometric redshift from Stefanon et al. (2017)

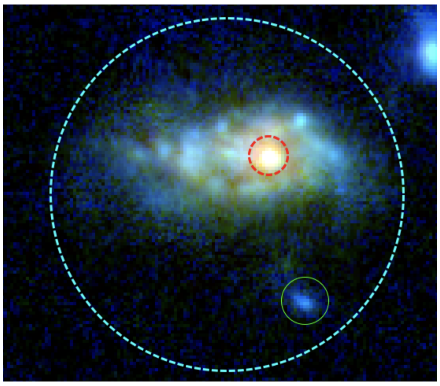

Figure 2: Illustration of the resolution power of NIRCam, RGB image (F444W,F200W,F115W) of ID13776. The blue circle has a diameter of 3.4" (pixel size: 0.03")

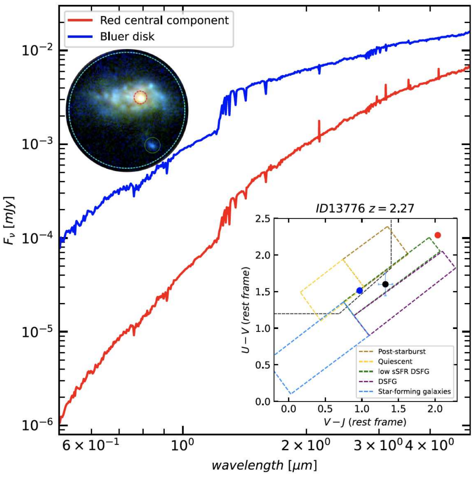

Figure 3: SEDs fitted using HST and NIRcam data of different region of the same galaxy. The regions are defined in the top-right RGB NIRCam image. The other panel shows the relative position of the regions in the UVJ diagram

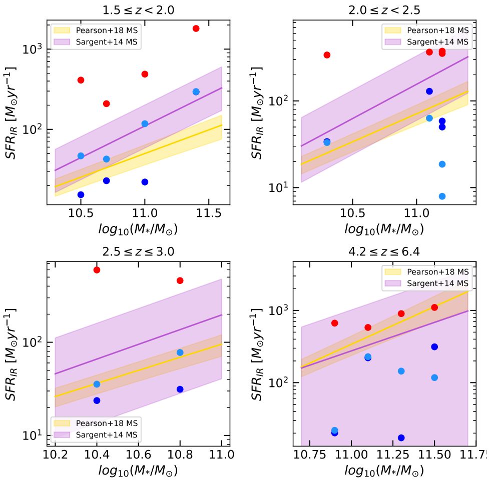

Figure 4: Position of the targets in comparison to the Main Sequence, the red dots use the FIR SFR from the Super-deblended catalog while the blue dots use the Opt/NIR SFR based on 2 models detailed in Stefanon et al.

ID	z_{phot}	$\log(M_*)$ $[\log(M_\odot)]$	SFR_{FIR} $[M_\odot.yr^{-1}]$	$F_{1.25mm}$ [mJy]	SNR_{pred}
2579	2.44	10.3	338	0.89 ± 0.13	≈ 11
4581	1.51	10.7	209	0.85 ± 0.19	≈ 11
6118	6.12	11.1	581	2.36 ± 0.15	≈ 30
6422	5.42	11.5	1100	3.32 ± 0.23	≈ 42
9333	1.68	11.0	488	1.16 ± 0.02	≈ 15
11526	1.87	10.5	411	0.99 ± 0.02	≈ 12
13776	2.27	11.1	365	0.96 ± 0.03	≈ 12
16017	2.58	10.8	459	1.34 ± 0.28	≈ 17
18278	2.00	11.2	352	1.09 ± 0.15	≈ 14
18307	2.78	10.4	597	1.80 ± 0.42	≈ 23
20341	6.36	11.3	903	2.70 ± 0.07	≈ 34
24433	4.22	10.9	667	1.82 ± 0.54	≈ 23
30186	1.92	11.4	1810	4.57 ± 0.63	≈ 57
31125	2.15	11.2	374	1.00 ± 0.11	≈ 13

Table 1: List of the 14 selected targets and their properties.

References

Daddi E., et al., 2007, *ApJ.* 670, 156 • Dekel A. Sari R., Ceverino D., 2009, *ApJ.* 703, 785 • Elbaz D., et al., 2018, *A&A.* 616, A110 • Franco M., et al., 2020, *A&A.* 643, A30 • Gomez-Guijarro C., et al., 2022a, *A&A.* 658, A43 • Gomez-Guijarro C., et al., 2022b, *A&A.* Submitted • Jimenez-Andrade E. F., et al., 2019, *A&A.* 625, A114 • Jimenez-Andrade E. F., et al., 2021, *ApJ.* 910, 106 • Jin S. et al., 2018, *ApJ.* 864, 56 • Kalita B. S., et al., 2022, *A&A.* in prep. • Liu D. et al., 2018, *ApJ.* 853, 172 • Puglisi A., et al., 2019, *ApJ.* 877, L23 • Puglisi A., et al., 2021, *MNRAS.* 508, 5217 • Schreiber C., et al., 2015, *A&A.* 575, A74 • Stefanon M., et al., 2017, *ApJ Supplement Series.* 229, 32 • Tacconi L. J., et al., 2008, *ApJ.* 680, 246 • Tadaki K.-I., et al., 2017a, *ApJ.* 834, 135 • Tadaki K.-I., et al., 2020, *ApJ.* 901, 74

10.3 . FIRST AUTHOR PAPER

I insert here my first author paper, it has been submitted to Astronomy & Astrophysics on July 14^{th}, 2023 and is under review. This paper present my study of DSFGs at Cosmic Noon and is entitled: *JWST/CEERS Sheds Light on Dusty Star-Forming Galaxies: Forming Bulges, Lopsidedness and Outside-In Quenching at Cosmic Noon*

A paper presenting and publicly releasing the “super-deblending" catalog is at the draft stage and should be submitted in the coming weeks/months.

Astronomy & Astrophysics manuscript no. ULIRGS_CEERS
July 14, 2023

JWST/CEERS Sheds Light on Dusty Star-Forming Galaxies: Forming Bulges, Lopsidedness and Outside-In Quenching at Cosmic Noon

Aurélien Le Bail[1], Emanuele Daddi[1], David Elbaz[1], Mark Dickinson[2], Mauro Giavalisco[3], Benjamin Magnelli[1], Carlos Gómez-Guijarro[1], Boris S. Kalita[4, 5, 6], Anton M. Koekemoer[7], Benne W. Holwerda[8], Frédéric Bournaud[1], Alexander de la Vega[9], Antonello Calabrò[10], Avishai Dekel[11], Yingjie Cheng[12], Laura Bisigello[13, 14], Maximilien Franco[15], Luca Costantin[16], Ray A. Lucas[7], Pablo G. Pérez-González[16], Shiying Lu[1], Stephen M. Wilkins[17, 18], Pablo Arrabal Haro[2], Micaela B. Bagley[15], Steven L. Finkelstein[15], Jeyhan S. Kartaltepe[19], Casey Papovich[20, 21], Nor Pirzkal[22], and L. Y. Aaron Yung[23]⋆

(Affiliations can be found after the references)

July 14, 2023

ABSTRACT

Context. We investigate the morphology and physical properties of a sample of 22 IR-selected dusty star-forming galaxies at Cosmic Noon ($z \sim 2$), using *James Webb Space Telescope* Near Infra-Red Camera images obtained in the Extended Groth Strip field for the Cosmic Evolution Early Release Science survey.

Aims. The exceptional resolution of the NIRCam images allows us to spatially resolve these galaxies up to 4.4μm and identify their bulge/core even when very extinguished by dust.

Methods. Based on red-green-blue images using the F115W, F200W and F444W filters, we divide each galaxy in several uniformly colored regions, fit their respective Spectral Energy Distribution and measure dust attenuations, stellar masses, star formation rates and ages. After classifying each region as star-forming or quiescent, we assign galaxies to three classes, depending on whether active star-formation is located in the core, in the disk or in both.

Results. (i) $\sim$ 70% of our DSFGs have a compact highly dust attenuated star-forming core that can contain up to 80% of the star-formation of the galaxy but only 20-30% of its stellar mass, and is always surrounded by a larger, less attenuated massive disk (no blue nuggets); (ii) 64% (27%) of disks are significantly (strongly) lopsided, likely due to asymmetric cold gas accretion, major mergers and/or large scale instabilities; (iii) 23% of galaxies have a star-forming core embedded in a quiescent disk, they are undergoing outside-in quenching, often facilitated by their strong lopsidedness inducing small and large scale instabilities; (iv) some galaxies host highly heterogeneous disks in term of RGB colors: these are driven by in-homogeneous dust attenuation; and (v) we find surprising evidence for clump-like substructures being quiescent and/or residing in quiescent regions.

Conclusions. This work demonstrates the major impact *JWST*/NIRCam has on understanding the complexity of the evolution of distant massive galaxies.

Key words. Galaxies: Bulges – Formation – Evolution – Star-formation – Structure

1. Introduction

Until recently, the existence of the so-called galaxy Main-Sequence, a correlation that the majority of star-forming galaxies observe in the stellar mass (M_*) versus star formation rate (SFR) plane up to redshift 3 (MS, e.g., Daddi et al. 2007; Elbaz et al. 2007; Noeske et al. 2007; Schreiber et al. 2015) and its tight scatter has been interpreted as evidence that star formation in most galaxies is a fairly ordered process (Schreiber & Wuyts 2020). The ‘consensus’ is that galaxies on the MS are forming stars in a quasi steady state inside gas-rich stellar disks (e.g., Sancisi et al. 2008; Dekel et al. 2009) whereas galaxies above the MS undergo a starburst, driven by stochastic processes such as major mergers, whose typical signature is compact star formation (e.g., Tacconi et al. 2008).

However, recent studies at $z \sim 1 - 3$ have shown that some massive ($M_* \geq 10^{11} M_\odot$) MS galaxies have a stellar distribution typical of late type galaxies but where the star formation only occurs in a compact nucleus (Elbaz et al. 2018; Puglisi et al. 2019, 2021; Tadaki et al. 2017, 2020; Franco et al. 2020; Gómez-Guijarro et al. 2022b; Jiménez-Andrade et al. 2019, 2021). The origin of these compact SF sub-mm galaxies (SMGs) observed with the *Atacama Large Millimeter Array* (*ALMA*) is yet to be fully understood. Three main scenarios to form the compact sub-mm nucleus are : (1) gas fueled to the core via violent disk instabilities (VDI) and clump migration, (2) a starburst induced by a major merger or (3) accretion and/or minor mergers (e.g. Gómez-Guijarro et al. 2022a). These compact SF nuclei could be an indication of an early quenching phase (Puglisi et al. 2019; Franco et al. 2020; Puschnig et al. 2023).

Besides the compact nucleus, high-z SF galaxies are observed to have giant SF clumps (radius $\sim$ 1kpc). The origin of these clumps has been investigated by many studies (Puschnig et al. 2023; Fensch & Bournaud 2021; Hodge et al. 2019; Rujopakarn et al. 2019; Mandelker et al. 2014; Wuyts et al. 2012; Elmegreen 1994, 1989). Mandelker et al. (2014) suggests that they can either be *in-situ* clumps, originating from VDI (e.g.

⋆ NASA Postdoctoral Fellow

Elmegreen 2011), in this case they are young and star-forming, or they can be *ex-situ* clumps, originating from minor mergers, in that case they will be older and with a low gas fraction and low specific star-formation rate (sSFR). A recent simulation showed that the formation of such long-lived giant clumps is only possible with a gas fraction of at least 50% (Fensch & Bournaud 2021). This large gas fraction is necessary to induce VDI that will produce clumps that will migrate toward the center, creating strong gas nuclear inflow and triggering an evolution of the structure of the galaxy, leading to a morphological evolution (Fensch & Bournaud 2021). This scenario is also favored by some observations (Förster-Schreiber et al. 2011; Guo et al. 2012). More recently, Puschnig et al. (2023) studied a local galaxy as proxy for high-z galaxies, confirming that the giant SF clumps mostly originate from a fragmentation of the disk, induced by VDI and not accretion or minor mergers. With its high spatial resolution, the *James Webb Space Telescope*'s (*JWST*) near-IR Camera (NIRCam) is able to better resolve such giant SF clumps and could help constraining this scenario. It is thus becoming clear that the galaxies within the MS scatter are not all largely unperturbed gas-rich disks. The compact SF cores, as well as the giant clumps, independently of their formation history, imply complex phenomenology at play, much different than local SF galaxies in the MS that are typically well behaved spirals.

Recently, emphasis has been brought onto other kind of asymmetries characterising high redshift SF galaxies. Kalita et al. (2022) discovered strong lopsidedness affecting the three massive SF galaxies in a $z = 2.91$ group core. They suggested a link between the lopsidedness of a galaxy in a dense environment to gas accretion and minor mergers. The lopsidedness would then be a marker of the point of impact of the accretion stream, following Bournaud et al. (2005) who investigated the origins of lopsidedness in simulated galaxies. Their conclusion is that it is very unlikely that the lopsidedness is the result of internal mechanisms but is more likely to be linked to the assembly history and the environment of the galaxy, to asymmetric gas accretion and to minor merger and interactions with neighbouring galaxies. This is also the conclusion of studies on lopsidedness of galaxies in the local universe (Jog & Combes 2009; Zaritsky et al. 2013). Rujopakarn et al. (2023) studied a galaxy in a dense environment with SF off-center substructures. They interpreted it as either forming spiral arms following a minor merger, an interaction with a neighbouring galaxy or a lopsided structure resulting from the point of impact of the cold gas accretion stream. Colina et al. (2023) reported *JWST* MIRI observations of GN20, an extremely luminous sub-mm galaxy residing in a $z = 4.05$ protocluster (Daddi et al. 2009). They reveal a massive extended disk surrounding the sub-mm compact nucleus, displaying strong lopsidedness. As of today, the lopsidedness has only been studied in dense environments and serendipitously. Observing lopsided disk in less crowded environment and inferring their prevalence in complete samples could shed further light on their presumed origin from interactions and accretion, and clarify whether a massive hosting dark matter halo is, or not, required.

By probing the rest-frame optical to near infrared (near-IR) at Cosmic Noon, *JWST*/NIRCam has a unique ability to fill the gap between the sub-mm compact nucleus observed with *ALMA* and the larger galactic disk observed in the optical and will help critically examining the competing scenarios. As an example, Rujopakarn et al. (2023) recently studied substructures within a dusty star forming galaxy (DSFG) at $z \sim 3$ imaged with both *ALMA* and *JWST*. From NIRCam images, they showed that the ALMA substructures are also visible at 4μm, demonstrating the direct link that one can draw between near-IR and sub-mm emissions. This suggests that the long wavelength channel of NIRCam might be a good tracer of compact obscured star formation in MS DSFGs.

The present study is part of the Cosmic Evolution and Epoch of Re-ionization Survey (CEERS[1]; ERS 1345, PI: S. Finkelstein) which is one of the Early Release Science (ERS) programs of the *JWST* (Gardner et al. 2023) that observed a part of the Extended Groth Strip (EGS) *Hubble Space Telescope* (*HST*) field with NIRCam (Rieke et al. 2023). EGS is too far North to be observed with *ALMA* and there is no high resolution imaging with the *Northern Extended Millimeter Array* (*NOEMA*) yet. However, the high sensitivity and exquisite spatial resolution of NIRCam towards 5μm can be used as a surrogate to identify the most obscured and massive regions within galaxies, hence those most likely vigorously star-forming.

Understanding how DSFGs are formed and evolve is crucial to get the larger picture of galaxy formation and evolution, and it could be a key element to explain the quenching of galaxies at and after Cosmic Noon. To this aim, *JWST*/CEERS allows a major step forward. Indeed Kartaltepe et al. (2023) already showed that *JWST* reveals the diversity of morphologies of galaxies at high redshift. *JWST* high spatial resolution and sensitivity is able to detect faint disks that were previously undetectable with *HST*. Moreover, a recent study by Kamieneski et al. (2023) uses *JWST*/NIRCam to probe the dust attenuation and sSFR of a lensed DSFG at $z = 2.3$. They demonstrate the power of *JWST*/NIRCam to precisely measure these properties at subgalactic scales, allowing them to conclude that despite a more dust attenuated bulge, the color gradient of this galaxy is mainly driven by an early stage of inside-out quenching. This makes *JWST*/NIRCam the best instrument to investigate the morphological evolution of DSFGs around Cosmic Noon, in terms of compact star formation, giant clumps and galaxy structure.

The paper is organized as follows. In Sect. 2 we present the data used in this study and the sample selection process. In Sect. 3, we detail the methods used to analyse each galaxy individually. In Sect. 4, we outline the main results of the analysis. Finally, in Sect. 5, we discuss the possible implications of the results in terms of formation and evolution of DSFGs at Cosmic Noon.

In this work, we adopt H_0 = 70km s^{-1} Mpc^{-1}, Ω_M = 0.3, Λ_0 = 0.7, and a Chabrier IMF (Chabrier 2003). When necessary, we converted stellar masses and SFR from Salpeter IMF (Salpeter 1955) to Chabrier IMF by subtracting 0.24dex.

2. Data

2.1. CEERS Imaging

For the purpose of this study, we used the NIRCam imaging of CEERS, reduced using a customized pipeline by the CEERS collaboration (Bagley et al. 2022). It includes images in 7 filters: F115W, F150W, F200W, F277W, F356W, F410M and F444W for an average 5σ depth of 28.6 AB mag (See Table 3 of Bagley et al. (2022) for more details, each filter/pointing as a slightly different depth). The Point-Spread-Function (PSF) Full-Width at Half-Maximum (FWHM) of those filters range from 0.040" to 0.145" for F115W and F444W respectively[2]. For this study, we used the CEERS imaging from the June 2022 pointings, which

---

[1] `https://ceers.github.io`

[2] `https://jwst-docs.stsci.edu/jwst-near-infrared-camera/nircam-performance/nircam-point-spread-functions`

represent 40% of the total area covered by NIRCam for CEERS between June and December 2022. We used the background subtracted images as we wanted to measure precise photometry. As we needed to extract galaxy properties based on spectral energy distributions (SEDs), we decided to complement shorter wavelengths by taking advantage of the existing *HST* imaging in the field. We used the publicly available *HST* data products version 1.9, available through CEERS. These mosaics were derived from *HST* archival data, but with improved calibration compared to the default pipeline products, and have astrometry tied to Gaia-EDR3 (Lindegren et al. 2021). As described in the accompanying data release, the mosaics were created from the combination of *HST* programs 10134, 12063, 12099, 12167, 12177, 12547, 13063, and 13792, and the reduction and calibration followed a similar procedure to those described in Koekemoer et al. (2011). We used two filters; F606W and F814W with a PSF FWHM of 0.115" and 0.110" respectively (Koekemoer et al. 2011). We did not use the *HST*/WFC3 images as these bands are redundant for bright galaxies, as they are covered by *JWST*/NIRCam images which are deeper and with better spatial resolution.

2.2. The "Super-deblended" FIR catalog

The goal of this paper is to study the morphology and SF activity of DSFGs. We select galaxies based on their IR detection in the state-of-the-art super-deblended far-IR (FIR) catalog of the EGS field (Le Bail et al., in preparation). FIR emission is a secure tracer of star formation (once the AGN components are removed), while optical/near-IR classification of SF galaxies is subject to larger uncertainties especially in the presence of dust. Hence, our FIR selection ensures the galaxies under scrutiny are truly highly SF.

The super-deblending is based on a well-established technique (Liu et al. 2018; Jin et al. 2018). It is a multi-wavelength fitting technique meant to optimize the number of priors fitted at each band to extract the deepest reachable information. They used images from *Spitzer* (24μm (FIDEL, Dickinson 2007)), *Herschel* (100μm and 160μm (PEP, Lutz et al. 2011), 250μm, 350μm, 500μm (HerMES, Oliver et al. 2012)), SCUBA2 (850μm (S2CLS, Geach et al. 2017), 450μm and 850μm from Zavala et al. (2017)) and AzTEC (1.1mm from Aretxaga (2015)). The key was to obtain an adaptive balance as a function of wavelength between the density of priors fitted, the quality of the fit, and the achievable deblending given the PSF sizes. They started with the deepest images and fitted band after band toward shallower images. Extensive Monte-Carlo simulations ensured that the uncertainties associated to the flux measurements were "quasi-Gaussian" (see Liu et al. 2018; Jin et al. 2018; A. Le Bail et al. in preparation).

2.3. Sample definition

We selected all sources securely detected in the FIR catalog (see Sect. 2.2) that fell in the CEERS/NIRCam regions observed in June 2022. Since short wavelength channels have a slightly different field of view than long wavelength channels, we checked that the sources are observed in all of them and that they were not too close to the edge of the images so that there were not partially cut. In detail, we require the galaxies to have $\mathrm{SNR}_{FIR} > 5$, where SNR_{FIR} is the signal-to-noise ratios (SNR) added in quadrature from 100μm to 1.1mm (Le Bail et al. in preparation) and have at least one detection (SNR> 3) in a *Herschel*/SPIRE band after deblending (required to reliably measure SF components in case of AGNs). The implication of the IR selection is that we don't have a stellar mass complete sample of SF galaxies (e.g., complete above some mass threshold), and we have instead something closer to a (redshift-dependent) SFR limit. We are aware that we are missing SF galaxies below our IR detection threshold, as we wish to focus to highly (and securely) star-forming galaxies.

We also limited the sample to galaxies within $1.5 < z < 3.0$, as we are willing to focus on galaxies at "Cosmic Noon", as recalled in the Introduction. To get accurate redshift estimates, we used the recent redshift compilation produced by Kodra et al. (2022), which includes photometric redshifts based on CANDELS (Grogin et al. 2011; Koekemoer et al. 2011) as well as grism-based redshifts from 3D-HST (Momcheva et al. 2016) and spectroscopic redshifts from the MOSDEF survey (Kriek et al. 2015).

This sample comprised a total of 26 IR-detected sources. From these, 4 had to be rejected after a clean up. After close inspection, three galaxies were in a blended region and/or close to a much brighter IR source, making the *Herschel* measurements less reliable. The last rejected source hosted an AGN (clear radio excess, ∼ 10× brighter than what is expected for the radio continuum based on IR emissions, and X-ray detected: ID15327, RA = 215.82825, Dec = 52.80844, $z_{phot} = 1.61$, $log_{10}(L_{AGN}/L_{\odot}) \gtrsim 11.3$), hence the majority of its IR luminosity does not come from SF regions which are the main objects of this study.

This left us with a clean sample of 22 FIR-bright DSFGs around Cosmic Noon. We illustrate in Fig. 1 the distribution of the sample in terms of stellar mass estimated in the pre-*JWST* era (Stefanon et al. 2017) and total IR luminosity (Le Bail et al. in preparation, calculated based on the equations in Press et al. (1992)) versus redshift (Kodra et al. 2022). We also show the distance from the MS (Schreiber et al. 2015) with a 0.6 dex total scatter (Rodighiero et al. 2011) defined as $\Delta_{MS} = SFR_{IR}/SFR_{MS}$. Schreiber et al. (2015) uses a Salpeter IMF (Salpeter 1955), we converted stellar masses and SFRs from Salpeter IMF to Chabrier IMF by subtracting 0.24 dex. The red shaded region corresponds to the pure starburst region as defined in Liu et al. (2018) ($log_{10}(SFR_{IR}/SFR_{MS}) > 0.6$ dex), we have two galaxies in our sample classified as pure starburst. The rest is mostly either within the scatter of the MS, but above its average trend, i.e. above the MS but below the starburst regime.

In Figs. 2.1, 2.2 and 2.3, we show RGB cutouts of our sample of galaxies using the F115W, F200W and F444W filters of NIRCam. The galaxies are separated in three classes, as discussed in detail in the next Section.

3. Methods

In this Section, we detail the methods used to analyze each galaxy, taking one of the objects (ID15371) as an example, to better clarify the procedure that we applied to all galaxies. For each galaxy, we started by creating cutouts in each band (*HST*/ACS F606W, F814W and *JWST*/NIRCam F115W, F150W, F200W, F277W, F356W, F410M, F444W). We show the cutouts of a DSFG in Fig. 3 where one can already see by eye a difference between the disk visible in all bands and the center of the galaxy invisible in the *HST* images but getting brighter at longer wavelengths, justifying the need to study each component individually rather than the galaxy as a whole. One of the first steps was to see if we could identify a bulge and a disk in each galaxies just like for ID15371, as discussed below.

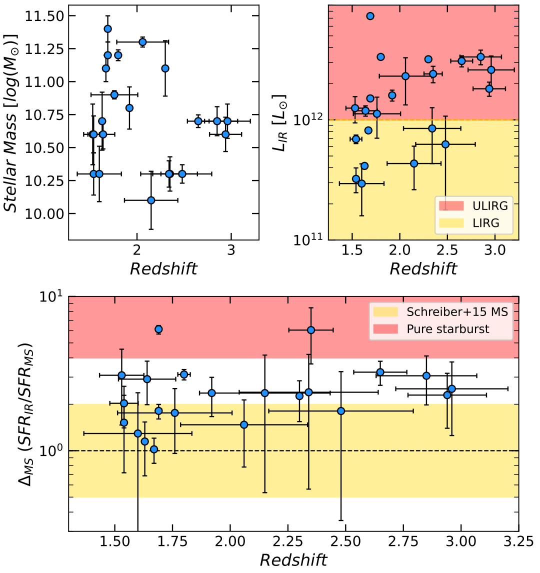

Fig. 1. Stellar Mass (upper-left panel), total IR luminosity (upper-right panel) (Le Bail et al. in preparation) and distance from the Main Sequence (MS, lower panel) of the galaxies in the selected sample versus their redshift. The colors on the upper-right panel delimits the luminous IR galaxies (LIRG, in yellow) and ultra-LIRG (ULIRG, in red) local regimes for information. On the lower panel, the yellow shaded region illustrates the MS from Schreiber et al. (2015) while the red shaded region illustrates the pure starburst regime (Liu et al. 2018).

JWST/NIRCam images have a spatial resolution ranging from 0.040″ at 1.15μm up to 0.145″ at 4.4μm. The larger 4.4μm PSF allows a resolution in physical size down to 1.23 (1.12) kpc for a galaxy at redshift 1.5 (3). This means that we were able to spatially resolve galaxy substructures down to a radius ∼ 0.6kpc. This made the resolution of F444W perfect for this study as we know the sizes of compact SF regions and giant clumps to be ∼ 1kpc (Gómez-Guijarro et al. 2022b; Rujopakarn et al. 2019; Förster-Schreiber et al. 2011).

3.1. Measuring galaxy sizes

Several studies have shown that the regions of star-formation, either traced by the dust emission at 1.1mm observed with *ALMA* or by the radio continuum emission detected by the *Very Large Array* (VLA), are more compact than the optical size of the galaxy (Puglisi et al. 2019; Gómez-Guijarro et al. 2022b; Fujimoto et al. 2017; Jiménez-Andrade et al. 2019, 2021).

JWST, with its sensitivity of the near and mid-IR, can detect both the obscured star-forming central part of each galaxy invisible with *HST* and the less obscured larger system, invisible with ALMA or *VLA* and bridge the gap.

To investigate this, we measured the total near-IR half-light radius ($R_{e,NIR}$) of each galaxy in the closest band to 1.6μm rest-frame (F410M or F444W filter depending on the redshift). This rest-frame wavelength was chosen as it is a known tracer of the stellar mass of galaxies and is not affected by dust attenuation (Hainline et al. 2011; Casey et al. 2014). Moreover a recent study using NIRCam/CEERS data showed the excellent agreement between the near-IR size and the stellar mass size of galaxies around Cosmic Noon (van der Wel et al. 2023). We measured $R_{e,NIR}$ from a curve of growth method, given that in all cases the PSF has a negligible effect (much smaller than any $R_{e,NIR}$). The $R_{e,NIR}$ was defined as the radius of a circular aperture, centered at the center of mass (barycenter) of the galaxy, which encompassed half of the total flux density of the galaxy at the considered wavelength. To estimate the uncertainty, we used the fact that we typically have a 5% uncertainty on the measurement of the total flux of the galaxy (see Sect. 3.5 for more details on the photometry measurements). We also measured the bias introduced when using a circular aperture for edge-on galaxies (like ID23510 in Fig. 2.1) by comparing the fluxes encompassed in an elliptical aperture and a circular aperture. The difference is about 5%. Hence, by changing the total flux of the galaxy within 10% we can estimate the uncertainty on $R_{e,NIR}$ for which 50% of the total flux is encompassed.

We also measured the total optical half-light radius ($R_{e,O}$) of each galaxy in the closest band to 550nm rest-frame following the same procedure to compare it with $R_{e,NIR}$.

3.2. Identification of cores/bulges

Depending on the redshift, the F444W filter of NIRCam probes the rest frame near-IR between 1.1μm and 1.8μm which is a good tracer of stellar mass (van der Wel et al. 2023). Hence, inspection of galaxy morphologies in this filter allowed us to search for the center of mass of each galaxy in our sample, or lack there-of, as a well defined peak in the F444W images. We were able to clearly identify a peak in the flux distribution of this filter for every galaxy. Depending on the galaxy, the peak was more or less pronounced, but always confidently there. We then defined a region in each galaxy encompassing the peak, as the core or the bulge of the galaxy. The regions are defined by eye as the peak is easily identifiable in every galaxies, the limit of the core is where the flux coming from the red F444W filter doesn't dominate anymore the RGB (F115W, F200W, F444W) color. Generally, a bulge is often defined in the literature as a quiescent central component with a high Sersic index (e.g., $n \sim 4$), and is a common component in local massive galaxies. In our study we did not attempt obtaining Sersic fits of separate components, and, more importantly, we anticipated that in many cases the central concentrations would not be quiescent, actually, most of them were highly SF and attenuated. We decided thus to call the central concentrations as cores when they were SF and bulges when they were quiescent. They are represented by the regions delimited by the red dotted lines in all galaxies in Fig. 2.1, 2.2 and 2.3.

We emphasize that for most of our sample, it would not have been possible to identify the center of mass only based on *HST* images (see e.g. ID15371 in Fig. 3 as an obvious example). This demonstrates once again the power of *JWST* when it comes to studying high-z DSFGs.

3.3. Lopsidedness

Having defined the core/bulge of each galaxy, we considered the rest to be the disk. Hence, we could obtain an evaluation of the lopsidedness for each galaxy. We considered it to be an important property to investigate because a lot of galaxies in our sample are obviously highly lopsided already by visual inspection (see for example ID11887, ID13776, ID18278, ID18694 in Fig. 2.1 and 2.2). To quantitatively study this phenomenon, we defined two

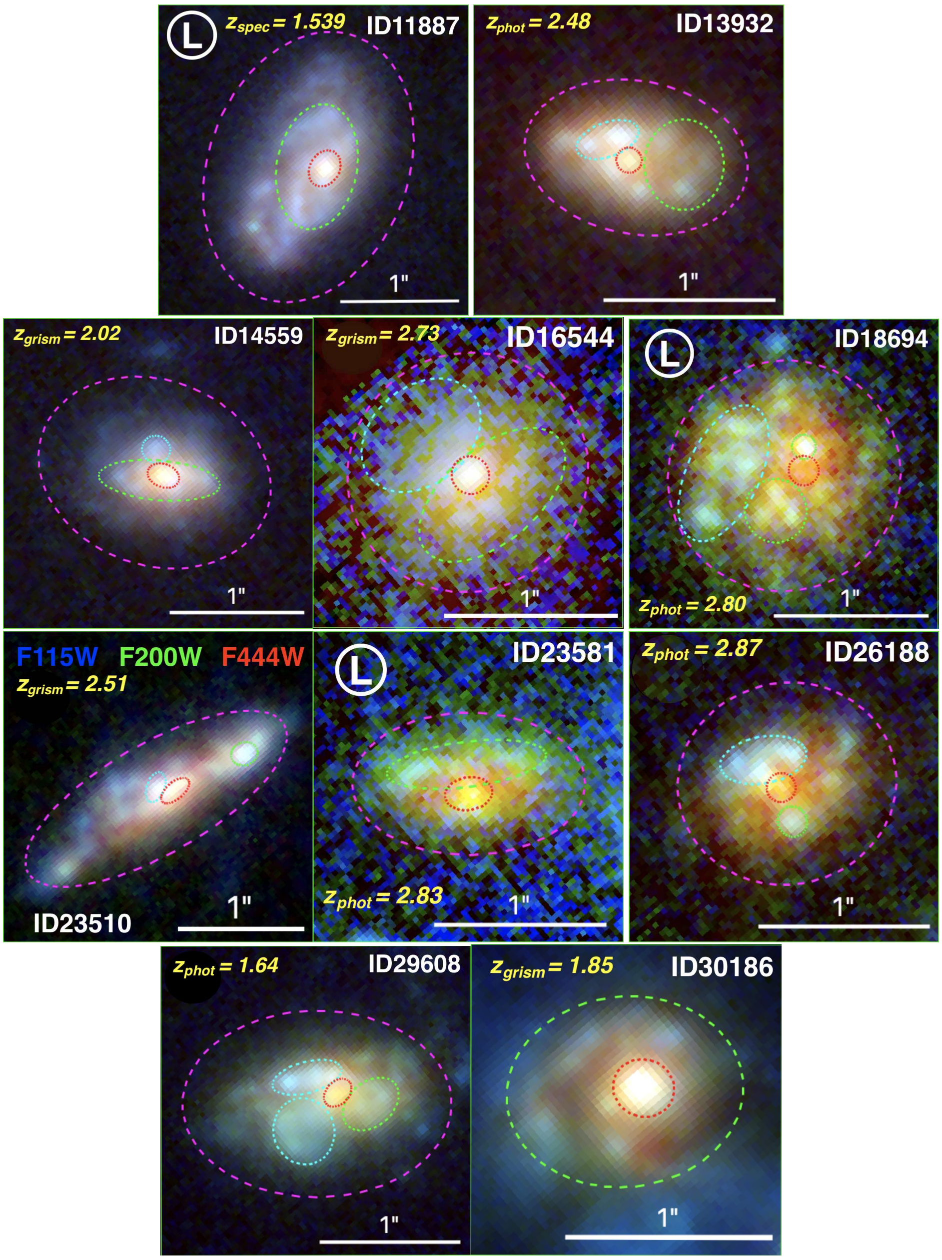

Fig. 2.1. Type I: *SF disks with a red SF core* (see Sect. 3.7). RGB (F115W, F200W, F444W) non PSF-matched cutouts. In each cutouts the white bar defines the scale of the image. The dotted regions correspond to the different studied components, the core/bulges are shown in red, the rest are the different parts of the disks (blue or green show patches when present, magenta is the remaining of the disk) see Sect. 3.5. The galaxies with a "Ⓛ" are the most lopsided galaxies of our sample, see Sect. 4.1.3.

parameters: the eccentricity, defined as:

$$E = \sqrt{\frac{(X_{core} - X_{disk})^2 + (Y_{core} - Y_{disk})^2}{R_{disk}^2}}, \tag{1}$$

where (X_{core}, Y_{core}) and (X_{disk}, Y_{disk}) are the coordinates of the central core of the galaxy and of its disk respectively, while R_{disk} is the radius of the disk. The center of the core was simply defined as the pixel with the maximum flux density in the F444W filter. The center of the disk was defined as the barycen-

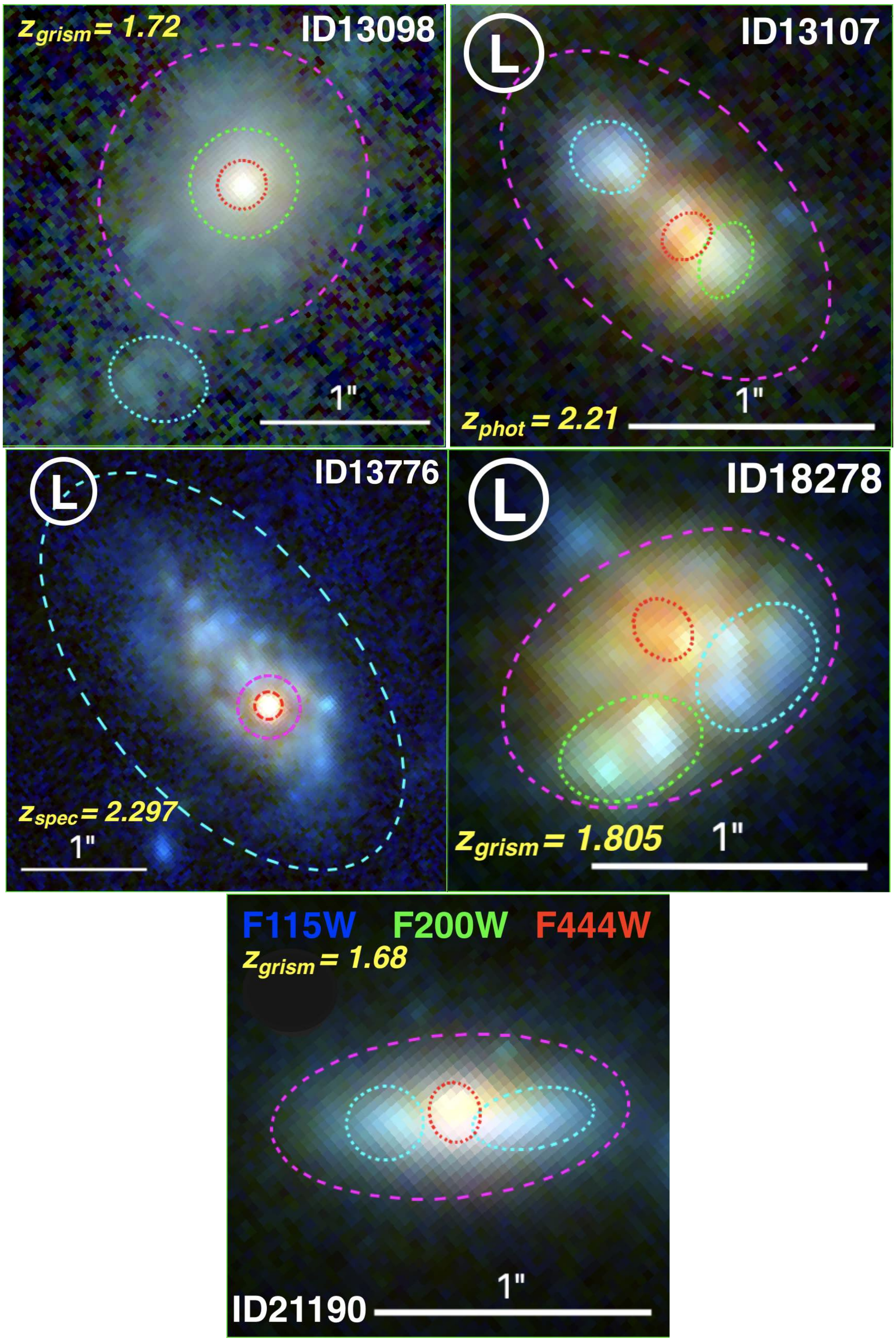

Fig. 2.2. Type II: *Quenched disks with a SF core* (see Sect. 3.7). Similar to Fig. 2.1.

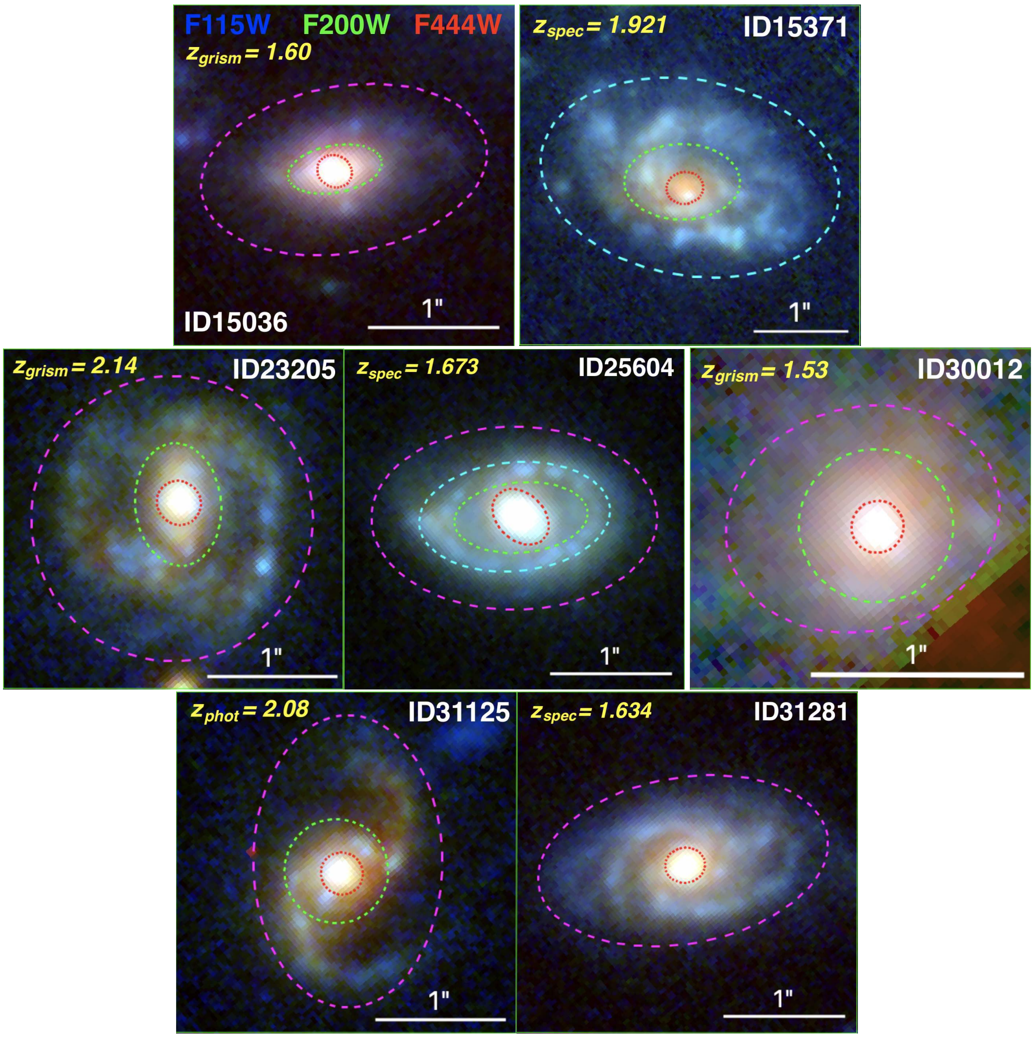

Fig. 2.3. Type III: *SF disks with a quenched bulge* (see Sect. 3.7). Similar to Fig. 2.1 and 2.2.

ter of the disk measured in the rest-frame optical band (F150W or F200W depending on redshift). We measure it in the optical and not in the near-IR because the disk is less attenuated than the core, hence brighter than the core at these wavelengths. To not be biased by the core, we applied a circular mask centered on (X_{core}, Y_{core}) with a radius defined by the closest pixel to the center that has a F444W flux density less than half the core center flux density. Finally, R_{disk} was calculated using a circular aperture centered on (X_{disk}, Y_{disk}) encompassing half of the disk flux density. This quantifies the eccentricity of the disk with respect to the core/bulge compared to its size and is a-dimensional.

The other quantity that we defined to probe the lopsidedness of the galaxies is the asymmetry. The asymmetry was calculated for the F444W NIRCam filter as we are trying to probe the mass distribution asymmetries and, as previously mentioned, F444W is the best tracer of the stellar mass distribution. We calculated the asymmetry by rotating each image by 180° and subtracting it from the original image, the center of rotation was (X_{core}, Y_{core}) from Eq. 1. The asymmetry is defined as:

$$A = \frac{\sum_{i=0}^{N} |F_i - F_i^{180^\circ}|}{F_{tot}}, \tag{2}$$

where F_i and $F_i^{180^\circ}$ are the flux of the *i-th* pixel and its 180° symmetric counterpart with respect to the center of the central core/bulge as defined in Equation 1. F_{tot} is the total flux of the galaxy. Since we worked on background subtracted images, we considered the background asymmetry to be negligible. This quantity describes how smoothly and how symmetrically the stellar mass is distributed around the central core/bulge of the galaxy and is also a-dimensional. Usually, the lopsidedness is probed using a Fourier decomposition (e.g. Dolfi et al. 2023; Kalita et al. 2022; Jog & Combes 2009; Bournaud et al. 2005). We decided to use a different, simpler method; the asymmetry,

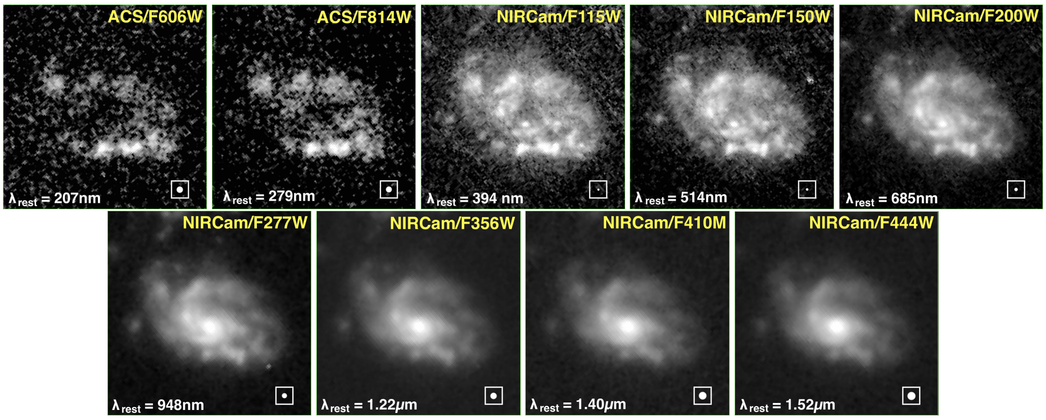

Fig. 3. Cutouts of *HST*/ACS and *JWST*/NIRCam images of the DSFG ID15371 at z_{spec} = 1.921. Cutout size: 3.6″× 3.6″. We also indicate the rest-frame wavelength corresponding to each filter (white label). The filled circle in the white box illustrate the PSF size for each filter.

that has already been used in gas velocity space and was found to correlate well with the Fourier analysis of stars (Bournaud et al. 2005; Matthews et al. 1998).

3.4. Clumpiness

After identifying the core or bulge of each galaxy, we investigated the surrounding disk-like structures. Some of the galaxies have a smooth disk, others have a much more perturbed/complex disk morphology showing a large number of clumps (see Fig. 2.1, 2.2 and 2.3).

We did not embark in a physical study of the clumps in this work. Our goal for this paper is to assess the presence or not of clumps in the disks and have an idea of how fragmented the disks are. Hence, we did not try to derive any physical properties of the individual clumps. We decided to measure a clumpiness index, defined as the number of clumps in the disk of each galaxy. We counted the number of clumps visually identifiable in the RGB (F115W, F200W, F444W) image, making sure that the bulge/central concentration was not counted as a clump. This number varies from 0 up to 7 for the clumpiest galaxy. To be counted as a clump, the feature had to be compact compared to the galaxy size, and either had to have a different RGB color from the surroundings and/or appear as a local brighter spot. The clumps appear most clearly at the shortest wavelength (F115W or F200W filters), as expected (Wuyts et al. 2012). For ID15371, we identify 4 clumps, there are shown by the white ellipses in the left panel of Fig. 4.

3.5. Spatially resolved photometry

To quantitatively study our galaxies, we needed photometry measurements. We decided to divide our galaxies in several components. For the simplest cases we only had the core/bulge and the disk, and when the disk had several clump/patches with different colors in the RGB image, we broke it down to several circular or elliptical regions. Each region was designed so that it had, qualitatively, a homogeneous (F115W, F200W, F444W) color. The division of the disk is once again done by visual inspection. We emphasize that we seek to study each region that has a different color, hence, if several clumps are close and with a similar RGB color, we consider them to be part of the same disk component. Moreover, due to the spatial resolution of the PSF-matched images, we did not want to design too small regions that could lead to biased flux measurements. We tried to respect a balance between the size of the component we defined (not too close to the PSF size) and the homogeneity of the RGB color inside it. We emphasize that the components are not necessarily concentric as most of the galaxies are not radially symmetric and are not limited in number. If we observed, for example, two blue disconnected patches in a galaxy, we defined them as two different components and fitted them individually. In the case of ID15371, we divided the galaxy in three regions, the red central core/bulge, the bluer disk and an intermediate region, that is still part of the disk but close to the red core and with intermediate colors (see Fig. 4).

In terms of rest-frame colors, since our sample of galaxies is distributed across $z \sim 1.5$ to $z \sim 3$, F115W probes the rest-frame near-UV/blue (300 − 460nm), F200W probes the rest-frame green/red (500−800nm) and F444W probes the rest-frame near-IR (1110 − 1780nm). The scatter in rest-frame wavelength is less or equal to the band-width of each filter. This means that we globally probed consistent colors between galaxies.

By dividing each galaxy in sub-galactic regions, there was a risk that small regions get close to the PSF FWHM of some filters. Hence, leading to an underestimation of the flux at the longest wavelengths, and an artificial deformation of the SED. To avoid this, we decided to work on PSF-matched images using the broader PSF of the F444W filter. In Fig. 4, we show RGB images of the DSFG ID15371 using (F115W, F200W, F444W) before and after PSF-matching. To make sure that we didn't underestimate stellar masses and SFR when running the SED fitting, we chose regions larger than the PSF FWHM (0.145”). In Fig. 2.1, 2.2 and 2.3, for each galaxy we overlay the delimitation of the different components we decided to study separately based on their color (those RGB images are showed before PSF-matching).

After having defined the regions to study, we measured the flux in each band for each region. To do so, we summed the value of each pixel in each region of the science image. The pixels were counted only once, meaning that the flux in the smaller regions (like the red ellipse for ID15371) was not included when calculating the flux of larger regions (like the green ellipse for ID15371, see Fig. 4).

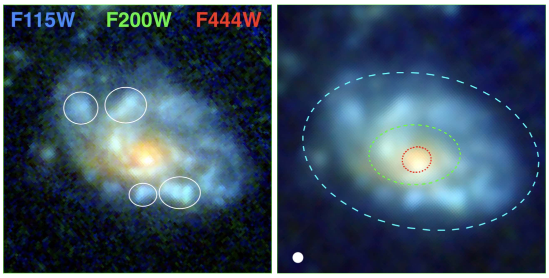

Fig. 4. RGB (F115W, F200W, F444W) image of the galaxy ID15371 (3.6"× 3.6") at z_{spec} = 1.921 before (left panel) and after (right panel) PSF-matching. In the left panel, the white ellipses show the features we identified and counted as clumps. In the right panel, the colored dotted lines correspond to the division of the galaxy in homogeneously colored regions and the white filled circle to the PSF size.

Our goal was to fit the SED of the different components of each galaxy. For the properties that we later extracted from these SEDs to be reliable, it was crucial that we had reliable uncertainties on the fluxes. To estimate the flux uncertainties, we re-normalized the errors propagated via the Root Mean Square (RMS) images. The uncertainty was defined as:

$$df = f_{\lambda,N} \times \sqrt{\sum_{i=0}^{N} \sigma_i^2}, \tag{3}$$

where the sum was made on all pixels in the region, σ_i is the RMS of the pixel i, and N the total number of pixel in the region. We decided to define $f_{\lambda,N}$, a normalisation factor that takes into account extra noise, e.g. from the correlated signal between pixels that is particularly important for the long wavelength filters that were drizzled from a pixel size of 63mas to 30mas. To calculate this factor, we measured the flux dispersion in ∼ 20 empty regions of the science image for several apertures in each band. We then compared this value to the RMS calculated from the RMS image in apertures of the same size and the normalisation factor is defined as their ratio. To be conservative, we never applied a factor leading to lower uncertainties. These factors are generally small, ($f_{\lambda,N} \sim 1.5$ at most).

3.6. SED Fitting

To characterize our sample of galaxies, we needed to have access to their resolved M_* and SFR. To this aim, we fitted each galaxy component SED using the Code Investigating GALaxy Emission (CIGALE, Boquien et al. 2019). We used a single declining exponential model also known as "τ model" to model the star formation history of each galaxy. We adopted the Bruzual & Charlot (2003) model for computing the spectral evolution of single stellar populations with a fixed solar metallicity of Z = 0.02 which is reasonable for $M_* \sim 10^{10-12} M_\odot$ DSFGs following the Mass-Metallicity relation (Ma et al. 2016). After testing with and without including nebular emissions, we decided not to include them as, for our sample, they lead to higher χ^2 with no noticeable effect on the extracted properties (A_V, SFR, M_* and redshift).

Some galaxies showed possible signature of strong emission lines, visible as green patches/clumps in Figs. 2.1, 2.2 and 2.3. However, including them had a negligible effect on the estimation of the SFR since it usually had a 50% uncertainties. We discuss this in more detail in Sect. 5.1.

We used a modified Charlot & Fall (2000) dust attenuation law and the Draine et al. (2007) dust emission models update from 2014 to predict FIR flux densities. The idea behind the modification of Charlot & Fall (2000) model is that young stars embedded in their birth cloud suffer from additional attenuation compared to stars that have broken out and escaped into the ISM, and that the attenuation curves associated to the birth cloud and the ISM must be different. In practice, this is modelled by assuming two different power-law attenuation curves of the form $A(\lambda) \propto \lambda^{\delta}$: one for the birth cloud with a slope of $\delta_{BC} = -1.3$, and one for the ISM with a slope of $\delta_{ISM} = -0.7$. Because radiation from young stars has to travel through both the birth cloud and the ISM to escape the galaxy, the spectrum of stars younger than 10Myr are attenuated by both the birth cloud and ISM curves. Stars older than 10Myr are only attenuated by the ISM curve (Boquien et al. 2019).

For the redshift, we used the Stefanon et al. (2017) catalog, as well as the latest redshift catalog published by Kodra et al. (2022). We encountered three different cases:

- If we had a high-quality spectroscopic redshift, then we used it and fixed it. We have 5 galaxies with a spectroscopic redshift.
- If we had a grism-based redshift from 3D-HST, we downloaded the spectrum and examined its quality, actual features detected, the redshift probability distribution and defined the redshift and its uncertainty accordingly. We have 10 galaxies for which we find a high-quality grism-based redshift.
- If we only had photometric data, we allowed $(1 + z)$ to vary within ±10%. We have 7 galaxies with a photometric redshift.

In Fig. 5, we show the best SED models corresponding to each region of our example galaxy defined in Fig. 4.

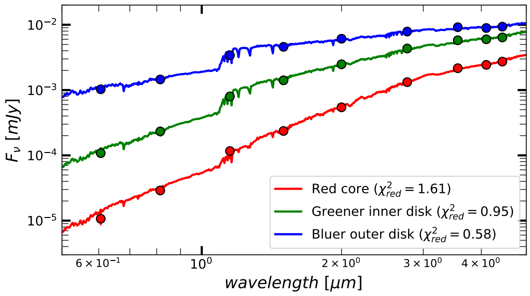

Fig. 5. Best SED models computed by CIGALE (Boquien et al. 2019) for the red core (in red), the blue disk (in blue) and the intermediate region (in green) of the DSFG ID15371 at z_{spec} = 1.921 (the same example galaxy shown in Figs. 3 and 4). We show in the legend the value of the reduced χ^2 (χ^2_{red}) for each SED fit.

To be able to extract reliable information from the SED fit, it was crucial to check the fit quality. To be conservative and have reasonable χ^2, we decided to limit the photometric accuracy of each band to $S/N = 20$. However, if the CIGALE fit returns high χ^2 values, there is a possibility that the input flux uncertainties are still underestimated. In that case, we increased the uncertainties by adding up 10% of the flux to the error in each band. To consider the fit acceptable, we want the reduced χ^2 such as $\chi^2_{red} \leq 1.67$, which is the reduced critical value corresponding to a significance level of 10% in the χ^2 test for 8 degrees of freedom.

To estimate the robustness of the best model, we studied the χ^2 distributions associated to the 3 main free input parameters: the dust attenuation, the age of the stellar population and the e-folding time. In Fig. 6, the upper-left panel shows the χ^2 distribution associated with the different values of the dust V-band attenuation A_V of the stellar continuum used to fit the SED of the red core of the DSFG ID15371. The upper-right panel shows the same information for t/τ with t and τ being the age of the oldest stars and e-folding time of the stellar population used to define the star formation history of the galaxy. Taking the width of these distribution at χ^2_{min} + 1 and χ^2_{min} + 2.7 give us the 68% and 95% confidence interval respectively (Avni 1976), illustrated by the horizontal thick and thin dashed lines in Fig. 6. The fact that we see only a portion of the distribution for t/τ comes from the fact that the age is getting close to the age of the Universe, allowing larger t would not make physical sense.

We can use the same reasoning for the properties extracted from the SED like the M_* or the SFR averaged over the last 10Myrs. We show an example in the lower panels of Fig. 6.

Just by looking at Fig. 6, we can already conclude that the red core of the DSFG ID15371 is dusty ($A_V \sim 2.73$) and weakly star-forming (SFR ∼ 18 - 40 $M_\odot/yr$ and $t/\tau \gg 1$).

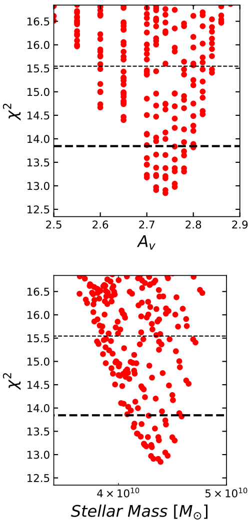

Fig. 6. χ^2 distributions associated with the dust attenuation (upper-left panel), t/τ (upper-right panel), the stellar mass (lower-left) panel and SFR averaged over the last 10Myrs (lower-right panel) produced by CIGALE (Boquien et al. 2019) for the fit of the red core SED of the galaxy ID15371 at z_{spec} = 1.921. The thick and thin black dashed lines corresponds to the 68% and 95% confidence interval respectively.

As a sanity check, we estimated the SED of the whole galaxy by summing up the SEDs of all the components. We then compared this SED with the near-IR and FIR flux densities measured in the super-deblended catalog (Stefanon et al. 2017, Le Bail et al. in preparation) to make sure that they were consistent. If the FIR flux densities are brighter than predicted by the SED fitting, it can be a hint that this galaxy is in a starburst episode and/or that there is a deeply attenuated component that is not visible even at 4.44μm. It can also be due to the presence of an AGN that boosts the FIR flux, this can be confirmed by a radio excess or an X-ray detection (Le Bail et al. in preparation, Stefanon et al. 2017). We recall that we removed from the sample only one galaxy where we knew that the FIR luminosity was dominated by the AGN luminosity (see Sect. 2.3) but kept those where the AGN luminosity didn't dominate the FIR luminosity. On the contrary, if the SED predicts a FIR flux density brighter than the one measured, it means that there is a problem in the fitting possibly linked to the grid of the input parameters. In Fig. 7, we show the comparison between the total SED of the galaxy ID15371 and the FIR flux densities. For this galaxy, the flux densities are consistent with the predicted FIR SED meaning that there is no hidden component. This is the case for all the galaxies in our sample except one (ID13107 for which we have a FIR detection brighter than the SED model, pointing toward either a deeply attenuated component or an AGN even though there is no AGN signature in X-ray or radio). However for 3 galaxies (ID13098, ID13776 and ID31281), the measured 100μm flux is boosted compared to the SED predicted flux, possibly a signature of a hot AGN, 2 of them have an X-ray detected AGN (Nandra et al. 2015). By observing Fig. 7, one can notice that the predicted IRAC fluxes are fainter than the actual measurement. This observation is not true for every galaxy, we measure the flux in the NIRCam F356W and F444W which probe the same wavelength as IRAC channel 1 and 2 to be fainter for this galaxy. This is mostly a sign of blending in the earlier IRAC imaging.

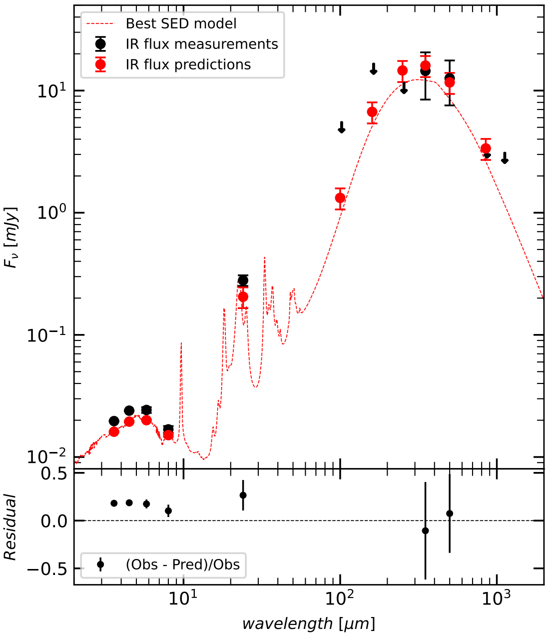

Fig. 7. Total SED of the galaxy ID15371 at z_{spec} = 1.921 in red. It was calculated by adding up the CIGALE best SED model of each component. The black points are the near-IR and FIR fluxes with their uncertainties or upper limits (arrows) from the super-deblended catalog (Le Bail et al. in preparation). From the FIR data points, we have $SFR_{IR} = (150 \pm 15)\mathrm{M}_\odot\ \mathrm{yr}^{-1}$ (Le Bail et al. in preparation), the CIGALE fits give a consistent total $SFR_{10Myrs} = (197 \pm 125)\mathrm{M}_\odot\ \mathrm{yr}^{-1}$. Given its stellar mass ($M_* = 10^{11}\mathrm{M}_\odot$), this galaxy is on the main sequence.

A caveat of this SED fitting method is that we used the same SFH and parameters for all regions, some with very different properties. We chose to use the simple tau model because of the meaning of t/τ regarding the star-forming activity of the galaxy. We decided to make a two-pass SED fitting, in the first pass, the goal was to separate the star-forming from quiescent regions. In the second pass, we fitted the star-forming regions with a nearly constant SFR (by imposing $\tau \gg t$). This allowed to have a good estimate of the recent SFR. Moreover, by comparing it to the far-IR SFR from the super-deblended catalog (Le Bail et. al, in preparation.) and to the relative position of each component with respect to the Main Sequence or the quiescent quadrant of the UVJ color-color diagram (see Sect. 3.7 for more detail on these last two points), we had a confirmation of the star-forming activity of each galaxy component. For the quiescent regions, there can be a degeneracy between the age and the dust attenuation, to tackle this, we imposed $t \gg \tau$. We estimated that the good quality of the photometry in the rest-frame near-IR and the two-pass SED fitting procedure allowed us to get robust estimates of both the stellar mass and the SFR of each component.

To tackle the great diversity of galaxies, we decided to divide them into several classes as defined in the next Section.

3.7. Classification

From the CIGALE SED fitting, we derived an estimation of the M_*, the SFR and the dust attenuation (A_V) of each component of the galaxies. For the galaxy ID15371, in the upper panel of Fig. 8, one can see the three components respective M_* and SFR plotted on the MS (Schreiber et al. 2015; Huang et al. 2023). All the components of the DSFG ID15371 have some ongoing star-formation, with the red core being on its way to quenching but still slowly star-forming.

Using the best SED models provided by CIGALE, we also estimated the rest-frame U, V and J AB magnitudes. We used Apellániz (2006) U and V filters, and for the J band, we used the 2MASS J relative spectral response curve. In Fig. 9, we display all the regions of our galaxies on the $(V-J, U-V)$ plane. We recover the sSFR effect: when moving from the lower right corner to the upper left corner, the sSFR decreases (Wang et al. 2017). This makes the UVJ color-color diagram ideal to separate SF galaxies from quiescent galaxies. We note that the galaxies with sSFR $\lesssim 0.1\mathrm{Gyr}^{-1}$ are all in the quiescent region defined by Whitaker et al. (2011) and delimited by the black dashed line in the Figure. The colored dotted lines delimit the regions defined by Zick et al. (2018).

For the DSFG ID15371, we have confirmation in the UVJ diagram that all the components are star-forming (lower panel of Fig. 8). Moreover, the three components are aligned on the diagonal of the diagram which is the signature of a gradient of dust attenuation from the center towards the outer parts (Calzetti et al. 2000). Indeed, from the SED fitting, we had $A_{V,red} = 2.70 \pm 0.11 > A_{V,green} = 2.09 \pm 0.23 > A_{V,blue} = 0.75 \pm 0.11$.

Generally, to estimate if a region was SF or quiescent, we used the UVJ color-color diagram (is the component in the quiescent quadrant or not ?), the position relative to the MS (is the component on/above the MS or well below it ?, what is its position compared to the other regions of the same galaxy ?) and, as we used a simple exponential model for the star-formation history, the value of t/τ is also an indicator of the star-formation activity. If $t/\tau \gg 1$, then the peak of star-formation is firmly in the past, and the component is on its way to quenching. On the contrary, if $t/\tau \lesssim 1$, the galaxy is still actively star-forming. Based on these three pieces of information, we were able to discriminate between SF and quiescent regions. Here, we defined a region as quiescent if below the Main Sequence and the other galaxy components (by ~ 0.6dex). Hence, some regions that we classified as quiescent are not completely passively evolving and could still be slowly star forming. Most of the time, the three indicators are in agreement, however, in some cases the results were ambiguous: the regions where all three indicators where not in agreement represent less than 5% of all the studied regions. In that case, we first looked at their position relative to the MS to see if it was consistent with the t/τ values from the best models and it always was. The inconsistency of the UVJ color-color diagram can be explained in several ways: the UVJ diagram uses only a part of the information (3 rest-frame bands) contrary to the other probes that uses the full SED. More importantly, real situations exist where the UVJ diagram characterizes correctly the presence of star formation but this star formation is suppressed as exemplified by the sub-MS location (suppressed with respect to the ensemble average given the mass) and by the t/τ (suppressed with respect to the past star formation history of this galaxy). That is the case for the central region of ID15371 (see Figs. 6 and 8). In the rare cases where the t/τ value didn't allow any conclusion ($t/\tau \sim 1$), we decided based on the MS and the UVJ color-color diagram that were consistently pointing either toward star-formation or quiescence. In all the cases, we were able to classify the regions as quiescent or star-forming.

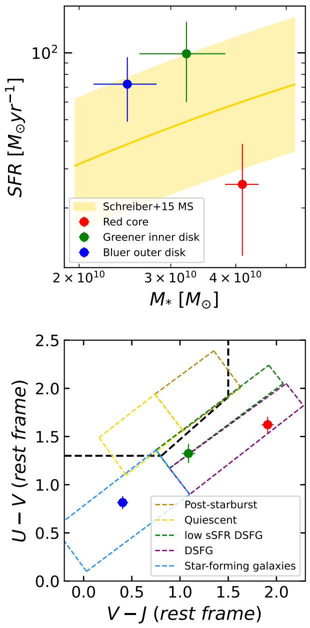

Fig. 8. Upper panel: Galaxy ID15371 components plotted over the Main Sequence (Schreiber et al. 2015; Huang et al. 2023). Lower panel: Galaxy ID15371 components in the UVJ color-color diagram, the black dotted line delimits the quiescent region (Whitaker et al. 2011) and the colored ones, the regions defined by Zick et al. (2018). See Fig. 4 for the definition of the components.

As a result of this analysis, we had 22 vastly different galaxies with various morphologies, colors (see Figs. 2.1, 2.2 and 2.3) and star-formation activity. We found that the variety of features could be meaningfully re-conducted to three galaxy groups:

- Type I: *SF disks with a red SF core*, characterized by the fact that all their regions are SF. Some have a complex multi-

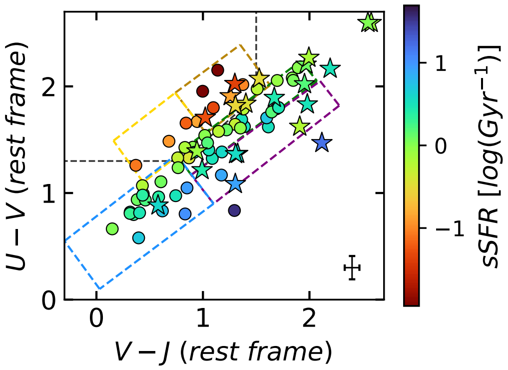

Fig. 9. UVJ color-color diagram. Each marker represents a region of a galaxy. The star-shaped markers are cores/bulges and circular markers are disk components. The color of the marker depends on the sSFR of the considered region. The error-bar in the lower right corner shows the average uncertainty. The black dotted line delimits the quiescent region (Whitaker et al. 2011) and the colored ones, the regions defined by Zick et al. (2018). The orange region corresponds to *Post-starbursts*, the yellow one to *Quiescent*, the green one to *low sSFR DSFG*, the magenta one to *DSFG* and the blue one to *Star-forming galaxies*.

color clumpy disk morphology in the RGB (F115W, F200W, F444W) image. They all have a dust attenuated red SF core.

- Type II: *Quenched disks with a SF core*, characterized by a dust attenuated red SF core and a quenched disk (in one case, partially quenched).
- Type III: *SF disks with a quenched bulge*, characterized by a quenched central bulge while the disk is still star-forming. These are similar to local spirals.

For the disks with several components, they usually were all either SF of quiescent. There was only one galaxy (ID18278) where only a fraction of the disk was quiescent (green region in Fig. 2.2), we decided to include it to the Type II as the quiescent part encompasses 16% of the disk stellar mass and could be considered as an early stage of quenching. 4 galaxies hosts X-ray AGNs that do not dominate the FIR emissions; 1 is a Type I galaxy (ID30186), 2 are Type II galaxies (ID13098 and ID13776) and the last one is a Type III galaxy (ID23205) (Nandra et al. 2015).

After having classified our sample of 22 galaxies, we had 10 Type I galaxies, 5 Type II and 7 Type III. The RGB cutouts of our sample are separated following the three Types, with Figs. 2.1, 2.2 and 2.3 showing the Type I, II and III galaxies respectively. This is summarized in the top panel Fig. 10 where each wedge size is proportional to the number of galaxies of the considered Type. We illustrate each Type with a pictogram, the color red representing quiescent regions and the color blue representing star-forming regions. The color of each wedge is linked to the Type, in all Figures in the rest of this paper, the red markers will represent Type I galaxies, green markers Type II and blue markers Type III. The lower panels of Fig. 10 summarize the properties of each Types by looking at the connection between sSFR and A_V and color (in mag AB) gradients. The first observation is that cores/bulges are systematically redder than disks and there is a strong correlation between A_V gradient and color gradient (Pearson coefficient = 0.83, p-value = 2e-6) while there is no correlation between sSFR gradient and color gradient (Pearson coefficient = 0.27, p-value = 0.23). This means that the color differences that we observe in Figs. 2.1, 2.2 and 2.3 trace dust density in-homogeneities and not older/younger stellar population. The Type I galaxies (in red) do not have a noticeable sSFR gradient ($sSFR_{core} \sim 1.2 \times sSFR_{disk}$), but have a strong A_V gradient, hence, the fact that the cores of Type I galaxies appear much redder than the disks in Fig. 2.1 is due to their high dust density; the blue regions are low A_V regions. For the Type II galaxies, we observe the sSFR gradient we expected, the core is star-forming while the disk is quenched ($sSFR_{core} \sim 6.5 \times sSFR_{disk}$), they have the strongest dust gradient because of their highly dust attenuated core and their quenched disk that has low level of dust attenuation. We note that the sSFR gradient should make the core appear bluer than the disk (because of the younger stellar population in the core), however we observe the exact opposite. The color gradients we observe in Fig. 2.2 are dominated by the dust attenuation gradient. Eventually, Type III galaxies have low attenuation both in their quenched bulge and star-forming disk, hence have a weak A_V gradient. Their sSFR gradient is however strong, as expected of the opposite sign compared to Type II (quenched bulge and star-forming disk, $sSFR_{core} \sim 0.2 \times sSFR_{disk}$). In Fig. 2.3 the color gradients mostly trace the age difference between the stellar populations of the (redder) bulge and the (bluer) disk.

We note that, the strong gradients we observe, both in sSFR and A_V justify the need to divide our galaxies in three Types to illustrate the three possible sSFR gradient and to divide them in several sub-galactic regions because of the huge dust gradient. Moreover, as expected by the selection criteria detailed in Sect. 2.3, we did not have any fully quiescent galaxy in our sample.

4. Results

In this section, we present the results of the analysis of the 22 galaxies in our sample, distinguishing among the three classes we just defined in the previous Section. We first looked at the properties of the whole galaxies in Sect. 4.1 and then at the resolved properties at a sub-galactic level in Sect. 4.2. In Table 1, we give the main properties of our sample of 22 galaxies.

In the following, we compared the behaviour of the different Types of galaxies. To assess the significance of the trends, we compared the difference between the mean of a property for each Type with the error on the mean. We emphasis that we also checked the median value and that it doesn't affect the observed trends. In the Figures, each star-shaped marker is the mean and the error bar is the error of the mean (defined as $err_{mean} = rms/\sqrt{N}$ with rms the root mean square of the distribution and N the number of galaxy in each Type).

4.1. General properties

4.1.1. Main Sequence galaxies

To characterize the different Types of galaxies, we first looked at their typical redshift, M_* and $sSFR_{IR}$. The redshifts and M_* were extracted from the SED fitting procedure described in Sect. 3.6 while the $sSFR_{IR}$ was computed by dividing the SFR_{IR} of each galaxy by the sum of the M_* of each component with the SFR_{IR} taken from the super-deblended catalog (Le Bail et al., in preparation).

In Fig. 11, a redshift trend is appearing: the Type I galaxies with their SF core and SF disk are on average at higher redshift

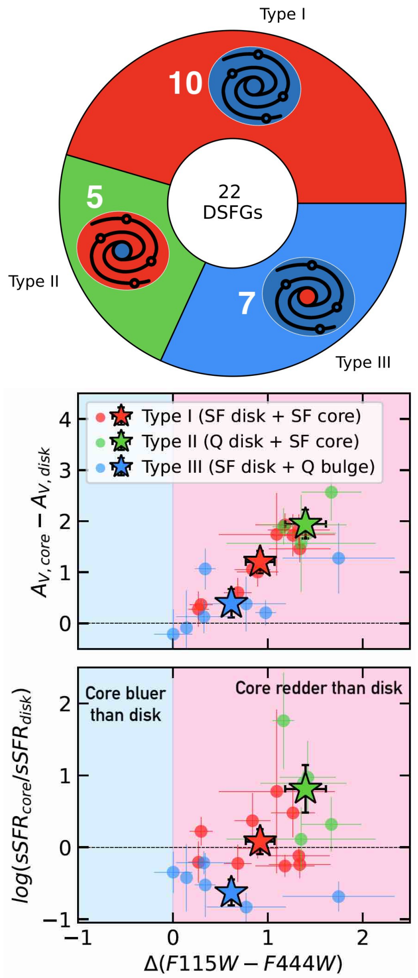

Fig. 10. Upper panel: Distribution of the galaxy sample in the different groups based on their resolved SF activity. Each region size is proportional to the number of galaxies in the group, written in white. The pictograms illustrate the properties of each Type, the blue and red colors representing SF and quiescent regions respectively. We link each Type of galaxy to a color as defined by the wedges color. Middle panel: A_V gradient vs color gradient (in AB mag), red, green and blue markers are linked to the Types defined in the top panel. Lower panel: sSFR gradient vs color gradient (in AB mag), red, green and blue markers are linked to the same Types as in the middle panel. Circular markers are individual galaxies, star markers are the mean value for each Type of galaxy with their associated error bar indicating the error of the mean.

($z = 2.32 \pm 0.15$) than the Type II galaxies with their SF core and quiescent disk ($z = 1.94 \pm 0.11$), that are themselves at a slightly higher redshift than the Type III galaxies ($z = 1.80 \pm 0.09$), analogs to the spiral galaxies we observe in the local universe with a quiescent bulge within a SF disk. The difference in redshift is 2σ between the Types I and II and 3σ between Type I and III. This suggests that this redshift trend is real and opens the possibility of an evolutionary link between class I and II/III.

All of our galaxies have a $M_* > 10^{10}$M$_\odot$ with an average of $M_* = 8.2^{+2.2}_{-1.7} \times 10^{10}M_\odot$ (left panel of Fig. 11). There is no correlation between the Types and the M_*, all Types have a similar average M_*. By comparing the $sSFR_{IR}$ of our galaxies with the MS of Schreiber et al. (2015) (right panel of Fig. 11), we confirmed that typically these galaxies are MS galaxies, consistently with Fig. 1 and Sect. 2.3. The MS sSFR at a fixed redshift was calculated by taking the mean M_* of our sample which is $< M_* > = 10^{10.92}$M$_\odot$. Moreover, the typical $sSFR_{IR}$ is observed to decrease at lower redshift, as expected from the cosmic trend.

The Type III galaxies, which have a quenched bulge, have the weakest $sSFR_{IR}$ on average ($sSFR_{IR} = 0.75^{+0.18}_{-0.14}$Gyr^{-1} for quenched bulges versus $sSFR_{IR} = 2.01^{+0.81}_{-0.56}$Gyr^{-1} for SF cores). They also are at lower redshift than the others. This suggests that they are more evolved than other classes.

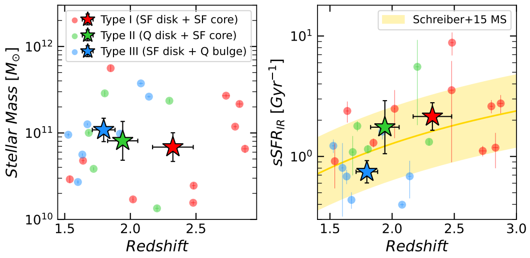

Fig. 11. Left panel: M_* versus redshift. Right panel: $sSFR_{IR}$ versus redshift, the yellow shaded region is the MS (Leslie et al. 2020; Huang et al. 2023). We show the error-bars for individual galaxies, when not visible, they are smaller than the marker. Circular markers are individual galaxies, star markers are the mean value for each Type of galaxy with their associated error bar indicating the error of the mean.

4.1.2. Galaxy near-IR sizes

The presence of highly obscured cores at the center of galaxies, like for ID15371 (see Fig. 3), can let us believe that we are studying the counterparts of the *ALMA* compact SF SMGs. Indeed, SMGs are known to be compact, dust obscured and with a high star formation efficiency.

The galaxies hosting a SF region at their center (Type I and II) tend to be slightly more compact in the near-IR, with $R_{e,NIR} = 2.34 \pm 0.37$kpc, than the galaxies with a quenched bulge (Type III), with $R_{e,NIR} = 2.93 \pm 0.42$kpc (this is tentative as there only is a 1σ difference, see Fig. 12). The Type II galaxies and their quiescent disk are on average the most compact galaxies in the near-IR with a typical size of 2.19 ± 0.30kpc.

In Fig. 12, we compare the $R_{e,NIR}$ to the $M_* - R_e$ relation from van der Wel et al. (2014) based on rest-frame optical measurements. Most of our 22 galaxies are more compact in the near-IR than in the optical, with ~ 40% being below the $M_* - R_e$ relation scatter. We also checked that the optical sizes of our galaxies are compatible with the $M_* - R_e$ relation. This demonstrates than in our galaxies, the dust, traced by the near-IR emissions, is more concentrated than the stellar light, traced by the optical emissions. This is a confirmation of an already well established fact (van der Wel et al. 2023; Gómez-Guijarro et al. 2022b; Jiménez-Andrade et al. 2021; Puglisi et al. 2019; Jiménez-Andrade et al. 2019; Fujimoto et al. 2017).

However, we note that the Type I galaxies have very comparable optical and near-IR sizes (~ 15% difference in size on average), their star-forming core is not as concentrated as for the other galaxies of the sample.

We discuss in Sect. 5.4 how the Type I and II galaxies might relate to the *ALMA* SMGs.

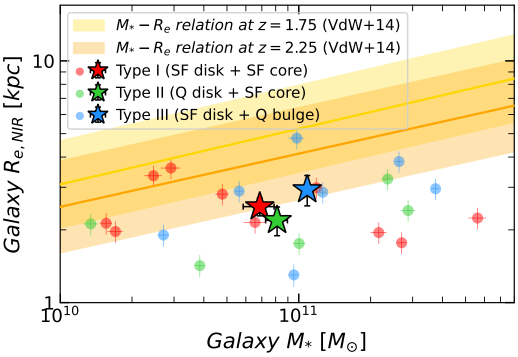

Fig. 12. Optical ($R_{e,O}$, left panel) and near-IR ($R_{e,NIR}$, right panel) half-light radius measured in the closest band to 550nm and 1.6μm rest-frame respectively versus the total M_* of the galaxy. Circular markers are individual galaxies, star markers are the mean value for each Type of galaxy with their associated error bar indicating the error of the mean. The yellow and orange shaded regions illustrate the Mass-Size relation derived by van der Wel et al. (2014) at the redshift of our sample.

However, studying the half-light radius is not enough as a large fraction of the galaxies in our sample are not symmetric (see Figs. 2.1, 2.2 and 2.3).

4.1.3. Widespread Lopsidedness

As one can see in Figs. 2.1, 2.2 and 2.3, some galaxies are strongly lopsided (marked with a 'Ⓛ'). They are asymmetric and/or their red central region is off-centered with respect to the disk. This lopsidedness appears to be quite common among Type I and II galaxies. In Figs. 2.1, 2.2 and 2.3, the marked galaxies are the 6 most lopsided galaxies, 3 are Type I (30% of the sample) and 3 are Type II (60% of the sample). The Type III galaxies look much more symmetric, these galaxies have a quenched bulge and are on average at lower redshift, they had presumably more time to evolve and stabilize their disk. To verify this, we investigate the lopsidedness of each galaxy.

As explained in Sect. 3.3, for each galaxy we calculated its asymmetry (A) and eccentricity (E). Type III galaxies appear to be much less lopsided, they have a low eccentricity ($9.8 \pm 2.5\%$) and asymmetry ($22.8 \pm 3.0\%$) while Type I and II galaxies, which show comparable lopsidedness, tend to be much more asymmetric ($33.0 \pm 3.5\%$) and off-centered ($30.3 \pm 4.0\%$) (see upper panel of Fig. 13). The difference has a 4.3σ and 2.2σ significance for the eccentricity and asymmetry respectively. In the upper panel of Fig. 13, we show the eccentricity vs the asymmetry. We considered the Type III galaxies as not lopsided, and used their typical eccentricity and asymmetry as a proxy for measurement errors and systematic effects. The thin black dotted line shows the threshold to define a galaxy as weakly lopsided ($A + E > 0.37$, this value corresponds to the average $[A + E] + 1\sigma$ of Type III galaxies). We have 14 galaxies that are at least weakly lopsided, representing 64% of the sample. If the galaxies are above the thick black dashed line, meaning that $A + E > 0.70$ (this value corresponds to the average $2 \times [A + E] + 1\sigma$ of Type III galaxies), we consider them as strongly lopsided, we encircled them in Fig. 13 and they are visible in Figs. 2.1, 2.2 and 2.3 with a Ⓛ. We have 6 strongly lopsided galaxies, representing 27% of the sample. Usually, a strong asymmetry is linked to a strong eccentricity, however we have galaxies with a low level of asymmetry but with a highly off-centered disk. All the strongly lopsided galaxies (circled in black) have high eccentricity. In other words, we observe a lack of strong asymmetry with low eccentricity.

The position of the average lopsidedness of Type I and II galaxies in Fig. 13, indicates that being lopsided might be a typical property of these galaxies.

In the lower panels of Fig. 13, Type III galaxies, which are more evolved and have a quiescent bulge have low level of asymmetry. On the contrary, Type I and II galaxies have a higher level of asymmetry. We observe (1) a lack of galaxies with a compact disk and high asymmetry and vice-versa, (2) a lack of galaxies with a high core mass fraction and high asymmetry and vice-versa and (3) the galaxies with a quiescent bulge with high mass fraction have low asymmetry. This is consistent with the observation of galaxies in the local universe, indeed, present-day late-type galaxies with more extended disks and lower central stellar mass density are typically more lopsided than early-type galaxies with smaller disks and higher central stellar mass density (Dolfi et al. 2023; Varela-Lavin et al. 2023). It seems that as the core grows in mass from accretion, the disk gets smaller and loses its lopsidedness, leading to Type I spiral-like galaxies.

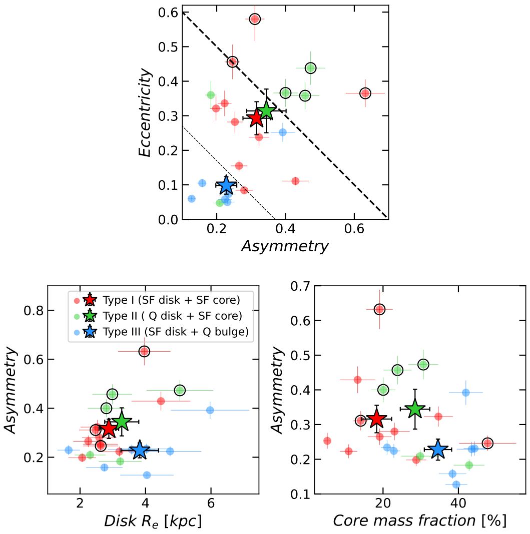

Fig. 13. Eccentricity and Asymmetry. Upper panel: Eccentricity versus Asymmetry, markers with a black circle are the strongly lopsided galaxies (see Figs. 2.1, 2.2 and 2.3), thin black dotted line delimits weakly lopsided galaxies, thick black dashed line delimits strongly lopsided galaxies. Lower left panel: Asymmetry versus Disk half-light radius as defined in Sect. 3.3. Lower right panel: Asymmetry versus mass fraction in the core/bulge of the galaxy, asymmetry is calculated using the F444W filter. Circular markers are individual galaxies, star markers are the mean value for each Type of galaxy with their associated error bar indicating the error of the mean.

Thanks to the spatial resolution of *JWST*, we had access to sub-galactic scales, which is crucial to understand the morphology and evolution of DSFGs.

4.2. Resolved properties

For each galaxy, each component has been classified either as star-forming or quiescent (see Sect. 3.7). In Fig. 14, we show that the quiescent regions are massive ($M_* \gtrsim 10^{10} M_\odot$) and have a relatively low dust attenuation with an average of $A_V \sim 1.6$ and maximum at $A_V \sim 3$ while SF regions have an average of $A_V \sim 2.3$ maximum at $A_V \sim 5.4$. The SF regions follow a correlation (with a Pearson coefficient of 0.62, p-value = 9e-8), the more massive components are more attenuated. This is consistent with the idea that the stellar mass is the main driver of dust attenuation in SF galaxies (Lorenz et al. 2023).

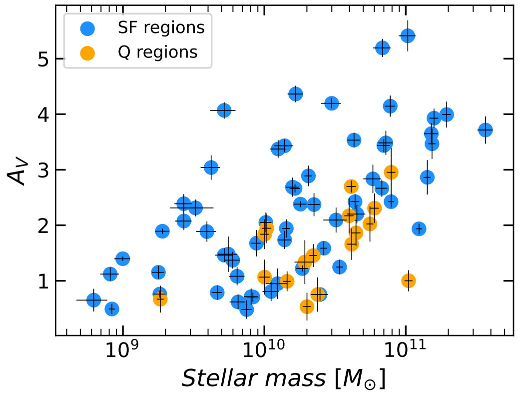

Fig. 14. A_V versus M_* for each regions identified in Figs. 2.1, 2.2 and 2.3. Quiescent regions are in orange and Star-forming regions in blue. At fixed stellar mass, star-forming regions are more attenuated, on average.

In the following Sections, we present the results regarding the core/bulge and disk of our galaxies.

4.2.1. Cores and bulges properties

We first looked at the red central region of each galaxy, as defined in Figs. 2.1, 2.2 and 2.3. In the left panel of Fig. 15, we show the dust attenuation versus the M_* of the red star-forming cores (in red and green) and quiescent bulges (in blue). As mentioned above, the dust attenuation of SF cores (Type I and II) correlates with its M_*: the more massive the core, the more dust attenuated (with a Pearson coefficient of 0.75, p-value = 0.001). Also, the bulges are less attenuated than SF cores, consistent with the fact that they are quiescent and host an evolved stellar population where the dust might have been consumed/destroyed.

Figure 15 also shows a trend in redshift. On average, the bulges are slightly more massive (M_*^B) than the SF cores (M_*^C) but with only a 1.5σ significance. The SF cores of Type II galaxies (M_*^{II}) and those of Type I galaxies (M_*^I) are consistent within errors.

$$M_*^B = 3.75^{+1.04}_{-0.81} \times 10^{10} M_\odot \gtrsim M_*^C = 1.81^{+1.19}_{-0.65} \times 10^{10} M_\odot \qquad (4)$$

$$M_*^{II} = 2.60^{+2.19}_{-1.19} \times 10^{10} M_\odot \approx M_*^I = 1.26^{+0.92}_{-0.53} \times 10^{10} M_\odot \qquad (5)$$

The weak trend between the M_* of higher-z SF cores and lower-z bulges is consistent with the idea of a bulge that grows in mass with time, fed by accretion from the disk, clump migration or minor/major mergers.

We compared the M_* and SFR fraction of the red cores and bulges with respect to the host galaxy (right panel of Fig. 15). For Type I galaxies, the red core M_* represents only 21.6 ± 4.0% of the M_* of the galaxy. This fraction is smaller than for the other galaxies of the sample where the red core represent 34.4 ± 6.2% for Type II (~ 2σ difference) and 35.9 ± 3.6% for Type III (~ 3σ difference) of their total M_*. This can be linked to the redshift trend, the Type I galaxies being at higher redshift, their core could still be at an early stage of growth. It also explains their lowest $R_{e,IR}/R_{e,O} = 0.89 \pm 0.14$, as their M_* is much less concentrated in the central region that the other two Types.

As expected from the definition of our Types of galaxies, the Type II galaxies have a red core with a SFR fraction (64 ± 18%) significantly greater than the M_* fraction (34.4 ± 6.2%) since the disk is mostly quenched, while the Type III galaxies have a red bulge M_* fraction (35.9 ± 3.6%) significantly more important than the SFR fraction (9.8 ± 3.4%) as the bulge is quenched.

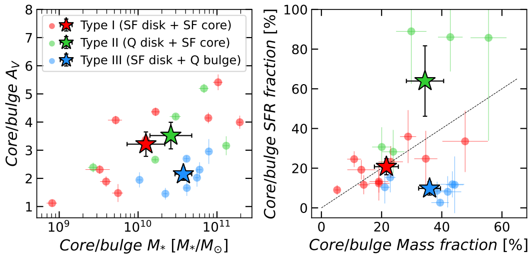

Fig. 15. Red regions properties. Left panel: Dust attenuation versus Stellar Mass. Right panel: SFR fraction versus M_* fraction in the red region. The black dotted lines is the 1:1 correlation. Circular markers are individual galaxies, star markers are the mean value for each Type of galaxy with their associated error bar indicating the error of the mean.

Some of these cores/bulges appeared to be compact, we decided to investigate them further in the next Section.

4.2.2. Compact cores and bulges

All of our galaxies have a central core/bulge appearing in the near-IR (filter F410M or F444W). For some galaxies, the core/bulge has a clear clump-like morphology, is much brighter than the surroundings and is clearly delimited (e.g. ID13776 and ID23205 in Fig. 16). We identified compact cores in 17 galaxies out of 22: 6 Type I galaxies with a compact core (60% of our sample), 4 Type II (80% of our sample) and all 7 Type III galaxies of our sample have a compact bulge. We decided to investigate further these compact cores/bulges by dividing the in two categories, the SF cores (from Type I and II) and the quiescent bulges (from Type III).

To do so, we measured the half-light radius of the compact cores and bulges defined as the radius of a circular aperture encompassing half of the flux of the core, we applied a similar technique as described in Sect. 3.1. The SF cores tend to be

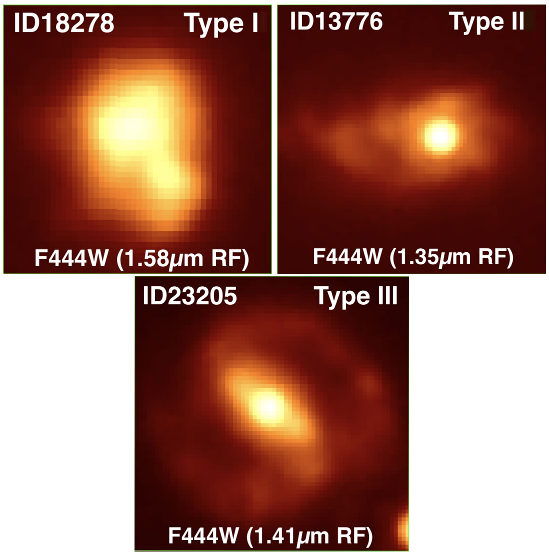

Fig. 16. Cutouts of a galaxy of each Type with the F444W filter. While a central clump-like core is clearly apparent for the ID13776 and ID23205, it is less clear in ID18278. We indicate the rest-frame central wavelength of the filter in parenthesis.

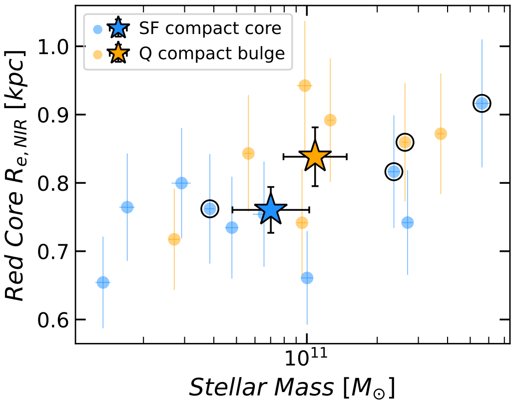

Fig. 17. Compact red cores and bulges half-light radius versus the stellar mass of the galaxy. Circular markers are individual galaxies, star markers are the mean value for each group of galaxy with their associated error bar indicating the error of the mean. Markers with a black circle are cores hosting an X-ray AGN (Nandra et al. 2015).

slightly more compact than the quiescent bulges (0.76 ± 0.03kpc vs 0.84 ± 0.04kpc, with a ∼ 1.5σ significance, see Fig. 17). The markers with a black circle are the compact core with an X-ray detection, possibly tracing an AGN. 3 of them are found in SF cores, and 2 are in the most massive galaxies with the largest SF cores. Even if the definition of the compact core is somehow arbitrary, and that there could be some level of contamination from the disk, this goes in the same direction as Cochrane et al. (2023) simulations. They found that without AGN feedback, the SF core would undergo a compaction event while the presence of AGN winds would prevent such compaction by evacuating the gas and precipitate the quenching of the core.

We also note that the quiescent bulge tends to be larger in more massive galaxies. Ikarashi et al. (2017) found that the most compact cores of SMGs are those where there is both star formation and an AGN. This is not what we observe for two of the SF cores hosting an X-ray AGN (showed with the encircled markers in Fig. 17), it is possible that in these galaxies the AGN has strong feedback and the system is quite evolved and ready to quench. The third SF core hosting an X-ray AGN is however compact and the presence of the AGN could facilitate this compaction.

The sizes of the SF compact cores are compatible with those measured in the sub-mm (See Sect. 5.4 for more details).

After analyzing the cores of our galaxies, we decided to investigate their differences with respect to the disk, especially the reasons of the redness of the core compared to the surroundings.

4.2.3. NIRCam color variations within the disks

In Sect. 3.7, we showed that the main driver of the color gradient between the cores and disks is the dust attenuation.

When looking at Figs. 2.1, 2.2 and 2.3 we noticed that some disks are also highly in-homogeneous in terms of color. To investigate the physical processes responsible for the color variations we observed in the disks, we compared the color variations with the dust attenuation and sSFR variations in a similar way we did in Sect. 3.7 when we investigated the gradients between the cores and the disks. When measuring the variations, we always measured the differences between a redder part of the disk and a bluer part (in other words $\Delta(F115W - F444W) > 0$ in AB mag). We compared all the components of the disks, meaning that if a disk was divided in 3 patches, there are 3 markers in Fig. 18 comparing the first and second, second and third and first and third component respectively. In the two upper panels of Fig. 18, we first clearly identify a correlation between the color variations and the dust extinction variations (Pearson coefficient = 0.78, p-value = 6e-11) consistent with the expectation that the redder regions are those with the greatest A_V (Calzetti et al. 2000). However, we do not identify any correlation between color variations and sSFR variations (Pearson coefficient = 0.16, p-value = 0.29), some color variations are even inconsistent as when $sSFR_{redder} > sSFR_{bluer}$, we are comparing a red patch hosting a younger stellar population (more star-forming) with a bluer patch hosting an older stellar population (less star-forming), hence the colors should be the other way around. This two observations demonstrate that the color variations we observe within the disks in Figs. 2.1, 2.2 and 2.3 are driven by dust. NIRCam colors at $z \sim 2$ trace dust, red spots are highly extinct while blue spots are weakly dust attenuated. This is consistent with previous studies based on NIRCam images (e.g. Miller et al. (2022)) .

As the clumps could play an important role in the color variations, it is important to investigate their abundance.

4.2.4. Clumpy disks

As one can see in Figs. 2.1, 2.2 and 2.3, some galaxies are very clumpy. The clumpiness does not seem to be linked to a particular Type of galaxy. Most of the clumps are observed in the shortest wavelength, consistent with Wuyts et al. (2012) who state that the number of clumps decrease when moving toward longer

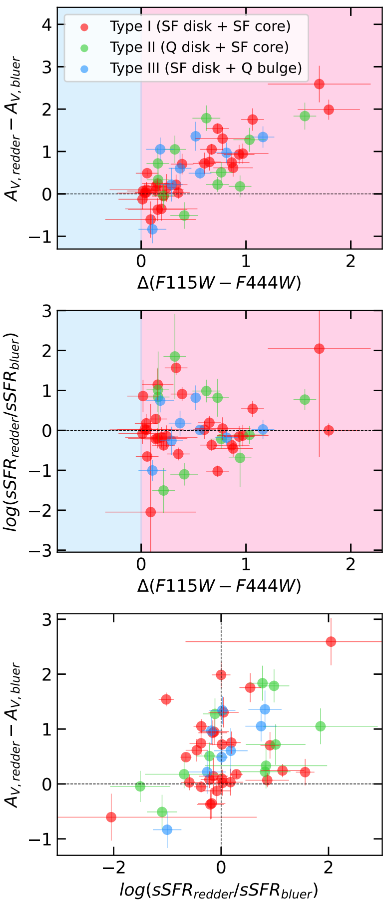

Fig. 18. Top panel: Comparison between the A_V and the F115W - F44W AB mag color between redder and bluer patches within the disks (if the disk has been divided in at least two components in Sect. 3.5). Middle panel: Comparison between the sSFR and the F115W - F44W AB mag color between redder and bluer patches within the disks. Lower panel: Comparison between the A_V and the sSFR between redder and bluer patches within the disks. Only variations are probed, not gradients, we do not look for radial effects has our galaxies have highly asymmetrical disks.

wavelength. In Fig. 19, we investigate the the possible link between the clumpiness and the disk and the core of the galaxy. In the left panel,we show the distribution of the number of clumps observed in each disk versus the SFR of the disk (defined as the sum of the SFR of the regions delimited in Figs. 2.1, 2.2 and 2.3) separating the SF disks from the quiescent disks. There is no apparent correlation between the star-forming activity of the disk and the number of clumps. The fact that we observe clumps in quiescent disks is quite surprising as they usually are supposed to be place of local starburst (Wuyts et al. 2012). We discuss the implication of this result in Sect. 5.3.

In the left panel of Fig. 19, we study the impact of the fraction of stellar mass in the core (in blue) or bulge (in red) on the number of clumps. The galaxies with a quiescent bulge, that we know to be at lower redshifts (see Sect. 4.1.1 and Fig. 11), have a higher fraction of their mass in their bulge (35.9% ± 3.6%) than the galaxies with a star-forming core have in their core (25.8% ± 3.7%) with a $\sim 2\sigma$ significance. They also tend to have a smaller number of clump: 1.7 ± 0.8 clumps on average for a galaxy with a bulge and 2.8 ± 0.6 clumps on average for a galaxy with a star-forming core (1.1σ significance). The plot also shows that by looking at galaxies with a star-forming core (in blue in Fig. 19), the ones with the smallest M_* fraction at their core are also the clumpiest. We see here both the effects of the redshift, lower redshift galaxies have less clumps and of the central M_* fraction, higher fraction leads to less clumps.

One could argue that the fact that galaxies with a star-forming core are at higher redshift than those with a quiescent bulge (Type III) means that we probe shorter rest-frame wavelength, hence, we have a higher probability of observing clumps in their disk (Wuyts et al. 2012). However, the range of redshift that we are probing here is quite narrow, and the clumps that we count are the brightest and visible in several filters. These galaxies actually are clumpier.

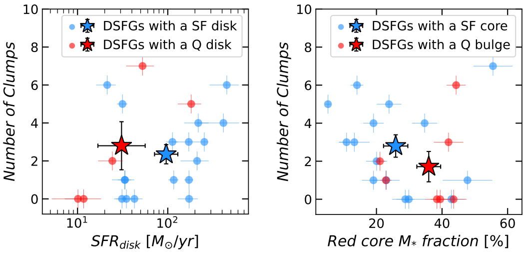

Fig. 19. Number of clumps in the disk versus its SFR. Circular markers are individual galaxies, star markers are the mean value for each Type of galaxy with their associated error bar indicating the error of the mean.

5. Discussion

In this Section, we first discuss the green patches/clump that are visible in the RGB cutouts in Figs. 2.1, 2.2 and 2.3 in Sect. 5.1. Then, we discuss the presence of blue clumps inside quiescent disks in Sect. 5.3. We investigate the possible link between the compact SMGs observed with *ALMA* and our DSFGs in Sect. 5.4. In Sect. 5.6, we discuss the origin and consequences of lopsidedness and its abundance. Eventually, in Sect. 5.7, we discuss two possible evolutionary paths that could lead to the formation of Type II galaxies.

5.1. Bright emission lines

When looking at Figs. 2.1, 2.2 and 2.3, one can notice that some of the disks have different colors, with a blue and a green part. The green clumps/patches are visible in all Types of galaxies. Considering their redshift, they probably are due to bright H_α or $[O_{III}]$ emission lines which are known tracer of star-formation. The H_α line will fall in the green filter (F200W) for galaxies with a redshift between 1.67 and 2.39 and the $[O_{III}]$ emission line will fall in the green filter for galaxies with a redshift between 2.52 and 3.47. On the 7 galaxies where we identify green patches, 2 are consistent with H_α emission from a star-forming region (ID15371 and ID29608) and 3 are consistent with $[O_{III}]$ emission from a star-forming region (ID18694, ID23510 and

ID23581). For the 2 remaining galaxies, it is more surprising, as the green patches/clump are observed in the quiescent disks of Type II galaxies.

For the ID13107 galaxy ($z = 2.21 \pm 0.02$), the green patch is close to the center of the galaxy, it is then possible that the H_α line is produced by the accretion disk of an AGN sitting at the center of the galaxy that becomes bright in this region because of a much weaker dust attenuation than in the core. Even though we have no radio or X-ray signature of an AGN in this galaxy, as mentioned before, the predicted SFR from the SED fitting is not enough to explain the FIR flux density observed with *Herschel* for this galaxy. This convinced us that there could be an AGN at the core of this galaxy.

For the ID18278 galaxy ($z = 1.805$), the situation is different, the green patch is in the outer region and composed of clumps. These clumps could have actually been ionized by the hot evolved low-mass stars (Cid Fernandes et al. 2011; Belli et al. 2017) with an enhanced H_α line due to shocks from the minor merger. Indeed, these clumps are old (age of oldest stars $= 2.5 \pm 0.5 Gyr$) and have a very low sSFR, consistent with the *ex-situ* clumps defined in Mandelker et al. (2014).

5.2. Origin of dusty patches within disks

In Sect. 3.7, we demonstrated that the color gradient is linked to the strong A_V gradient. The fact that the core is much more attenuated than the disk is expected because the SFR surface density is higher in the core than the disk, hence is the dust surface density and the dust column density.

However, the patchy distribution of dust within the disks is more surprising. From the lower panel of Fig. 18, we observe a correlation between dust density and sSFR for Type II and Type III galaxies (Pearson coefficient = 0.62 and 0.83 with p-value = 0.04 and 0.01 respectively). Meaning that for these galaxies, the patches could be linked to not yet quenched regions in the disks of Type II galaxies and partly quenching disk for Type III. The patches could then find their origin in internal instabilities, or interactions with the local environment. For Type I galaxies, we do not observe this correlation (Pearson coefficient = 0.35, p-value = 0.07). For these galaxies, the patches could be correlated either to metallicity, higher metallicity leading to higher dust column, or to geometry.

We investigated the origins of the patchy distribution by looking for correlations between the greatest difference in A_V in each disk and the redshift, the fraction of stellar mass in the core/bulge, the fraction of SFR in the core/bulge, the lopsidedness and the environment. We found no correlation (all p-value > 0.2). We then looked for a correlation between the number of patches/components of each disk (as defined in Figs. 2.1, 2.2 and 2.3) and the same parameters. The only correlation we found, that is visible in Fig. 20, is with the mass fraction in the core (Pearson coefficient of -0.60, p-value = 0.003), the number of patches/components gets smaller when the mass is more concentrated in the core of the galaxy. This is especially true for the galaxies with a star-forming core (Type I and II, with a Pearson coefficient of -0.67 and a p-value of 0.006, while Type III have a Pearson coefficient of 0.14 with p-value of 0.76). This correlation is expected from Hopkins et al. (2023); when the central gravitational potential well is deep enough, it stabilizes and homogenizes the disk. This correlation is consistent with the one we observed for the clumps (See Sect. 4.2.4 and Fig. 19). However, if this (anti-)correlation justify why we do not see patches in Type III galaxies, it doesn't clear up the mystery of their origin.

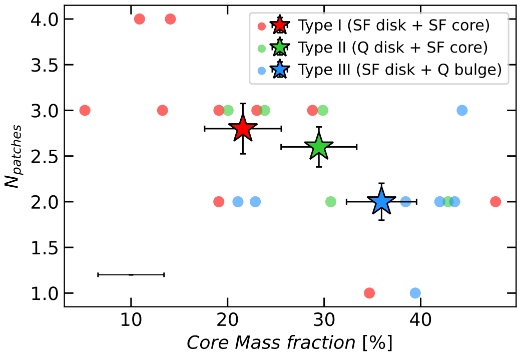

Fig. 20. Number of patches/component of each disk versus the stellar mass fraction in the core/bulge. In the lower left corner, we show the average error bar for individual galaxies. Circular markers are individual galaxies, star markers are the mean value for each Type of galaxy with their associated error bar indicating the error of the mean.

We would need spectroscopy to understand better what is happening in those disks, and even there the mystery would remain of why the disks are so in-homogeneous in dust attenuation, whether it is due to metallicity or geometry differences (and why these would persist over homogeneous patches within a disk, as opposed e.g. to simple radial gradients).

5.3. Clumps in DSFGs

In all the Types of galaxies, we identified the presence of clumps. We observed that galaxies at lower redshift tend to have less clumps, this suggests that the clumps either get destroyed within the disk and are not replaced by new clumps, or migrate toward the core and participate to its mass growth possibly triggering enhanced star formation. They might also be lower mass/less luminous, hence below our detection threshold. We do not see any evidence of recent major mergers in our galaxies, suggesting that most of the clumps we observe are originating from a fragmentation of a gas rich unstable SF disk, consistently with Puschnig et al. (2023) and Fensch & Bournaud (2021) that showed that large scale instabilities in gas-rich galaxies can create such star-forming giant molecular clumps.

We also noted that the most clumpy high-redshift galaxies also have the least concentrated cores, with less than 20% of their stellar mass at the center of the galaxy (see Fig. 19) and, on the contrary, the least clumpy galaxies at lower redshift have nearly 40% of their stellar mass in the quiescent bulge. We also showed in Fig. 15 that galaxies at later times have higher core mass fractions. This suggests that either, as the clumps migrate through the disk, they feed the central core, making it grow in mass or that, as the central gravitational potential well gets deeper, the disk is stabilized, the VDI are destroyed, and the galaxy can have a smoother spiral-like disk. Our observation are consistent with the simulations from Hopkins et al. (2023) that showed a well defined dynamical center is necessary to stabilize the disk and put an end to bursty star-formation. Also, we are in agreement with the new JWST results from Kalita et al. (2022), pointing to an increased galaxy fragmentation with decreasing bulge/core mass fraction.

When looking at Fig. 2.2, one can clearly identify clumps in the Type II galaxies. The blue clumps of these quiescent disks

(ID13107, ID18278 and ID13776 in Fig. 2.2) are due to a low dust attenuation and not a high sSFR. Indeed, the disk has $A_V = 1.0 \pm 0.2$ while the central SF core has $A_V = 3.5 \pm 0.2$. We recall that the blue colors in NIRCam color cutouts for these redshifts are typically a signature of low dust attenuation. This could indicate that clumps are not only formed in highly star-forming regions.

5.4. Are we observing compact SMGs counterparts ?

In most of our IR-luminous galaxies, a central compact clump-like highly dust attenuated SF red core is present. While it is nearly invisible in the optical rest-frame, it becomes bright in the near-IR (see Figs. 3 and 16). As we showed in Sect. 4.2.3, they are surrounded either by a SF (Type I) or a quiescent (Type II) disk with much lower dust attenuation. We identify 10 of those (see Table 1 and Sect. 4.2.2) in our sample.

When we measured the size of these red compact SF cores, we found that the average $R_{e,NIR}$ was about 0.76kpc (Fig. 17). This size is compatible with the sizes measured with *ALMA* for the compact SMGs : 0.6 ± 0.2kpc in Zavala et al. (2022), ∼ 0.73kpc in Gómez-Guijarro et al. (2022a) or 1 − 2kpc across in Rujopakarn et al. (2019). The NIRCam sizes tend to be slightly larger than the *ALMA* sizes, this is not due to a spatial resolution issue, but to the heavy dust obscuration of the core.

Moreover, compact SMGs at $z \sim 2-3$ are characterized by a SFR $\geq 100\mathrm{M}_\odot\ \mathrm{yr}^{-1}$ (Gómez-Guijarro et al. 2022a; Jiménez-Andrade et al. 2021, 2019; Hodge et al. 2019). 7 out of the 10 galaxies where we identified a compact star-forming core have a total SFR compatible with this criteria (see Table 1). 5 of them having SFR $\gtrsim 100\mathrm{M}_\odot\ \mathrm{yr}^{-1}$ in the core alone, 1 has SFR $\geq 50\mathrm{M}_\odot\ \mathrm{yr}^{-1}$ in the core and the remaining galaxy has a lower SFR in their core.

To confirm the possibility of SMGs counterpart, we can use the FIR super-deblended catalog in the EGS (Le Bail et al., in preparation.). 6 out of the 10 galaxies are detected at 2σ in SCUBA2/850μm among which 3 are 3σ detected. 3 out of the 4 undetected galaxies at 850μm are in the shallower part of the FIR catalog. Moreover, if we look at the predicted flux at 1.1mm for these galaxies, the mean predicted flux is 0.80mJy, and 4 of them are predicted to be brighter than 1mJy at 1.1mm. A total of 5 galaxies have either a 3σ detection in SCUBA2/850μm or a prediction > 1.1mJy at 1.1mm (ID13776 and ID21190 from the Type II class and ID16544, ID29608 and ID30186 from the Type I class). They correspond to the 5 galaxies measured with a SFR$\gtrsim 100\mathrm{M}_\odot\ \mathrm{yr}^{-1}$ in their core.

All these elements convinced us that we have at least 5 or 6 galaxies that are good candidates of compact SMGs counterparts, they are equally distributed between Type I and II.

Contrary to what is observed with *ALMA*, these compact cores are not isolated, they all are surrounded by a larger disk. The fact that their is a huge dust gradient between the core and the disk, as we showed in Sect. 3.7 might explain why we do not this the latter in sub-mm surveys: the core is bright in the rest-frame near-IR while the disk is bright in the rest-frame optical. The presence of a disk confirms Hodge et al. (2019) and Puglisi et al. (2019) who both stated that the compact SMGs are obscured part of a larger system.

The fact that some galaxies in our sample have highly extinct cores could link them the so-called *HST*-dark galaxies. We compared our sample with the *HST*-dark and *HST*-faint galaxies in the same field from Pérez-González et al. (2023). Our galaxies are in general agreement with the SFG at $z < 4$ in Pérez-González et al. (2023), especially with the fact that we observe highly dusty patches out to large radii. Four of the galaxies in our sample are classified as *HST*-faint (ID16544, ID18694, ID23581 and ID26188). All are Type I galaxies, which seems logical because quiescent regions have lower A_V, hence are brighter in *HST*. One of them (ID23581) has $A_{V,min} > 3$, hence expected to be *HST* faint/dark, while the remaining three galaxies have $A_{V,min} \sim 1.5$, which is the average $A_{V,min}$ of the sample. It is more surprising that those three galaxies are *HST* faint/dark. However, these 4 galaxies are actually the galaxies at the highest redshift of the sample ($2.7 < z < 2.9$), with photometric redshift from our SED fitting procedure consistent with the ones from Kodra et al. (2022) and the ones from the super-deblending (Le Bail et. al, in preparation). There is a chance that their HST faintness comes more from their higher redshift than their high level of dust (at least for 3 of them).

5.5. Relation to Blue Nuggets simulations

In the cosmological simulations from Lapiner et al. (2023), the typical high-redshift and low-mass galaxy is a gas-rich, star-forming, highly perturbed, and possibly rotating system, fed by intense streams from the cosmic web. When the stellar mass is in the ballpark of $\sim 10^{10}\mathrm{M}_\odot$, the galaxy undergoes a major, last, wet compaction into a 'Blue Nugget', starting with a compact gaseous star-forming system that rapidly turns into a compact stellar system. The galaxies that we observe are all above this $\sim 10^{10}\mathrm{M}_\odot$ threshold. However, non of them look like a blue nugget except possibly ID13098. We discuss the specific case of ID13098 in Sect. 5.7. The other ones that are in the range of mass where the wet compaction should happen do have a compact dusty star forming core, but they also have a much larger star-forming disk. Moreover, the more massive galaxies could be undergoing a rejuvenation event after blue nugget phase as it is suggested by Lapiner et al. (2023). However, when comparing the t_{50} of the disk and core, we find no evidence that the star-forming disks are younger than the cores. The fact that we do not observe any blue nuggets (or a single one) might be due to their low-mass, or low SFR, or that the previous observations were not deep enough to detect the low-luminosity disks. It may be possible that the most massive galaxies undergo a different quenching mechanism that lower-mass galaxies.

5.6. Investigating the lopsidedness

Galaxy lopsidedness has not so far attracted much attention at high redshift, probably because of a lack of spatial resolution and/or incomplete data since the most obscured part of the galaxies are not visible with pre-*JWST* telescopes. However, the spatial resolution of NIRCam shows that it is a common features of DSFGs around the Cosmic Noon. Indeed, we showed in Sect. 4.1.3 that being lopsided seem to be the typical morphology of Type I and II galaxies (see Figs. 2.1, 2.2 and 13). Bournaud et al. (2005) investigated the origins of lopsidedness in field galaxies and concluded that it is very unlikely the result of internal mechanisms but rather linked to the history and environment of the galaxies. With the NIRCam images, we have access to the spatially resolved morphology of these galaxies, and can try to better understand the causes of the lopsidedness.

Among the lopsided galaxies showed in Figs. 2.1 and 2.2, some have a clear compact central core and a rather homogeneously colored disks (e.g. ID11887, ID13776), others are mostly clumpy galaxies with a less compact core (e.g. ID18694, ID18278).

For the first category, even if we don't have the kinematics to confirm it, it seems that the galaxies have a stable disk, with no major merger features. This means that the lopsidedness of these galaxies, is probably due to accretion and minor mergers. This accretion would be happening via streams of cold gas that asymmetrically feed more generously one side of the galaxy making it grow larger than the opposite side. Moreover, the fact that these galaxies are clumpy (see Sect. 4.2.4) and that their disk is highly heterogeneous (see Sect. 4.2.3) favors the idea of accretion or minor mergers that could create clumps or patches in the disks with different SFRs or A_V. However, the fact that Type I galaxies have a star-forming disk and Type II a quiescent disk means that the properties of gas transport in Type I and Type II galaxies are different.

In Type I galaxies, the disk acquires its gas via accretion streams or minor mergers and forms stars, but the gas also goes to the core, which is SF as well. Bournaud et al. (2005) showed via simulations that the strong lopsidedness could be the result of gas accretion if it as asymmetric enough and that the lopsidedness from accretion is relatively long-lived ($\sim$ 3Gyr), hence easily observable. This has also been confirmed by a recent study based on the TNG50 simulation (Dolfi et al. 2023) where they conclude that the lopsidedness in local galaxies originates from accretion over several Gyr while symmetric galaxies formed earlier and within a shorter timescale.

In Type II galaxies, on the other hand, while the gas keeps going to the core and keeps it SF, the disk is quenched. This would seem to suggest that the gas does not stay in the disk, but goes straight to the center. A possible explanation would be that Type II galaxies have larger inflows or very powerful outflows that blow away and/or shock the gas in the disk (confirming this would require spectroscopy). It could also be that in Type II galaxies the accreted gas has a more radial accretion, with little angular momentum and goes straight into the central regions. Or, for some reason, the gas rapidly looses its angular momentum and abandon the disk and falls into the center. This would, depending on the direction of accretion, feed the lopsidedness. This effect has already been suggested by Kalita et al. (2022) where they were able to link the lopsidedness of 3 galaxies at $z \sim 3$ in a dense environment to cold gas accretion using Lyman-α emissions. The strong lopsidedness of these galaxies, would then be a tracer of the point of impact of the accretion streams.

For the clumpier galaxies, the disk is star-forming and not homogeneous. Kannan et al. (2015) showed with simulations that gas-rich disks are able to survive major mergers and that the following enhanced star-formation is not entirely happening in the core of the galaxy, but a substantial fraction takes place in the disk too. This is compatible with our Type I galaxies, the fact that their SF disks are clumpy and heterogeneous in terms of dust and sSFR could be a signature of a recent major merger (Calabrò et al. 2019). Moreover, Kannan et al. (2015) mention that the presence of a gas-rich disk contributes to reducing the efficiency of bulge formation, which is compatible with the non-compact core observed in some of these galaxies. Usually major mergers features are short lived, but the clumps we observe could be preserved due to Toomre instabilities. Indeed Fensch & Bournaud (2021) showed, via simulations, that a galaxy with a gas fraction greater than 50% will have strong disk instabilities leading to the formation of long-lived giant clumps and strong nuclear inflow affecting the structure of the galaxy and possibly introducing lopsidedness. It has already been observed in a local galaxy used as proxy for high redshift galaxies (Puschnig et al. 2023). A major merger could then result in a clumpy galaxy with a perturbed structure, which is what we have in Fig. 2.1 for some Type I galaxies. The color variations between clumps/regions in the galaxies could be tracers of the original galaxy they were a part of before the merging as they trace the dust attenuation. However, a major merger is not necessarily required, indeed, Rujopakarn et al. (2023) studied a lopsided galaxy at $z \sim 3$ and concluded that its lopsidedness did not originate from interaction with the environment but from internal, large scale instabilities, that could, in the end, form bars or spiral arms.

The lopsidedness of these galaxies could also be the signature of the bulge angular momentum build-up. Indeed, either via accretion, minor mergers, major mergers, internal instabilities and tidal effects, the lopsidedness will break the disk balance, consequently creating a torque on the bulge of the galaxy resulting in an angular momentum loss.

The significance of the difference of lopsidedness between Type III galaxies and the rest of the sample means that, by some mechanism, the galaxies become much more symmetric after the Cosmic Noon. Indeed, we recall that our Type III galaxies have $z = 1.80 \pm 0.09$ while Types I and II have $z = 2.19 \pm 0.14$. This could be due to increasing virialization with passing of time, also due to the stabilising effect of the larger bulge mass fraction (see lower right panel of Fig. 13).

5.7. Where do Type II galaxies come from ?

The Type II galaxies (see Sect. 3.7 and Fig. 2.2) have an unusual behavior. They have a compact star-forming core embedded in a quiescent disk, and represent $\sim$ 23% of the galaxies of our sample, so are relatively common. Kalita et al. (2022) studied such galaxies in a crowded environment at $z \sim 3$ and linked the quiescence of the disk to its strong lopsidedness which rapidly fuels the gas to the core of the galaxy. In our sample of Type II galaxies, 3 have a strong lopsidedness, 1 is only weakly lopsided and has an off-center core while 1 is not lopsided at all. This means that even if lopsidedness can be a driver of outside-in quenching, it is not the only one.

Based on our observations, we have three possible scenarios that could explain the observed suppression of star-formation in the disk.

The first scenario is the one developed by Kalita et al. (2022) with the lopsidedness either coming from a major merger strong enough to result in this off-centered core or from asymmetric accretion of gas via streams and minor mergers, feeding the disk preferentially on one side. The strong lopsidedness resulting from this is enough to explain the quenching of the disk as it greatly facilitates the transportation of the gas toward the core (Fensch & Bournaud 2021).

The second scenario is a wet compaction event leading to an apparent outside-in quenching. ID13098 is in the correct range of stellar mass and redshift to be in a 'blue nugget' phase (Lapiner et al. 2023; Dekel et al. 2009; Tacchella et al. 2016) where the galaxy undergo a wet compaction caused by gas-rich mergers or smoother gas streams, leading to an episode of high central star-formation and outside-in quenching. The presence of the low-luminosity quiescent disk might indicate that the compaction is not completely done yet. If it is a blue nugget, the outside-in quenching may not be final as when the gas has been consumed at the center and the bulge has grown, a star-forming ring can form in the disk via accretion of new gas-reach material from the inter-galactic medium leading to an inside-out quenching in the post-blue nugget phase.

The last scenario is an actual outside-in quenching linked to the strong lopsidedness but not resulting from a major merger. In Fig. 11, we show that the Type I galaxies are the most star-forming and at the higher redshift on average. They also have a stellar mass consistent with the Type II galaxies. This means that there could be an evolutionary path between Type I and Type II galaxies driven by VDI and lopsidedness. The idea is that the star-forming clumps of the Type I galaxies will migrate toward the center of mass of the galaxy (Mandelker et al. 2014). By doing so, they will fuel strong gas nuclear inflow creating a compact SF core (Fensch & Bournaud 2021). On their way to the center of the galaxy, the clumps will accrete the gas of the disk and could leave a completely gas deprived disk and a compact SF core. When growing, the SF core will prevent the formation of new clumps in the disk by stabilizing it (Hopkins et al. 2023) while the lopsidedness could be conserved due to the large scale instabilities. In this scenario, Type II galaxies are observed in a process of outside-in quenching.

Chandar et al. 2023 demonstrated that the local ULIRG Arp220 is composed of a central starburst and a larger quiescent disk. The starburst has been triggered by a major merger. The galaxy is classified as shocked post-starburst galaxy which is a stage prior to post-starburst. In that case, it appears that shocks induced by the merger forced the outer disk in this galaxy to turn quiescent. This is close to first scenario we described with the outside-in quenching originating from a major merger.

In our case, in the four remaining galaxies, two have clumpy heterogeneous disks (ID13107 and ID18278, see Fig. 2.2), the different properties of the patches, either linked to dust or sSFR (see Sect. 4.2.3) favors the idea of asymmetric accretion streams and minor mergers as the source of lopsidedness for these two galaxies. The ID13776 has a clumpy but more homogeneous disk, but highly off-centered. The eccentricity of this galaxy can both originate from asymmetric accretion making the disk grow on one side or from a major merger strong enough to shift the disk. In the same way, it is hard to conclude for the last galaxy (ID21190) which is not lopsided and seem to have a smooth homogeneous disk.

5.8. The role of environment

A way to discriminate between the scenarios of outside-in quenching and the origin of the lopsidedness of galaxies is to look at their local environment. To this aim, we use the environment density measurements from Chartab et al. (2020). They measure the density contrast of galaxies with a magnitude brighter than 26 AB mag in the H-band. The density contrast is defined as the number density enhancement with respect to the average density in the vicinity of the galaxy (local density/background density). In Fig. 21, we compare the local density contrast of our sample with the general population of galaxies in the EGS field.

The star markers in Fig. 21 are the Type II galaxies. They do not sit in any particular kind of environment, they are relatively close to the median of the general population showed by the blue dotted line. This suggest that outside-in quenching can happen both in dense environment via major mergers but also in lighter environment via internal effects. The galaxy at lower density is ID13098 that we discuss in Sect. 5.7. The fact that this galaxy is relatively isolated favors the scenario of wet compaction as the origin of its outside-in quenching. For the other galaxies, the local density is insufficient to discriminate between scenarios as they do not sit in strongly over/under crowded environments but show that they all are likely.

The color of the markers trace the lopsidedness of the galaxies. There is no obvious difference between the lopsided galaxies and the general population. We do not see any signature that could link the environment to the lopsidedness. The fact that we see lopsided galaxies not only in dense environment and that most of them have a regularly looking disk favors the idea that lopsidedness originates from accretion and/or VDI. However, this is only a tentative explanation, these measurements are not strong enough to say if environment could be a driver of lopsidedness. The circular marker showing a weakly lopsided galaxy in a high density environment is ID30186. This galaxy is the brightest galaxy of a group of ~ 16 members at $z_{spec} = 1.85$, is undergoing a major merger and is surrounded by quiescent intra-halo light (Coogan et al. 2023).

Discriminating further between the different scenarios would require spatially resolved spectroscopy to study the kinematics of each of these galaxies, and especially of the disk of each of them, to see if their disk is rotating, which would favor accretion and minor mergers, or if they are dominated by dispersion velocity favoring the scenario of major mergers and VDI.

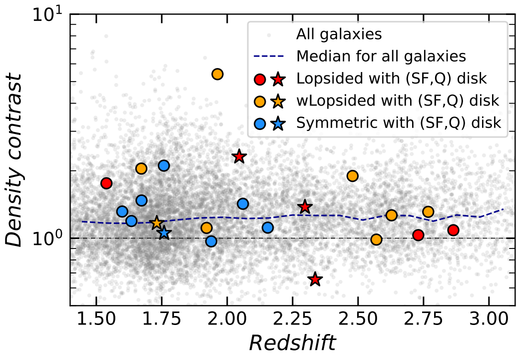

Fig. 21. Density contrast of galaxies versus their redshift. Density contrast is defined as the number density enhancement with respect to the average density in the vicinity of the galaxy (Chartab et al. 2020). Grey scatter is the general population of H-band mag AB ≤ 26, the black dotted line is 1, the blue dashed line is the median density contrast of the general population in redshift bins. Star-shaped markers are galaxies undergoing outside-in quenching (Type II). Circular marker are the Type I and III galaxies. The colors of the markers trace the lopsidedness.

6. Summary

In this paper, we used the new set of images in the near-IR from *JWST*/NIRCam in the EGS field from the CEERS collaboration to investigate the formation and evolution of DSFGs at Cosmic Noon. To start with, we selected a sample of DSFGs based on their FIR emissions and around Cosmic Noon ($1.5 < z < 3.0$). We ended up with 22 galaxies in the CEERS field. We studied each galaxy on a sub-galactic scale by dividing them in different regions based on their NIRCam (F115W, F200W, F444W) colors, taking advantage of the spatial resolution. Using the available photometry from *HST* and *JWST*, we ran SED fitting and derived physical parameters for each galaxy component and classified them as star-forming or quiescent. We classified the galaxies in different Types based on the star-forming activity in their core and disk. The Type I have a star-forming disk with a red star-forming core, the Type II are quiescent disks with a SF core and the Type III are star-forming disks with a quenched bulge. The main results of this study are:

Table 1. Main properties of our sample of 22 DSFGs. See Sect. 3.7 for Type definitions.

ID (CANDELS)	Redshift	Mass $log_{10}(M_*/\mathrm{M}_\odot)$	Mass$_{core}$ $log_{10}(M_*/\mathrm{M}_\odot)$	SFR $\mathrm{M}_\odot\ \mathrm{yr}^{-1}$	SFR$_{core}$ $\mathrm{M}_\odot\ \mathrm{yr}^{-1}$	Type	Morphology
11887	1.539[b]	10.5 ± 0.1	9.59 ± 0.07	38 ± 24	5 ± 3	Type I	cSFC+Lop
13098	1.720[a]	10.6 ± 0.1	10.22 ± 0.04	73 ± 63	62 ± 9	Type II	cSFC[c] +wLop
13107	2.21 ± 0.02	10.1 ± 0.1	9.43 ± 0.06	29 ± 21	10 ± 2	Type II	cSFC+Lop
13776	2.297[b]	11.4 ± 0.1	10.86 ± 0.05	340 ± 214	114 ± 64	Type II	cSFC[c] +Lop
13932	2.48 ± 0.02	10.2 ± 0.1	8.91 ± 0.07	35 ± 20	3 ± 1	Type I	wLop
14559	2.020 ± 0.004[a]	10.2 ± 0.1	9.59 ± 0.07	44 ± 25	10 ± 3	Type I	cSFC[c]
15036	1.60 ± 0.01[a]	10.5 ± 0.1	10.02 ± 0.03	36 ± 22	3 ± 2	Type III	...
15371	1.921[b]	11.0 ± 0.1	10.61 ± 0.03	197 ± 125	26 ± 13	Type III	wLop
16544	2.73 ± 0.03[a]	11.4 ± 0.1	10.89 ± 0.03	269 ± 186	97 ± 31	Type I	cSFC[c] +wLop
18278	1.805[a]	11.5 ± 0.1	10.84 ± 0.06	254 ± 168	72 ± 23	Type II	Lop
18694	2.80 ± 0.01	11.1 ± 0.1	10.22 ± 0.05	415 ± 244	52 ± 9	Type I	Lop
21190	1.68 ± 0.01[a]	11.0 ± 0.1	10.48 ± 0.07	106 ± 95	94 ± 20	Type II	cSFC[c]
23205	2.14 ± 0.01[a]	11.40 ± 0.05	10.78 ± 0.03	138 ± 87	21 ± 10	Type III	...
23510	2.51 ± 0.02[a]	10.4 ± 0.2	9.51 ± 0.15	141 ± 106	27 ± 6	Type I	wLop
23581	2.83 ± 0.02	11.3 ± 0.1	11.01 ± 0.06	259 ± 152	87 ± 38	Type I	Lop
25604	1.673[b]	11.1 ± 0.1	10.75 ± 0.02	24 ± 18	3 ± 4	Type III	...
26188	2.87 ± 0.02	10.8 ± 0.1	10.10 ± 0.05	257 ± 178	34 ± 11	Type I	cSFC+wLop
29608	1.64 ± 0.03	10.7 ± 0.1	9.72 ± 0.09	342 ± 181	84 ± 11	Type I	cSFC[c] +wLop
30012	1.53 ± 0.01[a]	11.0 ± 0.1	10.62 ± 0.03	49 ± 42	6 ± 3	Type III	...
30186	1.85[a]	11.7 ± 0.1	11.29 ± 0.03	550 ± 436	136 ± 57	Type I	cSFC[c] +wLop
31125	2.08 ± 0.02	11.60 ± 0.05	10.90 ± 0.03	237 ± 156	25 ± 18	Type III	...
31281	1.634[b]	10.80 ± 0.05	10.35 ± 0.03	36 ± 35	0.9 ± 0.5	Type III	...

Notes.
(a) Grism based redshift.
(b) Spectroscopic redshift.
(c) SMGs analog candidate (see Sect. 5.4).
'cSFC' and '(w)Lop' stand for *compact star-forming core* and *(weakly) lopsided* respectively.

- ~ 70% of the DSFGs in our sample have a red deeply dust attenuated compact star-forming core that can represent up to 80% of the total SFR of the galaxy but only 20-30% of its stellar mass. Contrary to the simulations that predict blue nuggets, these compact red cores are surrounded by large less obscured disks. Most of these cores are measured or predicted to be SMGs. However, telescopes like *ALMA* or *NOEMA* would only be sensitive to the most obscured part of the galaxy. This study demonstrates the necessity to combine near-IR imaging to sub-mm data to fully grasp the nature of DSFGs.
- 64% of our galaxies are at least weakly lopsided, and 27% strongly lopsided. The lopsidedness could be caused by asymmetric cold gas accretion and minor mergers feeding preferentially one side of the disk, which would, depending on the orientation of the accretion favor a star-forming or quiescent disk. Lopsidedness could also be triggered by a major merger disrupting the disk, and/or via large scale instabilities even if our study favors accretion. The fact that lopsidedness is so common among our sample means that most DSFGs have a complex SFH and do not calmly evolve without any interaction with their environment.
- 23% of the galaxies of our sample have a quiescent disk but a star-forming core. If one of them is compatible with a blue nugget, the others are not. Their observed outside-in quenching could then find its origins in their strong lopsidedness that favors VDI and rapid transportation of gas towards the center or from large scale instabilities and clump migration accreting the gas from the disk to feed it to the core.
- Most of the galaxies have a disk with patches/clumps of different RGB color that are not radially symmetric. The color variations within the disks are mostly driven by dust attenuation. These variations are another indicator that Main Sequence DSFGs have a complex SFH.
- Interestingly, among the quiescent disks, we find evidence of clump-like structures. These clumps are not (or very weakly) star-forming, they are mostly populated by old stars but seem to be to massive to be compared to the globular clusters we observe in the local universe.

This work demonstrates the power of the *JWST* in probing for the first time spatially resolved galaxies in the near-IR at Cosmic Noon, where the only available data was the unresolved images from *Spitzer*/IRAC. This allows reliable studies of quenching and dust attenuation at sub-galactic scales in DSFGs, facilitating the understanding of their morphologies and formation and evolution mechanisms that appear to be more complex than previously thought.

Acknowledgements. CGG acknowledges support from CNES. P.G.P.-G. acknowledges support from Spanish Ministerio de Ciencia e Innovación MCIN/AEI/10.13039/501100011033 through grant PGC2018-093499-B-I00.

References

Apellániz, J. M. 2006, The Astronomical Journal, 131, 1184, arXiv:astro-ph/0510785
Aretxaga, I. 2015, provided by the SAO/NASA Astrophysics Data System
Avni, Y. 1976, The Astrophysical Journal, 210, 642

Bagley, M. B., Finkelstein, S. L., Koekemoer, A. M., et al. 2022, CEERS Epoch 1 NIRCam Imaging: Reduction Methods and Simulations Enabling Early JWST Science Results, arXiv:2211.02495 [astro-ph]

Belli, S., Genzel, R., Schreiber, N. M. F., et al. 2017, The Astrophysical Journal, 841, L6, arXiv:1703.07778 [astro-ph]

Boquien, M., Burgarella, D., Roehlly, Y., et al. 2019, Astronomy & Astrophysics, 622, A103, arXiv:1811.03094 [astro-ph]

Bournaud, F., Combes, F., Jog, C. J., & Puerari, I. 2005, Astronomy & Astrophysics, 438, 507, arXiv:astro-ph/0503314

Bruzual, G. & Charlot, S. 2003, Monthly Notices of the Royal Astronomical Society, 344, 1000, arXiv:astro-ph/0309134

Calabrò, A., Daddi, E., Fensch, J., et al. 2019, Astronomy & Astrophysics, 632, A98, arXiv:1910.01661 [astro-ph]

Calzetti, D., Armus, L., Bohlin, R. C., et al. 2000, The Astrophysical Journal, 533, 682

Casey, C. M., Narayanan, D., & Cooray, A. 2014, Physics Reports, 541, 45, arXiv:1402.1456 [astro-ph]

Chabrier, G. 2003, Publications of the Astronomical Society of the Pacific, 115, 763, arXiv: astro-ph/0304382

Chandar, R., Caputo, M., Linden, S., et al. 2023, The Astrophysical Journal, 943, 142

Charlot, S. & Fall, S. M. 2000, The Astrophysical Journal, 539, 718

Chartab, N., Mobasher, B., Darvish, B., et al. 2020, The Astrophysical Journal, 890, 7

Cid Fernandes, R., Stasinska, G., Mateus, A., & Asari, N. V. 2011, Monthly Notices of the Royal Astronomical Society, 413, 1687, arXiv:1012.4426 [astro-ph]

Cochrane, R. K., Anglés-Alcázar, D., Mercedes-Feliz, J., et al. 2023, The impact of AGN-driven winds on physical and observable galaxy sizes, arXiv:2303.12858 [astro-ph]

Colina, L., Gómez, A. C., Álvarez Márquez, J., et al. 2023, Astronomy & Astrophysics, 673, L6, arXiv:2304.13529 [astro-ph]

Coogan, R. T., Daddi, E., Bail, A. L., et al. 2023, A z=1.85 galaxy group in CEERS: evolved, dustless, massive Intra-Halo Light and a Brightest Group Galaxy in the making, arXiv:2302.08960 [astro-ph]

Daddi, E., Dannerbauer, H., Krips, M., et al. 2009, The Astrophysical Journal, 695, L176, arXiv:0903.3046 [astro-ph]

Daddi, E., Dickinson, M., Morrison, G., et al. 2007, The Astrophysical Journal, 670, 156, arXiv:0705.2831 [astro-ph]

Dekel, A., Sari, R., & Ceverino, D. 2009, The Astrophysical Journal, 703, 785, arXiv:0901.2458 [astro-ph]

Dickinson, M. 2007, 39, 822, provided by the SAO/NASA Astrophysics Data System

Dolfi, A., Gomez, F. A., Monachesi, A., et al. 2023, Lopsidedness as a tracer of early galactic assembly history, arXiv:2306.04639 [astro-ph]

Draine, B. T., Dale, D. A., Bendo, G., et al. 2007, The Astrophysical Journal, 663, 866

Elbaz, D., Daddi, E., Borgne, D. L., et al. 2007, Astronomy & Astrophysics, 468, 33, arXiv:astro-ph/0703653

Elbaz, D., Leiton, R., Nagar, N., et al. 2018, Astronomy & Astrophysics, 616, A110, arXiv:1711.10047 [astro-ph]

Elmegreen, B. G. 1989, The Astrophysical Journal, 344, 306

Elmegreen, B. G. 1994, The Astrophysical Journal, 433, 39

Elmegreen, B. G. 2011, The Astrophysical Journal, 737, 10

Fensch, J. & Bournaud, F. 2021, Monthly Notices of the Royal Astronomical Society, 505, 3579, arXiv:2011.12966 [astro-ph]

Franco, M., Elbaz, D., Zhou, L., et al. 2020, Astronomy & Astrophysics, 643, A30, arXiv:2005.03043 [astro-ph]

Fujimoto, S., Ouchi, M., Shibuya, T., & Nagai, H. 2017, The Astrophysical Journal, 850, 83, arXiv:1703.02138 [astro-ph]

Förster-Schreiber, N. M., Shapley, A. E., Genzel, R., et al. 2011, The Astrophysical Journal, 739, 45, arXiv:1104.0248 [astro-ph]

Gardner, J. P., Mather, J. C., Abbott, R., et al. 2023, publisher: arXiv Version Number: 1

Geach, J. E., Dunlop, J. S., Halpern, M., et al. 2017, Monthly Notices of the Royal Astronomical Society, 465, 1789, arXiv: 1607.03904

Grogin, N. A., Kocevski, D. D., Faber, S. M., et al. 2011, The Astrophysical Journal Supplement Series, 197, 35, arXiv:1105.3753 [astro-ph]

Guo, Y., Giavalisco, M., Cassata, P., et al. 2012, The Astrophysical Journal, 749, 149, arXiv:1110.3801 [astro-ph]

Gómez-Guijarro, C., Elbaz, D., Xiao, M., et al. 2022a, Astronomy & Astrophysics, 658, A43, arXiv:2106.13246 [astro-ph]

Gómez-Guijarro, C., Elbaz, D., Xiao, M., et al. 2022b, Astronomy & Astrophysics, 659, A196, arXiv:2201.02633 [astro-ph]

Hainline, L. J., Blain, A. W., Smail, I., et al. 2011, The Astrophysical Journal, 740, 96

Hodge, J. A., Smail, I., Walter, F., et al. 2019, The Astrophysical Journal, 876, 130, arXiv:1810.12307 [astro-ph]

Hopkins, P. F., Gurvich, A. B., Shen, X., et al. 2023, What Causes The Formation of Disks and End of Bursty Star Formation?, arXiv:2301.08263 [astro-ph]

Huang, R., Battisti, A. J., Grasha, K., et al. 2023, Exploring the Intrinsic Scatter of the Star-Forming Galaxy Main Sequence at redshift 0.5 to 3.0, arXiv:2301.01995 [astro-ph]

Ikarashi, S., Caputi, K. I., Ohta, K., et al. 2017, The Astrophysical Journal, 849, L36

Jiménez-Andrade, E. F., Magnelli, B., Karim, A., et al. 2019, Astronomy & Astrophysics, 625, A114, arXiv:1903.12217 [astro-ph]

Jiménez-Andrade, E. F., Murphy, E. J., Heywood, I., et al. 2021, The Astrophysical Journal, 910, 106, arXiv:2103.07807 [astro-ph]

Jin, S., Daddi, E., Liu, D., et al. 2018, The Astrophysical Journal, 864, 56

Jog, C. J. & Combes, F. 2009, Physics Reports, 471, 75

Kalita, B. S., Daddi, E., Bournaud, F., et al. 2022, Astronomy & Astrophysics, 666, A44, arXiv:2206.05217 [astro-ph]

Kamieneski, P. S., Frye, B. L., Pascale, M., et al. 2023, Are $JWST$/NIRCam color gradients in the lensed $z=2.3$ dusty star-forming galaxy $El~Anzuelo$ due to central dust attenuation or inside-out galaxy growth?, arXiv:2303.05054 [astro-ph]

Kannan, R., Macciò, A. V., Fontanot, F., et al. 2015, Monthly Notices of the Royal Astronomical Society, 452, 4347

Kartaltepe, J. S., Rose, C., Vanderhoof, B. N., et al. 2023, The Astrophysical Journal Letters, 946, L15, arXiv:2210.14713 [astro-ph]

Kodra, D., Andrews, B. H., Newman, J. A., et al. 2022, Optimized Photometric Redshifts for the Cosmic Assembly Near-Infrared Deep Extragalactic Legacy Survey (CANDELS), arXiv:2210.01140 [astro-ph]

Koekemoer, A. M., Faber, S. M., Ferguson, H. C., et al. 2011, The Astrophysical Journal Supplement Series, 197, 36

Kriek, M., Shapley, A. E., Reddy, N. A., et al. 2015, The Astrophysical Journal Supplement Series, 218, 15

Lapiner, S., Dekel, A., Freundlich, J., et al. 2023, Monthly Notices of the Royal Astronomical Society, 522, 4515

Leslie, S. K., Schinnerer, E., Liu, D., et al. 2020, The Astrophysical Journal, 899, 58

Lindegren, L., Klioner, S. A., Hernández, J., et al. 2021, Astronomy & Astrophysics, 649, A2

Liu, D., Daddi, E., Dickinson, M., et al. 2018, The Astrophysical Journal, 853, 172

Lorenz, B., Kriek, M., Shapley, A. E., et al. 2023, An Updated Dust-to-Star Geometry: Dust Attenuation Does Not Depend on Inclination in $1.3\leq z\leq 2.6$ Star-Forming Galaxies from MOSDEF, arXiv:2304.08521 [astro-ph]

Lutz, D., Poglitsch, A., Altieri, B., et al. 2011, Astronomy & Astrophysics, 532, A90

Ma, X., Hopkins, P. F., Faucher-Giguère, C.-A., et al. 2016, Monthly Notices of the Royal Astronomical Society, 456, 2140

Mandelker, N., Dekel, A., Ceverino, D., et al. 2014, Monthly Notices of the Royal Astronomical Society, 443, 3675, arXiv:1311.0013 [astro-ph]

Matthews, L. D., van Driel, W., & Gallagher III, J. S. 1998, The Astronomical Journal, 116, 1169

Miller, T. B., Whitaker, K. E., Nelson, E. J., et al. 2022, Early JWST imaging reveals strong optical and NIR color gradients in galaxies at $z\sim2$ driven mostly by dust, arXiv:2209.12954 [astro-ph]

Momcheva, I. G., Brammer, G. B., van Dokkum, P. G., et al. 2016, The Astrophysical Journal Supplement Series, 225, 27

Nandra, K., Laird, E. S., Aird, J. A., et al. 2015, The Astrophysical Journal Supplement Series, 220, 10, arXiv:1503.09078 [astro-ph]

Noeske, K. G., Weiner, B. J., Faber, S. M., et al. 2007, The Astrophysical Journal, 660, L43, arXiv:astro-ph/0701924

Oliver, S. J., Bock, J., Altieri, B., et al. 2012, Monthly Notices of the Royal Astronomical Society, 424, 1614, arXiv: 1203.2562

Press, W., Teukolski, S., Vetterling, W., & Flannery, B. 1992, Numerical Recipes in C. The Art of Scientific Computing, 2nd edn. (Cambridge Univ. Press)

Puglisi, A., Daddi, E., Liu, D., et al. 2019, The Astrophysical Journal, 877, L23, arXiv:1905.02958 [astro-ph]

Puglisi, A., Daddi, E., Valentino, F., et al. 2021, Monthly Notices of the Royal Astronomical Society, 508, 5217, arXiv:2103.12035 [astro-ph]

Puschnig, J., Hayes, M., Agertz, O., et al. 2023, Unveiling the gravitationally unstable disc of a massive star-forming galaxy using NOEMA and MUSE, arXiv:2303.13858 [astro-ph]

Pérez-González, P. G., Barro, G., Annunziatella, M., et al. 2023, The Astrophysical Journal Letters, 946, L16

Rieke, M. J., Kelly, D. M., Misselt, K., et al. 2023, Publications of the Astronomical Society of the Pacific, 135, 028001

Rodighiero, G., Daddi, E., Baronchelli, I., et al. 2011, The Astrophysical Journal, 739, L40, arXiv:1108.0933 [astro-ph]

Rujopakarn, W., Daddi, E., Rieke, G. H., et al. 2019, The Astrophysical Journal, 882, 107, arXiv:1904.04507 [astro-ph]

Rujopakarn, W., Williams, C. C., Daddi, E., et al. 2023, JWST and ALMA imaging of dust-obscured, massive substructures in a typical $z \sim 3$ star-forming disk galaxy, arXiv:2304.04683 [astro-ph]
Salpeter, E. E. 1955, The Astrophysical Journal, 121, 161
Sancisi, R., Fraternali, F., Oosterloo, T., & van der Hulst, J. M. 2008, The Astronomy and Astrophysics Review, 15, 189, arXiv:0803.0109 [astro-ph]
Schreiber, C., Pannella, M., Elbaz, D., et al. 2015, Astronomy & Astrophysics, 575, A74
Schreiber, N. M. F. & Wuyts, S. 2020, Annual Review of Astronomy and Astrophysics, 58, 661, arXiv:2010.10171 [astro-ph]
Stefanon, M., Yan, H., Mobasher, B., et al. 2017, The Astrophysical Journal Supplement Series, 229, 32
Tacchella, S., Dekel, A., Carollo, C. M., et al. 2016, Monthly Notices of the Royal Astronomical Society, 458, 242, arXiv:1509.00017 [astro-ph]
Tacconi, L. J., Genzel, R., Smail, I., et al. 2008, The Astrophysical Journal, 680, 246, arXiv:0801.3650 [astro-ph]
Tadaki, K.-i., Belli, S., Burkert, A., et al. 2020, The Astrophysical Journal, 901, 74, arXiv:2009.01976 [astro-ph]
Tadaki, K.-i., Kodama, T., Nelson, E. J., et al. 2017, The Astrophysical Journal, 841, L25, arXiv:1703.10197 [astro-ph]
van der Wel, A., Franx, M., van Dokkum, P. G., et al. 2014, The Astrophysical Journal, 788, 28, arXiv:1404.2844 [astro-ph]
van der Wel, A., Martorano, M., Haussler, B., et al. 2023, Stellar Half-Mass Radii of $0.5<z<2.3$ Galaxies: Comparison with JWST/NIRCam Half-Light Radii, arXiv:2307.03264 [astro-ph]
Varela-Lavin, S., Gómez, F. A., Tissera, P. B., et al. 2023, Monthly Notices of the Royal Astronomical Society, stad1724, arXiv:2211.16577 [astro-ph]
Wang, W., Faber, S. M., Liu, F. S., et al. 2017, Monthly Notices of the Royal Astronomical Society, 469, 4063
Whitaker, K. E., Labbé, I., van Dokkum, P. G., et al. 2011, The Astrophysical Journal, 735, 86
Wuyts, S., Schreiber, N. M. F., Genzel, R., et al. 2012, The Astrophysical Journal, 753, 114, arXiv:1203.2611 [astro-ph]
Zaritsky, D., Salo, H., Laurikainen, E., et al. 2013, The Astrophysical Journal, 772, 135
Zavala, J. A., Aretxaga, I., Geach, J. E., et al. 2017, Monthly Notices of the Royal Astronomical Society, 464, 3369
Zavala, J. A., Casey, C. M., Spilker, J., et al. 2022, The Astrophysical Journal, 933, 242, arXiv:2206.02835 [astro-ph]
Zick, T. O., Kriek, M., Shapley, A. E., et al. 2018, The Astrophysical Journal, 867, L16, arXiv:1810.07204 [astro-ph]

---

[1] Université Paris-Saclay, Université Paris Cité, CEA, CNRS, AIM, 91191, Gif-sur-Yvette, France
[2] NSF's National Optical-Infrared Astronomy Research Laboratory, 950 N. Cherry Ave., Tucson, AZ 85719, USA
[3] University of Massachusetts Amherst, 710 North Pleasant Street, Amherst, MA 01003-9305, USA
[4] Kavli Institute for the Physics and Mathematics of the Universe, The University of Tokyo, Kashiwa, 277-8583, Japan
[5] Kavli Institute for Astronomy and Astrophysics, Peking University, Beijing 100871, People's Republic of China
[6] Center for Data-Driven Discovery, Kavli IPMU (WPI), UTIAS, The University of Tokyo, Kashiwa, Chiba 277-8583, Japan
[7] Space Telescope Science Institute, 3700 San Martin Drive, Baltimore, MD 21218, USA
[8] Physics & Astronomy Department, University of Louisville, 40292 KY, Louisville, USA
[9] Department of Physics and Astronomy, University of California, 900 University Ave, Riverside, CA 92521, USA
[10] INAF - Osservatorio Astronomico di Roma, via di Frascati 33, 00078 Monte Porzio Catone, Italy
[11] Racah Institute of Physics, The Hebrew University of Jerusalem, Jerusalem 91904, Israel
[12] University of Massachusetts Amherst, 710 North Pleasant Street, Amherst, MA 01003-9305, USA
[13] Dipartimento di Fisica e Astronomia "G.Galilei", Universitá di Padova, Via Marzolo 8, I-35131 Padova, Italy
[14] INAF–Osservatorio Astronomico di Padova, Vicolo dell'Osservatorio 5, I-35122, Padova, Italy
[15] Department of Astronomy, The University of Texas at Austin, Austin, TX, USA
[16] Centro de Astrobiología (CAB), CSIC-INTA, Ctra. de Ajalvir km 4, Torrejón de Ardoz, E-28850, Madrid, Spain
[17] Astronomy Centre, University of Sussex, Falmer, Brighton BN1 9QH, UK
[18] Institute of Space Sciences and Astronomy, University of Malta, Msida MSD 2080, Malta
[19] Laboratory for Multiwavelength Astrophysics, School of Physics and Astronomy, Rochester Institute of Technology, 84 Lomb Memorial Drive, Rochester, NY 14623, USA
[20] Department of Physics and Astronomy, Texas A&M University, College Station, TX, 77843-4242 USA
[21] George P. and Cynthia Woods Mitchell Institute for Fundamental Physics and Astronomy, Texas A&M University, College Station, TX, 77843-4242 USA
[22] ESA/AURA Space Telescope Science Institute
[23] Astrophysics Science Division, NASA Goddard Space Flight Center, 8800 Greenbelt Rd, Greenbelt, MD 20771, USA

Bibliography

Apellániz, J. M. 2006, The Astronomical Journal, 131, 1184, doi: `10.1086/499158`

Aravena, M., Decarli, R., Walter, F., et al. 2016, The Astrophysical Journal, 833, 68, doi: `10.3847/1538-4357/833/1/68`

Aretxaga, I. 2015. `https://ui.adsabs.harvard.edu/abs/2015IAUGA..2258051A`

Aretxaga, I., Wilson, G. W., Aguilar, E., et al. 2011, Monthly Notices of the Royal Astronomical Society, 415, 3831, doi: `10.1111/j.1365-2966.2011.18989.x`

Avni, Y. 1976, The Astrophysical Journal, 210, 642, doi: `10.1086/154870`

Bagley, M. B., Finkelstein, S. L., Koekemoer, A. M., et al. 2022, CEERS Epoch 1 NIRCam Imaging: Reduction Methods and Simulations Enabling Early JWST Science Results, arXiv. `http://arxiv.org/abs/2211.02495`

Belli, S., Genzel, R., Schreiber, N. M. F., et al. 2017, The Astrophysical Journal, 841, L6, doi: `10.3847/2041-8213/aa70e5`

Berta, S., Magnelli, B., Nordon, R., et al. 2011, Astronomy & Astrophysics, 532, A49, doi: `10.1051/0004-6361/201116844`

Bertin, E., & Arnouts, S. 1996, Astronomy and Astrophysics Supplement Series, 117, 393, doi: `10.1051/aas:1996164`

Biggs, A. D., & Ivison, R. J. 2006, Monthly Notices of the Royal Astronomical Society, 371, 963, doi: `10.1111/j.1365-2966.2006.10730.x`

Boquien, M., Burgarella, D., Roehlly, Y., et al. 2019, Astronomy & Astrophysics, 622, A103, doi: `10.1051/0004-6361/201834156`

Bournaud, F., Combes, F., Jog, C. J., & Puerari, I. 2005, Astronomy & Astrophysics, 438, 507, doi: `10.1051/0004-6361:20052631`

Brammer, G. B., van Dokkum, P. G., & Coppi, P. 2008, doi: `10.48550/ARXIV.0807.1533`

Bruzual, G., & Charlot, S. 2003, Monthly Notices of the Royal Astronomical Society, 344, 1000, doi: `10.1046/j.1365-8711.2003.06897.x`

Béthermin, M., De Breuck, C., Sargent, M., & Daddi, E. 2015, Astronomy & Astrophysics, 576, L9, doi: `10.1051/0004-6361/201525718`

Béthermin, M., Dole, H., Beelen, A., & Aussel, H. 2010, Astronomy and Astrophysics, 512, A78, doi: 10.1051/0004-6361/200913279

Béthermin, M., Le Floc'h, E., Ilbert, O., et al. 2012, Astronomy & Astrophysics, 542, A58, doi: 10.1051/0004-6361/201118698

Calabrò, A., Daddi, E., Fensch, J., et al. 2019, Astronomy & Astrophysics, 632, A98, doi: 10.1051/0004-6361/201935778

Calzetti, D., Armus, L., Bohlin, R. C., et al. 2000, The Astrophysical Journal, 533, 682, doi: 10.1086/308692

Casey, C. M., Narayanan, D., & Cooray, A. 2014, Physics Reports, 541, 45, doi: 10.1016/j.physrep.2014.02.009

Casey, C. M., Chen, C.-C., Cowie, L. L., et al. 2013, Monthly Notices of the Royal Astronomical Society, 436, 1919, doi: 10.1093/mnras/stt1673

Casey, C. M., Kartaltepe, J. S., Drakos, N. E., et al. 2023, COSMOS-Web: An Overview of the JWST Cosmic Origins Survey, arXiv. http://arxiv.org/abs/2211.07865

Cebrián, M., & Trujillo, I. 2014, Monthly Notices of the Royal Astronomical Society, 444, 682, doi: 10.1093/mnras/stu1375

Chabrier, G. 2003, Publications of the Astronomical Society of the Pacific, 115, 763, doi: 10.1086/376392

Chandar, R., Caputo, M., Linden, S., et al. 2023, The Astrophysical Journal, 943, 142, doi: 10.3847/1538-4357/acac96

Charlot, S., & Fall, S. M. 2000, The Astrophysical Journal, 539, 718, doi: 10.1086/309250

Chartab, N., Mobasher, B., Darvish, B., et al. 2020, The Astrophysical Journal, 890, 7, doi: 10.3847/1538-4357/ab61fd

Chen, C.-C., Cowie, L. L., Barger, A. J., et al. 2013, The Astrophysical Journal, 776, 131, doi: 10.1088/0004-637X/776/2/131

Cid Fernandes, R., Stasinska, G., Mateus, A., & Asari, N. V. 2011, Monthly Notices of the Royal Astronomical Society, 413, 1687, doi: 10.1111/j.1365-2966.2011.18244.x

Ciesla, L., Boquien, M., Boselli, A., et al. 2014, Astronomy & Astrophysics, 565, A128, doi: 10.1051/0004-6361/201323248

Clements, D. L., Rigby, E., Maddox, S., et al. 2010, Astronomy and Astrophysics, 518, L8, doi: 10.1051/0004-6361/201014581

Cochrane, R. K., Anglés-Alcázar, D., Mercedes-Feliz, J., et al. 2023, The impact of AGN-driven winds on physical and observable galaxy sizes, arXiv. http://arxiv.org/abs/2303.12858

Colina, L., Gómez, A. C., Álvarez Márquez, J., et al. 2023, Astronomy & Astrophysics, 673, L6, doi: 10.1051/0004-6361/202346535

Conselice, C. J. 2003, The Astrophysical Journal Supplement Series, 147, 1, doi: 10.1086/375001

Coogan, R. T., Daddi, E., Bail, A. L., et al. 2023, A z=1.85 galaxy group in CEERS: evolved, dustless, massive Intra-Halo Light and a Brightest Group Galaxy in the making, arXiv. http://arxiv.org/abs/2302.08960

Cowie, L. L., Barger, A. J., Hsu, L.-Y., et al. 2017, The Astrophysical Journal, 837, 139, doi: 10.3847/1538-4357/aa60bb

Daddi, E., Cimatti, A., Renzini, A., et al. 2004, The Astrophysical Journal, 617, 746, doi: 10.1086/425569

Daddi, E., Dannerbauer, H., Krips, M., et al. 2009, The Astrophysical Journal, 695, L176, doi: 10.1088/0004-637X/695/2/L176

Daddi, E., Dickinson, M., Morrison, G., et al. 2007, The Astrophysical Journal, 670, 156, doi: 10.1086/521818

Daddi, E., Elbaz, D., Walter, F., et al. 2010, The Astrophysical Journal, 714, L118, doi: 10.1088/2041-8205/714/1/L118

Dale, D. A., & Helou, G. 2002, The Astrophysical Journal, 576, 159, doi: 10.1086/341632

Davis, M., Guhathakurta, P., Konidaris, N. P., et al. 2007, The Astrophysical Journal, 660, L1, doi: 10.1086/517931

Dekel, A., & Birnboim, Y. 2006, Monthly Notices of the Royal Astronomical Society, 368, 2, doi: 10.1111/j.1365-2966.2006.10145.x

Dekel, A., Sari, R., & Ceverino, D. 2009, The Astrophysical Journal, 703, 785, doi: 10.1088/0004-637X/703/1/785

Delhaize, J., Smolčić, V., Delvecchio, I., et al. 2017, Astronomy & Astrophysics, 602, A4, doi: 10.1051/0004-6361/201629430

Dickinson, M. 2007, in (Bulletin of the American Astronomical Society), 822. https://ui.adsabs.harvard.edu/abs/2007AAS...211.5216D

Diolaiti, E., Bendinelli, O., Bonaccini, D., et al. 2000, Munich, Germany, 879–888, doi: 10.1117/12.390377

Dolfi, A., Gomez, F. A., Monachesi, A., et al. 2023, Lopsidedness as a tracer of early galactic assembly history, arXiv. http://arxiv.org/abs/2306.04639

Draine, B. T. 2003, The Astrophysical Journal, 598, 1017, doi: 10.1086/379118

Draine, B. T., & Li, A. 2007, The Astrophysical Journal, 657, 810, doi: 10.1086/511055

Draine, B. T., Dale, D. A., Bendo, G., et al. 2007, The Astrophysical Journal, 663, 866, doi: 10.1086/518306

Dunlop, J. S., McLure, R. J., Biggs, A. D., et al. 2017, Monthly Notices of the Royal Astronomical Society, 466, 861, doi: 10.1093/mnras/stw3088

Dyson, J. E., & Williams, D. A. 1997, The Physics of the Interstellar Medium (IOP Publishing Ltd), doi: 10.1887/075030460X

Elbaz, D., Daddi, E., Borgne, D. L., et al. 2007, Astronomy & Astrophysics, 468, 33, doi: 10.1051/0004-6361:20077525

Elbaz, D., Leiton, R., Nagar, N., et al. 2018, Astronomy & Astrophysics, 616, A110, doi: 10.1051/0004-6361/201732370

Elmegreen, B. G. 1989, The Astrophysical Journal, 344, 306, doi: 10.1086/167798

—. 1994, The Astrophysical Journal, 433, 39, doi: 10.1086/174623

—. 2011, The Astrophysical Journal, 737, 10, doi: 10.1088/0004-637X/737/1/10

Fensch, J., & Bournaud, F. 2021, Monthly Notices of the Royal Astronomical Society, 505, 3579, doi: 10.1093/mnras/stab1489

Finkelstein, S. L., Ryan, R. E., Papovich, C., et al. 2015, The Astrophysical Journal, 810, 71, doi: 10.1088/0004-637X/810/1/71

Finkelstein, S. L., Bagley, M. B., Haro, P. A., et al. 2022, A Long Time Ago in a Galaxy Far, Far Away: A Candidate z ~ 12 Galaxy in Early JWST CEERS Imaging, doi: 10.3847/2041-8213/ac966e

Franco, M., Elbaz, D., Zhou, L., et al. 2020, Astronomy & Astrophysics, 643, A30, doi: 10.1051/0004-6361/202038312

Fujimoto, S., Ouchi, M., Shibuya, T., & Nagai, H. 2017, The Astrophysical Journal, 850, 83, doi: 10.3847/1538-4357/aa93e6

Fujimoto, S., Finkelstein, S. L., Burgarella, D., et al. 2022, ALMA FIR View of Ultra High-redshift Galaxy Candidates at $z\sim$ 11-17: Blue Monsters or Low-z Red Interlopers?, arXiv. http://arxiv.org/abs/2211.03896

Förster-Schreiber, N. M., Shapley, A. E., Genzel, R., et al. 2011, The Astrophysical Journal, 739, 45, doi: 10.1088/0004-637X/739/1/45

Galliano, F., Galametz, M., & Jones, A. P. 2018, Annual Review of Astronomy and Astrophysics, 56, 673, doi: 10.1146/annurev-astro-081817-051900

Gardner, J. P., Mather, J. C., Abbott, R., et al. 2023, doi: 10.48550/ARXIV.2304.04869

Geach, J. E., Dunlop, J. S., Halpern, M., et al. 2017, Monthly Notices of the Royal Astronomical Society, 465, 1789, doi: 10.1093/mnras/stw2721

Grogin, N. A., Kocevski, D. D., Faber, S. M., et al. 2011, The Astrophysical Journal Supplement Series, 197, 35, doi: 10.1088/0067-0049/197/2/35

Gruppioni, C., Pozzi, F., Rodighiero, G., et al. 2013, Monthly Notices of the Royal Astronomical Society, 432, 23, doi: 10.1093/mnras/stt308

Guo, Y., Giavalisco, M., Cassata, P., et al. 2012, The Astrophysical Journal, 749, 149, doi: 10.1088/0004-637X/749/2/149

Gómez-Guijarro, C., Elbaz, D., Xiao, M., et al. 2022a, Astronomy & Astrophysics, 659, A196, doi: 10.1051/0004-6361/202142352

—. 2022b, Astronomy & Astrophysics, 658, A43, doi: 10.1051/0004-6361/202141615

Hainline, L. J., Blain, A. W., Smail, I., et al. 2011, The Astrophysical Journal, 740, 96, doi: 10.1088/0004-637X/740/2/96

Hodge, J. A., Smail, I., Walter, F., et al. 2019, The Astrophysical Journal, 876, 130, doi: 10.3847/1538-4357/ab1846

Hopkins, P. F., Gurvich, A. B., Shen, X., et al. 2023, What Causes The Formation of Disks and End of Bursty Star Formation?, arXiv. http://arxiv.org/abs/2301.08263

Huang, R., Battisti, A. J., Grasha, K., et al. 2023, Exploring the Intrinsic Scatter of the Star-Forming Galaxy Main Sequence at redshift 0.5 to 3.0, arXiv. http://arxiv.org/abs/2301.01995

Hurley, P. D., Oliver, S., Betancourt, M., et al. 2017, Monthly Notices of the Royal Astronomical Society, 464, 885, doi: 10.1093/mnras/stw2375

Ikarashi, S., Caputi, K. I., Ohta, K., et al. 2017, The Astrophysical Journal, 849, L36, doi: 10.3847/2041-8213/aa9572

Ivison, R. J., Chapman, S. C., Faber, S. M., et al. 2007, The Astrophysical Journal, 660, L77, doi: 10.1086/517917

Ivison, R. J., Lewis, A. J. R., Weiss, A., et al. 2016, The Astrophysical Journal, 832, 78, doi: 10.3847/0004-637X/832/1/78

Jarrett, T. H., Masci, F., Tsai, C. W., et al. 2013, The Astronomical Journal, 145, 6, doi: 10.1088/0004-6256/145/1/6

Jiménez-Andrade, E. F., Magnelli, B., Karim, A., et al. 2019, Astronomy & Astrophysics, 625, A114, doi: 10.1051/0004-6361/201935178

Jiménez-Andrade, E. F., Murphy, E. J., Heywood, I., et al. 2021, The Astrophysical Journal, 910, 106, doi: 10.3847/1538-4357/abe876

Jin, S., Daddi, E., Liu, D., et al. 2018, The Astrophysical Journal, 864, 56, doi: 10.3847/1538-4357/aad4af

Jog, C. J., & Combes, F. 2009, Physics Reports, 471, 75, doi: 10.1016/j.physrep.2008.12.002

Kalita, B. S., Daddi, E., Bournaud, F., et al. 2022, Astronomy & Astrophysics, 666, A44, doi: 10.1051/0004-6361/202243100

Kamieneski, P. S., Frye, B. L., Pascale, M., et al. 2023, Are $JWST$/NIRCam color gradients in the lensed $z=2.3$ dusty star-forming galaxy $El~Anzuelo$ due to central dust attenuation or inside-out galaxy growth?, arXiv. http://arxiv.org/abs/2303.05054

Kannan, R., Macciò, A. V., Fontanot, F., et al. 2015, Monthly Notices of the Royal Astronomical Society, 452, 4347, doi: 10.1093/mnras/stv1633

Karim, A., Schinnerer, E., Martínez-Sansigre, A., et al. 2011, The Astrophysical Journal, 730, 61, doi: 10.1088/0004-637X/730/2/61

Karim, A., Swinbank, A. M., Hodge, J. A., et al. 2013, Monthly Notices of the Royal Astronomical Society, 432, 2, doi: 10.1093/mnras/stt196

Kartaltepe, J. S., Rose, C., Vanderhoof, B. N., et al. 2023, The Astrophysical Journal Letters, 946, L15, doi: 10.3847/2041-8213/acad01

Kocevski, D. D., Barro, G., McGrath, E. J., et al. 2023, The Astrophysical Journal Letters, 946, L14, doi: 10.3847/2041-8213/acad00

Kodra, D., Andrews, B. H., Newman, J. A., et al. 2022, Optimized Photometric Redshifts for the Cosmic Assembly Near-Infrared Deep Extragalactic Legacy Survey (CANDELS), arXiv. http://arxiv.org/abs/2210.01140

Koekemoer, A. M., Faber, S. M., Ferguson, H. C., et al. 2011, The Astrophysical Journal Supplement Series, 197, 36, doi: 10.1088/0067-0049/197/2/36

Kriek, M., Shapley, A. E., Reddy, N. A., et al. 2015, The Astrophysical Journal Supplement Series, 218, 15, doi: 10.1088/0067-0049/218/2/15

Kriek, M., van Dokkum, P. G., Labbé, I., et al. 2018, Astrophysics Source Code Library, ascl:1803.008. https://ui.adsabs.harvard.edu/abs/2018ascl.soft03008K

Lapiner, S., Dekel, A., Freundlich, J., et al. 2023, Monthly Notices of the Royal Astronomical Society, 522, 4515, doi: 10.1093/mnras/stad1263

Lee, N., Sanders, D. B., Casey, C. M., et al. 2013, The Astrophysical Journal, 778, 131, doi: 10.1088/0004-637X/778/2/131

Leslie, S. K., Schinnerer, E., Liu, D., et al. 2020, The Astrophysical Journal, 899, 58, doi: 10.3847/1538-4357/aba044

Lindegren, L., Klioner, S. A., Hernández, J., et al. 2021, Astronomy & Astrophysics, 649, A2, doi: 10.1051/0004-6361/202039709

Liu, D., Daddi, E., Dickinson, M., et al. 2018, The Astrophysical Journal, 853, 172, doi: 10.3847/1538-4357/aaa600

Lorenz, B., Kriek, M., Shapley, A. E., et al. 2023, An Updated Dust-to-Star Geometry: Dust Attenuation Does Not Depend on Inclination in $1.3\leq z\leq 2.6$ Star-Forming Galaxies from MOSDEF, arXiv. http://arxiv.org/abs/2304.08521

Lutz, D., Poglitsch, A., Altieri, B., et al. 2011, Astronomy & Astrophysics, 532, A90, doi: 10.1051/0004-6361/201117107

Ma, X., Hopkins, P. F., Faucher-Giguère, C.-A., et al. 2016, Monthly Notices of the Royal Astronomical Society, 456, 2140, doi: 10.1093/mnras/stv2659

Madau, P., & Dickinson, M. 2014, Annual Review of Astronomy and Astrophysics, 52, 415, doi: 10.1146/annurev-astro-081811-125615

Magdis, G. E., Daddi, E., Béthermin, M., et al. 2012, The Astrophysical Journal, 760, 6, doi: 10.1088/0004-637X/760/1/6

Magnelli, B., Elbaz, D., Chary, R. R., et al. 2009, Astronomy & Astrophysics, 496, 57, doi: 10.1051/0004-6361:200811443

Magnelli, B., Popesso, P., Berta, S., et al. 2013, Astronomy & Astrophysics, 553, A132, doi: 10.1051/0004-6361/201321371

Magnelli, B., Ivison, R. J., Lutz, D., et al. 2015, Astronomy & Astrophysics, 573, A45, doi: 10.1051/0004-6361/201424937

Mandelker, N., Dekel, A., Ceverino, D., et al. 2014, Monthly Notices of the Royal Astronomical Society, 443, 3675, doi: 10.1093/mnras/stu1340

Matthews, L. D., van Driel, W., & Gallagher III, J. S. 1998, The Astronomical Journal, 116, 1169, doi: 10.1086/300492

Miller, T. B., Whitaker, K. E., Nelson, E. J., et al. 2022, Early JWST imaging reveals strong optical and NIR color gradients in galaxies at $z\sim2$ driven mostly by dust, arXiv. http://arxiv.org/abs/2209.12954

Momcheva, I. G., Brammer, G. B., van Dokkum, P. G., et al. 2016, The Astrophysical Journal Supplement Series, 225, 27, doi: 10.3847/0067-0049/225/2/27

Mullaney, J. R., Alexander, D. M., Goulding, A. D., & Hickox, R. C. 2011, Monthly Notices of the Royal Astronomical Society, 414, 1082, doi: 10.1111/j.1365-2966.2011.18448.x

Murray, N., Quataert, E., & Thompson, T. A. 2005, The Astrophysical Journal, 618, 569, doi: 10.1086/426067

Nandra, K., Laird, E. S., Aird, J. A., et al. 2015, The Astrophysical Journal Supplement Series, 220, 10, doi: 10.1088/0067-0049/220/1/10

Noeske, K. G., Weiner, B. J., Faber, S. M., et al. 2007, The Astrophysical Journal, 660, L43, doi: 10.1086/517926

Oliver, S. J., Wang, L., Smith, A. J., et al. 2010, Astronomy and Astrophysics, 518, L21, doi: 10.1051/0004-6361/201014697

Oliver, S. J., Bock, J., Altieri, B., et al. 2012, Monthly Notices of the Royal Astronomical Society, 424, 1614, doi: 10.1111/j.1365-2966.2012.20912.x

Oteo, I., Zwaan, M. A., Ivison, R. J., Smail, I., & Biggs, A. D. 2016, The Astrophysical Journal, 822, 36, doi: 10.3847/0004-637X/822/1/36

Padovani, P., Alexander, D. M., Assef, R. J., et al. 2017, The Astronomy and Astrophysics Review, 25, 2, doi: 10.1007/s00159-017-0102-9

Pannella, M., Carilli, C. L., Daddi, E., et al. 2009, The Astrophysical Journal, 698, L116, doi: 10.1088/0004-637X/698/2/L116

Peng, C. Y., Ho, L. C., Impey, C. D., & Rix, H.-W. 2002, The Astronomical Journal, 124, 266, doi: 10.1086/340952

—. 2010, The Astronomical Journal, 139, 2097, doi: 10.1088/0004-6256/139/6/2097

Pilbratt, G. L., Riedinger, J. R., Passvogel, T., et al. 2010, Astronomy and Astrophysics, 518, L1, doi: 10.1051/0004-6361/201014759

Press, W., Teukolski, S., Vetterling, W., & Flannery, B. 1992, Numerical Recipes in C. The Art of Scientific Computing, 2nd edn. (Cambridge Univ. Press)

Puglisi, A., Daddi, E., Renzini, A., et al. 2017, The Astrophysical Journal, 838, L18, doi: 10.3847/2041-8213/aa66c9

Puglisi, A., Daddi, E., Liu, D., et al. 2019, The Astrophysical Journal, 877, L23, doi: 10.3847/2041-8213/ab1f92

Puglisi, A., Daddi, E., Valentino, F., et al. 2021, Monthly Notices of the Royal Astronomical Society, 508, 5217, doi: 10.1093/mnras/stab2914

Puschnig, J., Hayes, M., Agertz, O., et al. 2023, Unveiling the gravitationally unstable disc of a massive star-forming galaxy using NOEMA and MUSE, arXiv. http://arxiv.org/abs/2303.13858

Pérez-González, P. G., Barro, G., Annunziatella, M., et al. 2023, The Astrophysical Journal Letters, 946, L16, doi: 10.3847/2041-8213/acb3a5

Rieke, M. J., Kelly, D. M., Misselt, K., et al. 2023, Publications of the Astronomical Society of the Pacific, 135, 028001, doi: 10.1088/1538-3873/acac53

Rodighiero, G., Daddi, E., Baronchelli, I., et al. 2011, The Astrophysical Journal, 739, L40, doi: 10.1088/2041-8205/739/2/L40

Rujopakarn, W., Daddi, E., Rieke, G. H., et al. 2019, The Astrophysical Journal, 882, 107, doi: 10.3847/1538-4357/ab3791

Rujopakarn, W., Williams, C. C., Daddi, E., et al. 2023, JWST and ALMA imaging of dust-obscured, massive substructures in a typical $z \sim 3$ star-forming disk galaxy, arXiv. http://arxiv.org/abs/2304.04683

Salpeter, E. E. 1955, The Astrophysical Journal, 121, 161, doi: 10.1086/145971

Sancisi, R., Fraternali, F., Oosterloo, T., & van der Hulst, J. M. 2008, The Astronomy and Astrophysics Review, 15, 189, doi: 10.1007/s00159-008-0010-0

Sargent, M. T., Daddi, E., Béthermin, M., et al. 2014, The Astrophysical Journal, 793, 19, doi: 10.1088/0004-637X/793/1/19

Schreiber, C., Pannella, M., Elbaz, D., et al. 2015, Astronomy & Astrophysics, 575, A74, doi: 10.1051/0004-6361/201425017

Schreiber, N. M. F., & Wuyts, S. 2020, Annual Review of Astronomy and Astrophysics, 58, 661, doi: 10.1146/annurev-astro-032620-021910

Shapiro, K. L., Genzel, R., Schreiber, N. M. F., et al. 2008, The Astrophysical Journal, 682, 231, doi: 10.1086/587133

Shirley, R., Duncan, K., Varillas, M. C. C., et al. 2021, Monthly Notices of the Royal Astronomical Society, 507, 129, doi: 10.1093/mnras/stab1526

Stefanon, M., Yan, H., Mobasher, B., et al. 2017, The Astrophysical Journal Supplement Series, 229, 32, doi: 10.3847/1538-4365/aa66cb

Tacchella, S., Dekel, A., Carollo, C. M., et al. 2016, Monthly Notices of the Royal Astronomical Society, 458, 242, doi: 10.1093/mnras/stw303

Tacconi, L. J., Genzel, R., Smail, I., et al. 2008, The Astrophysical Journal, 680, 246, doi: 10.1086/587168

Tadaki, K.-i., Kodama, T., Nelson, E. J., et al. 2017, The Astrophysical Journal, 841, L25, doi: 10.3847/2041-8213/aa7338

Tadaki, K.-i., Belli, S., Burkert, A., et al. 2020, The Astrophysical Journal, 901, 74, doi: 10.3847/1538-4357/abaf4a

Tan, Q., Daddi, E., Magdis, G., et al. 2014, Astronomy & Astrophysics, 569, A98, doi: 10.1051/0004-6361/201423905

Toomre, A. 1964, The Astrophysical Journal, 139, 1217, doi: 10.1086/147861

van der Wel, A., Franx, M., van Dokkum, P. G., et al. 2014, The Astrophysical Journal, 788, 28, doi: 10.1088/0004-637X/788/1/28

van der Wel, A., Martorano, M., Haussler, B., et al. 2023, Stellar Half-Mass Radii of $0.5<z<2.3$ Galaxies: Comparison with JWST/NIRCam Half-Light Radii, arXiv. http://arxiv.org/abs/2307.03264

Varela-Lavin, S., Gómez, F. A., Tissera, P. B., et al. 2023, Monthly Notices of the Royal Astronomical Society, stad1724, doi: `10.1093/mnras/stad1724`

Wang, W., Faber, S. M., Liu, F. S., et al. 2017, Monthly Notices of the Royal Astronomical Society, 469, 4063, doi: `10.1093/mnras/stx1148`

Whitaker, K. E., Labbé, I., van Dokkum, P. G., et al. 2011, The Astrophysical Journal, 735, 86, doi: `10.1088/0004-637X/735/2/86`

Wuyts, S., Schreiber, N. M. F., Genzel, R., et al. 2012, The Astrophysical Journal, 753, 114, doi: `10.1088/0004-637X/753/2/114`

Yun, M. S., Reddy, N. A., & Condon, J. J. 2001, The Astrophysical Journal, 554, 803, doi: `10.1086/323145`

Zaritsky, D., Salo, H., Laurikainen, E., et al. 2013, The Astrophysical Journal, 772, 135, doi: `10.1088/0004-637X/772/2/135`

Zavala, J. A., Aretxaga, I., Geach, J. E., et al. 2017, Monthly Notices of the Royal Astronomical Society, 464, 3369, doi: `10.1093/mnras/stw2630`

Zavala, J. A., Casey, C. M., Spilker, J., et al. 2022, The Astrophysical Journal, 933, 242, doi: `10.3847/1538-4357/ac7560`

Zavala, J. A., Buat, V., Casey, C. M., et al. 2023, Dusty Starbursts Masquerading as Ultra-high Redshift Galaxies in JWST CEERS Observations, doi: `10.3847/2041-8213/acacfe`

Zick, T. O., Kriek, M., Shapley, A. E., et al. 2018, The Astrophysical Journal, 867, L16, doi: `10.3847/2041-8213/aae887`